

**On the development  
and application  
of linear stability methods  
for two-phase shear flows**

**Simon Schmidt**





# **On the development and application of linear stability methods for two-phase shear flows**

vorgelegt von

M. Sc.

**Simon Schmidt**

ORCID: 0000-0003-3607-4944

an der Fakultät V – Verkehrs- und Maschinensysteme  
der Technischen Universität Berlin  
zur Erlangung des akademischen Grades

Doktor der Ingenieurwissenschaften

– Dr.-Ing. –

genehmigte Dissertation

## **Promotionsausschuss**

Vorsitzende: Prof. Dr. Neda Djordjevic

Gutachter: Prof. Dr. Kilian Oberleithner

Gutachter: Prof. Dr. Lutz Lesshafft

Gutachter: Prof. Dr. Stéphane Popinet

Gutachter: Prof. Dr. Oliver Schmidt

Tag der wissenschaftlichen Aussprache: 14. März 2022

Berlin 2022



# Vorwort

Der Grundstein für diese Dissertation wurde während meiner Arbeit bei der *FDX Fluid Dynamix GmbH* gelegt. Als ich Anfang 2016 anfang dort als Student zu arbeiten, war *FDX* ein junges Unternehmen, das von drei ehemaligen Doktoranden am Institut für experimentelle Strömungsmechanik der TU Berlin gegründet wurde. Sie forschten an der Verwendung fluidischer Oszillatoren zur Nutzung als Düsen, um oszillierende flüssige Strahlen zu erzeugen. Bei meiner studentischen Arbeit und während meiner Masterarbeit, die ich dort schrieb, entdeckte ich die Welt der numerischen Simulation zweiphasiger Strömungen, die mich dann sogleich in ihren Bann zog. Unser Büro befand zu dieser Zeit noch im Institutsgebäude und so lief ich jeden Tag an diversen Postern zu den Forschungsarbeiten der anderen Wissenschaftler am Institut vorbei. Einige davon handelten von Strömungsinstabilitäten und kohärenten Strukturen, die mittels linearer Stabilitätsanalyse untersucht wurden. Lineare Stabilitätsanalyse: Davon hatte ich in Vorlesungen gehört und wusste so ungefähr Bescheid, aber so richtig greifbar war es nicht. Das faszinierte mich. Es wäre doch spannend zweiphasige Strömungen und lineare Stabilitätsanalyse zusammenzubringen! Als ich den Entschluss fasste, zu promovieren, klopfte ich an der Bürotür von Kilian Oberleithner, er war Autor der ganzen Poster und angehender Juniorprofessor, und erzählte ihm von meiner Idee. So begann ich dann im Sommer 2018 mit der Arbeit an dieser Dissertation.

Mein Dank gilt allen voran Kilian Oberleithner, der sich bereit erklärt hat mein Doktorvater zu sein und mich stets unterstützt hat mit guten Ratschlägen und mir zu jeder Zeit das nötige Vertrauen für meine Ideen entgegenbrachte. Sein freundschaftlicher Umgang ist unschätzbar und machte die Zeit meiner Forschung sehr angenehm. Auch prägte sein Drang, die Dinge stets im Detail verstehen zu wollen, meine Arbeit enorm. Immer wenn ich ein Ergebnis oder Phänomen einfach so hinnahm, fragte er "warum?" und wir gingen der Sache auf den Grund.

Auch gilt mein Dank den drei Gründern von *FDX*, Oliver Krüger, Bernhard Bobusch und Jens Wintering, sowie allen anderen Mitarbeiterinnen und Mitarbeitern. Vielen Dank, dass ich neben meiner Promotion weiter bei euch arbeiten konnte und ihr mir immer die Freiheit gegeben habt, in stressigen Phasen, vor nahenden Deadlines, den Fokus auf meiner Forschung zu behalten. Die Arbeit für die Firma ist stets eine willkommene Abwechslung gewesen, wenn ich während der Promotion mal wieder nicht weiter wusste.

Dank gebührt auch Outi Tammissola, Professorin an der *KTH* in Stockholm, und Lutz Lesshafft, Professor an der *École polytechnique* in Palaiseau, mit deren wertvoller Hilfe das zweite und zentrale Paper dieser Arbeit entstanden ist.

Zu guter Letzt, möchte ich meiner Familie danken, vor allem meiner Mutter, der diesen Moment zu erleben, leider nicht mehr vergönnt war, sowie Tra Giang. Ohne deine Geduld

und die Stütze, die du bist, wenn die Dinge nicht so liefen, wie ich sie mir wünsche, hätte ich diese Arbeit vermutlich nie zu Ende geschrieben.

Ich möchte mich außerdem recht herzlich beim Land Berlin für die Gewährung des Elsa-Neumann-Stipendiums bedanken, welches mir die Finanzierung dieser Promotion ermöglicht hat.

# Zusammenfassung

Zweiphasenströmungen sind für eine Vielzahl von industriellen Anwendungen von großer Bedeutung. Sie treten beispielsweise überall dort auf, wo eine Flüssigkeit verteilt wird, sei es der flüssige Kraftstoff in einem Verbrennungsmotor oder die Tinte in einem Tintenstrahldrucker. Sie sind auch bei der Papierherstellung oder als Manifestation von Kavitation in Wasserturbinen unter Teil- oder Vollastbedingungen von Bedeutung. Folglich ist es wichtig, diese Strömungen genau modellieren zu können, um eine solide Kenntnis ihrer physikalischen Grundlagen und der Feinheiten zu erlangen, die durch die Wechselwirkung der beiden Phasen entstehen. Insbesondere ist es notwendig, die lineare und nichtlineare Dynamik dieser Strömungen analysieren zu können, da diese den Schlüssel nicht nur für ein schlüssiges Verständnis der auftretenden Strömungsinstabilitäten, sondern auch für eine erfolgreiche Strömungskontrolle darstellt. Zu diesem Zweck ist die Entwicklung effizienter und genauer numerischer Modelle unerlässlich. Neben der Simulation der vollständig nichtlinearen Strömung, hat sich die lineare Stabilitätsanalyse als unschätzbare Werkzeug zur Analyse der linearen Strömungsdynamik erwiesen. In den letzten Jahren wurden erhebliche Fortschritte bei der Entwicklung solcher Methoden für die Analyse einphasiger Strömungen erzielt. Mit der zunehmenden Verfügbarkeit von Rechenleistung ist es möglich geworden, die genaue lineare Modellierung von großen dreidimensionalen und turbulenten Strömungen mit Hilfe der globalen Stabilitätsanalyse und der Stabilitätsanalyse des mittleren Feldes zu erleichtern. Die Entwicklung dieser Methoden für die lineare Analyse von Zweiphasenströmungen hinkt jedoch hinterher.

Ziel dieser Arbeit ist es, einen Schritt in Richtung der Entwicklung und Anwendung dieser Werkzeuge für Zweiphasenströmungsprobleme zu machen. Die Schwerpunkte liegen dabei auf der Anwendung der Stabilitätsanalyse des mittleren Feldes für Zweiphasenströmungen und der Entwicklung eines flexiblen Frameworks für die globale lineare Stabilitätsanalyse von Zweiphasenströmungen. Das Potenzial des entwickelten globalen Stabilitätslösers wird anhand der Anwendung auf eine komplexe dreidimensionale Strömung demonstriert.

Um das Potenzial der Stabilitätsanalyse des mittleren Feldes für Zweiphasenströmungen zu bewerten, wird die lineare Dynamik eines extern angeregten, planaren Flüssigkeits-/Gasstrahls in einem lokalen Stabilitätsframework analysiert und ein Modell entwickelt, das die Position der Phasengrenzfläche des Strahls in der zeitlich gemittelten Strömung berücksichtigt. Mit dem entwickelten Modell kann die Genauigkeit der linearen Analyse erheblich verbessert werden, und es wird eine ausgezeichnete Übereinstimmung der linearen und nichtlinearen Ergebnisse für eine geringe Anregungsamplitude des Strahls erzielt. Bei größeren Anregungsamplituden wird die Strömung jedoch von der nichtlinearen Dynamik bestimmt, was zu einer Verschlechterung der Genauigkeit des

linearen Modells führt. Außerdem entkräftet die Nichtparallelität der Strömung die Annahmen, die für die Anwendung eines lokalen Stabilitätsframeworks gemacht wurden. Folglich wird für die Analyse von nichtparallelen zwei- und dreidimensionalen Strömungen ein matrixfreies Framework entwickelt, das eine flexible und effiziente Analyse solcher Strömungen ermöglicht. Zu diesem Zweck wird ein hochgenauer DNS-Löser, der Zweiphasenströmungen simulieren kann, linearisiert. Lineare globale Moden werden durch Zeitintegration des linearisierten Löser in Verbindung mit einer Arnoldi-Methode berechnet. Das Potenzial des Löser wird demonstriert, indem zunächst lineare globale Moden einer planaren Zweiphasen-Nachlaufströmung berechnet werden, die allein durch die Wirkung der Oberflächenspannung destabilisiert werden. Dies erfordert eine genaue Darstellung der Phasengrenzfläche und Oberflächenspannung für eine erfolgreiche Berechnung. Die Analyse zeigt eine reichhaltige lineare Dynamik durch die Destabilisierung mehrerer globaler Moden auf. Ein Vergleich mit den Ergebnissen nichtlinearer Simulationen zeigt eine hervorragende Übereinstimmung. Schließlich wird die lineare Dynamik einer laminaren zweiphasigen Drallströmung mit dem entwickelten Löser analysiert. Die Analyse wird ergänzt durch die Durchführung nichtlinearer Simulationen, wodurch die Grundlage für eine umfassende Analyse der nichtlinearen Dynamik neben der linearen Analyse geschaffen wird. Die lineare Analyse zeigt die gleichzeitige Destabilisierung zweier globaler Moden, einer einfach und einer doppelt helikalen, die zu einer starken resonanten triadischen Wechselwirkung in der nichtlinearen Strömung führen. Bei Erhöhung des Dralls führt die Bifurkation zusätzlicher Moden zu einer Wechselwirkungskaskade in der nichtlinearen Strömung und dem Auftreten einer Vielzahl zusätzlicher Moden. Die Analyse demonstriert das Potenzial des in dieser Arbeit entwickelten globalen Stabilitätslöser für die Analyse komplexer dreidimensionaler Strömungen und liefert darüber hinaus wichtige Erkenntnisse über die Dynamik zweiphasiger Drallströmungen.

# Abstract

Two phase flows are of significant importance for a wide range of industrial applications. They, for instance, occur wherever a liquid is distributed, be it the liquid fuel inside a combustion engine or the ink from an ink-jet printer. They are also relevant in the paper making process or as a manifestation of cavitation in hydro turbines under part or full load conditions. As a consequence, it is important to be able to accurately model these flows in order to gain a solid knowledge of their physical fundamentals and the intricacies, introduced by the interaction of the two phases. In particular, it is necessary, to be able to analyse the linear and nonlinear dynamics of these flows, as they hold the key to not only forming a conclusive understanding of the occurring flow instabilities but also for a successful flow control. To this end, the development of efficient and accurate numerical models is essential. Besides simulation of the full nonlinear flow, linear stability analysis has proven as an invaluable tool to analyse linear flow dynamics. In recent years, considerable advances have been made in developing such methods for the analysis of single-phase flows. With the ever-increasing availability of computational power, it has become possible to facilitate accurate linear modelling of large-scale three-dimensional and turbulent flows by means of global stability analysis and mean field stability analysis. However, the development of these methods for the linear analysis of two-phase flows lags behind.

This thesis aims to take a step towards development and application of these tools for two-phase flow problems. A focus is set on the application of mean field stability analysis for two-phase flows and the development of a flexible framework for the global linear stability analysis of two-phase flows. The potential of the global stability solver is demonstrated with the application to a complex three-dimensional flow.

To assess the potential of mean field stability analysis for two-phase flows, the linear dynamics of an externally forced, plane liquid/gas jet are analysed in a local framework and a model is developed to account for the interface position of the jet in the time-averaged flow. With the developed model, the accuracy of the linear analysis can be substantially improved and an excellent agreement of linear and nonlinear results is obtained for a low amplitude forcing of the jet. For larger forcing amplitudes, however, nonlinear dynamics govern the flow, thus leading to a deterioration of the accuracy of the linear model. Further, the non-parallelity of the flow invalidates the assumptions made for the application of a local stability framework.

Consequently, for the analysis of non-parallel two- and three-dimensional flows, a matrix-free framework is developed which allows for a flexible and efficient analysis of such flows. To this end, a highly accurate DNS solver, capable of simulating two-phase flows, is linearised. Linear global modes are computed by time-stepping of the linearised solver in

conjunction with an Arnoldi method. The potential of the solver is demonstrated by first computing linear global modes of a plane two-phase wake flow, that is destabilised solely through the action of surface tension. This requires an accurate representation of interface and surface tension for a successful analysis. The analysis reveals a rich linear dynamics through the destabilisation of several global modes. A comparison with the results from nonlinear simulations shows an excellent agreement. Finally, the linear dynamics of a laminar two-phase swirling flow is analysed by using the developed solver. The analysis is accompanied by performing accurate nonlinear simulations, thus providing the basis for a comprehensive analysis of the nonlinear dynamics alongside the linear computations. The linear analysis reveals the simultaneous destabilisation of two global modes, single helical and double helical, that lead to a strong resonant triadic interaction in the nonlinear flow. At larger swirl, the bifurcation of additional modes leads to an interaction cascade in the nonlinear flow and the emergence of a variety of additional modes. The study demonstrates the potential of the global stability framework, developed in this thesis, for the analysis of complex three-dimensional flows and further yields important insights into the dynamics of two-phase swirling flows.

# Contents

<b>Vorwort</b>	<b>v</b>
<b>Zusammenfassung</b>	<b>vii</b>
<b>Abstract</b>	<b>ix</b>
<b>Contents</b>	<b>xi</b>
<b>1 Introduction</b>	<b>1</b>
1.1 Motivation: Cavitation in hydro turbines . . . . .	1
1.1.1 Hydro power as a pillar for clean energy . . . . .	1
1.1.2 The cavitating vortex rope in Francis turbines . . . . .	2
1.1.3 Avenues towards modelling the CVR as a global mode . . . . .	3
1.2 Instabilities in two-phase shear flow . . . . .	5
1.2.1 A note on terminology . . . . .	5
1.2.2 Instabilities of a liquid jet . . . . .	6
1.3 Modelling of immiscible two-phase flows . . . . .	7
1.3.1 Governing equations . . . . .	7
1.3.2 Numerical modelling . . . . .	8
1.4 Linear stability analysis of immiscible two-phase flows . . . . .	9
1.4.1 Local analysis . . . . .	10
1.4.2 Global analysis . . . . .	12
1.4.3 Mean flow stability . . . . .	14
1.5 Nonlinear dynamics of incompressible flow . . . . .	15
1.6 Outline of the thesis . . . . .	17
<b>2 Instability of forced planar liquid jets: mean field analysis and nonlinear simulation</b>	<b>19</b>
2.1 Introduction . . . . .	20
2.2 Nonlinear simulation of a liquid jet . . . . .	21
2.2.1 Problem formulation . . . . .	23
2.2.2 General jet evolution . . . . .	25
2.3 Linear stability model . . . . .	27
2.3.1 Perturbation and mean flow equations . . . . .	27
2.3.2 Solution method and validation . . . . .	29
2.3.3 Mean flow configuration and parameterisation . . . . .	32
2.3.4 General stability properties of the jet . . . . .	34

2.4	Comparison of nonlinear simulation and linear stability model . . . . .	37
2.4.1	Stream-wise and cross-wise eigenfunctions . . . . .	37
2.4.2	Growth rates and phase velocity . . . . .	38
2.4.3	Relation to previous studies on the stability of forced liquid jets . . . . .	40
2.5	Interaction of the fundamental wave with higher harmonics . . . . .	41
2.5.1	Vorticity dynamics . . . . .	47
2.6	Summary and conclusions . . . . .	49
2.7	Appendix . . . . .	50
2.7.1	Derivation of the conditions for stress continuity . . . . .	50
2.7.2	Convergence analysis of the linear stability model . . . . .	51
2.7.3	Flow conditions of the two-layer Poiseuille flow by [78] . . . . .	51
2.7.4	Stability maps with the scaling of [21] . . . . .	52
2.7.5	The energy budget for spatial modes in two-phase flows . . . . .	52
2.7.6	Comparison of DNS and the base flow model . . . . .	53
2.7.7	Illustration of the Fourier modes . . . . .	53
<b>3</b>	<b>Global stability and nonlinear dynamics of wake flows with a two-fluid interface</b>	<b>55</b>
3.1	Introduction . . . . .	56
3.2	Numerical methods for two-phase flows . . . . .	57
3.2.1	Governing equations for interfacial two-phase flow . . . . .	57
3.2.2	Interface representations . . . . .	58
3.2.3	Discretisation in Basilisk . . . . .	60
3.3	Linearisation procedure . . . . .	60
3.3.1	Derivation of the linearised equations . . . . .	60
3.3.2	Implementation of linearised advection and diffusion terms . . . . .	62
3.3.3	Implementation of linearised interface advection . . . . .	62
3.3.4	Implementation of the linearised surface tension force . . . . .	64
3.4	Formulation and solution of the eigenvalue problem . . . . .	65
3.4.1	Eigenvalue Problem . . . . .	65
3.4.2	Iterative Solution . . . . .	66
3.5	Global modes of a planar wake under the influence of surface tension . . . . .	66
3.5.1	Nonlinear simulation . . . . .	66
3.5.2	Base flows . . . . .	70
3.5.3	Computation of linear global modes . . . . .	72
3.5.4	Comparison of nonlinear and linear dynamics . . . . .	76
3.5.5	Discussion and relations to other studies . . . . .	78
3.6	Conclusions . . . . .	80
3.7	Appendix . . . . .	81
3.7.1	Derivation of the linearised normal vector and curvature . . . . .	81
<b>4</b>	<b>Triadic resonance of single and double helical global modes in a variable viscosity two-phase swirling flow</b>	<b>83</b>
4.1	Introduction . . . . .	84
4.2	Numerical simulation and modal decomposition methods . . . . .	86
4.2.1	Nonlinear simulation . . . . .	86
4.2.2	Linear stability analysis . . . . .	88
4.2.3	Flow configuration . . . . .	89
4.2.4	Modal decomposition of the nonlinear flow . . . . .	90
4.3	Steady axisymmetric breakdown states . . . . .	93
4.4	Linear global modes . . . . .	96

4.5	Analysis of helical instability in the nonlinear flow . . . . .	98
4.5.1	Vortex dynamics . . . . .	98
4.5.2	Time traces and disturbance growth . . . . .	99
4.5.3	Modal analysis . . . . .	100
4.5.4	Triadic mode interactions . . . . .	104
4.6	Discussion . . . . .	108
4.6.1	Impact of the viscosity variation on vortex breakdown and helical instability . . . . .	108
4.6.2	Resonant triadic interaction of the unstable global modes . . . . .	110
4.7	Conclusions . . . . .	111
4.8	Appendix . . . . .	111
<b>5</b>	<b>Conclusion</b>	<b>115</b>
5.1	Summary and Discussion . . . . .	115
5.1.1	Mean field stability analysis of two-phase flows . . . . .	115
5.1.2	Global stability analysis of two-phase flows . . . . .	116
5.1.3	Comparing explicit and implicit interface representations . . . . .	118
5.2	Perspectives . . . . .	120
	<b>Bibliography</b>	<b>123</b>

# List of Figures

1.1	(a) Electricity generation from renewable energy sources from 1990-2019; (b) Electricity generation from hydroelectric power from 1971-2019 [1, 2] . . . . .	2
1.2	Schematic drawing of a Francis turbine (adapted from [5]). . . . .	3
1.3	Photographs of typical flow patterns observed in a Francis turbine at full load (a), around the BEP (b) and at part load (c) (from [6]). The cavitation at part and full load is clearly visible. . . . .	3
1.4	Illustrations of liquid jets. Left side: (top and middle) Photographs of high speed waters jets in still air with shear-induced instability and droplet breakup (from [28]); (bottom) Numerical simulation of an oscillating liquid jet in still air undergoing breakup (from [29]). Right side: (top) Photographs of a dripping water column, including the formation of satellite droplets (from [30]); (bottom) Photograph of a swirling oil jet issued into still air and undergoing helical destabilisation (adapted from [31]) . . . . .	5
1.5	One-dimensional numerical approximations of $H$ and $\delta$ for CSF-VOF (dashed line) and CSF-LS (solid line) . . . . .	9
1.6	(a) The wake of a circular cylinder at $Re = 140$ is an example of an oscillator flow; (b) An axisymmetric air jet at $Re = 10^4$ is an example of an amplifier flow [44]. . . . .	11
2.1	Schematic illustration of the computational domain and the adaptive grid (a) and grid sensitivity assessment using the stream-wise development of the time-averaged shear layer momentum thickness $\delta$ for $A = 0.05$ (b) . . . . .	25
2.2	Instantaneous view of the interface via the volume fraction field $C$ for (a) $A = 0.01$ , (b) $A = 0.05$ . The blue area corresponds to $C > 0.5$ , denoting the liquid phase while the white area, $C < 0.5$ , denotes the gas phase. In (c) the envelope of the interfacial instability wave is shown as an iso-line of $\bar{C} = 0.01$ . . . . .	25
2.3	Spatio-temporal diagram of the nondimensional centre-line vorticity $\frac{\Omega}{U/D}(x, y = 0, t)$ (filled contour) and the centre-line volume fraction $C(x, y = 0, t) = 0.5$ (black contour line) for $A = 0.05$ . . . . .	26
2.4	Instantaneous view of the nondimensional vorticity field $\frac{\Omega}{U/D}$ for (a) $A = 0.01$ , (b) $A = 0.05$ . The Interface $C = 0.5$ is shown as black contour line. . . . .	26
2.5	Comparison of the mean flow profiles and an error-function profile (as in Tammisola et al. (2011)) for the unforced flow (a), and forced flow with (b) $A = 0.01$ , (c) $A = 0.05$ . Plot positions are $x/D = 0.01, 1, 2, 5, 10, 20$ . For $A = 0.05$ , positions $x/D = 10, 20$ are omitted due to very large deviations from the error-function profile . . . . .	33
2.6	Mean flow profiles of the jet forced at $A = 0.01$ (blue); $A = 0.05$ (black). The spreading of the mean interface position, derived from figure 2.7 is shown as dashed line. . . . .	34

2.7	Illustration of the mean interface spreading. The top row shows a contour plot of the mean volume fraction field $\bar{\rho}/\rho_l$ of the nonlinear simulation and the interpolated interface position for the linear stability model as black line, for (a) $A = 0.01$ ; (b) $A = 0.05$ . The black dotted line represents the presumed, fixed interface position of the unforced flow. Red areas corresponds to regions of small interface amplitudes while lighter shades indicate areas of increased amplitudes. The second row shows the cumulative integral of $\frac{\bar{\rho}}{\rho_l D}$ along $y$ for several stream-wise positions, for (c) $A = 0.01$ ; (d) $A = 0.05$ . The interface at $x = 0$ (vertical line) determines the initial mass of the liquid. The interface is constructed such that the liquid mass is conserved (horizontal line). . . . .	34
2.8	Stability map for the base flow model (Mode I (a), Mode II (b)), fixed interface model (Mode I) at $A = 0.01$ (c), varying interface model (d). Shown is the spatial growth rate $-\alpha_i D$ and the curve indicating neutral stability, i.e. $\alpha_i D = 0$ , in red. . . . .	36
2.9	Illustration of the fundamental wave packet ( $n = 1$ ), obtained from the DNS and comparison of the computed amplitude functions from the linear stability model and the DNS for (a) $A = 0.01$ , $\hat{u}$ ; (b) $A = 0.01$ , $\hat{v}$ ; (c) $A = 0.05$ , $\hat{u}$ ; (d) $A = 0.05$ , $\hat{v}$ . Figures show the real part, imaginary part, the absolute value and corresponding amplitudes (for the fixed and varying interface model) normalised by their maximum value, from top to bottom. Blue lines show the DNS while black lines show the LSA . . . . .	39
2.10	Comparison of the computed growth rates $-\alpha_i D$ from the linear stability model and $-\tilde{\alpha}_i D$ from the DNS for (a) $A = 0.01$ , (b) $A = 0.05$ . LSA <sub>b</sub> denotes the base flow model, LSA <sub>v</sub> and LSA <sub>f</sub> the varying and fixed interface model. . . . .	40
2.11	Comparison of the computed phase velocities $c_{ph}/U$ from the linear stability model and $\tilde{c}_{ph}/U$ from the DNS for (a) $A = 0.01$ , (b) $A = 0.05$ . LSA <sub>b</sub> denotes the base flow model, LSA <sub>v</sub> and LSA <sub>f</sub> the varying and fixed interface model. . . . .	41
2.12	Variation of the cross-wise maximum of the total turbulent kinetic energy . . . . .	42
2.13	Ratio of the energy of the harmonics to the energy of the fundamental wave (a) and ratio of nonlinear to linear terms in equation (2.34) (b) . . . . .	44
2.14	Amplitudes $\tilde{A}_n$ of the fundamental wave and its higher harmonics for (a) $A = 0.01$ , (b) $A = 0.05$ . . . . .	44
2.15	Energy production $\mathcal{P}_n$ of the fundamental wave and its higher harmonics for (a) $A = 0.01$ , (b) $A = 0.05$ . . . . .	46
2.16	Instantaneous, cross-wise integrated baroclinic vorticity $\mathcal{B}$ and snapshot of the corresponding field normalised by its maximum for (a) $A = 0.01$ , (b) $A = 0.05$ . . . . .	48
2.17	Instantaneous, cross-wise integrated vorticity dissipation $\mathcal{D}$ and snapshot of the corresponding field normalized by its maximum for (a) $A = 0.01$ , (b) $A = 0.05$ . . . . .	48
2.18	Stream-wise evolution of the Fourier decomposition of the cross-wise averaged baroclinic vorticity for $A = 0.05$ . The spectrum along the stream-wise coordinate is shown (a) as well as the stream-wise development of the energy of the first three harmonics. . . . .	49
2.19	Convergence of the real part of the traced eigenvalue, $\alpha_\rho$ , at the neutral point and position of the neutral point, $x/D$ , for various numbers $N$ of collocation points . . . . .	51
2.20	Stability map for the base flow model (Mode I (a), Mode II (b)), fixed interface model (Mode I) at $A = 0.01$ (c), varying interface model (d). Shown is the spatial growth rate $-\alpha_i D/2$ and the curve indicating neutral stability, i.e. $\alpha_i D/2 = 0$ , in red. The axes scaling is as in [21], where $\omega = \pi f D/U$ . . . . .	52

2.21	Comparison of the computed amplitude functions, normalised by their maximum value, from the base flow model and the DNS for $A = 0.01$ , (a) $\hat{u}$ ; (b) $\hat{v}$ . Blue lines show the DNS while black lines show the LSA . . . . .	53
2.22	Comparison of the computed growth rates $-\alpha_i D$ from the linear stability model and $-\tilde{\alpha}_i D$ the DNS (a) and phase velocities $c_{\text{ph}}/U$ , $\tilde{c}_{\text{ph}}/U$ (b) for $A = 0.01$ . .	54
2.23	Real part of the fundamental, second and third harmonic wave (from top to bottom) for (a) $A = 0.01$ , $\hat{u}$ ; (b) $A = 0.01$ , $\hat{v}$ ; (c) $A = 0.05$ , $\hat{u}$ ; (d) $A = 0.05$ , $\hat{v}$ . Note, that each mode and component is normalized individually by its maximum for improved readability. . . . .	54
3.1	(a) Velocity profile at the inlet and interface separating the fluid phases at subcritical conditions ( $We = \infty$ ). (b) Velocity field $u$ and interface at the same conditions. . . . .	67
3.2	(a) Magnitude of the DMD modes at each frequency, extracted from the nonlinear simulation. (b) Shapes of the dominant modes at the respective Weber numbers. . . . .	69
3.3	(a) Dominant frequencies of the appearing modes extracted from the DMD in the flow for all investigated Weber numbers. (b) Bifurcations illustrated by the min-max values of $v$ at $(x, y) = (5, 0)$ . . . . .	70
3.4	(a) Interface position and (b) curvature of the respective baseflows. . . . .	72
3.5	(a) Comparison of the mode frequencies and (b) growth rates at the respective Weber numbers. . . . .	74
3.6	(a) Comparison of the velocity disturbance growth of the nonlinear simulation $v$ at $(x, y) = (5, 0)$ and the exponential growth rate of the most unstable linear global modes of the present analysis. (b) Mode shapes of the respective eigenmodes. The corresponding eigenvalue $\lambda$ is given for each mode. . . . .	75
3.7	Qualitative representation of the velocity phase trajectories at $(x, y) = (8, 0)$ ( $We = 12.5$ ), $(x, y) = (8, 0)$ ( $We = 10$ ), $(x, y) = (6, 0)$ ( $We = 6.\bar{6}$ ) and $(x, y) = (4, 0)$ ( $We = 5$ ). The upper row in black shows the full dynamics and the lower row in blue the reconstructed dynamics. All plots are equally scaled. . . . .	77
3.8	Qualitative Poincaré sections of the trajectories presented in figure 3.7. Sections are chosen such that trajectories cross every completed cycle $n$ . The upper row in black shows the full dynamics and the lower row in blue the reconstructed dynamics. All plots are equally scaled. . . . .	77
4.1	Schematic view of the computational domain. . . . .	91
4.2	(a) In blue: Critical swirl $S_c$ in relation to $\tilde{\mu}$ above which axisymmetric breakdown is observed. As black dots: configurations plotted in figures 4.2b, 4.2c and 4.3a, 4.3b. (b) Minimum axial velocity at every stream-wise location for $S = 0.8$ and varying $\tilde{\mu}$ . (c) Similar plot for $\tilde{\mu} = 0.5$ and varying $S$ . (d) Comparison of single-phase ( $\tilde{\mu} = 1$ ) and two-phase flow ( $\tilde{\mu} = 0.5$ ) for varying $S$ . . . . .	95
4.3	Contour plots of $u_z$ of axisymmetric flows for $S = 0.8$ and varying $\tilde{\mu}$ (a) and $S$ (b) (for the grey dots in figure 4.2b). The interface is shown as solid white line and the $u_z = 0$ contour, indicating reverse flow, as dashed line. The location of the minimum of $u_z$ is shown as red dot. . . . .	95
4.4	(a) Plot of the growth rates $\text{Re}(\lambda)$ of the unstable linear global modes $\omega^l$ , obtained from the linear analysis, over several $S$ . The grey circles denote stable modes. (b) Comparison of the frequencies $\text{Im}(\lambda)$ of the linear global modes $\omega^l$ (denoted by $\circ$ ) with the limit cycle oscillations $\omega$ (denoted by $\diamond$ ) of the nonlinear flow in §4.5. The dashed lines connecting the data points are printed for improved readability and should not be interpreted as a linear variation of the data. . .	97

4.5	Shapes of the unstable linear global modes at the respective swirl numbers. The pictographic bar charts show the relative contributions of the respective wavenumbers $m = 0, 1, 2, 3$ (from left to right) to each mode. . . . .	98
4.6	Visualisation of the instantaneous flow. The upper image shows the unstable axisymmetric basic state and the lower image the fully developed flow. Isosurfaces: interface ( $c = 0.5$ , in translucent grey) and vortical structures ( $\lambda_2 = -0.5$ , in dark blue; $\lambda_2 = -0.25$ , in light translucent blue). . . . .	100
4.7	(a) Time signal $u'_\theta$ of the monitor point as given in the title of each figure. The insets show a zoomed interval with $z$ -position as annotated. (b) Disturbance growth of $\hat{u}_{\theta,m}$ , for azimuthal wavenumbers $m = 1, m = 2$ , and exponential growth rate obtained from the linear analysis. The straight lines denoting the growth rate are shifted to align with the respective time signals. . . . .	101
4.8	(a) Magnitude of the DMD modes per frequency, extracted from the nonlinear simulation. (b) Magnitude of the DMD modes per frequency and stream-wise stations every $\Delta z = 10$ . The colours denote the different wavenumbers. The peaks of the annotated modes are marked by $\circ$ . (c) The spatial mode shapes ( $\text{Re}(\hat{u}_\theta)$ in red, $\text{Re}(\hat{\phi})$ in blue) corresponding to the annotated modes in (a). The pictographic bar charts show the relative contributions of the respective wavenumbers $m = 0, 1, 2, 3$ (from left to right) to each mode. . . . .	103
4.9	Upper row: Scatter plot of the local maxima of the mode bispectrum. The dashed diagonal lines denote triadic interactions forming the same frequency, as annotated at the respective lines. Relevant triadic interactions mentioned in the text are marked by $\circ$ . The dot diameters and colour coding are scaled with $ \lambda_1 $ , such that small, bright dots correspond to weak interactions and large, dark dots to strong interactions. Lower row: Bar chart showing the three most energetic interactions contributing to the denoted frequencies. Each bar is corresponding to a peak in the bispectrum above and the largest interaction for each frequency corresponds to the interactions marked by $\circ$ in the bispectrum. . . . .	106
4.10	Left: The mode cross-bispectrum for the dominant azimuthal wavenumber interactions. The partaking wavenumber doublets $[m_p, m_q]$ are denoted in the plots. Right: The three most energetic wavenumber interactions contributing to the denoted wavenumbers. . . . .	108
4.11	Comparison of the computed modes of the linear stability analysis (LSA), the bispectral mode decomposition (BMD) and the dynamic mode decomposition (DMD) for $S = 0.8$ . All modes are computed from $u_\theta$ or $u'_\theta$ . The real part of the respective modes is shown. For the BMD, the bispectral modes $\phi$ as well as the interaction map $\psi$ is displayed. . . . .	113

## List of Tables

2.1	Fluid properties of the liquid and gas phase . . . . .	24
2.2	Dimensionless numbers, based on $U, D$ and the forcing frequency $f^*$ . . . . .	24
2.3	Validation of two-layer Poiseuille flow using temporal analysis ( $\alpha = 1$ ). Displayed are the corresponding unstable eigenvalues $c \equiv \omega/\alpha$ . . . . .	32
2.4	Energy budget of mode I of the linear stability model at $x/D = 10$ . . . . .	37

2.5	Influence of the quadratic harmonic interactions in the mean flow equation and mean flow correction. The quasi-stationary solution of the unforced flow is taken as base flow $u_{i,b}$ . . . . .	43
3.1	Relative error of the basic state interface $I$ . Errors are measured against the streamline-constructed interface of the single phase flow $I_s$ . The Weber numbers of the respective two-phase solutions are stated as subscripts. . . . .	72
3.2	Convergence of the nonlinear and linear flow for increasing level of refinement. Shown is the relative error of the basic state interface for $We_{base} = \infty$ , the convergence of the frequency $\text{Im}(\lambda)$ of the dominant DMD mode of the nonlinear simulation and of the most unstable eigenvalue $\lambda$ of the linear analysis for $We = 12.5$ . . . . .	72
3.3	Eigenvalues $\lambda$ of the present linear analysis, the ones of [24] and frequencies $\text{Im}(\lambda)$ of the dominant DMD modes of the nonlinear simulation at the respective Weber numbers. . . . .	73
4.1	Tabulated values of growth rates $\text{Re}(\lambda)$ and frequencies $\text{Im}(\lambda)$ of the linear modes $\omega^l$ . The corresponding frequencies $\omega$ , obtained from the nonlinear flow in §4.5 are shown for comparison. . . . .	97
4.2	Convergence of the unstable eigenvalue for $Re = 200$ , $S = 1$ , $\tilde{\mu} = 1$ on different meshes and comparison with previous studies. As the present computations are 3D in cartesian coordinates, radial measures $r$ correspond to the respective measures in $y$ and $z$ . The mesh $M_{ref}$ is used throughout the study. . . . .	112
4.3	Frequencies occurring for $S = 1.0$ and dominant triadic interaction forming them . . . . .	112

# Introduction

# 1

## 1.1 Motivation: Cavitation in hydro turbines

### 1.1.1 Hydro power as a pillar for clean energy

The transition of the world's fossil fuel-driven electricity production towards renewable energies, to drastically lower carbon emissions and to combat the anthropogenic climate change, is led by three technologies: Wind, solar and hydro power.

Thanks to the rapid development and increased deployment of wind and solar power facilities in recent years, a significant medial focus is resting on these two technologies. However, the intermittent character of wind and solar energy sources has a tremendous impact on the balance of power supply and consumption, thus posing significant challenges for the electrical grid. It is therefore necessary to have sufficient storage capacities as well as grid control available for agile load balancing of the electrical grid. Pumped storage and hydraulic power plants possess the necessary flexibility to account for both of these requirements.

Hydro power currently (2019) accounts for 69% of the world's electricity production through renewable technologies and for 16% of the total electricity production. While the OECD countries' share of global capacity expansions of hydro power since 1990 has been modest (14%), China alone has been responsible for 50% of the global gross capacity expansion within this period (figure 1.1) [1, 2]. To reach the necessary targets for net-zero carbon economies set by governments around the globe, hydro power is and will remain a crucial component.

Despite the firm placement of hydro power as a key component of the energy transition, there are a number of challenges associated with the operation of hydro turbines under non-optimal conditions, in order to respond to varying load demands by the electrical grid. Thus, turbines may be required to operate significantly below or above their designed, optimal specifications which leads to cavitation and the formation of a two-phase flow in the turbine. Under certain conditions, this may provoke a significant decrease in turbine efficiency as well as pressure pulsations which, at worst, may jeopardise the safe operation of the turbine or the power plant. It is therefore necessary to have a detailed understanding of the underlying physical mechanisms leading to the emergence of this phenomenon, in order to be able to suppress its occurrence or at least mitigate its effects.

1.1	Motivation: Cavitation in hydro turbines . . . . .	1
1.2	Instabilities in two-phase shear flow . . . . .	5
1.3	Modelling of immiscible two-phase flows . . . . .	7
1.4	Linear stability analysis of immiscible two-phase flows . . . . .	9
1.5	Nonlinear dynamics of incompressible flow . . . . .	15
1.6	Outline of the thesis . . . . .	17

[1]: IEA (2021), *World hydroelectricity production by region 1971-2019*

[2]: IEA (2021), *Renewable electricity generation by source (non-combustible), World 1990-2019*

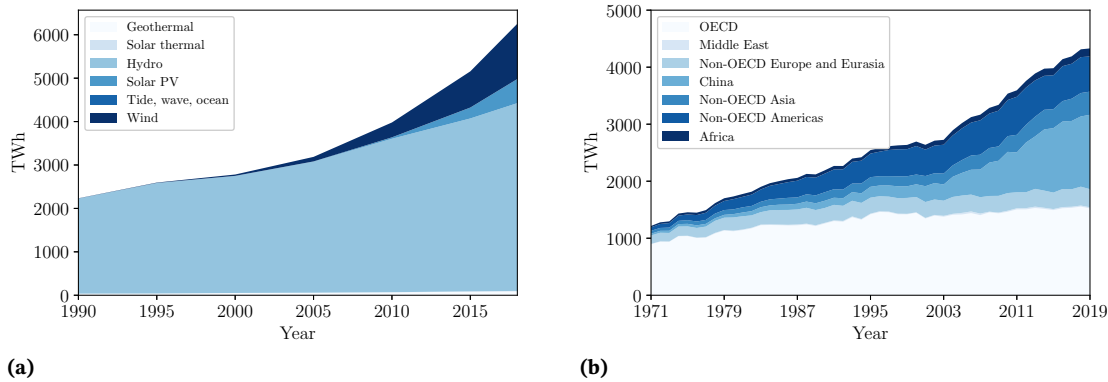


**Figure 1.1:** (a) Electricity generation from renewable energy sources from 1990-2019; (b) Electricity generation from hydroelectric power from 1971-2019 [1, 2]

### 1.1.2 The cavitating vortex rope in Francis turbines

The Francis turbine is the most commonly used type of hydro turbine and accounts for about 60% of the installed turbines in hydro power plants around the world. Its main components are a spiral casing, a set of stay and guide vanes, a runner and a draft tube. The working fluid enters the spiral casing at high pressure and is distributed circumferentially around the vanes, creating an angular momentum in the flow. Part of the pressure energy is converted into kinetic energy in the casing, resulting in an increased flow impulse at the vanes. The radial, inward oriented flow then passes the vanes and the runner where most of the pressure and kinetic energy are extracted. Under optimal conditions, it leaves the runner in axial direction and enters the draft tube which recovers pressure energy from the remaining kinetic energy of the flow. A schematic drawing of a Francis turbine is shown in figure 1.2.

At optimal operating conditions (best efficiency point - BEP), Francis turbines may achieve efficiencies well above 90%, thus being highly efficient. However, when operating significantly below (part load) or above (full load) the BEP, efficiency declines significantly. At part load, this is due to the formation of a swirling flow in the draft tube, which results in vortex breakdown and the formation of a helical precessing vortex core. The resulting low pressure inside the vortex core may lead to cavitation and the formation of an interconnected region of water vapour if the local static pressure falls below the water vapour pressure. The result is a two-phase flow, termed cavitating vortex rope (CVR). Photographs of the occurring instabilities at part or full load are shown in figure 1.3. The oscillating vortex rope represents an external excitation source to the hydraulic system which may lead to hydro-acoustic instabilities and resonant behaviour if the precession frequency is matched with the natural frequency of the system [3, 4]. An understanding of the underlying physics is therefore crucial for exploring solutions to mitigate the effect or the occurrence of the CVR.

[3]: Favrel et al. (2015), 'Study of the vortex-induced pressure excitation source in a Francis turbine draft tube by particle image velocimetry'

[4]: Alligne et al. (2014), 'Cavitation surge modelling in Francis turbine draft tube'

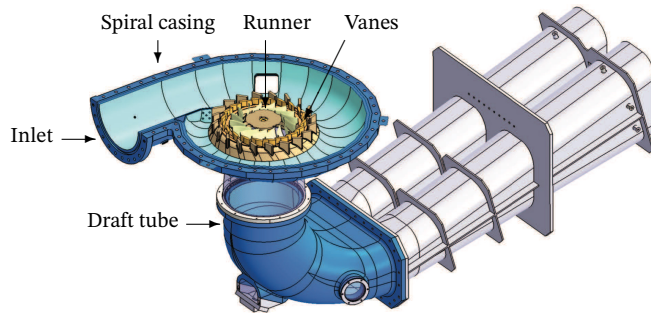


**Figure 1.2:** Schematic drawing of a Francis turbine (adapted from [5]).

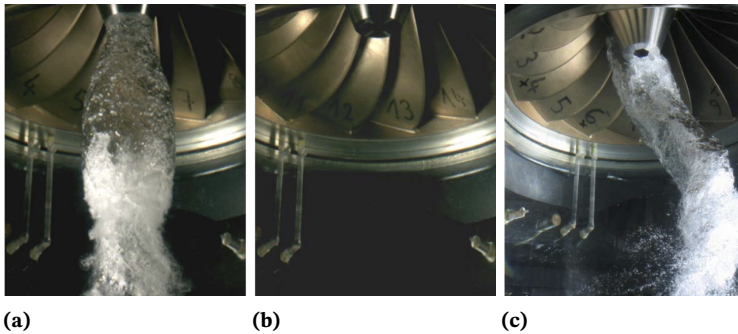


**Figure 1.3:** Photographs of typical flow patterns observed in a Francis turbine at full load (a), around the BEP (b) and at part load (c) (from [6]). The cavitation at part and full load is clearly visible.

### 1.1.3 Avenues towards modelling the CVR as a global mode

In the body of literature, recent approaches have aimed to describe the helical instability of the fluid flow inside the draft tube at part load conditions as a global mode, stemming from a linear instability mechanism. This approach has been successfully applied to various kinds of swirling flows in other academical and industrial flow configurations in the past (e.g. [7–11]). In the context of hydro turbines, the studies of [12] and [13] used global stability analysis around the turbulent mean flow, obtained by numerical simulation or Particle Image Velocimetry of the flow in a model draft tube at part load, to compute linear global modes. In both works an unstable or marginally stable eigenmode was found which resembled the coherent helical structure observed in the nonlinear flow and whose frequency was in good agreement with the reference data. The successful description of the occurring helical instability through a linear instability mechanism, thus, gives valuable insights about its physical nature and provides an important step towards active control approaches targeting its suppression.

However, the linear analyses in the referenced numerical studies make an important simplification, as they assume a single phase flow, thus not taking into account the phase change through cavitation. The resulting two-phase flow is likely to have non-negligible influence on the linear and nonlinear dynamics of the flow, given that the gaseous phase, composed of water vapour, has a different density and viscosity than the water of the liquid phase and both phases are separated by an interface along which surface tension acts.

The formation and collapse of cavitation bubbles is a tremendously complex phenomenon of fast out-of-equilibrium processes, involving compressible flow, as well as heat and mass transfer between the two phases.

[7]: Ruith et al. (2003), ‘Three-dimensional vortex breakdown in swirling jets and wakes: direct numerical simulation’

[8]: Gallaire et al. (2006), ‘Spiral vortex breakdown as a global mode’

[9]: Meliga et al. (2012), ‘A weakly nonlinear mechanism for mode selection in swirling jets’

[10]: Oberleithner et al. (2011), ‘Three-dimensional coherent structures in a swirling jet undergoing vortex breakdown: stability analysis and empirical mode construction’

[11]: Tammisola et al. (2016), ‘Coherent structures in a swirl injector at  $Re=4800$  by nonlinear simulations and linear global modes’

[12]: Pasche et al. (2017), ‘Part load vortex rope as a global unstable mode’

[13]: Müller et al. (2021), ‘Prediction of vortex precession in the draft tube of a model hydro turbine using mean field stability theory and stochastic modelling’

[14]: Brennen (2014), *Cavitation and bubble dynamics*

[15]: Fuster (2019), 'A review of models for bubble clusters in cavitating flows'

[16]: Ferrari (2017), 'Fluid dynamics of acoustic and hydrodynamic cavitation in hydraulic power systems'

[17]: Squire (1953), 'Investigation of the instability of a moving liquid film'

[18]: Yih (1967), 'Instability due to viscosity stratification'

[19]: Hagerty et al. (1955), 'A study of the stability of moving liquid film'

[20]: Lin et al. (1990), 'Absolute and convective instability of a liquid sheet'

[21]: Söderberg (2003), 'Absolute and convective instability of a relaxational plane liquid jet'

[22]: Boeck et al. (2005), 'Viscous versus inviscid instability of two-phase mixing layers with continuous velocity profile'

[23]: Tammisola et al. (2011), 'Effect of surface tension on global modes of confined wake flows'

[24]: Tammisola et al. (2012), 'Surface tension-induced global instability of planar jets and wakes'

If the local tension, given by the difference of vapour pressure and local pressure, exceeds the tensile strength of the liquid [14], a cavitation inception is triggered, resulting in the rapid expansion of bubble nuclei at time scales significantly faster than any diffusion time scales in the flow. Therefore, it is generally assumed that heat and mass transfer are negligible at this stage [15, 16]. As the bubbles are advected in the flow, they reach regions of larger local pressure which slows the expansion of the cavitation bubbles. Eventually, the local liquid pressure re-approaches the vapour pressure, heat and mass transfer between liquid and vapour become relevant and interaction of bubbles may occur, resulting in coalescence and the formation of large scale vapour pockets if surface tension of the initial bubbles is overcome. As soon as the vapour pressure is locally recovered, condensation occurs, resulting in the violent collapse of the cavitation pockets. During collapse, a drastic pressure and temperature increase may occur inside the pockets.

Consequently, direct numerical modelling of cavitating flows is an open field of research. Studies are yet limited to single bubbles or bubble clusters and various simplifications are to be made, in particular with regard to the incorporation of heat and mass transfer across interfaces, as well as the modelling of nucleation events [15]. Thus, accurate modelling of cavitating flows as a whole, by means of direct numerical simulation or large eddy simulation, is not feasible in the context of large scale flows as they occur in hydro turbines. This also implies that linear stability analysis of such flows remains out of range.

We may, therefore, take a step back and reduce the complexity of the problem by assuming an equilibrium of formation and collapse of cavitation pockets. In the context of CVRs this assumption is not far-fetched as, under constant operating conditions, their spatio-temporal features are quite persistent. If further, we assume that heat and mass transfer are negligible, the flow may essentially be viewed as an incompressible two-phase flow whose linear stability properties can be assessed. In particular, it is now possible to investigate the influence of variable viscosity and density in the flow, introduced by the gas phase, as well as of surface tension on the stability of the flow.

Nevertheless, the task of computing the linear stability of a three-dimensional (potentially turbulent) two-phase flow in a complex geometry remains challenging. On the one hand, this is because established methods for the linear analysis of single-phase flows have only seldom or not yet at all been applied to two-phase flows. On the other hand, the accurate modelling of a fluid-fluid interface and the resulting discontinuity across the phases poses a challenge from a numerical perspective. The majority of past studies is essentially limited to local stability analyses by assuming a parallel flow, resulting in a one dimensional model (e.g. [17–22]). A notable exception are the studies of [23, 24] where, for the first time, the global linear stability of general plane two-phase flows was assessed. In all of these studies, the two fluid phases are modelled using a Lagrangian approach where each phase is discretised on a separate mesh. The interface, including surface tension, is accounted for by formulating coupling conditions at the mesh boundaries. While this allows for a very accurate interface representation, the methodology is potentially inflexible if applied to more complex interface topologies and three-dimensional flows. An avenue towards performing global stability analysis for general three-dimensional flows is to resort

to a purely Eulerian methodology to model fluid phases and interface as it is done in level-set or Volume-Of-Fluid methods that are employed in most current nonlinear solvers for two-phase flows (e.g. [25–27]). More advanced concepts in the context of global linear stability analysis such as mean field analysis, global adjoint stability and global transient growth analysis have not been applied to two-phase flows yet.

In the following sections of this chapter, first, a general introduction to some instabilities occurring in two-phase shear flows is given. We then proceed to an overview on theoretical and numerical concepts for modelling two-phase flows: We start by presenting the nonlinear equations and subsequent models required for the numerical simulation of two-phase flows (§1.3). In §1.4, we continue with the derivation of the linearised equations in a local and global framework and their implementation. In §1.5, we give an overview on the methodology to analyse the nonlinear dynamics of incompressible flow. This aids in the quantification of nonlinear interaction taking place in the flow and, thus, also is useful to assess the validity of the linear analysis.

[25]: Popinet (2003), ‘Gerris: a tree-based adaptive solver for the incompressible Euler equations in complex geometries’

[26]: Popinet (2009), ‘An accurate adaptive solver for surface-tension-driven interfacial flows’

[27]: Abadie et al. (2015), ‘On the combined effects of surface tension force calculation and interface advection on spurious currents within Volume of Fluid and Level Set frameworks’

## 1.2 Instabilities in two-phase shear flow

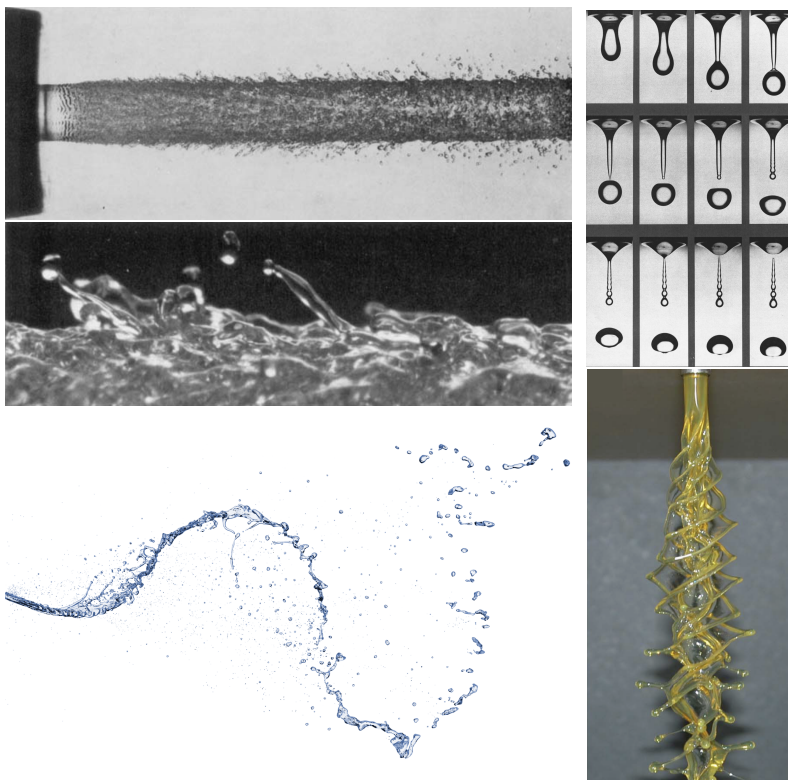


**Figure 1.4:** Illustrations of liquid jets. Left side: (top and middle) Photographs of high speed water jets in still air with shear-induced instability and droplet breakup (from [28]); (bottom) Numerical simulation of an oscillating liquid jet in still air undergoing breakup (from [29]). Right side: (top) Photographs of a dripping water column, including the formation of satellite droplets (from [30]); (bottom) Photograph of a swirling oil jet issued into still air and undergoing helical destabilisation (adapted from [31])

### 1.2.1 A note on terminology

The term *two-phase flow* describes a flow that involves two phases that may or may not interact with each other. Two-phase flow therefore is a subcategory of multiphase flow which encompasses flows with any

number of phases. Generally, it is assumed that each phase exhibits a certain amount of separation above the molecular level to exclude flows where both phases are macroscopically well mixed. The flow may then be further categorised according to the level of separation of the involved phases, reaching from *separated* in case where both phases are completely separated (for instance the water flowing from the exit of a faucet into the surrounding air) to *dispersed* where one phase is finely dispersed within the other phase (a liquid spray in air).

The term *phase* implies a varying state of matter between the phases. Therefore, two-phase flows may as well be distinguished by the state of the phases, for instance liquid/gas (water-air flow), liquid/liquid (oil-water flow), solid/liquid (the flow of sediment in water), solid/gas (the flow of sand/dust in the air). It is clear that the spectrum of multiphase flows in general and two-phase flows in particular, is vast.

Within the scope of this thesis, the focus lies solely on two-phase flows which are well separated and which include two fluids (gas or liquid). Thus, the resulting two-phase flows may as well be termed *immiscible two-phase flows* or *immiscible two-fluid flows*. Throughout the thesis, we will use both terms synonymously and may omit the term *immiscible*.

## 1.2.2 Instabilities of a liquid jet

A liquid jet issued in a still gaseous environment is a paradigm of a two-phase flow. There are innumerable examples of it occurring in nature or industrial applications, be it the water jet from a garden hose, the high-pressure fuel injection in an internal combustion engine or the water jet ejected from a geyser. More subtly, liquid jets are also observed in ink-jet printers or as the result of cavity closure, resulting from droplet impact on the surface of a similar liquid. They are also a tangible specimen to observe some of the most common dynamics and instabilities occurring in two-phase shear flows. A number of selected illustrations is presented in figure 1.4.

In the most simple case, we consider a laminar, circular jet in a surrounding still gas. Considering the flow from a faucet, it is seen, that at low velocity, the tip of the water column almost immediately breaks up into a droplet while the remaining water column retracts until a new column is formed which breaks up again. This is the dripping regime. From the pioneering work of [32] and [33] it is known that this phenomenon is caused by the capillarity of the water column. Along the circumference of the column, surface tension is acting. Consequently, the radius of the column is associated with a specific surface energy. A modulation of the radius, therefore, also evokes a change of surface energy. If a modulation has a wavelength larger than the circumference of the column, this modulation lowers the surface energy and thus will grow, leading to the eventual breakup of the column. This is the Plateau-Rayleigh instability. The initial disturbance growth is well represented by linear theory. However, the ultimate breakup of the droplet, as well as the formation of satellite droplets which occurs under certain conditions, are nonlinear phenomena.

If the velocity is increased, the dripping column is replaced by a continuous jet and droplet breakup is shifted downstream. Upon further velocity

[32]: Plateau (1873), *Statique expérimentale et théorique des liquides soumis aux seules forces moléculaires*

[33]: Rayleigh (1879), 'On the capillary phenomena of jets'

increase, capillary effects will eventually be overcome by inertial effects. At high jet velocity, typical shear layer instabilities of Kelvin-Helmholtz type will dominate. Here, surface tension acts as a damping force [34]. If the shear between the quiescent gas and the liquid is sufficiently strong, instability growth will be dominated by nonlinear effects and droplets significantly smaller than the jet diameter will be peeled from the jet. With further destabilisation, complete disintegration of the jet into ligaments and droplets occurs. The formation of ligaments and droplets is accompanied by yet another type of instability: Through the transverse acceleration of the liquid/gas interface a baroclinic torque is created due to a misalignment of pressure and density gradient across the interface which, again, leads to disturbance growth. This is the Rayleigh-Taylor instability. If swirl is added to the jet, the centrifugal forces acting on the dense liquid aid destabilisation by the same mechanism, as acceleration is pointed radially outwards into the less dense gas [31].

The dynamics described here for a liquid jet in a gaseous environment may in principle also be observed in gaseous jets in a liquid environment. However, some aspects may vary, as for instance droplets are replaced by bubbles or centrifugal forces acting on a gas column are stabilising, as the acceleration points into the denser fluid.

[34]: Marmottant et al. (2004), 'On spray formation'

[31]: Kubitschek et al. (2007), 'Helical instability of a rotating viscous liquid jet'

## 1.3 Modelling of immiscible two-phase flows

The physics of flows that involve two immiscible fluids are notably more complex than those of flows that only involve a single fluid. On a macroscopic level, the flows of two different fluids with different properties (e.g. viscosity and density) have to be accounted for while, on a microscopic level, molecular forces, acting along the contact area of the fluids, come into play. Additionally, if phase change (e.g. cavitation, boiling or evaporation) occurs, mass and heat transfer between both fluids have to be accounted for.

Given the complexity of the flow and the range of length and time scales involved, a number of simplifications are commonly made. From a physical perspective, the interface is assumed to have negligible thickness, resulting in a discontinuity of the density and viscosity field. The imbalance of molecular forces along the fluid interface results in a surface tension force located at the interface. Consequently, velocity and tangential stress are continuous across the interface, while the normal stress encounters a jump, balanced by the surface tension. From a numerical perspective, a common approach then is to model the resulting fluid system in a unified formulation over both phases, known as the one-fluid formulation [35].

[35]: Tryggvason et al. (2011), *Direct Numerical Simulations of Gas-Liquid Multiphase Flows*

### 1.3.1 Governing equations

We define a unified velocity vector and pressure of the flow,  $\mathbf{u} = (u, v, w)^T$  and  $p$ , as well as a unified density and dynamic viscosity,  $\rho$  and  $\mu$ . In the absence of heat and mass transfer, the continuity and momentum equation, including the incompressibility condition are given across both fluid phases as

$$\partial_t \rho + \mathbf{u} \cdot \nabla \rho = 0, \quad (1.1a)$$

$$\rho(\partial_t \mathbf{u} + \mathbf{u} \cdot \nabla \mathbf{u}) = -\nabla p + \nabla \cdot (\mu D) + \sigma \kappa \mathbf{n} \delta(\mathbf{x} - \mathbf{x}_s), \quad (1.1b)$$

$$\nabla \cdot \mathbf{u} = 0, \quad (1.1c)$$

where  $D = \nabla \mathbf{u} + \nabla^T \mathbf{u}$  is the deformation tensor. The rightmost term in equation (1.1b) represents the surface tension force along the interface, consisting of a surface tension coefficient  $\sigma$ , the local interface curvature  $\kappa$ , the unit normal vector of the interface  $\mathbf{n}$  and  $\delta$ , the Dirac  $\delta$ -function that is non-zero on the interface. The position of the interface itself is given as  $\mathbf{x}_s$ . Using a Heaviside function  $H(\mathbf{x} - \mathbf{x}_s)$ , that is 1 in phase 1 and 0 in phase 2,  $\rho$  and  $\mu$  can be expressed as

$$\rho = \rho_2 + H(\rho_1 - \rho_2), \quad (1.2a)$$

$$\mu = \mu_2 + H(\mu_1 - \mu_2). \quad (1.2b)$$

We see that density and viscosity differ between the phases but are constant within each phase.

### 1.3.2 Numerical modelling

The numerical methods for modelling two-phase flows can be divided into two broader categories, Lagrangian and Eulerian, depending on the representation of the phases and the interface. In Lagrangian methods, the phases or the interface are treated explicitly, for instance by employing boundary-fitted meshes that are aligned with the interface [36] or by the use of marker particles [37] to differentiate between the phases. These methods allow for highly accurate interface representations but come at the expense of an increased algorithmic complexity, as well as challenges when dealing with large interface deformations or topology changes (e.g. liquid breakup). The group of Eulerian methods uses implicit representations of the phases and the interface and essentially consists of the Volume-Of-Fluid (VOF) method [38], the level-set method (LS) [39] and phase-field methods [40]. They have potentially less accurate interface representations but are relatively easy to implement and can inherently deal with topology changes and large interface deformations. Most modern solvers therefore implement either VOF, LS methods or variants derived thereof. Among these, VOF methods are known to possess excellent mass conservation properties whereas LS methods allow for a more accurate computation of the geometrical properties of the interface.

The representation of the phases and the interface in equation (1.1) relies on  $H$  and  $\delta$  which are approximated numerically by  $H_\epsilon$  and  $\delta_\epsilon$  where  $\epsilon$  is a characteristic length scale related to the local grid size. A numerical representation of the surface tension force is found by converting the surface force formulation given in equation (1.1) to a volume force formulation as

$$\sigma \kappa \mathbf{n} \delta(\mathbf{x} - \mathbf{x}_s) = \sigma \kappa \nabla H_\epsilon(\mathbf{x} - \mathbf{x}_s). \quad (1.3)$$

[36]: Fyfe et al. (1988), ‘Surface tension and viscosity with Lagrangian hydrodynamics on a triangular mesh’

[37]: Unverdi et al. (1992), ‘A front-tracking method for viscous, incompressible, multi-fluid flows’

[38]: Scardovelli et al. (1999), ‘Direct numerical simulation of free-surface and interfacial flow’

[39]: Sussman et al. (1994), ‘A level set approach for computing solutions to incompressible two-phase flow’

[40]: Anderson et al. (1998), ‘Diffuse-interface methods in fluid mechanics’

A representation of  $H_\epsilon$  is found using the continuum surface force method (CSF) [41]. Combined with the VOF method we simply set

$$H_\epsilon(\mathbf{x} - \mathbf{x}_s) = c(\mathbf{x}) = \begin{cases} 0, & \text{for } \mathbf{x} \text{ in phase 1,} \\ 1, & \text{for } \mathbf{x} \text{ in phase 2,} \\ 0.5, & \text{for } \mathbf{x} \text{ at the interface,} \end{cases} \quad (1.4)$$

[41]: Brackbill et al. (1992), 'A continuum method for modeling surface tension'

where  $c$  is the volume fraction field and  $\epsilon = \Delta$ , the grid size. We then find  $\mathbf{n}\delta = \nabla c$ . Similarly, when combining the CSF method with a LS method, we can find a smooth approximation

$$H_\epsilon(\mathbf{x} - \mathbf{x}_s) = H_\epsilon(\phi(\mathbf{x})) = \begin{cases} 0, & \text{if } \phi < -\epsilon, \\ 1, & \text{if } \phi > \epsilon, \\ \frac{1+\phi/\epsilon+\sin(\pi\phi/\epsilon)/\pi}{2}, & \text{otherwise.} \end{cases} \quad (1.5)$$

where  $\phi$  is usually chosen as a signed distance function with respect to the interface:

$$\phi(\mathbf{x}) = \begin{cases} \phi > 0, & \text{for } \mathbf{x} \text{ in phase 1,} \\ \phi < 0, & \text{for } \mathbf{x} \text{ in phase 2,} \\ \phi = 0, & \text{for } \mathbf{x} \text{ at the interface.} \end{cases} \quad (1.6)$$

Here, we find  $\mathbf{n}\delta = \nabla\phi/|\nabla\phi|\delta_\epsilon$  where the smooth Delta function can be obtained as  $\delta_\epsilon = dH_\epsilon(\phi)/d\phi$ . An illustration of the representations of  $H_\epsilon$  and  $\delta_\epsilon$  for both methods is given in figure 1.5.

Since  $\rho$  is directly coupled to  $c$  or  $\phi$ , respectively, equation (1.1a) is equivalent to the advection of  $\psi$ :

$$\partial_t \psi + \nabla \cdot (\psi \mathbf{u}) = 0 \quad \begin{cases} \psi = c & \text{if VOF} \\ \psi = \phi & \text{if LS} \end{cases} \quad (1.7a)$$

The computation of the normals and curvature depends on the method used for the interface representation and further details thereon are given in Chapter 3

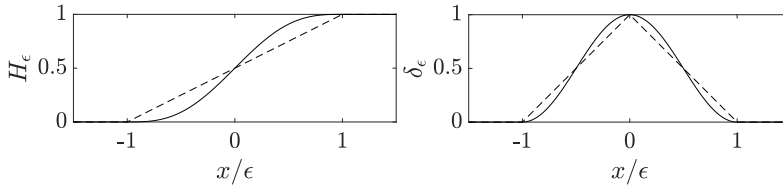


**Figure 1.5:** One-dimensional numerical approximations of  $H$  and  $\delta$  for CSF-VOF (dashed line) and CSF-LS (solid line)

## 1.4 Linear stability analysis of immiscible two-phase flows

Linear stability analysis in the context of fluid flows generally refers to the analysis of exponential growth or decay of infinitesimal perturbations on a

steady solution of the Navier Stokes equations. To this end, a flow quantity  $\mathbf{q}$  is decomposed into a base flow  $\mathbf{Q}$  and an infinitesimal perturbation  $\zeta \mathbf{q}'$  with  $\zeta \ll 1$  such that

$$\mathbf{q}(\mathbf{x}, t) = \mathbf{Q}(\mathbf{x}) + \zeta \mathbf{q}'(\mathbf{x}, t). \quad (1.8)$$

By choosing a Fourier ansatz for the perturbation quantities and linearising the Navier-Stokes operator around a steady base flow, the linearised system can be recast as an eigenvalue problem. The resulting eigenvalues and eigenvectors then determine the stability of the system. Consequently, disturbances associated with an unstable eigenvalue will grow exponentially while disturbances associated with stable eigenvalues decay.

### 1.4.1 Local analysis

In the most simple case, where the spatial gradients of the base flow are dominated by a single coordinate, e.g. the crosswise coordinate  $y$ , we may approximate the base flow as  $\mathbf{Q}(\mathbf{x}) \approx \mathbf{Q}(y)$  where further  $\mathbf{U}(y) = (U(y), 0, 0)$ . Consequently, the flow reduces to a set of one dimensional equations. This is called *parallel flow assumption*. The disturbances  $\mathbf{q}'$  are decomposed into Fourier modes

$$\mathbf{q}'(\mathbf{x}, t) = \hat{\mathbf{q}}(y) e^{i(\alpha x - \omega t) + \beta z} \quad (1.9)$$

where  $i$  is the imaginary unit,  $\alpha, \beta$  are the stream-wise and span-wise perturbation wavenumbers and  $\omega$  is the frequency. Both,  $\alpha$  and  $\omega$  are generally complex-valued. Further,  $\hat{\mathbf{q}}$  is the complex-valued eigenfunction or -mode and describes the spatial shape of the disturbance. In the following we will focus on two-dimensional disturbances  $\mathbf{q}'(x, y, t)$  and thus set  $\beta = 0$ .

From the decomposition it is clear that we may either look at the spatial, the temporal or the spatio-temporal growth of disturbances. In a spatial analysis,  $\omega$  is real-valued and known; modes grow in space if  $-\alpha_i > 0$  and decay if  $-\alpha_i < 0$ . Similarly, in a temporal analysis,  $\alpha$  is real-valued and known; modes grow in time if  $\omega_i > 0$  and decay if  $\omega_i < 0$ . In a spatio-temporal analysis, both  $\alpha$  and  $\omega$  may be complex-valued and either one of them may be known or unknown.

In this context, the concepts of *absolute* and *convective* instability are introduced [42, 43]. They describe the linear impulse response of the flow to a localised disturbance at a time instant. If the system is unstable, the impulse response grows in time without limit. If, at the same time, the generated wave packet is advected downstream on the base flow, the instability is called *convective* (noise amplifier flow). If the source of disturbance is removed from the flow, a noise amplifier flow will return to its basic state after all disturbances are advected away. In contrast, when the generated wave packet remains stationary, the growing disturbance will contaminate the whole domain for  $t \rightarrow \infty$  and the instability is called *absolute* (oscillator flow). A disturbance in an oscillator flow will keep growing even as its source is removed. An illustration of both types of instability in a flow is given in figure 1.6.

[42]: Briggs (1964), *Electron-stream interaction with plasmas*

[43]: Huerre et al. (1990), 'Local and global instabilities in spatially developing flows'

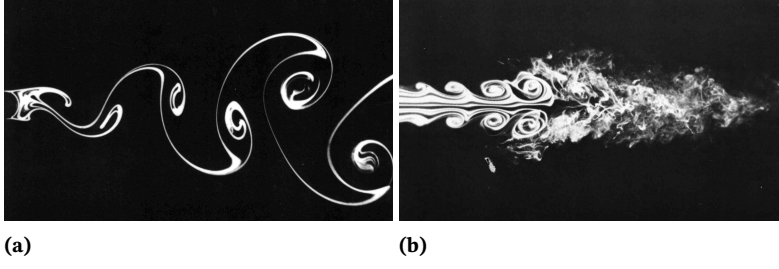


**Figure 1.6:** (a) The wake of a circular cylinder at  $Re = 140$  is an example of an oscillator flow; (b) An axisymmetric air jet at  $Re = 10^4$  is an example of an amplifier flow [44].

To derive the linear perturbation equations for a two-phase flow, a Lagrangian approach is employed here and boundary fitted domains are assumed. Consequently, a separate domain is considered for each fluid phase and coupling conditions are formulated at the domain boundaries to account for the action of the interface. This approach has commonly been used in many previous studies (e.g. [21, 22, 45]). Starting point are the incompressible Navier Stokes equations for a single fluid in each phase, 1 and 2, where  $\mathbf{q} = (\mathbf{u}_1, \mathbf{u}_2, p_1, p_2, h)$  and  $h$  denotes the interface. We consider a plane flow such that  $\mathbf{u} = (u, v)$ . The equations are formulated in nondimensional form as

$$\partial_t \mathbf{u}_{1,2} + \mathbf{u}_{1,2} \cdot \nabla \mathbf{u}_{1,2} = -\nabla p_{1,2} + \frac{1}{Re_{1,2}} \Delta \mathbf{u}_{1,2}, \quad (1.10a)$$

$$\nabla \cdot \mathbf{u}_{1,2} = 0, \quad (1.10b)$$

where  $Re_{1,2} = \rho_{1,2} U_{\text{ref}} D_{\text{ref}} / \mu_{1,2}$  is the Reynolds number in each phase. The decomposition (1.8) is inserted in equation (1.10) and  $\zeta$  is dropped for convenience. As we are interested in the growth of infinitesimal disturbances, only terms that are perturbed at leading order are retained and all quadratic perturbations are assumed zero. Since the base flow satisfies the stationary equivalent of equation (1.10), all base flow terms may be removed from the resulting equation. Consequently, we arrive at the linear perturbation equations

$$\partial_t \mathbf{u}'_{1,2} + \mathbf{U}_{1,2} \cdot \nabla \mathbf{u}'_{1,2} + \mathbf{u}'_{1,2} \cdot \nabla \mathbf{U}_{1,2} = -\nabla p'_{1,2} + \frac{1}{Re_{1,2}} \Delta \mathbf{u}'_{1,2}, \quad (1.11a)$$

$$\nabla \cdot \mathbf{u}'_{1,2} = 0. \quad (1.11b)$$

The two fluid phases are separated by an interface of the form  $y = h(x, t)$ . Similarly to equation (1.9), the interface is perturbed as

$$h(x, t) = H(x) + \zeta h'(x, t) \quad \text{and} \quad h'(x, t) = \hat{h} e^{i(\alpha x - \omega t)}. \quad (1.12)$$

For the derivation of the coupling conditions, a constant  $H$  is assumed. Formally, these conditions are valid at the perturbed interface  $h(x, t)$ . However, by means of a Taylor expansion of  $h(x, t)$  around  $y = H$  and by neglecting terms of second order or higher, a linear approximation at the unperturbed interface is obtained. For satisfying the continuity of the velocity across the interface, it holds

[21]: Söderberg (2003), 'Absolute and convective instability of a relaxational plane liquid jet'

[22]: Boeck et al. (2005), 'Viscous versus inviscid instability of two-phase mixing layers with continuous velocity profile'

[45]: Tammisola et al. (2011), 'Stabilizing effect of surrounding gas flow on a plane liquid sheet'

$$\left[ \left[ u' + U + h' \frac{dU}{dy} \right] \right]_{y=H,1} - \left[ \left[ u' + U + h' \frac{dU}{dy} \right] \right]_{y=H,2} = 0, \quad (1.13a)$$

$$\left[ v' \right]_{y=H,1} - \left[ v' \right]_{y=H,2} = 0, \quad (1.13b)$$

where quantities inside  $\left[ \cdot \right]_{y=H,1,2}$  belong to phase 1 or 2 respectively. Further, the continuity of shear stress requires

$$\left[ \left[ \frac{\partial v'}{\partial x} + \frac{\partial u'}{\partial y} + h' \frac{d^2 U}{dy^2} \right] \right]_{y=H,1} - \tilde{\mu} \left[ \left[ \frac{\partial v'}{\partial x} + \frac{\partial u'}{\partial y} + h' \frac{d^2 U}{dy^2} \right] \right]_{y=H,2} = 0, \quad (1.14)$$

and the continuity of normal stress yields

$$\left[ \left[ p' - \frac{2}{Re_1} \frac{\partial v'}{\partial y} \right] \right]_{y=H,1} - \left[ \left[ \tilde{\rho} p' - \frac{2\tilde{\mu}}{Re_1} \frac{\partial v'}{\partial y} \right] \right]_{y=H,2} + \frac{1}{We} \frac{\partial^2 h'}{\partial x^2} = 0, \quad (1.15)$$

where  $\tilde{\mu} = \mu_2/\mu_1$  is the ratio of the dynamic viscosities of the two fluids,  $\tilde{\rho} = \rho_2/\rho_1$  is the density ratio and  $We = \rho_1 U_{ref}^2 D_{ref} / \sigma$  is the Weber number. The kinematic condition for the interface is

$$\left[ \left[ \frac{\partial h'}{\partial t} + U \frac{\partial h'}{\partial x} = v' \right] \right]_{y=H,1,2}. \quad (1.16)$$

It is useful to bear in mind that with the Lagrangian approach used here to account for the fluid phases and interface, the linearised equations describing each phase are similar to those obtained for a single-phase flow. The interface at which surface tension acts is only introduced by the coupling conditions along the phase boundary. The system (1.11), together with the coupling conditions (1.13)-(1.16) and a set of problem-specific boundary conditions, can be recast and solved as an eigenvalue problem where either  $\omega$  (in case of a temporal analysis) or  $\alpha$  (in case of a spatial analysis) are the complex eigenvalues. For a temporal analysis, the linear eigenvalue problem is given as

$$\mathbf{A}\mathbf{q} = \omega\mathbf{B}\mathbf{q}. \quad (1.17)$$

Upon a suitable numerical discretisation, equation (1.17) may be solved using standard linear algebra techniques.

## 1.4.2 Global analysis

In §1.4.1, the linear stability was assessed under the parallel flow assumption, to reduce the spatial in-homogeneity of the base flow to a single coordinate. For the global analysis, this assumption is relaxed such that the base flow  $\mathbf{Q}(\mathbf{x})$  and the perturbations  $\mathbf{q}'(\mathbf{x})$  may be in-homogeneous in all spatial coordinates. The global perturbation ansatz becomes

$$\mathbf{q}'(\mathbf{x}, t) = \hat{\mathbf{q}}(\mathbf{x})e^{-i\omega t}. \quad (1.18)$$

Consequently, global analysis is only concerned with the temporal exponential growth of disturbances (oscillator flows), as opposed to a local analysis. A disturbance that is associated with an unstable eigenvalue will grow in time without limit and contaminate the whole domain for  $t \rightarrow \infty$ . The resulting instability is *global*.

To derive the linear perturbation equations for a two-phase flow in a global framework, it is in principle possible to proceed with similar methodology as for the local analysis: By using a Lagrangian approach with boundary fitted domains and subsequent formulation of a matrix eigenvalue problem. This approach has been followed by [23, 24] for the computation of two-dimensional global modes of selected two-phase shear flows. However, for large-scale two-dimensional or three-dimensional flow domains, the required memory to form the matrices of the eigenvalue problem quickly becomes prohibitively large, making a direct solution infeasible. A common approach to circumvent this limitation, is to use a matrix-free time-stepping approach. To this end, it is possible to linearise an available nonlinear solver, that has, for instance, been used to compute the base flow, and perform the necessary time-stepping [46, 47]. Additionally, the method can be coupled with a Krylov subspace method (e.g. an Arnoldi method [48]) to iteratively compute the wanted eigenvalues. This method has become the quasi-standard approach for global stability analysis of large-scale single-phase flows but an application for two-phase flows poses several challenges and has not yet been attempted. The development of such a solver is described in Chapter 3.

Here, a general overview is given on the derivation of the linearised perturbation equations for a two-phase flow, based on the unified formulation of the nonlinear two-phase Navier-Stokes equations (1.1). Upon non-dimensionalisation, using  $\rho_1$ ,  $\mu_1$  and suitable length and velocity scales, we obtain the following form of the two-phase Navier-Stokes equations in a level-set formulation

$$\begin{aligned} [\tilde{\rho} + H_\epsilon(\phi)(1 - \tilde{\rho})](\partial_t \mathbf{u} + \mathbf{u} \cdot \nabla \mathbf{u}) = \\ - \nabla p + \frac{1}{Re} \nabla \cdot [(\tilde{\mu} + H_\epsilon(\phi)(1 - \tilde{\mu}))(\nabla \mathbf{u} + \nabla^T \mathbf{u})] + \frac{1}{We} \kappa \mathbf{n} \delta_\epsilon(\phi), \end{aligned} \quad (1.19a)$$

$$\partial_t \phi + \nabla \cdot (\phi \mathbf{u}) = 0, \quad (1.19b)$$

$$\nabla \cdot \mathbf{u} = 0 \quad (1.19c)$$

where the Reynolds number is  $Re = \rho_1 U_{\text{ref}} D_{\text{ref}} / \mu_1$ , the Weber number is  $We = \rho_1 U_{\text{ref}}^2 D_{\text{ref}} / \sigma$ ,  $\tilde{\rho} = \rho_2 / \rho_1$  and  $\tilde{\mu} = \mu_2 / \mu_1$ . Further, we define the vector  $\mathbf{q} = (\mathbf{u}, p, \phi)^T$  containing the flow quantities. The ansatz (1.18) is inserted in equation (1.19) and similarly to the procedure in §1.4.1,  $\zeta$  is dropped for convenience. Again, only terms that are perturbed at leading order are retained and all quadratic (and higher-order) perturbations are

[23]: Tammmisola et al. (2011), ‘Effect of surface tension on global modes of confined wake flows’

[24]: Tammmisola et al. (2012), ‘Surface tension-induced global instability of planar jets and wakes’

[46]: Tuckerman et al. (2000), ‘Bifurcation analysis for timesteppers’

[47]: Barkley et al. (2008), ‘Direct optimal growth analysis for timesteppers’

[48]: Saad (2011), *Numerical Methods for Large Eigenvalue Problems: Revised Edition*

assumed zero. Consequently, we arrive at the following linear perturbation equations:

$$\begin{aligned} & [\bar{\rho} + H_\epsilon(\Phi)(1 - \bar{\rho})](\partial_t \mathbf{u}' + \mathbf{u}' \cdot \nabla \mathbf{U} + \mathbf{U} \cdot \nabla \mathbf{u}') + 2[\delta_\epsilon(\Phi)\phi'(1 - \bar{\rho})](\mathbf{U} \cdot \nabla \mathbf{U}) \\ &= -\nabla p' + \frac{1}{Re} \nabla \cdot [(\tilde{\mu} + H_\epsilon(\Phi)(1 - \tilde{\mu}))(\nabla \mathbf{u}' + \nabla^T \mathbf{u}')] \\ &+ \frac{1}{Re} \nabla \cdot [(\delta_\epsilon(\Phi)\phi'(1 - \tilde{\mu}))(\nabla \mathbf{U} + \nabla^T \mathbf{U})] + \mathbf{F}_s(\Phi, \phi'), \end{aligned} \quad (1.20a)$$

$$\partial_t \phi' + \nabla \cdot (\Phi \mathbf{u}') + \nabla \cdot (\phi' \mathbf{U}) = 0, \quad (1.20b)$$

$$\nabla \cdot \mathbf{u}' = 0. \quad (1.20c)$$

Upon inspection of the linearised equations it is seen that they contain a number of additional terms that are not present in the formulation in equation (1.11). This stems from the fact, that the present formulation is derived in an Eulerian framework, as opposed to equation (1.11) which is formulated in a Lagrangian framework. Therefore, the present equations account for both phases and density and viscosity are nonuniform. The additional advection and diffusion term, as well as the linearised surface tension  $\mathbf{F}_s(\Phi, \phi')$  in equation (1.20a) replace the global equivalent of the coupling conditions (1.13)-(1.15). Similar, the linearised level-set transport equation (1.20c) replaces the kinematic condition (1.16). Further explanations of the involved terms and the exact form of the linearised surface tension  $\mathbf{F}_s(\Phi, \phi')$  are given in Chapter 3. Solutions to equation (1.20) may be obtained by time-stepping of the linearised solver.

### 1.4.3 Mean flow stability

Until now, the methods for linear analysis have been derived by linearising the Navier-Stokes operator around a stationary solution. However, this ignores any influence of dynamic fluctuations on the time-averaged mean flow such as the nonlinear saturation of the oscillatory flow [49]. Further, there are many practical flow scenarios where a stationary solution does not exist, such as externally forced or turbulent flows. In such cases it may be appropriate to assess the stability of the time-averaged mean flow, obtained from the oscillatory flow once it has reached its limit cycle. Accordingly, the decomposition (1.8) is replaced by the triple decomposition [50]

$$\mathbf{q}(\mathbf{x}, t) = \bar{\mathbf{q}}(\mathbf{x}) + \tilde{\mathbf{q}}(\mathbf{x}, t) + \mathbf{q}''(\mathbf{x}, t). \quad (1.21)$$

Here  $\bar{(\cdot)}$  denotes time-averaged quantities whereas  $\tilde{(\cdot)}$  and  $(\cdot)''$  denote harmonic quantities and stochastic fluctuations respectively.

In the context of an incompressible single-phase flow, the decomposition (1.21) is inserted in equation (1.10), considering only a single fluid phase. Phase<sup>1</sup>- and time-averaging are performed to obtain the time-averaged Navier-Stokes equations

[49]: Noack et al. (2003), 'A hierarchy of low-dimensional models for the transient and post-transient cylinder wake'

[50]: Reynolds et al. (1972), 'The mechanics of an organized wave in turbulent shear flow. Part 3. Theoretical models and comparisons with experiments'

1: Here, the term *phase* refers to the phase of a periodic oscillation and not the fluid phase.

$$\bar{\mathbf{u}} \cdot \nabla \bar{\mathbf{u}} = -\nabla \bar{p} + \frac{1}{Re} \Delta \bar{\mathbf{u}} + \mathcal{Q}, \quad (1.22a)$$

$$\nabla \cdot \bar{\mathbf{u}} = 0. \quad (1.22b)$$

The dynamic equation of the harmonic fundamental wave is found by inserting the decomposition (1.21) in equation (1.10), phase-averaging and subtraction of equation (1.22). It is given as

$$\partial_t \tilde{\mathbf{u}} + \bar{\mathbf{u}} \cdot \nabla \tilde{\mathbf{u}} + \tilde{\mathbf{u}} \cdot \nabla \bar{\mathbf{u}} = -\nabla \tilde{p} + \frac{1}{Re} \Delta \tilde{\mathbf{u}} + \mathcal{Q}^*, \quad (1.23a)$$

$$\nabla \cdot \tilde{\mathbf{u}} = 0. \quad (1.23b)$$

The terms  $\mathcal{Q}$  and  $\mathcal{Q}^*$  contain the quadratic nonlinear terms which remain from the insertion of the triple decomposition in the advective term of equation (1.10) and are given as

$$\mathcal{Q} = -\nabla \cdot (\overline{\tilde{\mathbf{u}}\tilde{\mathbf{u}}}) - \nabla \cdot (\overline{\mathbf{u}''\mathbf{u}''}), \quad (1.24a)$$

$$\mathcal{Q}^* = -\nabla \cdot (\overline{\tilde{\mathbf{u}}\tilde{\mathbf{u}}}) - \nabla \cdot (\overline{\mathbf{u}''\mathbf{u}''}). \quad (1.24b)$$

The term  $\mathcal{Q}$  accounts for the nonlinear modification of the mean field by harmonic and stochastic Reynolds stresses. Consequently, the mean flow is not a steady solution of the Navier Stokes equations as it differs from the steady solution by the action of  $\mathcal{Q}$ . The term  $\mathcal{Q}^*$  accounts for the quadratic nonlinear interactions of the harmonics waves and the stochastic fluctuations that modify the dynamics of the fundamental wave. For a mean flow analysis, the term  $\mathcal{Q}$  is indirectly incorporated in the model through the use of the time-averaged mean flow. The term  $\mathcal{Q}^*$  is neglected, as it is assumed that the influence of the quadratic harmonic interactions is small, although the harmonic waves themselves might not necessarily be small. The validity of this assumption must be carefully checked in order for the analysis to be meaningful [51, 52].

In case of a two-phase flow, the mean flow analysis introduces an ambiguity as it is not *a priori* clear how the representation of a time-averaged interface  $\bar{h}$  or level-set function  $\bar{\phi}$  (depending on which type of framework is chosen) should be interpreted. Since the interface represents a discontinuity, a simple time-average may not be meaningful. This problem, including a possible model for a local stability analysis, is addressed in Chapter 2.

## 1.5 Nonlinear dynamics of incompressible flow

The results of a linear stability analysis around a base flow differ from the actual dynamics of the nonlinear flow as they do not incorporate the action of the quadratic nonlinearities ( $\mathcal{Q}, \mathcal{Q}^*$ ). To evaluate the validity of the linear

[51]: Sipp et al. (2007), 'Global stability of base and mean flows: a general approach and its applications to cylinder and open cavity flows'

[52]: Turton et al. (2015), 'Prediction of frequencies in thermosolutal convection from mean flows'

analysis, it is therefore important to be able to quantify these terms. Further, they provide the basis for a detailed investigation the nonlinear dynamics of the flow. By expanding the harmonic part of the triple decomposition (1.21) as a Fourier series

$$\hat{\mathbf{u}}_n(\mathbf{x}) = \sum_{n \neq 0} \tilde{\mathbf{u}}(\mathbf{x}, t) e^{-in\omega t}, \quad (1.25)$$

we can restate (1.23) in compact form as

$$in\omega \bar{\mathbf{u}}_n + \mathcal{L}(\bar{\mathbf{u}}, \hat{\mathbf{u}}_n) = \mathcal{Q}^*(\hat{\mathbf{u}}_n, \mathbf{u}''). \quad (1.26)$$

This represents an infinite expansion of nonlinear equations, each accounting for the dynamics of the  $n$ -th harmonic wave. At the zeroth and each higher harmonic the quadratic nonlinearity may as well be expanded as

$$\mathcal{Q} = - \sum_{m \neq 0} \nabla \cdot (\hat{\mathbf{u}}_m \hat{\mathbf{u}}_{-m}) - \nabla \cdot (\overline{\mathbf{u}'' \mathbf{u}''}), \quad (1.27a)$$

$$\mathcal{Q}_n^* = - \sum_{m \neq n, 0} \nabla \cdot (\hat{\mathbf{u}}_m \hat{\mathbf{u}}_{n-m}) - \nabla \cdot (\widetilde{\mathbf{u}'' \mathbf{u}''}). \quad (1.27b)$$

The first term represents the expansion of the nonlinear mean flow harmonics, at each level of expansion, consisting of a quadratic self interaction of the respective harmonic. The second term expands the nonlinear interaction acting on the  $n$ -th harmonic. The analysis of higher harmonic interactions is further explored in Chapters 2 and 4.

## 1.6 Outline of the thesis

Linear stability analysis is a powerful tool to obtain detailed insights about the linear dynamics of flows and the origins of flow instability or to build reduced-order models. Within the last decades, considerable research has been conducted to develop new and improve existing methods and tools for linear analysis that researchers have at their disposal. Thus, methods like global stability analysis or mean flow analysis are now firmly established for the analysis of single-phase flows. However, in the context of two-phase flows, the development of such tools does significantly lag behind and the availability of agile methods for global stability analysis is scarce. Mean flow analysis of a two-phase flow has not been attempted.

Within the scope of this thesis, we aim to take a step towards the application of these methods for two-phase flows. To do so, the thesis is divided into three parts, each one of them representing a separate publication.

In **Publication 1** (Chapter 2), the linear and nonlinear dynamics of a transversely forced liquid jet are investigated. As externally forced flows do not possess stationary solutions, linear stability around a base flow solution is not applicable. In this chapter, we therefore explore the potential of a linear stability analysis around the time-averaged mean flow, within the framework of a local analysis and develop a model to account for the influence of the fluid interface in the mean flow.

In **Publication 2** (Chapter 3), a framework for the global stability analysis of two-phase flows is developed. The methodology is based on an Eulerian representation of the fluid phases and interface as described in §1.4.2. The method is constructed by linearising a nonlinear solver for two-phase flows and performing time-stepping of the linearised equations. Principally, the matrix-free framework allows for the flexibility to compute linear solutions of large-scale two- and three-dimensional flows with arbitrary interface topologies.

In **Publication 3** (Chapter 4), the global stability solver derived in Chapter 3 is applied to compute fully three-dimensional linear global modes of a laminar two-phase swirling flow. The linear analysis reveals the existence of two unstable global modes that oscillate at harmonic frequencies and subsequent nonlinear simulation of the flow reveals a strong triadic resonance of these modes in the flow. The work in this chapter demonstrates the potential of the developed methods towards future applications to more complex flow configurations and provides new insights regarding the influence of viscosity stratified two-phase flow on vortex breakdown and helical instability.

The following three chapters contain, verbatim, contents published in or submitted to the *Journal of Fluid Mechanics*. Consequently, the nomenclature within each chapter is subject to change and textual redundancies between the chapters and the introduction may appear.



# Instability of forced planar liquid jets: mean field analysis and nonlinear simulation

# 2

## Abstract

The stability of forced planar liquid jets in a still gaseous environment is explored using nonlinear simulation and spatial linear stability analysis. Harmonic modulation of the transverse component of the inlet velocity leads to an excitation of sinuous modes in the jet. Two forcing amplitudes, 1 % and 5 %, are investigated. While for 1 % forcing, the interfacial disturbance retains a sinuous shape throughout the domain, for 5 % forcing, an increasing downstream deviation from the sinuous wave shape is found. Both forcings lead to sufficient mean flow correction to render linear stability analysis on a base flow unfeasible. Hence, an analysis on the time-averaged mean flow is performed. A correction scheme is introduced, to account for the spreading of the interface position in the mean flow. Comparison of eigenfunctions and growth rates with their counterparts from the nonlinear simulation shows an excellent agreement for 1 % forcing. For 5 % forcing, agreement of the eigenfunctions deteriorates significantly and growth rates are falsely predicted, resulting in a break-down of the stability model. Subsequent analysis reveals a strong interaction of the fundamental wave with the second higher harmonic wave for 5 % forcing and a reversed energy flow from the coherent motion to the mean flow. These findings provide an explanation for the failure of the linear stability model for large forcing amplitudes. The study extends the applicability of mean flow stability analysis to convectively unstable planar liquid/gas jets and supports previous findings on the limits of mean flow stability, involving pronounced influence of higher harmonic modes.

2.1	Introduction . . . . .	20
2.2	Nonlinear simulation of a liquid jet . . . . .	21
2.3	Linear stability model . . . . .	27
2.4	Comparison of nonlinear simulation and linear stability model . . . . .	37
2.5	Interaction of the fundamental wave with higher harmonics . . . . .	41
2.6	Summary and conclusions . . . . .	49
2.7	Appendix . . . . .	50

The contents of this chapter have been **published** in revised form in the *Journal of Fluid Mechanics*:

S. Schmidt, and K. Oberleithner. 'Instability of forced planar liquid jets: mean field analysis and nonlinear simulation.' In: *Journal of Fluid Mechanics* 883 (2020). DOI: <https://doi.org/10.1017/jfm.2019.855>

This version (accepted manuscript) is free to view and download for private research and study only. Not for re-distribution or re-use. ©copyright holder.

## 2.1 Introduction

The breakup of liquid jets is relevant to a broad range of industrial applications, including ink-jet printers or fuel injection in e.g. diesel engines or gas turbines. In such cases a high velocity liquid stream is injected into a still gaseous environment through a high pressure nozzle. The resulting two-fluid system is subjected to extrinsic and intrinsic mechanisms of destabilisation. Extrinsic factors for instance, are given by pressure fluctuations in the supplied liquid stream or forced oscillatory movement of the jet within the nozzle. Forced destabilisation can be achieved with the use of a fluidic oscillator, to create a spatially or temporarily oscillating jet [29, 53, 54]. These effects possibly promote the development of intrinsic destabilisation mechanisms that arise through the shear of the adjacent parallel fluid layers, the presence of surface tension at the liquid/gas interface or unstable stratification of denser and lighter fluid.

Besides experiments or direct numerical simulation (DNS) to capture the full nonlinear dynamics of the flow, assessment of the various occurring flow instability can be made by means of linear stability analysis (LSA). The early studies of [55] consider the inviscid analysis of a low-velocity cylindrical liquid jet. In this configuration disturbances in the jet radius, and thus in the capillary pressure gradient, with wavelengths exceeding the jet perimeter may grow in time and break up the jet under the influence of surface tension.

Investigations by [17], however, showed that surface tension acts stabilising if the jet is planar since there is no circumferential connection of the upper and lower interface. Instability has therefore to be rooted in the shear layer of the fluids, caused by either the momentum, density or viscosity defect [18, 56]. With increasing jet velocity aerodynamic effects become relevant. Thus the incorporation of the surrounding fluid is necessary as investigated by [19] for an inviscid ambient gas and later in the studies of [20], [57] and [58] for a viscous gas. However, neither considered a gas boundary layer, which was studied by e.g. [45]. For a fully viscous shear layer, approximated by a tanh-profile, [22] found three competing unstable modes, attributed to the viscosity ratio (H mode), the inviscid Kelvin-Helmholtz and the viscous Tollmien-Schlichting mechanism. In the context of plane liquid jets [21] found up to five unstable modes, three asymmetric and two symmetric modes using both spatial and temporal LSA. The jet velocity profile was obtained by numerical analysis and the gas velocity profile was approximated by a spatial transformation of Stokes first problem [59]. Downstream amplitude growth was evaluated and compared to experimental results with good agreement. Similarly, a cylindrical jet in the first wind-induced break-up regime was analysed by [60] using a constant jet velocity. In the above works either the gas phase or liquid phase baseflow profiles were modeled using analytical approximations of the actual velocity profile. A fully numerical baseflow computation by means of Direct Numerical Simulation was used by [24] for global stability analysis of confined planar liquid jets and wakes.

The classical approach to LSA by linearising the Navier-Stokes operator around a theoretical, steady baseflow, however, neglects possible nonlinear dynamics of the underlying flow as well as any incoherent, turbulent fluctuations. A way to account for these aspects is to linearise around the time-averaged mean flow. The approach has been successfully used for e.g.

[29]: Schmidt et al. (2018), 'Numerical investigation of the breakup behavior of an oscillating two-phase jet'

[53]: Bobusch et al. (2013), 'Experimental study of the internal flow structures inside a fluidic oscillator'

[54]: Krüger et al. (2013), 'Numerical modeling and validation of the flow in a fluidic oscillator'

[55]: Rayleigh (1878), 'On The Instability Of Jets'

[17]: Squire (1953), 'Investigation of the instability of a moving liquid film'

[18]: Yih (1967), 'Instability due to viscosity stratification'

[56]: Drazin et al. (2004), *Hydrodynamic Stability*

[19]: Hagerty et al. (1955), 'A study of the stability of moving liquid film'

[20]: Lin et al. (1990), 'Absolute and convective instability of a liquid sheet'

[57]: Li et al. (1991), 'On the temporal instability of a two-dimensional viscous liquid sheet'

[58]: Li (1993), 'Spatial instability of plane liquid sheets'

[45]: Tammisola et al. (2011), 'Stabilizing effect of surrounding gas flow on a plane liquid sheet'

[22]: Boeck et al. (2005), 'Viscous versus inviscid instability of two-phase mixing layers with continuous velocity profile'

[21]: Söderberg (2003), 'Absolute and convective instability of a relaxational plane liquid jet'

[59]: Schlichting et al. (2006), *Grenzschicht-Theorie*

[60]: Gordillo et al. (2005), 'Aerodynamic effects in the break-up of liquid jets: on the first wind-induced break-up regime'

[24]: Tammisola et al. (2012), 'Surface tension-induced global instability of planar jets and wakes'

the prediction of finite vortex shedding behind a cylinder at post-critical Reynolds numbers [61, 62] or the spatial development of a forced single-phase jet [63]. Limits of the mean flow model have been revealed by [51] for an open cavity flow due to significant resonance of the fundamental wave with its first harmonic. To the best of the authors knowledge the concept of mean flow stability has not been applied to the scenario of forced liquid jets so far.

In the present work a jet is forced sinusoidally at the domain inlet, resulting in the development of finite amplitude waves that grow and decay in downstream direction, resulting in a convectively unstable flow. The aim of the investigation is twofold. First, we explore the potential of the mean field model for LSA to predict the spatial development of the excited instability waves in a forced liquid jet. Modelling using mean flow analysis has the potential of providing a simplified model to capture coherent structures of an unsteady flow without the necessity of computing the full nonlinear representation of the flow. Second, the subsequent downstream nonlinear evolution of fundamental wave and interaction with developing higher harmonic waves are studied using direct numerical simulation of the jet. The fully nonlinear, unsteady flow representation also allows for a thorough study of the phenomenological manifestation of the nonlinear wave interaction in the flow.

The paper is structured as follows: In Section II we briefly summarise the numerical methods and present the general results of the nonlinear simulation to establish a phenomenological overview of the studied cases. In Section III the mean flow perturbation equations are derived and the methodology for two-phase flows is explained. We present the parameterisation of the mean flow and analyse general stability properties of an unforced and forced jet. A detailed comparison of the nonlinear results and the LSA is conducted in Section IV where growth rates and mode shapes, derived for both methods, are presented. To conclude, in Section V shortcomings of the stability model are investigated by help of the nonlinear simulations. The developing nonlinearities in the downstream development of the excited waves are analysed and linked to the vortex dynamics of the unsteady flow.

## 2.2 Nonlinear simulation of a liquid jet

Physically, the conservation laws for flows involving two immiscible and incompressible fluids are derived with two additional assumptions over the single-phase formulation, regarding the interface, separating the two phases. First, the interface is assumed to have negligible thickness, resulting in a discontinuity of the density and viscosity field. Second, the imbalance of molecular forces along the fluid interface results in a surface tension force located at the interface. Consequently, velocity and tangential stress are continuous across the interface, while the normal stress encounters a jump, balanced by the surface tension. Numerically, the system is modelled in a unified formulation over both phases, known as the one-fluid formulation [35], where continuity equation and momentum

[61]: Pier (2002), ‘On the frequency selection of finite-amplitude vortex shedding in the cylinder wake’

[62]: Barkley (2006), ‘Linear analysis of the cylinder wake mean flow’

[63]: Oberleithner et al. (2014), ‘Mean flow stability analysis of oscillating jet experiments’

[51]: Sipp et al. (2007), ‘Global stability of base and mean flows: a general approach and its applications to cylinder and open cavity flows’

[35]: Tryggvason et al. (2011), *Direct Numerical Simulations of Gas-Liquid Multiphase Flows*

balance are given by

$$\frac{\partial \rho}{\partial t} + \frac{\partial \rho u_i}{\partial x_i} = 0, \quad (2.1a)$$

$$\rho \left( \frac{\partial u_i}{\partial t} + u_j \frac{\partial u_i}{\partial x_j} \right) = -\frac{\partial p}{\partial x_i} + \frac{\partial}{\partial x_j} \left[ \mu \left( \frac{\partial u_i}{\partial x_j} + \frac{\partial u_j}{\partial x_i} \right) \right] + \sigma \kappa n_i \delta_s, \quad (2.1b)$$

with  $u_i = (u, v)^T$  representing the components of the velocity vector ( $i = 1, 2$ ),  $x_i = (x, y)^T$  the spatial coordinates,  $\rho$  the density,  $\mu$  the dynamic viscosity and  $p$  the pressure. The density and viscosity field are given as

$$\rho = \rho_g + (\rho_l - \rho_g)C, \quad (2.2a)$$

$$\nu = \nu_g + (\nu_l - \nu_g)C, \quad (2.2b)$$

where the indices g and l refer to the gaseous or liquid phase, respectively. Thus, density and viscosity vary between the phases but are constant within each phase. The volume fraction  $C(x_i, t)$  is a Heaviside function, defined as the ratio of liquid volume to total volume.

The term  $\sigma \kappa n_i \delta_s$  in equation (2.1b) accounts for surface tension forces along the interface where  $\sigma$  denotes the surface tension coefficient,  $\kappa$  is the mean interface curvature, and  $n_i$  is the outward pointing normal vector. It is formulated according to the continuum surface force method (CSF) [41]. The equations are solved using the finite volume method in the open-source toolbox BASILISK, developed by Stéphane Popinet (<http://basilisk.fr>). For a detailed description of the implemented numerical schemes, see [25, 26].

The interface is tracked with the Volume-of-Fluid (VoF) method [64] using the advection of  $C(x_i, t)$  as

$$\frac{\partial C}{\partial t} + \frac{\partial C u_i}{\partial x_i} = 0. \quad (2.3)$$

Computational cells where  $C = 1$  are located in the liquid phase and cells with  $C = 0$  are situated in the gaseous phase. Consequently, in interfacial cells  $0 < C < 1$ . Given the velocity field, the volume fraction field is successively advected along each dimension with a one-dimensional scheme. The local volume fraction fluxes are calculated from the local velocities and geometric reconstruction of the interface. In two dimensions the interface segment, dividing a computational cell, is reconstructed by knowledge of the value of  $C$  in the cell. Therefore, the orientation of the segment is evaluated by computing the normal vector to the segment  $n_i = \partial C / \partial x_i$ . The segment then is described by  $n_i x_i = c$ , where  $c$  is the shortest distance from the segment to the current coordinate below the segment. In practice,  $c$  can be determined by an analytic formula [38].

The surface tension term in equation (2.1b) is implemented using a balanced CSF formulation [65] to avoid the problem of parasitic currents [66]. The method relies on an accurate computation of the interface curvature which is obtained with a height-function method, that gives second-order accurate curvature estimates [67, 68].

[41]: Brackbill et al. (1992), ‘A continuum method for modeling surface tension’

[25]: Popinet (2003), ‘Gerris: a tree-based adaptive solver for the incompressible Euler equations in complex geometries’

[26]: Popinet (2009), ‘An accurate adaptive solver for surface-tension-driven interfacial flows’

[64]: Hirt et al. (1981), ‘Volume of fluid (VOF) method for the dynamics of free boundaries’

[38]: Scardovelli et al. (1999), ‘Direct numerical simulation of free-surface and interfacial flow’

[65]: Francois et al. (2006), ‘A balanced-force algorithm for continuous and sharp interfacial surface tension models within a volume tracking framework’

[66]: Harvie et al. (2006), ‘An analysis of parasitic current generation in volume of fluid simulations’

[67]: Torrey et al. (1985), *NASA-VOF2D: A Computer Program for Incompressible Flows With Free Surfaces*

[68]: Cummins et al. (2005), ‘Estimating curvature from volume fractions’

For large density ratios in e.g. water/air flow, a momentum conserving scheme is used for the advection term in equation (2.1b) in order to avoid numerical instabilities.

The spatial discretisation is based on a uniform or non-uniform structured grid. In the latter case, a hierarchical quad-/octree structure is used to dynamically refine the grid at each time step according to a specified adaptation criterion. The dynamic grid helps to retain a high resolution in regions of large gradients while simultaneously allowing for coarse resolution away from the region of interest and therefore greatly decreases computational costs.

### 2.2.1 Problem formulation

The BASILISK solver is used to simulate the temporal and spatial evolution of a transversely forced planar liquid jet in a still ambient gas. The computational domain is square with an edge length  $L = 200D$ , the inlet has a width  $D = 2 \times 10^{-3}$  m and is located in the centre of the left boundary. The computational domain is significantly larger than the relevant area for this study. For the remaining sections of this work, only the area  $-5 < y/D < 5$ ,  $0 < x/D < 40$  will be considered and referred to as domain. The domain is initialised with  $u_i = 0$ ,  $C = 0$ . We use Dirichlet boundary conditions at the inlet and impose a sinusoidal oscillation in the transverse velocity component. The inlet conditions at  $\Omega_1$  in the centre of the left domain edge reads

$$u|_{\Omega_1} = U, \quad (2.4a)$$

$$v|_{\Omega_1} = U \times A \sin(2\pi f^* t), \quad (2.4b)$$

$$\frac{\partial p}{\partial x}|_{\Omega_1} = 0, \quad (2.4c)$$

$$C|_{\Omega_1} = 1, \quad (2.4d)$$

where  $U = 4$  m/s is the plug flow velocity at the inlet. The forcing frequency is  $f^* = 200$  Hz and  $A = 0.01, 0.05$ . Additionally, a simulation of the unforced jet is conducted. On the remainder of the left edge ( $\Omega_2$ ) a no-slip boundary is imposed. The top and lower edges  $\Omega_3$  are equipped with symmetry boundaries. Along the right edge  $\Omega_4$  a standard outflow condition

$$\frac{\partial u_i}{\partial x}|_{\Omega_4} = 0, \quad (2.5a)$$

$$p|_{\Omega_4} = 0, \quad (2.5b)$$

$$\frac{\partial C}{\partial x}|_{\Omega_4} = 0, \quad (2.5c)$$

is imposed. Further, a sponge region is employed, by enforcing a coarse mesh for  $x > L/4$ . Thereby, vorticity is efficiently dissipated in order to avoid backflow issues at the domain outlet. A schematic description of the computational domain is given in figure 2.1a.

**Table 2.1:** Fluid properties of the liquid and gas phase

Name	Variable	Value	Unit
liquid density	$\rho_l$	997	kg/m <sup>3</sup>
gas density	$\rho_g$	1.177	kg/m <sup>3</sup>
liquid viscosity	$\mu_l$	$8.90 \times 10^{-4}$	kg/(ms)
gas viscosity	$\mu_g$	$1.84 \times 10^{-5}$	kg/(ms)
surface tension	$\sigma$	$72.5 \times 10^{-3}$	N/m

**Table 2.2:** Dimensionless numbers, based on  $U$ ,  $D$  and the forcing frequency  $f^*$ 

Name	Relation	Value
liquid Reynolds number	$Re_l = \rho_l U D / \mu_l$	8962
gas Reynolds number	$Re_g = \rho_g U D / \mu_g$	512
Weber number	$We = \rho_l U^2 D / \sigma$	440
Strouhal number	$St = f^* D / U$	0.1

The fluid properties of the respective phases, corresponding to water and air, and the corresponding dimensionless quantities based on  $U$ ,  $D$  and the forcing frequency  $f^*$  are given in tables 2.1, 2.2. The flow parameters and the domain extend are chosen such that the complete destabilisation cycle of the velocity field, including growth, saturation and onset of decay of the forced instability wave is captured within the area of interest. Further, the choice of flow parameters ensures that the jet remains intact throughout the domain such that no breakup of liquid structures occurs.

A dynamic quadtree-structured grid is chosen as spatial domain discretisation. To check whether a cell needs refinement, its level is reduced by one and increased again. This corresponds to down- and up-sampling of the stored scalar fields. The original field  $\psi$  is compared to the up-sampled field  $\psi^*$  to estimate the error  $\epsilon = \|\psi - \psi^*\|$ . The cell is refined if  $\epsilon > \theta$  and coarsened if  $\epsilon < 2/3 \theta$  where  $\theta$  is the error threshold of the specific scalar field. A more detailed description is given by [69].

[69]: Hooft et al. (2018), ‘Towards adaptive grids for atmospheric boundary-layer simulations’

For the present work, we set  $\theta = 5 \times 10^{-3}$  for both velocity components and the volume fraction. The maximum resolution is limited to 15 levels of refinement, corresponding to a minimum nondimensional cell edge length of  $\Delta x / D \approx 0.0157$ . To evaluate the adequacy of the chosen adaptation criteria and mesh resolution, the time-averaged shear layer momentum thickness, defined as

$$\delta(x) = \int_0^\infty \frac{\bar{u}}{U} \left(1 - \frac{\bar{u}}{U}\right) dy, \quad (2.6)$$

where  $\bar{u}$  denotes the time-averaged stream-wise velocity, is computed for 13 to 15 levels of refinement in figure 2.1b. No visible improvement is seen between the latter two levels, hence the chosen parameters should be sufficient.

Simulations are run for  $TU/D = 409.6$  nondimensional time units, corresponding to 40.96 oscillation cycles. Time stepping is adaptive based, on a Courant condition

$$\Delta t \leq 0.5 \min \left\{ \frac{\Delta x}{u}, \sqrt{\frac{\rho_l \Delta x^3}{\pi \sigma}} \right\}. \quad (2.7)$$

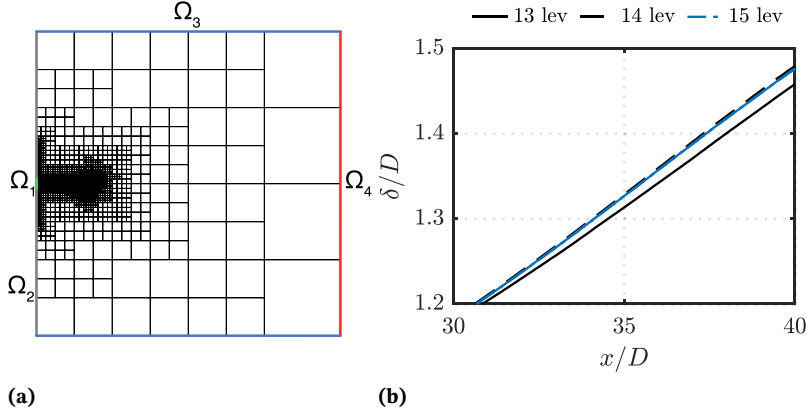


**Figure 2.1:** Schematic illustration of the computational domain and the adaptive grid (a) and grid sensitivity assessment using the stream-wise development of the time-averaged shear layer momentum thickness  $\delta$  for  $A = 0.05$  (b)

### 2.2.2 General jet evolution

The liquid jet, injected on the left side of the domain, evolves in stream-wise direction and remains intact throughout the area of interest. The harmonic transverse forcing at the inlet introduces an initially monochromatic wave that grows in space while being convected downstream. The disturbance amplitude is clearly visible in the fluid interface, shown in figure 2.2, for  $A = 0.01$  and  $A = 0.05$ . For further illustration, the envelope of the interfacial instability wave is shown for both forcing amplitudes by plotting an iso-line of the time-averaged volume fraction field  $\bar{C}$ .

For both amplitudes, the interface disturbance grows in stream-wise direction over the whole domain. For  $x > 15D$  the interfacial disturbance wave starts saturating and approaches its maximum amplitude. The point where the interfacial disturbance is saturated completely is outside the investigated domain ( $x/D \approx 45$ ). For  $A = 0.05$ , the influence of the harmonic forcing on the interface is much more prominent, resulting in significantly larger amplitude growth. Further, for  $A = 0.05$  an increasing deviation from the initial wave pattern is evident from figure 2.2 for  $x/D > 20$ . This results in a characteristic agglomeration of liquid around the wave crests as well as a shift from a sinuous wave shape to a triangular shape.

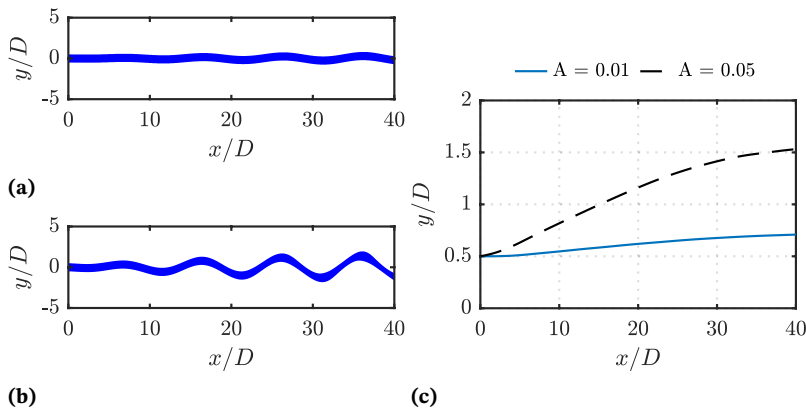


**Figure 2.2:** Instantaneous view of the interface via the volume fraction field  $C$  for (a)  $A = 0.01$ , (b)  $A = 0.05$ . The blue area corresponds to  $C > 0.5$ , denoting the liquid phase while the white area,  $C < 0.5$ , denotes the gas phase. In (c) the envelope of the interfacial instability wave is shown as an iso-line of  $\bar{C} = 0.01$ .

The spatio-temporal evolution of the interfacial wave and secondary structures is illustrated by the diagram of  $C(x, y = 0, t)$  and the instantaneous vorticity field  $\Omega = \partial v / \partial x - \partial u / \partial y$  in figure 2.3. The contour lines of  $C$  illustrate the amplitude growth and saturation of the interfacial wave, while  $\Omega$  visualises the interaction of the interface with the instability growth in the

respective fluid phases. Initially, the interfacial amplitude is small and the vorticity of the liquid phase is virtually zero which is marked as white area in the diagram. Downstream of around  $x/D = 10$ , the amplitude growth leads to sufficient deflection of the interface to intermittently expose the growing non-zero gas phase vorticity. In the subsequent development, the saturation of the interfacial wave is seen in the diagram as the gaps approach a constant thickness. The development of secondary structures is indicated by increasingly complex vortical patterns which manifest in the appearance of clockwise and anti-clockwise rotating vortical patterns in each gap during their downstream evolution.

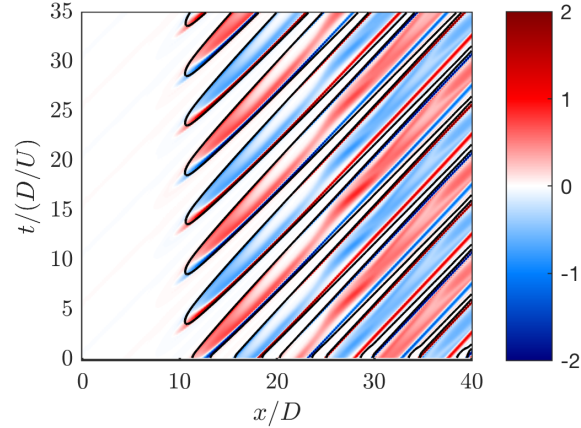


**Figure 2.3:** Spatio-temporal diagram of the nondimensional centre-line vorticity  $\frac{\Omega}{U/D}(x, y = 0, t)$  (filled contour) and the centre-line volume fraction  $C(x, y = 0, t) = 0.5$  (black contour line) for  $A = 0.05$

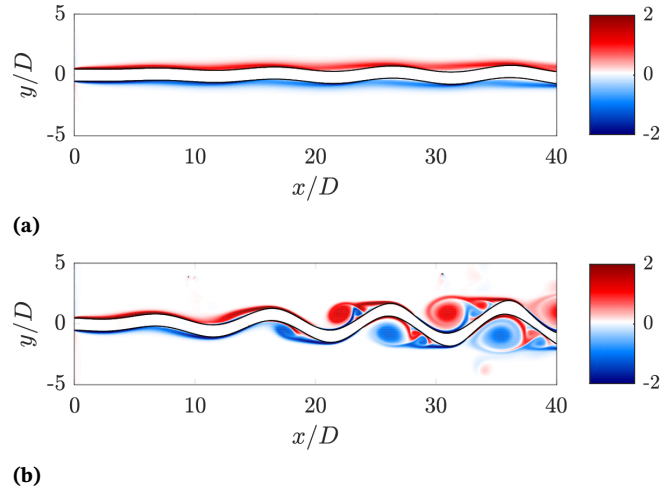


**Figure 2.4:** Instantaneous view of the nondimensional vorticity field  $\frac{\Omega}{U/D}$  for (a)  $A = 0.01$ , (b)  $A = 0.05$ . The Interface  $C = 0.5$  is shown as black contour line.

For further clarification of the evolving vortical structures, the instantaneous vorticity field for both forcing amplitudes is shown in figure 2.4. For  $A = 0.01$ , a single vorticity sheet evolves along each side of the interface and remains intact throughout its downstream development, indicating linear disturbance growth. Contrastingly, for  $A = 0.05$ , the vorticity sheet in the initial shear layer is disturbed by the growing oscillation of the interface, which promotes agglomeration into discrete vortical structures from around  $x/D \approx 15$ . These structures develop along the interfacial wave crests when the curvature of the deflected interface becomes sufficiently large such that the vorticity sheet detaches from the interfacial curve. The formed structures travel in the wave troughs of the excited jet. While initially a single vortical structure is present, additional, secondary structures form during the downstream evolution of the jet.

Similar flow features are observable in the flow visualisation conducted by [45]. In their experimental work a planar liquid sheet is sinusoidally forced with loudspeakers. Although their focus lies on frequency variation and the influence of gas co-flow, the sheet's response to the forcing produces comparable results to this study. In particular, for higher amplitudes, the shift from a sinusoidal to a triangular wave pattern is clearly seen. The increased interface corrugations further suggest a pronounced influence of gas-phase vorticity on the jet.

A somewhat extreme illustration of the effects of large forcing amplitudes on a liquid jet is given in [29] where a liquid jet, emitted by an industrial-type fluidic oscillator is studied numerically and experimentally. The primary instability mechanism studied in the present case is likely to play no role at that scale, as turbulence and early onset of breakup are too pronounced for instability growth to manifest. However, it is observable that the oscillation at large amplitudes, induces significant instabilities along the liquid jet surface. These in turn, have been found to drastically facilitate jet destabilisation, leading to reduced breakup length and smaller diameters in the produced droplet spectrum.

[45]: Tammissola et al. (2011), 'Stabilizing effect of surrounding gas flow on a plane liquid sheet'

[29]: Schmidt et al. (2018), 'Numerical investigation of the breakup behavior of an oscillating two-phase jet'

## 2.3 Linear stability model

In this section, we establish a local linear stability model for a forced liquid jet and apply it to the configurations described in the previous section. The aim is to quantify the observed instability wave growth and decay using a simplified linear model. Therefore, we derive the linearised perturbation equations for infinitesimal disturbances of an interfacial flow. We briefly describe the implementation and validation and give notes about the parameterisation of the mean flow on which the stability analysis is conducted. Thereafter, stability properties are analysed. Special attention is given to the spatial development of the eigenfunction shapes and the corresponding growth rates.

### 2.3.1 Perturbation and mean flow equations

The derivation of the perturbation equations is based on the Navier-Stokes equations for an incompressible Newtonian fluid. In contrast to section 2.2, they are formulated separately for each phase as

$$\frac{\partial u_{i,l,g}}{\partial x_i} = 0, \quad (2.8a)$$

$$\frac{\partial u_{i,l,g}}{\partial t} + u_{j,l,g} \frac{\partial u_{i,l,g}}{\partial x_j} = -\frac{\partial p_{l,g}}{\partial x_i} + \frac{1}{Re_{l,g}} \frac{\partial^2 u_{i,l,g}}{\partial x_j^2}, \quad (2.8b)$$

where equation (2.8b) has been non-dimensionalised with the Reynolds number. The subscripts l, g denote the liquid and gaseous phase respectively. For improved readability, the phase-denoting subscripts will be dropped unless explicit distinction is necessary. For analysing the growth of intrinsic disturbances, the velocity and pressure field are decomposed into a basic state and disturbed state

$$u_i(x_i, t) = u_{b,i}(y) + \epsilon u'_i(x_i, t) \quad \text{and} \quad p(x_i, t) = p_{b,i}(y) + \epsilon p'(x_i, t). \quad (2.9)$$

where  $\epsilon \ll 1$  is a small amplitude. The time-independent base flow is denoted by the subscript b. Since a local analysis is performed, the base flow is assumed to be parallel and of the form  $u_{b,i}(y) = (u_b(y), 0)^T$ . The parameter  $\epsilon$  will be dropped for the remainder of this work. The decomposition, equation (2.9), is substituted in equation (2.8). Since the base flow satisfies equation (2.8), all base flow terms vanish. By ignoring the nonlinear term  $u'_j \frac{\partial u'_i}{\partial x_j}$  the linearised form of the perturbation equations yields

$$\frac{\partial u'_i}{\partial x_i} = 0, \quad (2.10a)$$

$$\frac{\partial u'_i}{\partial t} + u_{b,j} \frac{\partial u'_i}{\partial x_j} + u'_j \frac{\partial u_{b,i}}{\partial x_j} = -\frac{\partial p'}{\partial x_i} + \frac{1}{Re} \frac{\partial^2 u'_i}{\partial x_j^2}. \quad (2.10b)$$

The equations describe the response of the underlying steady base flow to infinitesimal disturbances. However, basing the analysis on the base flow ignores any influence of dynamic fluctuations on the time-averaged mean flow such as the nonlinear saturation of the oscillatory flow [49]. Additionally, in case of an externally forced flow, a steady solution might not even exist. Therefore, since we are interested in the stability of the time-averaged flow, obtained from the oscillatory flow, once it has reached its limit cycle, it is appropriate to choose the triple decomposition of the flow field [50],

$$u_i(x_i, t) = \bar{u}_i(y) + \tilde{u}_i(x_i, t) + u''_i(x_i, t) \quad \text{and} \quad p(x_i, t) = \bar{p}(y) + \tilde{p}(x_i, t) + p''(x_i, t), \quad (2.11)$$

where  $\bar{u}_i$  and  $\bar{p}$  are the time-averaged velocity and pressure field respectively,  $\tilde{u}_i$ ,  $\tilde{p}$  the periodic parts and  $u''_i$ ,  $p''$  the fluctuating parts. Upon substitution of the ansatz into equation (2.8), phase-averaging and time-averaging, the time-averaged Navier-Stokes equations are given as

$$\frac{\partial \bar{u}_i}{\partial x_i} = 0, \quad (2.12a)$$

$$\bar{u}_j \frac{\partial \bar{u}_i}{\partial x_j} = -\frac{\partial \bar{p}}{\partial x_i} + \frac{1}{Re} \frac{\partial^2 \bar{u}_i}{\partial x_j^2} + \mathcal{F}_i, \quad (2.12b)$$

where

$$\mathcal{F}_i = -\frac{\partial}{\partial x_j} (\overline{\tilde{u}_i \tilde{u}_j}) - \frac{\partial}{\partial x_j} (\overline{u''_i u''_j}) \quad (2.13)$$

is interpreted as nonlinear modification of the mean field by Reynolds stresses of the periodic and fluctuating field. This also implies that the

[49]: Noack et al. (2003), 'A hierarchy of low-dimensional models for the transient and post-transient cylinder wake'

[50]: Reynolds et al. (1972), 'The mechanics of an organized wave in turbulent shear flow. Part 3. Theoretical models and comparisons with experiments'

mean flow is not a solution of the steady Navier Stokes equation, as noted by [62].

The ansatz (2.11) is inserted in (2.8), phase-averaging is performed and (2.12) is subtracted, to yield the dynamic equation of the fundamental wave

$$\frac{\partial \tilde{u}_i}{\partial x_i} = 0, \quad (2.14a)$$

$$\frac{\partial \tilde{u}_i}{\partial t} + \bar{u}_j \frac{\partial \tilde{u}_i}{\partial x_j} + \tilde{u}_j \frac{\partial \tilde{u}_i}{\partial x_j} = -\frac{\partial \tilde{p}}{\partial x_i} + \frac{1}{Re} \frac{\partial^2 \tilde{u}_i}{\partial x_j^2} + \mathcal{F}_i^*, \quad (2.14b)$$

where

$$\mathcal{F}_i^* = -\frac{\partial}{\partial x_j} (\tilde{u}_i \tilde{u}_j) - \frac{\partial}{\partial x_j} (\widetilde{u''_i u''_j}). \quad (2.15)$$

For the mean flow analysis, we assume that the influence of the quadratic harmonic interactions is small, although the harmonic waves themselves might not necessarily be small. Further, we assume the fluctuating velocity is small compared to the harmonic velocity (which is demonstrated in section 2.5). We therefore ignore  $\mathcal{F}_i^*$  and conduct an *a posteriori* analysis of the nonlinear terms in section 2.5 to check the validity of this assumption.

### 2.3.2 Solution method and validation

The coherent perturbations are decomposed into Fourier modes

$$\tilde{u}_i(x_i, t) = \hat{u}_i(y) e^{i(\alpha x - \omega t)} \quad \text{and} \quad \tilde{p}(x_i, t) = \hat{p}(y) e^{i(\alpha x - \omega t)} \quad (2.16)$$

where  $i$  denotes the imaginary unit,  $\alpha$  the stream-wise wavenumber of the perturbation and  $\omega$  the stream-wise frequency, both of which are generally complex.  $\hat{u}_i$  and  $\hat{p}$  are the complex eigenfunctions of respective perturbations in velocity and pressure. We are interested in the spatial growth and decay of disturbances. Hence, a spatial stability analysis is pursued where  $\omega$  is a known, real valued frequency and  $\alpha$  is complex valued and unknown. The ansatz (2.16) is introduced in equation (2.14) to obtain the Fourier-transformed perturbation equations.

Note, that the assumption of a parallel mean flow in the present case is worth questioning. In case of a laminar unforced jet, the liquid phase might retain an approximately constant diameter and an unaltered velocity profile between to respective downstream positions. This is the case if the jet exhibits a block-like velocity profile, as in e.g. [45]. However, for a parabolic inflow profile [21], the liquid interfaces notably contracts until it reaches a relaxed state. Additionally, the shear layer spreading within the gaseous phase invalidates the strict assumption of a parallel flow.

In case of a forced jet as in the present case, the downstream spreading of the mean flow certainly violates the parallel flow assumption for both phases. Nevertheless, local analysis has shown remarkable robustness in predicting stability properties for a variety of nonparallel flows (see e.g.

[62]: Barkley (2006), 'Linear analysis of the cylinder wake mean flow'

[45]: Tammissola et al. (2011), 'Stabilizing effect of surrounding gas flow on a plane liquid sheet'

[21]: Söderberg (2003), 'Absolute and convective instability of a relaxational plane liquid jet'

[61]: Pier (2002), ‘On the frequency selection of finite-amplitude vortex shedding in the cylinder wake’

[70]: Cohen et al. (1987), ‘The evolution of instabilities in the axisymmetric jet. Part 1. The linear growth of disturbances near the nozzle’

[71]: Oberleithner et al. (2014), ‘On the impact of swirl on the growth of coherent structures’

[72]: Terhaar et al. (2015), ‘Key parameters governing the precessing vortex core in reacting flows: An experimental and analytical study’

[73]: Emerson et al. (2016), ‘Local stability analysis and eigenvalue sensitivity of reacting bluff-body wakes’

[63]: Oberleithner et al. (2014), ‘Mean flow stability analysis of oscillating jet experiments’

[74]: Crighton et al. (1976), ‘Stability of slowly diverging jet flow’

[75]: Herbert (1997), ‘Parabolized stability equations’

[76]: Cheung et al. (2010), ‘Linear and nonlinear instability waves in spatially developing two-phase mixing layers’

[77]: Beneddine et al. (2016), ‘Conditions for validity of mean flow stability analysis’

[21]: Söderberg (2003), ‘Absolute and convective instability of a relaxational plane liquid jet’

[60]: Gordillo et al. (2005), ‘Aerodynamic effects in the break-up of liquid jets: on the first wind-induced break-up regime’

[61, 70–73]). Alternatively, axial spreading can be accounted for by using a correction scheme for weakly non-parallel flows by introducing a slowly varying axial scale [63, 74] or within the framework of parabolized stability equations [75, 76]. Yet, another approach is to compute the optimal response to a forcing from the resolvent norm around the mean flow, taking into account the non-normality of the linearised operator [77]. However, for the present work, the focus lies on the applicability of a simple linear model to capture the overall phenomena of the underlying nonlinear flow. A detailed representation is already available through the nonlinear simulation results. Therefore, we stick to the parallel flow assumption.

As noted above, for the analysis of immiscible interfacial flows, the perturbation equations are formulated separately for each phase (see e.g. [21, 60]). By imposing symmetry conditions along the jet centre-line, it is sufficient to only consider the top half of the jet. At the interface position, coupling conditions are formulated to satisfy equation (2.14) across the interface. Formally the interface position is of the form  $y = h(x, t)$  and is assumed to be decomposed and perturbed similarly to equations (2.11) (where the fluctuations are neglected) and (2.16) so that

$$h(x, t) = \bar{h}(x) + \tilde{h}(x, t) \quad \text{and} \quad \tilde{h}(x, t) = \hat{h}(x)e^{i(\alpha x - \omega t)}. \quad (2.17)$$

For an unforced jet, the mean interface position is assumed to be approximately equal to the unperturbed interface position of the steady base flow, which is taken to be constant in  $x$ . Hence,  $\bar{h}$  is constant. In the time-averaged flow of the forced state it is not. Following the triple decomposition,  $\bar{h}$  should be obtained by time-averaging the instantaneous interface positions at each  $x$ . However, this approach yields unsatisfactory results as seen in section 2.4. Therefore, an alternative modelling approach is given in section 2.3.3 which does not follow the triple decomposition.

For the derivation of the coupling conditions, a constant  $\bar{h}$  is assumed. Formally, these conditions are valid at the perturbed interface  $h(x, t)$ . However, by means of a Taylor expansion of  $h(x, t)$  around  $y = \bar{h}$  and by neglecting terms of second order or higher, a linear approximation at the unperturbed interface is obtained. In the following, the approximated conditions at the unperturbed interface are presented. For satisfying the continuity of the velocity across the interface, it holds

$$\left[ \tilde{u} + \bar{u} + \tilde{h} \frac{d\bar{u}}{dy} \right]_{y=\bar{h}, l} - \left[ \tilde{u} + \bar{u} + \tilde{h} \frac{d\bar{u}}{dy} \right]_{y=\bar{h}, g} = 0, \quad (2.18a)$$

$$[[\tilde{v}]]_{y=\bar{h}, g} - [[\tilde{v}]]_{y=\bar{h}, l} = 0, \quad (2.18b)$$

where quantities inside  $[[\cdot]]_{y=\bar{h}, l, g}$  belong to the liquid or gas phase respectively. Further, the continuity of shear stress requires

$$\left[ \frac{\partial \tilde{v}}{\partial x} + \frac{\partial \tilde{u}}{\partial y} + \tilde{h} \frac{d^2 \bar{u}}{dy^2} \right]_{y=\bar{h}, l} - m \left[ \frac{\partial \tilde{v}}{\partial x} + \frac{\partial \tilde{u}}{\partial y} + \tilde{h} \frac{d^2 \bar{u}}{dy^2} \right]_{y=\bar{h}, g} = 0, \quad (2.19)$$

and the continuity of normal stress yields

$$\left[ \tilde{p} - \frac{2}{Re_1} \frac{\partial \tilde{v}}{\partial y} \right]_{y=\bar{h}, l} - \left[ r\tilde{p} - \frac{2m}{Re_1} \frac{\partial \tilde{v}}{\partial y} \right]_{y=\bar{h}, g} + \frac{1}{We} \frac{\partial^2 \tilde{h}}{\partial x^2} = 0, \quad (2.20)$$

where  $m = \mu_g/\mu_l$  is the ratio of the dynamic viscosities of the two fluids and  $r = \rho_g/\rho_l$  is the density ratio. A detailed derivation of the stress conditions is given in appendix 2.7.1. The kinematic condition for the interface is

$$\left[ \frac{\partial \tilde{h}}{\partial t} + \bar{u} \frac{\partial \tilde{h}}{\partial x} = \tilde{v} \right]_{y=\bar{h}, l, g}. \quad (2.21)$$

Note that it is possible to formulate the kinematic condition for the gas phase velocity at the interface as well as for the liquid phase velocity. The coupling conditions are complemented by boundary conditions to close the system.

Only asymmetric waves are considered in the stability analysis, since in the nonlinear simulation, the jet is forced sinusoidally in the  $v$ -component of the velocity to excite asymmetric modes. From the analysis of the simulation it is evident, that the dominant mode at the forcing frequency remains asymmetric throughout the downstream development of the jet and the aim of the work is to investigate the potential of the mean flow stability model to predict the growth and saturation of this forced wave. Therefore, a symmetry condition

$$\left[ \tilde{u} = 0, \frac{\partial \tilde{v}}{\partial y} = 0, \tilde{p} = 0 \right]_{y=0, l} \quad \text{for asymmetric modes} \quad (2.22a)$$

is imposed, as well as a no-slip condition

$$\left[ \frac{\partial \tilde{u}}{\partial y} = 0, \tilde{v} = 0, \frac{\partial \tilde{p}}{\partial y} = 0 \right]_{y \rightarrow \infty, g}. \quad (2.23)$$

The closed system (equations (2.14), (2.18) - (2.23)) with the ansatz (2.16), (2.17) is solved using a Chebyshev spectral collocation method. The grid of the liquid phase extends over  $0 \leq y \leq \bar{h}(x)$  where  $\bar{h}(x=0) = 0.5$ . The grid of the gas phase extends from  $\bar{h}(x) < y \leq 4D$ . Each grid is discretised using  $N = 110$  collocation points, resulting in  $2 \times N \times 3 = 1980$  degrees of freedom. Convergence is demonstrated in appendix 2.7.2. The resulting quadratic eigenvalue problem is of the form

$$(\alpha^2 \mathbf{A}_2 + \alpha \mathbf{A}_1 + \mathbf{B}) \mathbf{q} = \mathbf{0}. \quad (2.24)$$

The Matrices  $\mathbf{A}_2$ ,  $\mathbf{A}_1$  and  $\mathbf{B}$  contain the mean flow profiles  $\bar{u}_{l,g}$ , and  $\mathbf{q} = (\hat{u}_1, \hat{v}_1, \hat{p}_1, \hat{u}_g, \hat{v}_g, \hat{p}_g, \hat{h})^T$ . Using the companion linearisation, equation (2.24) is reduced to a linear problem

$$\left[ \begin{pmatrix} \mathbf{B} & \mathbf{0} \\ \mathbf{0} & \mathbf{I} \end{pmatrix} + \alpha \begin{pmatrix} \mathbf{A}_1 & \mathbf{A}_2 \\ -\mathbf{I} & \mathbf{0} \end{pmatrix} \right] \begin{pmatrix} \mathbf{q} \\ \alpha \mathbf{q} \end{pmatrix} = \mathbf{0}, \quad (2.25)$$

**Table 2.3:** Validation of two-layer Poiseuille flow using temporal analysis ( $\alpha = 1$ ). Displayed are the corresponding unstable eigenvalues  $c \equiv \omega/\alpha$

	Interface mode	Shear mode
present	$1.003907431 + 0.001791888361i$	$0.2578942009 + 0.0008778900946i$
[78]	$1.003907431 + 0.001791888368i$	$0.2578942002 + 0.0008778915187i$

[78]: Dongarra et al. (1996), ‘Chebyshev tau-QZ algorithm methods for calculating spectra of hydrodynamic stability problems’

[45]: Tammissola et al. (2011), ‘Stabilizing effect of surrounding gas flow on a plane liquid sheet’

where  $\mathbf{I}$  is the identity matrix. The linear system, equation (2.25), is consecutively solved at each stream-wise position using the QZ algorithm in MATLAB’s eig function which simultaneously delivers all eigenvalues, to obtain the spatial evolution of  $\alpha$  and the corresponding eigenfunctions. The eigenvalues and -vectors added by  $\alpha\mathbf{q}$  are discarded. For validating the code, the temporal stability results of the two-layer Poiseuille flow by [78] are reproduced. The resulting unstable eigenvalues are listed in table 2.3 and the flow conditions are restated in appendix 2.7.3. As their results exclude the influence of surface tension, the results of [45] (figure 16 a) in their work) are qualitatively reproduced as well.

### 2.3.3 Mean flow configuration and parameterisation

The  $u$ -component of the mean flow velocity field, is obtained by averaging  $2^{11}$  consecutive snapshots of the fully developed flow of the nonlinear simulation in section 2.2 at time increments  $\Delta t U/D = 0.15$  and within an area  $-5 < y/D < 5, 0 < x/D < 40$ . These are mapped on an equidistant Cartesian grid with a resolution of  $800 \times 200$  px where  $1 \text{ px} = 1 \times 10^{-4} \text{ m}$ . The mean flow field should be symmetric with respect to the jet centre-line. Therefore, remaining minor asymmetries in the time-averaged flow are eliminated by taking the symmetric part

$$\bar{u}_{\text{sym}} = \frac{1}{2}(\bar{u}(y) + \bar{u}(-y)). \quad (2.26)$$

The symmetric, time-averaged mean flow is shown in figure 2.6.

[60]: Gordillo et al. (2005), ‘Aerodynamic effects in the break-up of liquid jets: on the first wind-induced break-up regime’

In [45] and [60] analytic base flows were used and a constant velocity profile of the liquid phase was assumed. The gas boundary layer was approximated using an error function profile. A comparison of the mean flow profiles with these analytic profiles is given in figure 2.5. It is seen that for the unforced flow, the error-function profile slightly over-estimates the developing shear-layer, although differences are minor. More prominent deviations are observed along the interface, since the assumption of a constant liquid velocity does not hold for the nonlinear simulation. Further, the zero Dirichlet condition for the gas velocity causes a reversed flow in the gas phase close to the inlet, which possibly influences the development of the initial boundary layer and could have an effect on the growth rate of the instability wave. For the forced flow, the mean flow profile quickly deviates from the error-function profile, as the oscillation significantly thickens the mean flow shear layer, especially for  $A = 0.05$ . In conclusion, the analytic profile might be a sufficient approximation for an unforced jet but not for a forced jet.

The necessity to model the position of the mean interface in the mean flow, noted in the previous section, is addressed here. Within the parallel

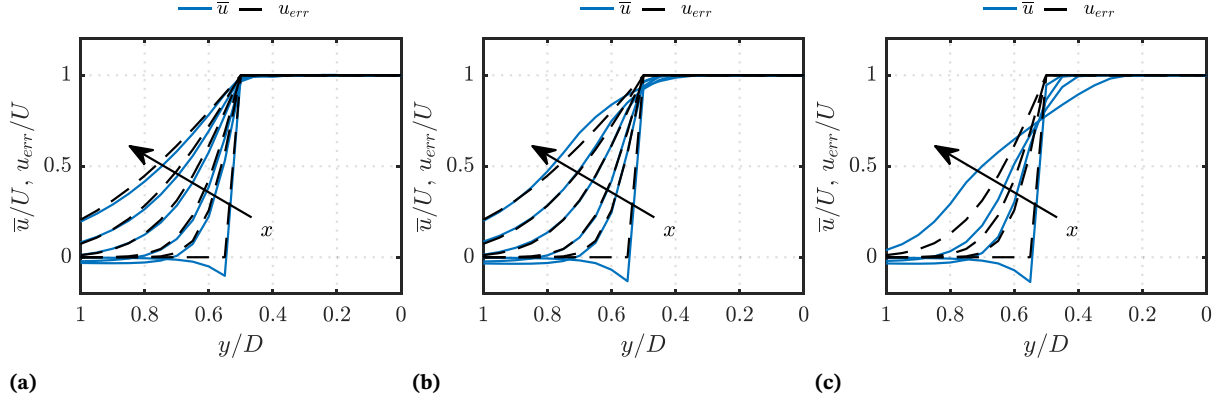


**Figure 2.5:** Comparison of the mean flow profiles and an error-function profile (as in Tammissola et al. (2011)) for the unforced flow (a), and forced flow with (b)  $A = 0.01$ , (c)  $A = 0.05$ . Plot positions are  $x/D = 0.01, 1, 2, 5, 10, 20$ . For  $A = 0.05$ , positions  $x/D = 10, 20$  are omitted due to very large deviations from the error-function profile

flow framework, the interface between the liquid and gaseous phase is located at a fixed position  $y = h_b$  which is determined by the solution of the underlying steady base flow. For instance, in [45] and [60] the interface position remained constant in downstream direction. In [21] a numerical base flow for the liquid phase was computed with varying interface positions in downstream direction.

For this study a simple model is constructed, that requires the mass of the liquid phase at  $x/D = 0$  to be conserved for all stream-wise positions in the mean flow. The initial mass is determined by the initial interface position  $\bar{h}(x = 0) = 0.5$ . Then, the time-averaged density field  $\bar{\rho}$  is integrated at each  $x$ , from  $0 < y < \bar{h}(x)$ . The upper integration bound  $\bar{h}(x)$ , defining the interface within the mean flow, is chosen such that

$$\int_0^{0.5} \frac{\bar{\rho}(x = 0, y)}{\rho_1 D} dy = \int_0^{\bar{h}(x)} \frac{\bar{\rho}(x, y)}{\rho_1 D} dy. \quad (2.27)$$

An illustration of this procedure is shown in figure 2.7 along with the resulting interface curve within the mean flow. As is seen, the model moves the interface reasonably into the mean flow shear layer.

When using a true stationary solution, the interface position can simply be defined by the volume fraction  $C = 0.5$ , as in the VoF method. However, this assumption does not hold in the time-averaged flow (for the time-averaged volume fraction  $\bar{C} \approx \bar{\rho}/\rho_1$ ) which is seen in figure 2.7: Using  $\bar{C} = 0.5$  the interface would move towards the centre-line of the jet. A consistent approach to obtaining the interface position according to the triple decomposition would be to take the time-averaged position. However, for a transverse sinusoidal forcing, the growing interface disturbance should approximate a growing sine wave on each side of the plane jet/sheet. As the jet oscillates symmetrically around its (theoretical) centre-line, the time averaged position of the interface would be  $\bar{h}(x) = \pm 0.5$  for all stream-wise positions which corresponds to the position of the unperturbed flow. Another approach to obtain the interface position in the mean flow that might seem plausible at first sight, is to derive the location with the highest probability of interface residence at each stream-wise position, i.e. a probability density. However, for a sine wave this would yield an interface position

[45]: Tammissola et al. (2011), ‘Stabilizing effect of surrounding gas flow on a plane liquid sheet’

[60]: Gordillo et al. (2005), ‘Aerodynamic effects in the break-up of liquid jets: on the first wind-induced break-up regime’

[21]: Söderberg (2003), ‘Absolute and convective instability of a relaxational plane liquid jet’

at either of the extrema of the sine wave. This does not seem plausible, since it traverses the interface almost out of the mean flow shear-layer. The effect of the interface correction is further assessed in the following sections.

**Figure 2.6:** Mean flow profiles of the jet forced at  $A = 0.01$  (blue);  $A = 0.05$  (black). The spreading of the mean interface position, derived from figure 2.7 is shown as dashed line.

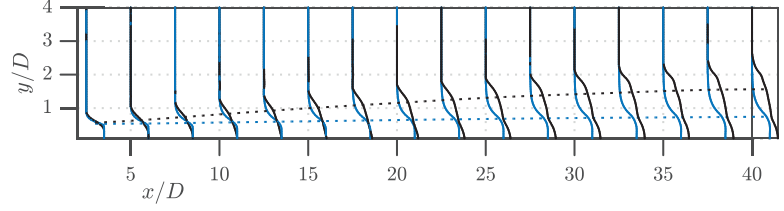
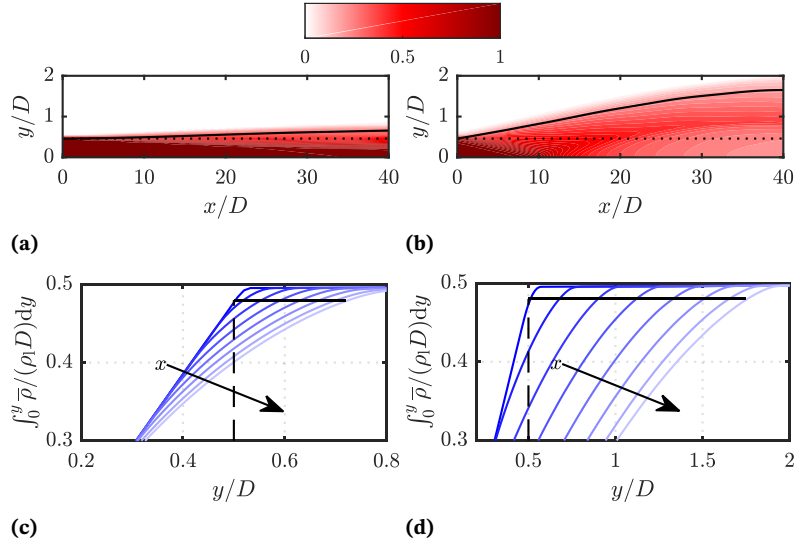


**Figure 2.7:** Illustration of the mean interface spreading. The top row shows a contour plot of the mean volume fraction field  $\bar{\rho}/\rho_1$  of the nonlinear simulation and the interpolated interface position for the linear stability model as black line, for (a)  $A = 0.01$ ; (b)  $A = 0.05$ . The black dotted line represents the presumed, fixed interface position of the unforced flow. Red areas corresponds to regions of small interface amplitudes while lighter shades indicate areas of increased amplitudes. The second row shows the cumulative integral of  $\frac{\bar{\rho}}{\rho_1 D}$  along  $y$  for several stream-wise positions, for (c)  $A = 0.01$ ; (d)  $A = 0.05$ . The interface at  $x = 0$  (vertical line) determines the initial mass of the liquid. The interface is constructed such that the liquid mass is conserved (horizontal line).



### 2.3.4 General stability properties of the jet

For the stability analysis, three different cases will be of interest. The first case is based on the mean-flow of the unforced jet. As within the current numerical framework, natural disturbances of the unforced jet remain very small (at least in the considered domain), it closely corresponds to an equilibrium or base flow solution, i.e. the interface remains at the initial, unperturbed position within the sampling accuracy ( $\bar{h}(x) = 0.5$ ), as has been carefully checked. We denote this case as *base flow model*. The second case is based on the mean-flow of the forced jet but ignores the interface displacement in the mean flow, such that  $\bar{h}(x) = 0.5$  (equivalent to a triple decomposition of the interface). This case is denoted as *fixed interface model*. The third case is similar to the second one but includes the proposed interface correction model to account for the interface displacement. This case is denoted as *varying interface model*.

To obtain a general overview on the stability properties of the present jet configuration, in figures 2.8a and 2.8b the stream-wise distribution of spatial growth rates is derived for the base flow model for a broad range of frequencies. There are two unstable modes found which together render the jet convectively unstable for all applied frequencies within the displayed domain.

In detail, mode I is unstable for all shown frequencies and shows an increasing maximum growth rate as the frequency increases up to  $fD/U = 0.27$ . Characteristic for this mode are the almost vertical contour lines within the initial region of the jet, that make the upstream stability behaviour of the jet virtually similar for a range of applied frequencies of approximately  $0.1 < fD/U < 0.3$ . The upstream appearance of the mode is qualitatively reminiscent of the sinuous mode of type I found in [21].

For frequencies  $fD/U < 0.27$  mode II is unstable as well in the upstream region of the jet. However, prolonged downstream influence of this mode is only observed for  $fD/U < 0.1$  where the point of neutral stability moves beyond  $x/D = 10$ . Contrasting to mode I, the contour lines follow a more horizontal trend, especially in the lower frequencies. Additionally, the mode shows significantly smaller growth rates within the initial jet region, compared to mode I. The low-frequency region of this mode partially resembles the sinuous mode of type II found in [21]. For better comparison the stability maps are re-plotted in appendix 2.7.4, using similar scaling as in [21]. However, contrastingly to his findings no third unstable physical eigenvalue is found for the present configuration.

There is however one additional marginally stable eigenvalue found which might correspond to the third mode found in [21] but since it is not unstable we shall not investigate it further in this work. Also mode II is either stable or exhibits weaker growth for the forcing frequencies applied in this work and thus will be excluded from further investigations as well.

The stability map of mode I is also derived for the fixed and varying interface model with  $A = 0.01$  at  $St = 0.1$  in figure 2.8d. As can be seen, the mean flow for the fixed interface model significantly alters the stability map. Using the forced flow, the threshold for neutral stability moves into the domain for all frequencies and is located between  $x/D = 20$  and  $x/D = 30$  for  $fD/U > 0.05$ . For lower frequencies the neutral point reaches approximately  $x/D = 10$ . When the displacement of the mean interface position is taken into account (varying interface model), the neutral stability curve shifts even further upstream for most frequencies and renders all positions downstream  $x/D = 20$  stable. This indicates that the spreading of the mean interface has indeed an impact on the stability properties of the jet even at small forcing amplitudes and as shown below is even necessary to correctly recover the point of neutral stability of the excited instability wave. The maps derived for the fixed and varying interface model are obtained using the time-averaged flow at  $St = 0.1$ . Therefore, the growth rates shown in figure 2.8c and 2.8d correspond to modes existing on this specific mean flow. For deriving maps where the displayed growth rates correspond to the most unstable eigenmode at the forcing frequency, a separate mean flow with a forcing at the respective frequency would have to be used for each eigenmode.

The origin of the unstable mode can be inspected by analysing its energy budget as carried out by [79] and [80]. Therefore an energy balance over both fluid phases is derived as

$$MFL_l + MFL_g = REY_l + REY_g + TAN + NOR + DIS_l + DIS_g \quad (2.28)$$

[21]: Söderberg (2003), 'Absolute and convective instability of a relaxational plane liquid jet'

[79]: Boomkamp et al. (1996), 'Classification of instabilities in parallel two-phase flow'

[80]: Otto (2012), 'Spatio-Temporal Stability Analysis in Two-Phase Mixing Layers'

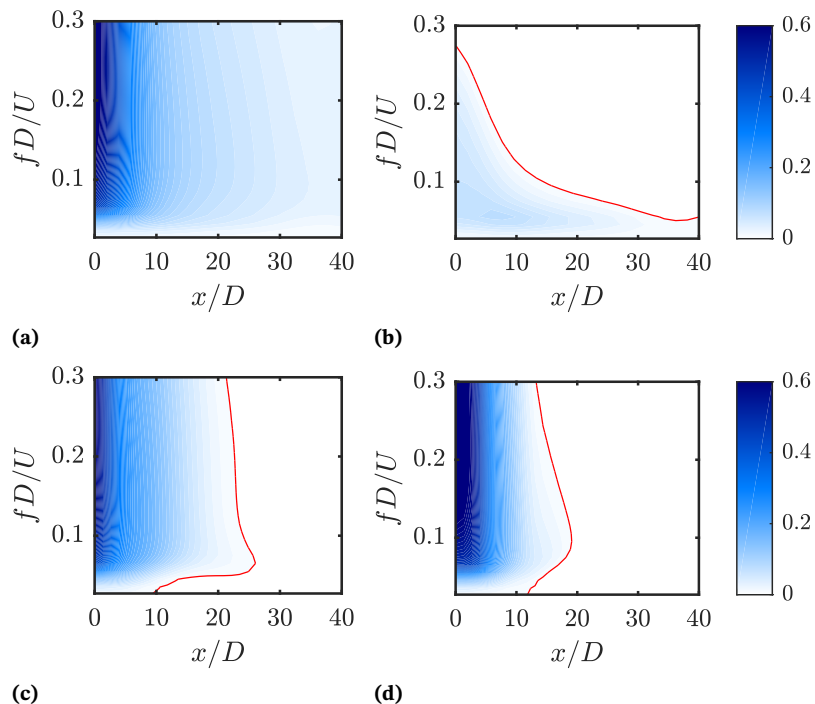


**Figure 2.8:** Stability map for the base flow model (Mode I (a), Mode II (b)), fixed interface model (Mode I) at  $A = 0.01$  (c), varying interface model (d). Shown is the spatial growth rate  $-\alpha_i D$  and the curve indicating neutral stability, i.e.  $\alpha_i D = 0$ , in red.

Where MFL is corresponding to the stream-wise mean energy flux. The flux is balanced by a production term accounting for energy transfer from the mean flow to the perturbation through Reynolds stresses  $REY$ . The energy transfer to the velocity perturbations along the interface is accounted for by  $TAN$  and  $NOR$ , representing the work of tangential and normal stress. The perturbation energy dissipation is given by  $DIS$ . It is always negative by definition while the sign of the other quantities might change depending of the flow configuration. Every quantity is normalised by the sum of all quantities. The complete expressions for the respective terms are given in appendix 2.7.5. The contributions of the respective terms, calculated exemplarily at  $x/D = 10$ , are given table 2.4.

For  $A = 0.01$  the energy budget is dominated by the contribution of tangential stresses, caused by the viscosity jump across the interface. Additionally, the energy transfer from the mean flow to the perturbed flow through Reynolds stresses within the liquid phase as well as the contribution of normal stresses from the pressure jump have some influence, although they are significantly weaker than the tangential stresses. Energy dissipation almost exclusively takes place in the liquid phase. Overall the gaseous phase has negligible contribution to the perturbation energy budget. For increased forcing the influence of  $TAN$  and  $REY_g$  decreases while for  $REY_l$  and  $NOR$  it increases.

The interface correction is seen to increase the influence of the  $REY_l$  and lower the influence of  $TAN$  which is to be expected since the correction shifts the interface position outwards into the mean flow shear layer where the mean flow gradient is larger than in proximity to the jet centre-line and so are the Reynolds stresses.

When comparing the contributions at the respective amplitudes it is seen that the contribution of  $REY_g$  decreases for increasing forcing amplitude which seems counter-intuitive. However, due to the increased mean flow spreading for larger forcing amplitudes, the transverse gradient of the

**Table 2.4:** Energy budget of mode I of the linear stability model at  $x/D = 10$ 

Case	$St$	$A$	$REY_g$	$REY_l$	TAN	NOR	$DIS_g$	$DIS_l$
fixed interface model	0.1	0.01	0.0012	0.0180	0.9903	0.0074	-1.4354e-4	-0.0168
varying interface model	0.1	0.01	0.0014	0.0580	0.9424	0.0107	-1.3422e-4	-0.0124
fixed interface model	0.1	0.05	0.0005	0.1066	0.8844	0.0262	-2.9122e-4	-0.0175
varying interface model	0.1	0.05	0.0013	0.5085	0.4395	0.0557	-2.6337e-4	-0.0047

mean flow velocity in the gas phase, as seen in figure 2.6, reduces which provides an explanation for the lower values of  $REY_g$ . In contrast, the gradient within the liquid part of the mean flow shows a slight increase which is in line with the increase of  $REY_l$  for larger forcing amplitudes.

## 2.4 Comparison of nonlinear simulation and linear stability model

The findings of the previous section have shown plausible results for  $A = 0.01$  when the stream-wise spreading of the mean interface position is accounted for. In the following, the eigenfunctions and corresponding growth rates of the stability analysis are compared to their equivalents of the nonlinear simulation (DNS). Therefore, a decomposition of the coherent flow field of the DNS into a Fourier series yields the complex Fourier coefficients

$$\hat{u}_{i,n}(x_i) = \frac{1}{2\pi T} \sum_{n \neq 0} \tilde{u}_i e^{-i2\pi nft}. \quad (2.29)$$

To obtain the coherent velocity  $\tilde{u}_i$ , formally,  $\bar{u}_i$  is subtracted from the phase averaged velocity field to exclude any incoherent fluctuations. However, as demonstrated in section 2.5, the incoherent motion is negligibly small compared to the coherent motion. Therefore,  $\tilde{u}_i \approx u_i - \bar{u}_i$  has proven as adequate choice.

We investigate the potential of the linear model for both forcings  $A = 0.01$  and  $A = 0.05$ . For the sake of completeness and to underline the benefits of the mean flow model, the main results of this section are reproduced for the base flow model in appendix 2.7.6.

### 2.4.1 Stream-wise and cross-wise eigenfunctions

The eigenfunctions  $\hat{u}$  and  $\hat{v}$  of the linear stability analysis and the fundamental wave packet ( $n = 1$ ) of the DNS, derived from equation (2.29), are shown in figure 2.9. The region of linear growth is followed by the nonlinear saturation and decay of the amplitude.

For  $A = 0.01$  and the fixed interface model, an overall very good agreement is found for  $\hat{v}$ . Particularly in the gaseous part of the shear layer, there is an excellent correspondence of the eigenfunctions throughout the domain. Along the liquid jet centre-line, amplitude prediction is very good as well up to around  $x/D = 20$ . However, beyond that point there are some visible discrepancies around the interface where the steep gradient of the

[81]: Orszag et al. (1970), 'Instability of a vortex sheet leaving a semi-infinite plate'

[63]: Oberleithner et al. (2014), 'Mean flow stability analysis of oscillating jet experiments'

amplitude is not followed as rigorously by the linear model. For  $x/D > 30$  the agreements between simulation and linear stability model deteriorates further within the liquid part of the shear layer. The under-prediction for  $x/D < 5$  within the liquid phase is possibly attributed to the influence of the inlet wall in the simulation which should approximately resemble the nozzle in the experiments of [81] and [63]. They argue that discrepancies in this area are likely caused by an interaction of the instability wave with the nozzle that is not covered by the linear model. For  $\hat{u}$  similar agreement is found. The discrepancies along the interface are seen here as well and visualised as a slight lateral shift of the amplitude maximum.

For the varying interface model the eigenfunctions of linear stability analysis and their equivalents of the DNS become virtually indistinguishable throughout the domain (apart from the near-nozzle region that remains unaffected by the correction). This shows that accounting for the displacement interface in the spreading mean flow is indeed necessary to obtain a correct representation of the eigenfunctions. In conjunction with the findings in table 2.4, neglecting the interface spreading leads to a under-representation of Reynolds stresses in the mean flow stability model and an insufficient representation of the perturbation shear-layer.

For  $\hat{u}$  a similar trend is found. With the fixed interface model, increasing discrepancies along the interface are seen here as well for  $x/D > 15$  and manifest in the absence of a lateral shift of the amplitude maximum as well as the formation of a erroneous double spike in the amplitude. For the varying interface model, the outward spreading of the amplitude is followed by the linear model.

For  $A = 0.05$ , the overall agreement is significantly less accurate. Nevertheless for  $x/D < 20$ , the  $\hat{v}$ -component shows very good agreement despite the significant transverse spreading of the shear layer (varying interface model). With the fixed interface model this trend is not followed, resulting in visible deviations already at  $x/D = 7.5$ . However, beyond  $x/D = 20$  both methods fail to correctly represent the wave packet amplitude of the nonlinear flow. The portray of  $\hat{u}$  shows the same trend, though the qualitative differences are somewhat more pronounced.

## 2.4.2 Growth rates and phase velocity

In the linear model, growth rates of the instability wave are readily given through the imaginary part of the eigenvalue  $\alpha_i$ , introduced in equation (2.16). Deriving a correspondent measure for the amplitude growth from the DNS introduces an ambiguity to the analysis. For the present work, the most suitable measure was found to be based on the energy norm of the two-phase velocity field. The amplitude is computed as

$$\tilde{A}_n(x; \hat{\rho}_n; \hat{u}_n; \hat{v}_n) = \frac{\sqrt{2}}{UD/2} \left( \int_0^\infty |\hat{\rho}_n| [|\hat{u}_n|^2 + |\hat{v}_n|^2] dy \right)^{1/2}, \quad (2.30)$$

where  $\hat{\rho}_n, \hat{u}_n, \hat{v}_n$  are obtained from equation (2.29). This corresponds to the amplitude of the velocity fluctuation of the respective harmonics, integrated across the shear layer of the jet [82], [63]. Other plausible energy

[82]: Delbende et al. (1998), 'Absolute/-convective instabilities in the Batchelor vortex: a numerical study of the linear impulse response'

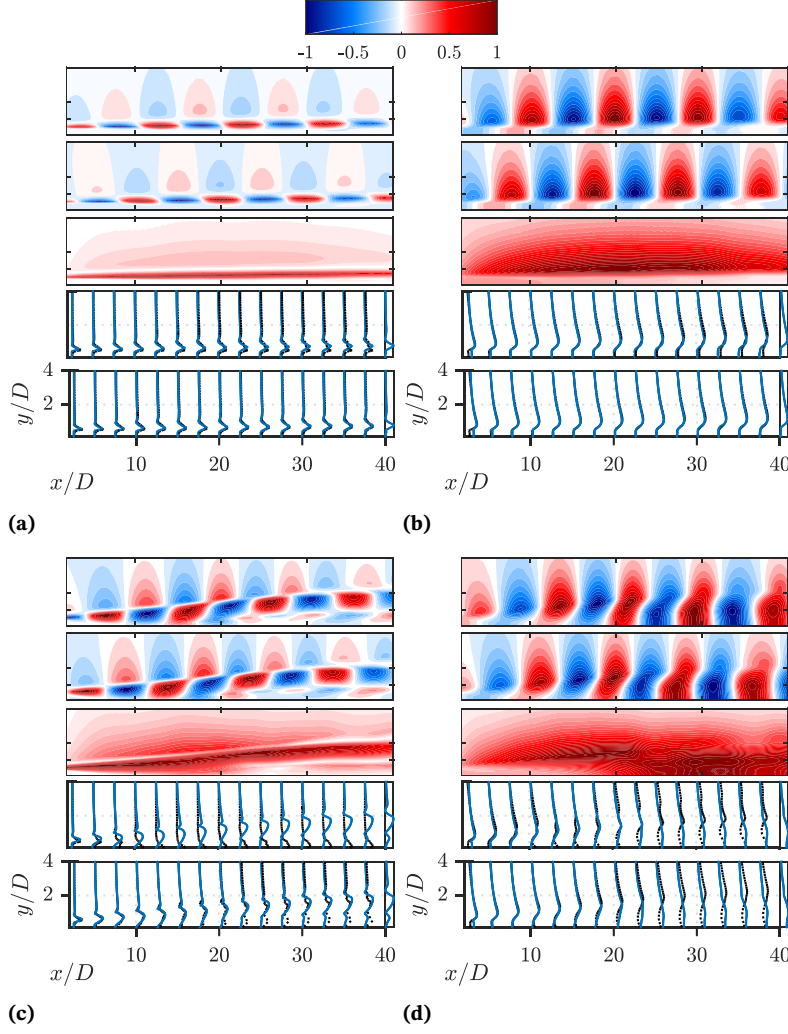


**Figure 2.9:** Illustration of the fundamental wave packet ( $n = 1$ ), obtained from the DNS and comparison of the computed amplitude functions from the linear stability model and the DNS for (a)  $A = 0.01$ ,  $\hat{u}$ ; (b)  $A = 0.01$ ,  $\hat{v}$ ; (c)  $A = 0.05$ ,  $\hat{u}$ ; (d)  $A = 0.05$ ,  $\hat{v}$ . Figures show the real part, imaginary part, the absolute value and corresponding amplitudes (for the fixed and varying interface model) normalised by their maximum value, from top to bottom. Blue lines show the DNS while black lines show the LSA

norms include a separate formulation for the velocity of the respective fluid phases or a formulation for the density field only. A separate measure of the velocity of each fluid phase did not reveal any significant differences in the evolution of the growth rates as compared to the chosen method. However, when using a formulation over the density field, a slower decay of the instability wave is observed (not shown). The stream-wise growth rate then is defined as

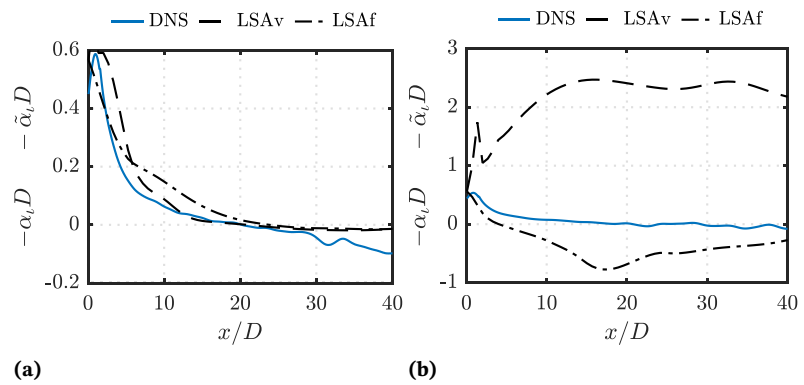
$$-\tilde{\alpha}_i(x) = \frac{d(\ln \tilde{A}_1)}{dx}. \quad (2.31)$$

The predicted growth rates of both models are given in figure 2.10. For  $A = 0.01$ , very good agreement is reached between the DNS and the linear stability model. For the fixed interface model, the growth rates in the initial region up to  $x/D = 5$  are very well recovered. Thereafter, the predicted growth rate decreases slower than in the DNS leading to a slightly delayed saturation and zero crossing of the growth rate of the linear model. Further downstream, the stable wave decays slightly slower than predicted by the DNS. Using the varying interface model, the initial growth rate is slightly over-predicted. However, for  $10 < x/D < 30$  an excellent agreement is found and the neutral point is (if slightly under-predicted) recovered

better than for the fixed interface model. In comparison, the growth rates obtained from the base flow model (appendix 2.7.6) do not predict the neutral point to be within the considered domain at all. Therefore, the mean flow model generally seems to yield more accurate results than the base flow model.

For  $A = 0.05$  in figure 2.10b, the agreement of the predicted growth rates is poor throughout the domain which is to be expected from the substantial deviations of the eigenfunctions shown above. The fixed interface model predicts the instability wave to decay much faster than in the DNS, leading to a significant under-prediction of the neutral point. For the varying interface model, the growth rate prediction of the linear model is even worse and predicts an increasing destabilisation of the instability wave such that no saturation is predicted at all.

**Figure 2.10:** Comparison of the computed growth rates  $-\alpha_i D$  from the linear stability model and  $-\tilde{\alpha}_i D$  from the DNS for (a)  $A = 0.01$ , (b)  $A = 0.05$ . LSA<sub>b</sub> denotes the base flow model, LSA<sub>v</sub> and LSA<sub>f</sub> the varying and fixed interface model.



For comparing the real part of the eigenvalue,  $\alpha_\rho$ , to the wavelength of the forced instability, observed in the DNS, the phase velocity is derived as  $c_{\text{ph}} = \omega/\alpha_\rho$ . The corresponding phase velocity  $\tilde{c}_{\text{ph}}(x)$  from the DNS is obtained by the relation  $\alpha_\rho = (\partial\phi/\partial x)$ , where we define an integral measure for the phase angle of the fundamental wave as  $\phi(x) = \int_0^\infty \arg(\hat{v}_1(x, y)) dy$ .

The comparison of the LSA and the DNS is shown in figure 2.11. For  $A = 0.01$  very good agreement away from the near-nozzle region  $x/D > 10$  is found for the varying interface model. For the fixed interface model, slightly increasing deviation is observed downstream around  $x/D = 15$ . For  $A = 0.05$ , agreement deteriorates which is to be expected in light of the poor reproduction of the growth rates at this forcing amplitude. However, by taking the interface displacement into account the trend seen in the DNS is partially recovered and the overall quantitative discrepancies are reduced.

### 2.4.3 Relation to previous studies on the stability of forced liquid jets

From the body of literature available on the linear stability of liquid jets, the works of [21] and [45] were found to bear closest resemblance to the present study and a brief comparison shall be conducted here.

Although the forcing frequencies in [45] are lower than in the present case (the Strouhal number is approximately 1/10 that of the present case), as are  $Re$  and  $We$  and no specific information on the forcing amplitude

[21]: Söderberg (2003), ‘Absolute and convective instability of a relaxational plane liquid jet’

[45]: Tammissola et al. (2011), ‘Stabilizing effect of surrounding gas flow on a plane liquid sheet’

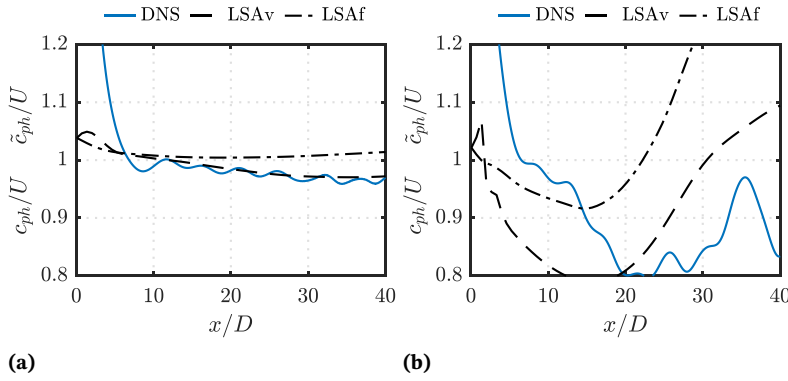


**Figure 2.11:** Comparison of the computed phase velocities  $c_{ph}/U$  from the linear stability model and  $\tilde{c}_{ph}/U$  from the DNS for (a)  $A = 0.01$ , (b)  $A = 0.05$ . LSA<sub>b</sub> denotes the base flow model, LSA<sub>v</sub> and LSA<sub>f</sub> the varying and fixed interface model.

can be deduced, some basic comparisons of the present scenario with figure 14, showing photographs of the jet oscillation, in their work is possible. As has been discussed, the eigenfunctions of the linear model show reasonable agreement with the DNS for  $x/D < 20$  for  $A = 0.05$ . The visual amplitude of the DNS at  $x/D = 20$ , derived from figure 2.2, reaches  $1.2 y/D$ . This amplitude is comparable to that observed in the region around  $x_{Tam} = 1500$  in figure 14 (left) of [45]. Similarly, the amplitude for  $A = 0.01$ , at  $x/D = 20$ , where excellent agreement with the DNS is found, reaches  $0.6 y/D$ , corresponding to the same region in figure 14 (right). As noted by [45], the linear analysis around the base flow was obtained far upstream of this region where linear growth could be assumed ( $x_{Tam} = 600$ ). Therefore, the mean flow model of the present work could possibly extend the applicability of linear stability analysis in a similar framework to positions further downstream. However, for larger amplitudes as seen in the lower part figure 14 (left), the mean flow model is likely to fail as well. It is worth noting that the growth rates obtained from the DNS and from the mean flow analysis are substantially larger in the near nozzle region, than they are in [45] ( $\max(\alpha_{i,Tam}) = 0.0054$ ). However, as stated, the growth rates in their analysis were obtained from a position sufficiently far away from the nozzle where growth rates are expectedly smaller than close to the nozzle. In [21] the measured growth rates close to the nozzle are larger than in [45] and comparable to the presently obtained growth rates ( $\max(\alpha_{i,Söd}) = 0.4$ ), though the corresponding Strouhal number is approximately 10 times larger than in the present case and  $Re$  and  $We$  are, significantly lower. So, again, no direct comparison is possible. Further, we have checked the influence of using an analytic flow profile as in [45] which results in growth rates near the nozzle that are up to 6 times smaller than for the mean flow profile. As discussed in section 2.3.3, the differences in the growth rates might be attributed to the form of mean flow profiles near the nozzle.

## 2.5 Interaction of the fundamental wave with higher harmonics

In the previous section we revealed the potential and limits of the linear stability model to predict the growth and decay of instability waves. While for  $A = 0.01$  very good agreement is found for both, eigenfunctions and growth rates, strong discrepancies are found for  $A = 0.05$  which raises the question why the linear model fails to predict the stability behaviour of a

[45]: Tammisola et al. (2011), ‘Stabilizing effect of surrounding gas flow on a plane liquid sheet’

[21]: Söderberg (2003), ‘Absolute and convective instability of a relaxational plane liquid jet’

[63]: Oberleithner et al. (2014), ‘Mean flow stability analysis of oscillating jet experiments’

jet forced with this amplitude. This is in contrast to the single-phase experiments of [63] where excellent agreement at similar and higher forcing amplitudes was found.

Introducing the Fourier decomposition (2.29) in (2.14), we obtain

$$in\omega\hat{u}_{i,n} + \mathcal{L}_{i,n} = \mathcal{F}_{i,n}^*, \quad (2.32)$$

where  $\mathcal{L}_{i,n}$  contains the linear terms. Similarly, we have an infinite expansion, governing the harmonics of the flow

$$\mathcal{F}_i = - \sum_{m \neq 0} \frac{\partial}{\partial x_j} (\hat{u}_{i,m} \hat{u}_{j,-m}) - \frac{\partial}{\partial x_j} (\overline{u'_i u'_j}), \quad (2.33a)$$

$$\mathcal{F}_{i,n}^* = - \sum_{m \neq n, 0} \frac{\partial}{\partial x_j} (\hat{u}_{i,m} \hat{u}_{j,n-m}) - \frac{\partial}{\partial x_j} (\overline{u'_i u'_j}), \quad (2.33b)$$

where  $\hat{u}_{i,-n} = \hat{u}_{i,n}^*$ , with the asterisk denoting the complex conjugate. The fluctuating Reynolds stresses remain small in the present scenario, as is seen by evaluating the turbulent kinetic energy normalised by either the inflow kinetic energy or the coherent kinetic energy (figure 2.12). In both cases, the fluctuations remain below 1 % for most of the domain.

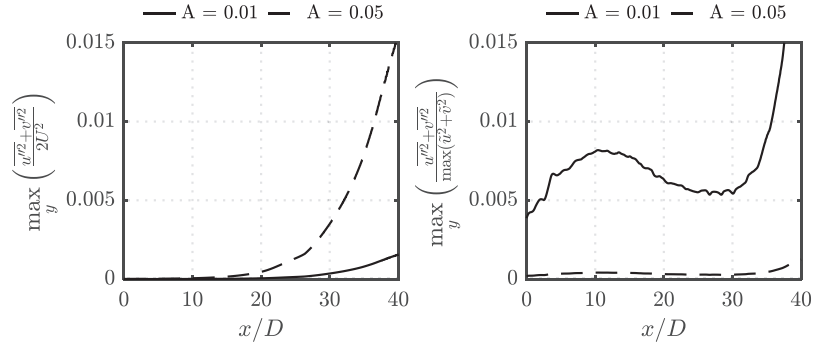


**Figure 2.12:** Variation of the cross-wise maximum of the total turbulent kinetic energy

The forcing in equation (2.33a) is expanded for the respective harmonics as follows

$$\mathcal{F}_i = - \frac{\partial}{\partial x_j} (\hat{u}_{i,1} \hat{u}_{j,-1} + \hat{u}_{i,-1} \hat{u}_{j,1} + \hat{u}_{i,2} \hat{u}_{j,-2} + \hat{u}_{i,-2} \hat{u}_{j,2}) + \dots, \quad (2.34a)$$

$$\mathcal{F}_{i,1}^* = - \frac{\partial}{\partial x_j} (\hat{u}_{i,2} \hat{u}_{j,-1} + \hat{u}_{i,-1} \hat{u}_{j,2} + \hat{u}_{i,3} \hat{u}_{j,-2} + \hat{u}_{i,-2} \hat{u}_{j,3}) + \dots, \quad (2.34b)$$

$$\mathcal{F}_{i,2}^* = - \frac{\partial}{\partial x_j} (\hat{u}_{i,1} \hat{u}_{j,1} + \hat{u}_{i,3} \hat{u}_{j,-1} + \hat{u}_{i,-1} \hat{u}_{j,3} + \hat{u}_{i,4} \hat{u}_{j,-2} + \hat{u}_{i,-2} \hat{u}_{j,4}) + \dots, \quad (2.34c)$$

$$\mathcal{F}_{i,3}^* = - \frac{\partial}{\partial x_j} (\hat{u}_{i,1} \hat{u}_{j,2} + \hat{u}_{i,4} \hat{u}_{j,-1} + \hat{u}_{i,-1} \hat{u}_{j,4}) + \dots \quad (2.34d)$$

The terms for  $n = 0$  represent the interaction of the fundamental and higher harmonic waves with their respective conjugates, forming a steady flow field which modifies the base flow (which is a solution of the stationary Navier-Stokes equation) towards the mean flow. For the generation of

	$A = 0.01$	$A = 0.05$
$  \partial x_j (\hat{u}_{i,1}\hat{u}_{j,-1} + \hat{u}_{i,-1}\hat{u}_{j,1})   /  \mathcal{L}_{i,0}  $	0.1022	0.2356
$  \partial x_j (\hat{u}_{i,2}\hat{u}_{j,-2} + \hat{u}_{i,-2}\hat{u}_{j,2})   /  \mathcal{L}_{i,0}  $	0.0014	0.3481
$  \partial x_j (\hat{u}_{i,3}\hat{u}_{j,-3} + \hat{u}_{i,-3}\hat{u}_{j,3})   /  \mathcal{L}_{i,0}  $	0.0005	0.0983
$  u_{i,b} - \bar{u}_i   /  u_{i,b}  $	0.0774	0.7288

**Table 2.5:** Influence of the quadratic harmonic interactions in the mean flow equation and mean flow correction. The quasi-stationary solution of the unforced flow is taken as base flow  $u_{i,b}$ .

higher harmonics, the following process emerges: The second harmonic is generated by interaction of the fundamental wave with itself and feeds back on the fundamental wave (through interaction with the fundamental wave and higher harmonics), itself and subsequent higher harmonic waves. The third harmonic and subsequent harmonics are generated similarly through interaction of the fundamental wave or higher harmonics with other harmonics. The harmonics themselves are expanded as

$$u_i = \bar{u}_i + \hat{u}_{i,1} + \hat{u}_{i,2} + \hat{u}_{i,3} + \dots \quad (2.35)$$

As noted by [52], the harmonics then often decay as  $\hat{u}_{i,n} \propto O(\epsilon^n)$  where  $\epsilon$  is the amplitude of the fundamental mode. Given the assumption holds for the present case, when investigating equation (2.32), it should hold  $\mathcal{F}_{i,1}^* \propto O(\epsilon^3)$  while  $\mathcal{L}(u_{i,1}) \propto O(\epsilon)$ . Further it is then required that the amplitude of second harmonic is (at least) approximately an order of magnitude weaker than that of the fundamental mode.

[52]: Turton et al. (2015), ‘Prediction of frequencies in thermosolutal convection from mean flows’

In the body of literature regarding mean flow stability analysis, a number examples are found where the mean flow model fails to accurately predict the evolution of the fundamental mode of the flow. For instance, [51] performed a weakly nonlinear analysis of a cylinder wake and an open cavity flow and determined which contributions to the nonlinear terms had to be retained in order to fulfil the marginal stability criterion of the mean flow. While they found excellent agreement for the the cylinder wake, a similar analysis of the cavity flow revealed the mean flow to remain strongly unstable. Similarly, [52] found a disagreement for the case of a standing wave in thermosolutal convection. In these cases, failure of the mean flow model is due to a strong nonlinear interaction of the first and second harmonic such that  $\mathcal{F}_{i,1}^*$  is not small. In [83] the study of linear response to harmonic forcing of a shear layer over a cavity revealed good agreement with a corresponding large eddy simulation, despite non-negligible influence of the second harmonic, i.e.  $||\hat{u}_{i,1}|| \gg ||\hat{u}_{i,2}||$ . This is attributed to small interaction of the second harmonic with the fundamental wave. The nonlinear modification of the mean flow is also the basis for a self-consistent model, proposed by [84], which retains the nonlinear forcing of the fundamental wave on the mean flow, in order to iteratively (without *a priori* knowledge of the mean flow) obtain stability properties of a cylinder wake, by requiring the resulting mean flow to be marginally stable. In the light of these findings, we investigate the development of higher harmonic waves in the present flow for  $A = 0.01$  and  $A = 0.05$ , based on the results of the DNS to pinpoint possible reasons for the failure of the linear model for stronger forcings.

[51]: Sipp et al. (2007), ‘Global stability of base and mean flows: a general approach and its applications to cylinder and open cavity flows’

[83]: Boujo et al. (2018), ‘Saturation of a turbulent mixing layer over a cavity: response to harmonic forcing around mean flows’

[84]: Mantić-Lugo et al. (2014), ‘Self-consistent mean flow description of the nonlinear saturation of the vortex shedding in the cylinder wake’

We inspect the energy ratio of the fundamental wave and higher harmonics by their respective matrix norms, induced by the Euclidean norm, in figure 2.13a. A clear separation between the fundamental wave and the second harmonic is seen for  $A = 0.01$  (the ratio of the respective norms is of almost 16). For  $A = 0.05$  this separation is lost, with the second harmonic

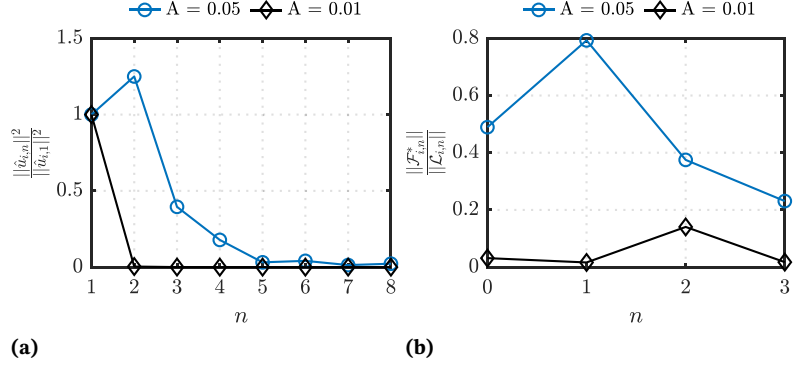


**Figure 2.13:** Ratio of the energy of the harmonics to the energy of the fundamental wave (a) and ratio of nonlinear to linear terms in equation (2.34) (b)

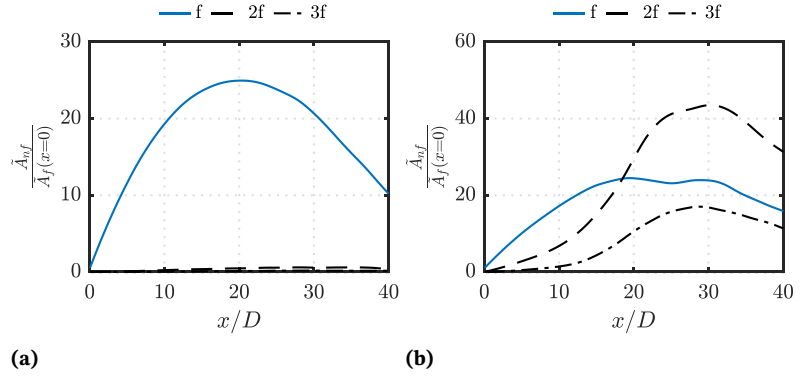


**Figure 2.14:** Amplitudes  $\hat{A}_n$  of the fundamental wave and its higher harmonics for (a)  $A = 0.01$ , (b)  $A = 0.05$

being even more energetic than the fundamental wave (the ratio of the norms is 0.9).

To get a more direct view on the growth of the harmonic waves, we compute their amplitudes from equation (2.30). They are shown in figure 2.14. All amplitudes are normalized with respect to the initial value of the fundamental wave at  $x = 0$ . For  $A = 0.01$  the fundamental wave saturates around  $x/D = 20$  and starts decaying shortly thereafter, reaching a maximum gain of approximately 25. The second and third harmonic saturate further downstream around  $x/D = 25$  and reach a maximum gain of approximately 0.5 and 0.25, respectively. Again a clear separation is evident, as the gain of the fundamental mode is higher by a factor of 50, respectively 100. At a forcing amplitude  $A = 0.05$ , the maximum gain of the fundamental wave is slightly reduced to around 24 and the point of saturation is shifted upstream to around  $x/D = 19$ . In contrast to  $A = 0.01$  the saturation level is sustained much longer and the wave starts decaying only after  $x/D = 30$ . As expected, the growth of the second and third harmonic is dramatically increased, reaching gains of approximately 43 and 16 respectively. Both waves saturate at around  $x/D = 28$ . Hence, the gain of the fundamental wave is exceeding that of the second and third harmonic by a factor of 0.56 and 1.5 respectively.

The influence of the quadratic nonlinearities  $\mathcal{F}_{i,n}^*$  is shown in figure 2.13b. They are evaluated using the terms displayed in equation (2.34). For  $A = 0.01$ , they are dominated by the first and second term for  $n = 0, 1$  and the first term for  $n = 2, 3$ . For  $A = 0.05$  all displayed terms have non-negligible contributions. For  $A = 0.01$ , the influence of  $\mathcal{F}_{i,1}^*$  is negligible ( $\mathcal{F}_{i,1}^* \propto O(\epsilon^3)$ ), leaving the dynamics of the fundamental wave unaffected by higher harmonic interaction. In contrast, for  $A = 0.05$ , the influence is profound and the nonlinear modification to the fundamental wave even

exceeds that of the mean flow ( $\mathcal{F}_{i,1}^* \gg O(\epsilon^3)$ ). Interestingly, for  $A = 0.01$ ,  $\mathcal{F}_{i,2}^*$  is non-negligible and exceeds the zero-order terms, which is in contrast to the findings of [52], who argued that  $\frac{\partial}{\partial x_j} (\hat{u}_{i,1} \hat{u}_{j,1})$  (which generates  $u_{i,2}$ ) should be small compared to  $\frac{\partial}{\partial x_j} (\hat{u}_{i,1} \hat{u}_{j,-1} + \hat{u}_{i,-1} \hat{u}_{j,1})$ . However, since from equation 2.35 it should hold  $\mathcal{F}_{i,2}^* \propto O(\epsilon^2)$  and  $\mathcal{L}(u_{i,2}) \propto O(\epsilon^2)$ , this does not violate our assumption. In summary, two main effects are observed that likely lead to failure of the mean flow stability model for  $A = 0.05$ : The missing spectral energy separation of the second (and third) harmonic compared to the fundamental wave and the nonlinear modification of the fundamental wave through harmonic-fundamental/harmonic-harmonic interaction which is explicitly violating the assumption we have made for the mean flow analysis in section 2.3.1.

The influence of the harmonic interactions on the mean flow is assessed in table 2.5. The mean flow correction for  $A = 0.01$  is generally small and solely dominated by the fundamental wave, whereas for  $A = 0.05$  significant influence of the second and also third harmonic is observed. To get a clearer picture of the spatial development of the mean flow forcing, the energy transfer between the mean field and the harmonic-harmonic interactions is investigated. Following [63] and [50], by neglecting any viscous involvement, the energy equation for the mean flow across both fluid phases can be stated as

$$\frac{1}{2} \frac{d}{dx} \int_0^\infty \bar{u}^3 dy \approx - \sum_{n=0}^{\infty} \left( \underbrace{\int_0^\infty -\hat{u}_n \hat{v}_n^* \frac{\partial \bar{u}}{\partial y} dy}_{\mathcal{P}_n} \right) - \int_0^\infty -\overline{u''v''} \frac{\partial \bar{u}}{\partial y} dy, \quad (2.36)$$

where only terms dominating the balance have been retained and the coherent term is expanded as in equation (2.34a). The first term on the right-hand side refers to the energy production by action of the mean field on the coherent Reynolds stresses, while the second term accounts similarly for the energy production by action of the mean field on the fluctuating Reynolds stresses.

The stream-wise contributions of the coherent production terms  $\mathcal{P}_n$  is given in figure 2.15. Since the fluctuations are very small, they are, again, neglected. Further, the production for  $A = 0.01$  is essentially limited to the fundamental wave and therefore is not further discussed. The balance is dominated by the energy production of the fundamental wave, which draws energy from the mean field (since it is positive) throughout the domain and reaches its maximum at  $x/D = 22$  shortly downstream of the saturation point of the fundamental wave  $\mathcal{P}_1$ . The energy that is fed to the now saturated fundamental wave is distributed on the higher harmonics that are still growing as seen in figure 2.14.  $\mathcal{P}_2$  is always negative, thus continuously transferring energy back to the mean flow.  $\mathcal{P}_3$  is positive for  $15 < x/D < 25$  and peaks around the same position as the fundamental wave. For  $x/D > 22$  the contribution  $\mathcal{P}_1$  and  $\mathcal{P}_3$  diminishes and  $\mathcal{P}_3$  becomes negative as well.

[52]: Turton et al. (2015), ‘Prediction of frequencies in thermosolutal convection from mean flows’

[63]: Oberleithner et al. (2014), ‘Mean flow stability analysis of oscillating jet experiments’

[50]: Reynolds et al. (1972), ‘The mechanics of an organized wave in turbulent shear flow. Part 3. Theoretical models and comparisons with experiments’

It might seem counter-intuitive that the production of the fundamental wave is significantly larger than that of the second harmonic, whereas, for the harmonics themselves and their self-interaction on the mean flow, the second harmonic dominates. Indeed, for the normal Reynolds stresses the dominating influence is that of the second harmonic. However, for the tangential stresses, the contribution of the fundamental mode is largest. Since,  $\partial\bar{u}/\partial y \gg \partial\bar{u}/\partial x \approx \partial\bar{v}/\partial y \approx \partial\bar{v}/\partial x$ , the tangential stresses dominate  $\mathcal{P}$ .

The negative production in  $\mathcal{P}_2, \mathcal{P}_3$  corresponds to a reversed energy cascade from small scale oscillations to the large scale mean flow. It was hypothesized by [63] that while such a reversed energy cascade is acting, there is no linear dependency between the mean field and the coherent motion which could lead to a break-down of the linear stability model. In the present case, although  $\mathcal{P}_1$  remains positive,  $\mathcal{P}_2$  is increasingly feeding energy back to the mean flow during the growth phase of the forced instability wave, while having a profound influence on the systems stability behaviour as is evident from its gain. It therefore seems possible that the reversed energy cascade, caused by modification of the mean flow through the second harmonic, is another cause for the break-down of the stability model for  $A = 0.05$ .

[63]: Oberleithner et al. (2014), ‘Mean flow stability analysis of oscillating jet experiments’

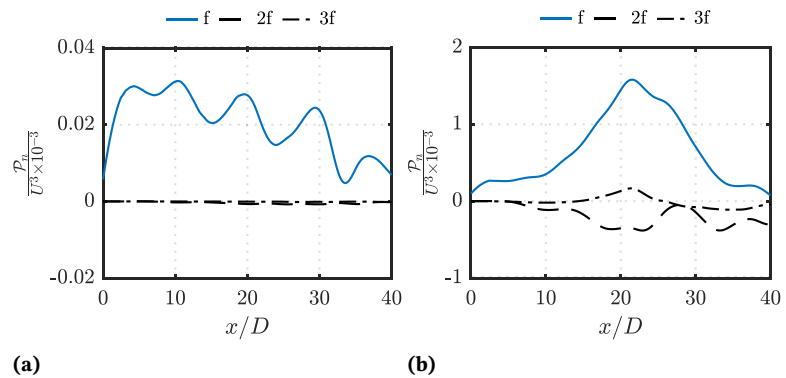


**Figure 2.15:** Energy production  $\mathcal{P}_n$  of the fundamental wave and its higher harmonics for (a)  $A = 0.01$ , (b)  $A = 0.05$

The present work solely focuses on modal growth to explain the developing instabilities. It is possible that non-modal growth, caused by non-orthogonality of the eigenvectors, has an influence on the short-time behaviour of the forced jet and, if significant, possibly could explain some of the short-comings of the linear stability analysis. There have been some studies on transient growth on two-phase mixing layers and jets by e.g. [85] and [86]. In both studies a possibility of transient growth in the respective flows was found, however, no validation using experimental or numerical data has been conducted and it remains unknown whether these effects actually have significant influence on the flow.

[85]: Yecko et al. (2005), ‘Transient growth in two-phase mixing layers’

[86]: De Luca (2001), ‘Non-modal growth of disturbances in free-surface flows’

From a phenomenological viewpoint, the strong involvement of the higher harmonics can be attributed to the formation of vortical structures, observed in the gas phase around the oscillating jet. Further, while due to the transverse forcing at the inlet, the fundamental mode is sinuous, the second harmonic wave is dilatational as can be deduced from the display of the higher harmonic waves in appendix 2.7.7. Similar findings of a strong interaction between the sinuous fundamental wave and a dilatational second harmonic are given by [87] and [88]. The superposition of both modes

[87]: Mehring et al. (1999), ‘Nonlinear capillary wave distortion and disintegration of thin planar liquid sheets’

[88]: Clark et al. (1972), ‘Aerodynamic instability and disintegration of inviscid liquid sheets’

leads to characteristic agglomeration of liquid along the wave crests and thinning along the jet axis as seen in figure 2.2b.

### 2.5.1 Vorticity dynamics

The evolution of vortical structures shown in figure 2.4 shows increasingly complex patterns starting with an initial vorticity sheet close to the inlet that develops into discrete vortical structures with subsequent interaction and roll-up in the enlarging wave troughs of the unstable liquid jet. Detailed numerical studies of liquid jets by [89] and [90] show significant interaction between vortex and interface dynamics in the process of interface deformation and breakup. To investigate the vorticity generation we evaluate the terms in the vorticity equation of an incompressible fluid

$$\frac{\partial \Omega_i}{\partial t} + u_j \frac{\partial \Omega_i}{\partial x_j} = \Omega_j \frac{\partial u_i}{\partial x_j} + \frac{1}{\rho^2} \epsilon_{ijk} \frac{\partial \rho}{\partial x_j} \frac{\partial p}{\partial x_k} + \nu \frac{\partial^2 \Omega_i}{\partial x_j^2} \quad (2.37)$$

where the terms on the right-hand side correspond to vortex stretching or tilting by velocity gradients, the baroclinic torque and vorticity diffusion. In two-dimensional flows the vorticity reduces to a scalar quantity and vortex stretching or tilting is absent so that the vorticity equation reduces to

$$\frac{\partial \Omega}{\partial t} + u \frac{\partial \Omega}{\partial x} + v \frac{\partial \Omega}{\partial y} = \frac{1}{\rho^2} \left( \frac{\partial \rho}{\partial x} \frac{\partial p}{\partial y} - \frac{\partial \rho}{\partial y} \frac{\partial p}{\partial x} \right) + \nu \left( \frac{\partial^2 \Omega}{\partial x^2} + \frac{\partial^2 \Omega}{\partial y^2} \right). \quad (2.38)$$

As shown by [89], the baroclinic term dominates for large density ratios. Their results are in line with observations from experimental investigations of liquid jets in high-velocity gas co-flow by [34]. They found that while primary destabilisation of the interface is due to Kelvin-Helmholtz type shear instabilities, at later stages when the interface is significantly corrugated, secondary instabilities evolve which they attribute to Rayleigh-Taylor type baroclinic instabilities. In the present work the transverse oscillation of the jet induces an acceleration of the interface perpendicular to the jet axis. Together with the curved interface this leads to a misalignment of pressure and density gradients. As a result the baroclinicity along the interface is expected to grow in downstream direction.

The normalised, instantaneous stream-wise development of the baroclinicity, integrated across the jet

$$B(x, t) = \frac{D}{U^2} \int_0^\infty \left| \frac{(\nabla \rho \times \nabla p)}{\rho^2} \right| dy, \quad (2.39)$$

is given in figure 2.16. As can be seen the term varies periodically with half the wavelength of the forced oscillation at a relatively steady amplitude for throughout the domain for  $A = 0.01$ . For  $A = 0.05$  the term shows a significant downstream growth and becomes highly irregular for  $x/D > 20$  with peaks which are about a factor 5 larger than the initial amplitude.

[89]: Jarrahbashi et al. (2014), 'Vorticity dynamics for transient high-pressure liquid injection'

[90]: Zandian et al. (2018), 'Understanding liquid-jet atomization cascades via vortex dynamics'

[34]: Marmottant et al. (2004), 'On spray formation'

From the viewpoint of instability waves the increase in baroclinicity coincides with the growth of the higher harmonic waves analysed in section 2.5. In fact the Fourier transformation of  $\mathcal{B}$  shown in figure 2.18 expectedly shows the fundamental frequency at twice the frequency of the forced oscillation. However, from the stream-wise evolution of the harmonics it is evident that the energy content of the second harmonic exceeds that of the fundamental frequency for  $22 < x < 30$  of the nonlinear region which concurs with the qualitative development of the harmonics in section 2.5. This suggests that the steep increase in baroclinicity is linked to the growth of higher harmonic waves in the unstable jet.

For completeness the viscous dissipation of vorticity

$$\mathcal{D}(x, t) = \frac{D}{U^2} \int_0^\infty |\nu \Delta \Omega| dy \tag{2.40}$$

is shown in figure 2.17. Its qualitative stream-wise development is comparable to that of the baroclinicity, although its influence is considerably weaker, given that values of the baroclinicity are around an order of magnitude larger. Additionally, its growth within the nonlinear region is not as pronounced as for the baroclinicity.

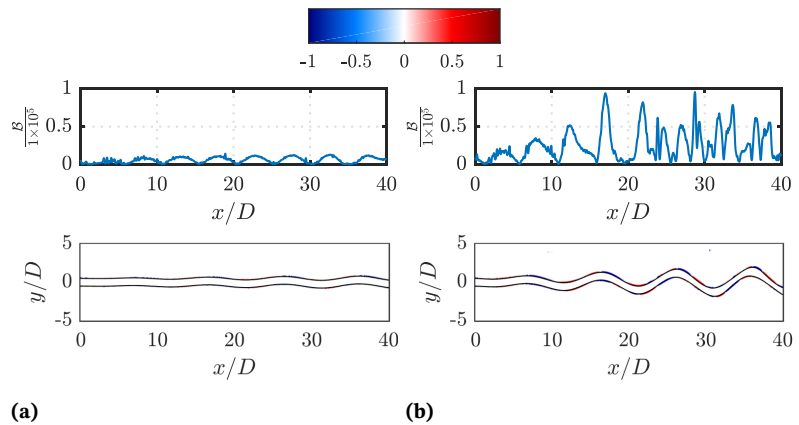


**Figure 2.16:** Instantaneous, cross-wise integrated baroclinic vorticity  $\mathcal{B}$  and snapshot of the corresponding field normalised by its maximum for (a)  $A = 0.01$ , (b)  $A = 0.05$

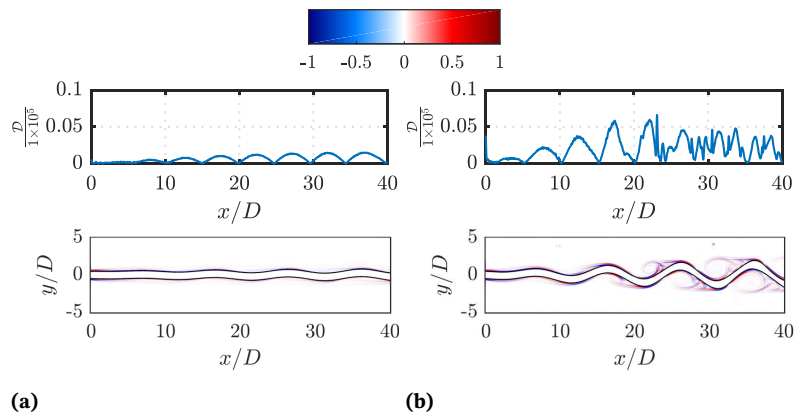


**Figure 2.17:** Instantaneous, cross-wise integrated vorticity dissipation  $\mathcal{D}$  and snapshot of the corresponding field normalised by its maximum for (a)  $A = 0.01$ , (b)  $A = 0.05$

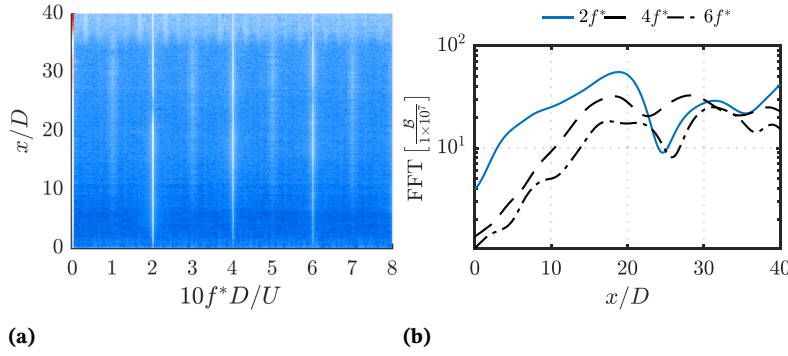


**Figure 2.18:** Stream-wise evolution of the Fourier decomposition of the cross-wise averaged baroclinic vorticity for  $A = 0.05$ . The spectrum along the stream-wise coordinate is shown (a) as well as the stream-wise development of the energy of the first three harmonics.

## 2.6 Summary and conclusions

The linear and nonlinear stability of a transversely forced planar liquid jet in a still ambient gas is studied using nonlinear numerical simulation and local linear stability analysis, based on a time-averaged mean flow representation of the unsteady nonlinear flow.

The simulated jet, with a  $Re_1 = 8962$  and  $We = 440$ , is forced at two forcing amplitudes  $A = 0.01, 0.05$ . The forcing produces an initially monochromatic instability wave that grows in space until it saturates and decays.

For the linear stability model, the time-averaged mean flow is obtained from the nonlinear simulation. Due to the non-parallelism of the forced flow, a mass-conserving model is proposed to account for the spreading of the interface position in the mean flow.

General stability properties are derived, based on the unforced flow, for a wide range of frequencies. Two unstable modes are found of which mode I is relevant for the present forcing cases. The modes are vaguely corresponding to the modes I and II found by [21]. By analysing the energy budget of mode I it is found that the instability is mainly driven by the viscosity defect of the adjacent fluid streams in the shear layer.

Detailed comparison of the stability model using the forced mean flow with the DNS shows excellent agreement for  $A = 0.01$  and the proposed interface correction results in an improved replication of the transverse shear layer spreading in the eigenfunctions. Also, without correction the position of the neutral point is somewhat over-predicted. For  $A = 0.05$ , significant deviations in the eigenfunctions for  $x/D > 20$  is observed. The linear model completely fails to predict correct growth rates for this forcing amplitude.

Reasons for the failure of the linear model at  $A = 0.05$  are found by analysis of higher harmonic wave growth in the flow. While for  $A = 0.01$  the fundamental wave dominates the stability behaviour, for  $A = 0.05$  significant influence of the second and third harmonic is observed. The second harmonic thereby reaches gain levels exceeding that of the fundamental wave. As a result, the fundamental wave exhibit strong nonlinear modification through higher harmonics which explains the failing of the linear model. Similar limitations to mean flow stability have been revealed by [51] and [52].

In conclusion, the linear stability model performs well for low forcing amplitudes over the whole spatial extend even in the presence of moderate

[21]: Söderberg (2003), ‘Absolute and convective instability of a relaxational plane liquid jet’

[51]: Sipp et al. (2007), ‘Global stability of base and mean flows: a general approach and its applications to cylinder and open cavity flows’

[52]: Turton et al. (2015), ‘Prediction of frequencies in thermosolutal convection from mean flows’

[63]: Oberleithner et al. (2014), ‘Mean flow stability analysis of oscillating jet experiments’

nonlinear effects. The inclusion of a mean interface correction scheme has proven to increase reliability of the mean flow based linear stability model. These results are in line with the conclusions drawn by [63]. However, strong discrepancies arise for stronger forcings when nonlinear interactions between the fundamental mode and higher order modes significantly alter the flow. From the viewpoint of vorticity dynamics, the higher harmonics waves correspond to a substantial growth of baroclinic vorticity along the liquid/gas interface.

## 2.7 Appendix

### 2.7.1 Derivation of the conditions for stress continuity

For an incompressible Newtonian fluid, the stress tensor of each fluid phase is written as

$$\mathcal{S}_{ij,l,g}^* = p_{l,g}^* \delta_{ij} + \mu_{l,g} \left( \frac{\partial u_{i,l,g}^*}{\partial x_j^*} + \frac{\partial u_{j,l,g}^*}{\partial x_i^*} \right). \quad (2.41)$$

The stars indicate dimensioned quantities. To obtain the normal and tangential components of equation (2.41), we need the unit normal vector of the interface which is given as

$$n_i^* = \frac{\nabla \tilde{H}^*}{|\nabla \tilde{H}^*|} = \frac{-(\partial \tilde{h}^* / \partial x^*, 1)^T}{\sqrt{(\partial \tilde{h}^* / \partial x^*)^2 + 1}}, \quad (2.42)$$

where  $\tilde{H}^*(x, y, t) = y^* - \tilde{h}^*(x, t) = 0$  is the curve defining the interface. For small surface displacements, we neglect quadratic terms of disturbed quantities and arrive at  $n_i^* = (-\partial \tilde{h}^* / \partial x^*, 1)^T$ . The tangent vector is readily given as  $t_i^* = (1, \partial \tilde{h}^* / \partial x^*)^T$ .

The continuity of shear stress is given as  $t_i^* \mathcal{S}_{ij,l}^* n_j^* = t_i^* \mathcal{S}_{ij,g}^* n_j^*$ . Inserting the decomposition (2.11) (neglecting the fluctuations), using Taylor expansion of  $h^*(x^*, t^*)$  around  $y^* = \bar{h}^*$  and neglecting quadratic terms of disturbed quantities, we obtain

$$\mu_l \left[ \left[ \frac{\partial \tilde{v}}{\partial x} + \frac{\partial \tilde{u}}{\partial y} + \tilde{h} \frac{d^2 \bar{u}}{dy^2} \right]_{y=\bar{h}, l}^* \right] - \mu_g \left[ \left[ \frac{\partial \tilde{v}}{\partial x} + \frac{\partial \tilde{u}}{\partial y} + \tilde{h} \frac{d^2 \bar{u}}{dy^2} \right]_{y=\bar{h}, g}^* \right] = 0. \quad (2.43)$$

Dividing by  $\mu_l U/D$  we arrive at the dimensionless form

$$\left[ \left[ \frac{\partial \tilde{v}}{\partial x} + \frac{\partial \tilde{u}}{\partial y} + \tilde{h} \frac{d^2 \bar{u}}{dy^2} \right]_{y=\bar{h}, l} \right] - m \left[ \left[ \frac{\partial \tilde{v}}{\partial x} + \frac{\partial \tilde{u}}{\partial y} + \tilde{h} \frac{d^2 \bar{u}}{dy^2} \right]_{y=\bar{h}, g} \right] = 0, \quad (2.44)$$

where  $m = \mu_g / \mu_l$ .

Similarly, the continuity of normal stress is given as  $n_i^* \mathcal{S}_{ij,l}^* n_j^* = n_i^* \mathcal{S}_{ij,g}^* n_j^* - \sigma \partial n_i^* / \partial x^*$ . Using Taylor expansion again and dividing by  $\rho_l U^2 / D$  we get

$$\left[ \tilde{p} - \frac{2}{Re_1} \frac{\partial \tilde{v}}{\partial y} \right]_{y=\bar{h}, l} - \left[ r \tilde{p} - \frac{2m}{Re_1} \frac{\partial \tilde{v}}{\partial y} \right]_{y=\bar{h}, g} + \frac{1}{We} \frac{\partial^2 \tilde{h}}{\partial x^2} = 0. \quad (2.45)$$

## 2.7.2 Convergence analysis of the linear stability model

A convergence analysis, to estimate the necessary amount of collocation points, is performed at the point of neutral stability for the varying interface model with  $A = 0.01$ . The number of collocation points is successively increased from  $N = 20$  to  $N = 200$  points in each phase. The convergence of the stream-wise position of the neutral point and the corresponding real part of the eigenvalue,  $\alpha_\rho$ , is shown in figure 2.19. As is seen, the choice of  $N = 110$  is adequate.

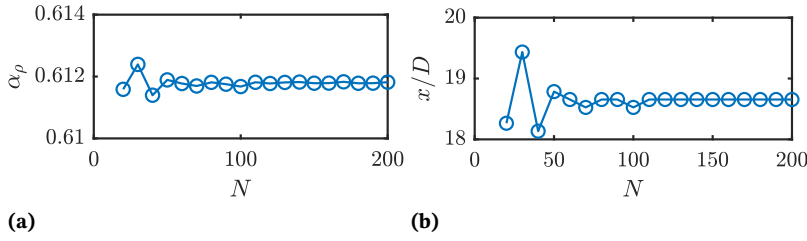


**Figure 2.19:** Convergence of the real part of the traced eigenvalue,  $\alpha_\rho$ , at the neutral point and position of the neutral point,  $x/D$ , for various numbers  $N$  of collocation points

## 2.7.3 Flow conditions of the two-layer Poiseuille flow by [78]

[78] computed unstable eigenvalues for a two-layer plane Poiseuille flow that is used for validating the present two-phase linear stability solver. The flow conditions are restated here for convenience. The basic flow is

$$u_1(y) = A_1 y^2 + a_1 y + 1, \quad -1 < y < 0, \quad (2.46)$$

$$u_2(y) = A_2 y^2 + a_2 y + 1, \quad 0 < y < n, \quad (2.47)$$

where

$$A_1 = \frac{-(m+n)}{n(n+1)}, \quad a_1 = \frac{n^2 - m}{n(n+1)}, \quad A_2 = \frac{A_1}{m}, \quad a_2 = \frac{a_1}{m}. \quad (2.48)$$

The viscosity ratio is  $m = \mu_2 / \mu_1 = 2$ , the depth ratio is  $n = d_2 / d_1 = 1.2$  where  $d$  denotes the extend of the respective domains. The density ratio is  $r = 1$  and the surface tension is  $\sigma = 0$ . The obtained eigenvalues using temporal analysis with  $\alpha = 1$  are stated in table 2.3.

[78]: Dongarra et al. (1996), 'Chebyshev tau-QZ algorithm methods for calculating spectra of hydrodynamic stability problems'

### 2.7.4 Stability maps with the scaling of [21]

The stability maps, derived in section 2.3.4, are reprinted here using the axes scaling of [21] for direct comparison (figure 2.20).

[21]: Söderberg (2003), ‘Absolute and convective instability of a relaxational plane liquid jet’

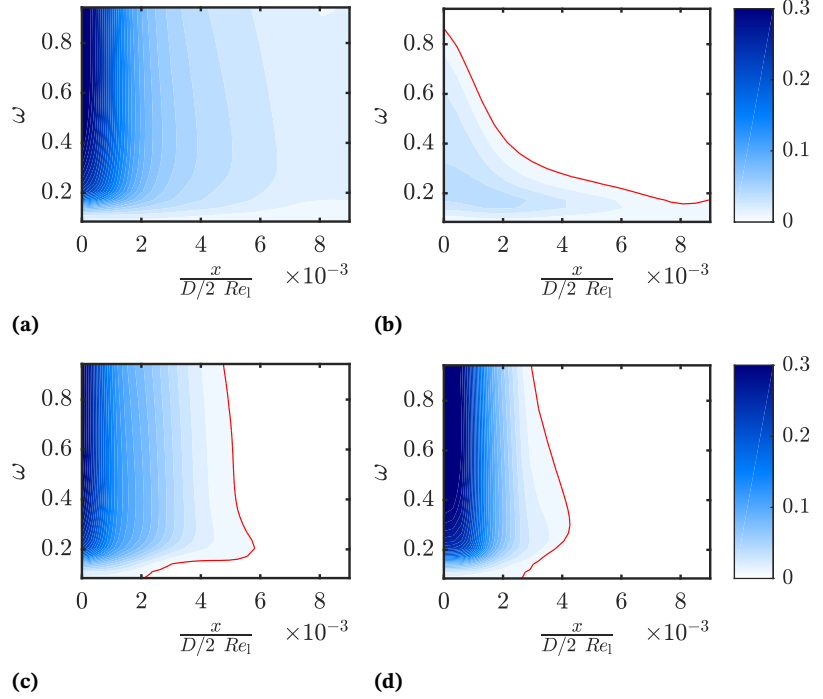


**Figure 2.20:** Stability map for the base flow model (Mode I (a), Mode II (b)), fixed interface model (Mode I) at  $A = 0.01$  (c), varying interface model (d). Shown is the spatial growth rate  $-\alpha_l D/2$  and the curve indicating neutral stability, i.e.  $\alpha_l D/2 = 0$ , in red. The axes scaling is as in [21], where  $\omega = \pi f D/U$ .

### 2.7.5 The energy budget for spatial modes in two-phase flows

[79]: Boomkamp et al. (1996), ‘Classification of instabilities in parallel two-phase flow’

[80]: Otto (2012), ‘Spatio-Temporal Stability Analysis in Two-Phase Mixing Layers’

Closely following [79] and [80], a balance for the coherent kinetic energy  $\tilde{u}_i \tilde{u}_i$  in each fluid phase is obtained by taking the inner product of equation (2.14) with  $\tilde{u}_i$ . Upon averaging over one period,  $\gamma = 2\pi/\omega$ , integration along  $y$  and by adding the results over both fluid phases, equation (2.28) is obtained.

The respective terms on the right-hand side of the equation are given as

$$\begin{aligned} \text{MFL}_1 = \frac{1}{\gamma} \frac{\partial}{\partial x} \int_0^\gamma \int_0^D \left[ \frac{\bar{u}_1}{2} (\tilde{u}_1 + \tilde{v}_1) + \tilde{u}_1 \tilde{p}_1 \right. \\ \left. - \frac{1}{Re_1} \left( 2\tilde{u}_1 \frac{\partial \tilde{u}_1}{\partial x} + \tilde{v}_1 \frac{\partial \tilde{u}_1}{\partial y} + \tilde{v}_1 \frac{\partial \tilde{v}_1}{\partial y} \right) \right] dy dt, \end{aligned} \quad (2.49a)$$

$$\begin{aligned} \text{MFL}_g = \frac{1}{\gamma} \frac{\partial}{\partial x} \int_0^\gamma \int_D \left[ \frac{r\bar{u}_g}{2} (\tilde{u}_g + \tilde{v}_g) + r\tilde{u}_g \tilde{p}_g \right. \\ \left. - \frac{m}{Re_1} \left( 2\tilde{u}_g \frac{\partial \tilde{u}_g}{\partial x} + \tilde{v}_g \frac{\partial \tilde{u}_g}{\partial y} + \tilde{v}_g \frac{\partial \tilde{v}_g}{\partial y} \right) \right] dy dt, \end{aligned} \quad (2.49b)$$

$$\text{DIS}_1 = \frac{1}{\gamma} \frac{1}{Re_1} \int_0^\gamma \int_0^D \left[ 2 \left( \frac{\partial \tilde{u}_1}{\partial x} \right)^2 + \left( \frac{\partial \tilde{u}_1}{\partial y} + \frac{\partial \tilde{v}_1}{\partial x} \right)^2 + 2 \left( \frac{\partial \tilde{v}_1}{\partial y} \right)^2 \right] dy dt, \quad (2.50a)$$

$$\text{DIS}_g = \frac{1}{\gamma} \frac{m}{Re_1} \int_0^\gamma \int_D^\infty \left[ 2 \left( \frac{\partial \tilde{u}_g}{\partial x} \right)^2 + \left( \frac{\partial \tilde{u}_g}{\partial y} + \frac{\partial \tilde{v}_g}{\partial x} \right)^2 + 2 \left( \frac{\partial \tilde{v}_g}{\partial y} \right)^2 \right] dy dt, \quad (2.50b)$$

$$\text{REY}_1 = \frac{1}{\gamma} \int_0^\gamma \int_0^D \left[ (-\tilde{u}_1 \tilde{v}_1) \frac{\partial \bar{u}_1}{\partial x} \right] dy dt, \quad (2.51a)$$

$$\text{REY}_g = \frac{1}{\gamma} r \int_0^\gamma \int_D^\infty \left[ (-\tilde{u}_g \tilde{v}_g) \frac{\partial \bar{u}_g}{\partial x} \right] dy dt, \quad (2.51b)$$

$$\text{TAN} = \frac{1}{\gamma} \frac{1}{Re_1} \int_0^\gamma \left[ m \left( \frac{\partial \tilde{u}_1}{\partial y} + \frac{\partial \tilde{v}_1}{\partial x} \right) \tilde{u}_1 - \left( \frac{\partial \tilde{u}_g}{\partial y} + \frac{\partial \tilde{v}_g}{\partial x} \right) \tilde{u}_g \right]_{y=\bar{h}} dt, \quad (2.52a)$$

$$\text{NOR} = \frac{1}{\gamma} \int_0^\gamma \left[ \left( r \tilde{p}_1 + \frac{2m}{Re_1} \frac{\partial \tilde{v}_1}{\partial y} \right) \tilde{v}_1 - \left( \tilde{p}_g + \frac{2}{Re} \frac{\partial \tilde{v}_g}{\partial y} \right) \tilde{v}_g \right]_{y=\bar{h}} dt. \quad (2.52b)$$

## 2.7.6 Comparison of DNS and the base flow model

For completeness, we briefly present the results of section 2.4 for the base flow model and the DNS ( $A = 0.01$ ) here. In figure 2.21, the stream-wise comparison of the eigenfunctions is shown. The growth rates and phase velocities are compared in figure 2.22. The results corroborate the advantage of the mean flow model. During the downstream development of the jet increasing discrepancies are evident from the eigenfunction profiles, as the mean flow spreading, induced by the oscillation is not taken into account in the base flow. As a result, no point of neutral stability is predicted (as already evident from figure 2.8a), and growth rates are generally overpredicted. Similar results are seen for the phase velocity.

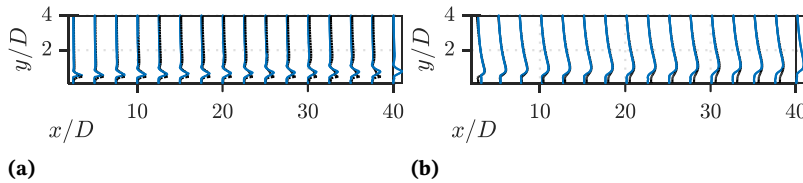


**Figure 2.21:** Comparison of the computed amplitude functions, normalised by their maximum value, from the base flow model and the DNS for  $A = 0.01$ , (a)  $\hat{u}$ ; (b)  $\hat{v}$ . Blue lines show the DNS while black lines show the LSA

## 2.7.7 Illustration of the Fourier modes

The higher harmonic waves, derived from the Fourier decomposition (equation (2.29)) of the velocity field, are displayed here for further clarification (figure 2.23).

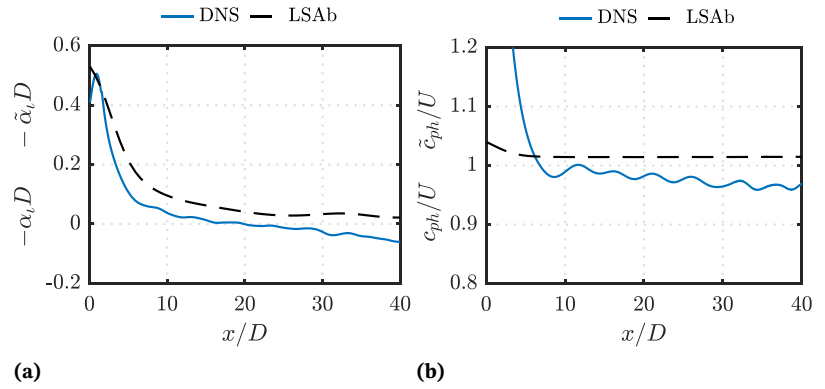


**Figure 2.22:** Comparison of the computed growth rates  $-\alpha_t D$  from the linear stability model and  $-\tilde{\alpha}_t D$  the DNS (a) and phase velocities  $c_{ph}/U$ ,  $\tilde{c}_{ph}/U$  (b) for  $A = 0.01$

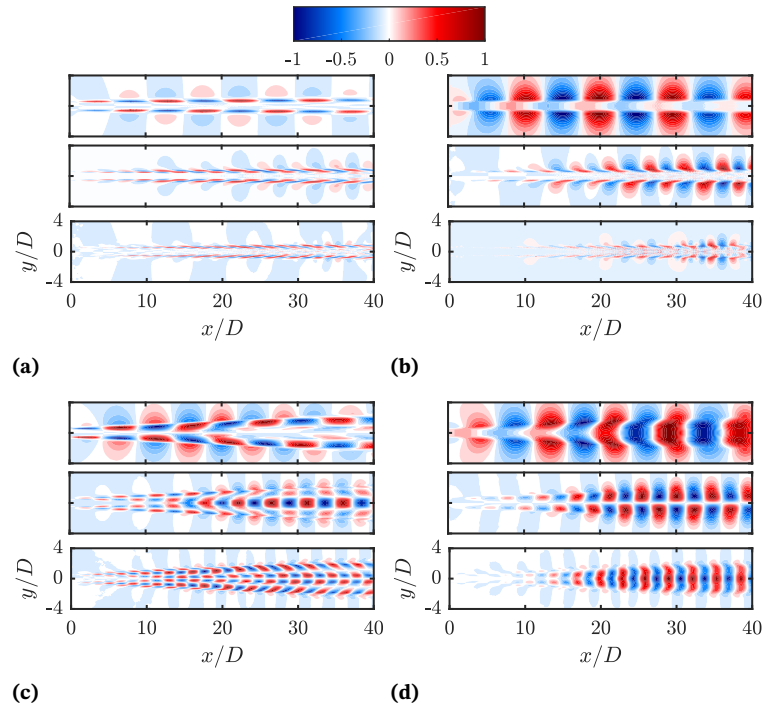


**Figure 2.23:** Real part of the fundamental, second and third harmonic wave (from top to bottom) for (a)  $A = 0.01$ ,  $\hat{u}$ ; (b)  $A = 0.01$ ,  $\hat{v}$ ; (c)  $A = 0.05$ ,  $\hat{u}$ ; (d)  $A = 0.05$ ,  $\hat{v}$ . Note, that each mode and component is normalized individually by its maximum for improved readability.

# Global stability and nonlinear dynamics of wake flows with a two-fluid interface

# 3

## Abstract

A framework for the computation of linear global modes, based on time-stepping of a linearised Navier-Stokes solver with an Eulerian interface representation, is presented. The method is derived by linearising the nonlinear solver BASILISK, capable of computing immiscible two-phase flows, and offers several advantages over previous, matrix-based, multi-domain approaches to linear global stability analysis of interfacial flows. Using our linear solver, we revisit the study of [24], who found a counter-intuitive, destabilising effect of surface tension in planar wakes. Since their original study does not provide any validation, we further compute nonlinear results for the studied flows. We show that a surface-tension-induced destabilisation of plane wakes is observable which leads to periodic, quasiperiodic or chaotic oscillations depending on the Weber number of the flow. The predicted frequencies of the linear global modes, computed in the present study, are in good agreement with the nonlinear results, and the growth rates are comparable to the disturbance growth in the nonlinear flow before saturation. The bifurcation points of the nonlinear flow are captured accurately by the linear solver and the present results are as well in correspondence with the study of [24].

3.1	Introduction . . . . .	56
3.2	Numerical methods for two-phase flows . . . . .	57
3.3	Linearisation procedure	60
3.4	Formulation and solution of the eigenvalue problem . . . . .	65
3.5	Global modes of a planar wake under the influence of surface tension	66
3.6	Conclusions . . . . .	80
3.7	Appendix . . . . .	81

[24]: Tammisola et al. (2012), 'Surface tension-induced global instability of planar jets and wakes'

The contents of this chapter have been **published** in revised form in the *Journal of Fluid Mechanics*:

S. Schmidt, O. Tammisola, L. Lesshafft and K. Oberleithner. 'Global stability and nonlinear dynamics of wake flows with a two-fluid interface.' In: *Journal of Fluid Mechanics* 915 (2021). DOI: <https://doi.org/10.1017/jfm.2021.150>

This version (accepted manuscript) is free to view and download for private research and study only. Not for re-distribution or re-use. ©copyright holder.

### 3.1 Introduction

Shear flows involving two (or more) immiscible fluids can exhibit distinctively different stability characteristics than their single-phase equivalents. This can be due to the presence of not only a momentum gradient of the adjacent fluids but also a density and viscosity gradient. Furthermore, the presence of a surface tension force at the interface(s) can influence the stability of the flow.

As a consequence, stability properties of multiphase flows are significantly more complex and involve a larger parameter space than their single phase equivalents. The Weber number can be used to express the ratio of momentum to surface tension force in the flow. In general, for liquid jets with low Weber numbers, the influence of surface tension is dominating and, depending on whether the liquid layer is planar or round, can either stabilize [17, 19] or destabilize the flow [55]. At higher Weber numbers, aerodynamic forces, through the momentum or density/viscosity gradient [18, 22, 56], overcome the effects of surface tension. However, in the case of confined plane jets and wakes, a study by [24] found that for certain configurations, surface tension might as well destabilise a plane flow which is stable in its absence. These somewhat surprising results are partially confirmed in a subsequent study by [91] who found an unstable global mode for some of the configurations of the former study. However, for other configurations they found no global instability, thereby raising doubts concerning the validity of the surface tension-induced destabilisation found by [24].

Flow stability is usually assessed through the framework of linear stability analysis, which seeks solutions of the Navier-Stokes operator, linearised around steady or time-periodic base flows (see e.g. [92]). By choosing a Fourier ansatz for the perturbation quantities, the linearised system is recast as an eigenvalue problem, where the resulting eigenvalues yield information about the exponential growth or decay of the respective eigenvectors. In a local analysis, the underlying base flow is assumed to be parallel and therefore only dependent on one spatial coordinate, while for a global analysis it might be inhomogeneous in all spatial coordinates.

However, for large-scale flows or three-dimensional base flows, memory requirements for storing the operator matrix are still prohibitive. In such cases direct construction of the Jacobian matrix can be avoided by employing iterative techniques where the high-dimensional system is orthogonally projected onto a low-dimensional subspace which in turn allows for direct computation of its eigenvalues. In practice, construction of the subspace can be achieved using standard time-stepping techniques and in principle any nonlinear DNS solver can be utilized, as demonstrated by [47].

Although global analysis has become a standard tool for analysing single-phase flows, its application to multiphase flow has only rarely been attempted so far. There have been numerous approaches through local absolute stability analysis (e.g. [93–95]), and by analysing the growth of small perturbations around base flows in direct numerical simulations [96]. However, to our knowledge, the work of [23],[24] is one of the very few reported applications of linear global analysis to a two-dimensional immiscible two-phase flow. In their approach, the linearised operator is

[17]: Squire (1953), ‘Investigation of the instability of a moving liquid film’

[19]: Hagerty et al. (1955), ‘A study of the stability of moving liquid film’

[55]: Rayleigh (1878), ‘On The Instability Of Jets’

[18]: Yih (1967), ‘Instability due to viscosity stratification’

[22]: Boeck et al. (2005), ‘Viscous versus inviscid instability of two-phase mixing layers with continuous velocity profile’

[56]: Drazin et al. (2004), *Hydrodynamic Stability*

[24]: Tammisola et al. (2012), ‘Surface tension-induced global instability of planar jets and wakes’

[91]: Biancofiore et al. (2014), ‘Direct numerical simulations of two-phase immiscible wakes’

[92]: Schmid et al. (2012), *Stability and transition in shear flows*

[47]: Barkley et al. (2008), ‘Direct optimal growth analysis for timesteppers’

[93]: Söderberg (2003), ‘Absolute and convective instability of a relaxational plane liquid jet’

[94]: Rees et al. (2009), ‘The effect of surface tension on the stability of unconfined and confined planar jets and wakes’

[95]: Sevilla (2011), ‘The effect of viscous relaxation on the spatiotemporal stability of capillary jets’

[96]: Tammisola et al. (2017), ‘Effect of viscosity ratio on the self-sustained instabilities in planar immiscible jets’

[23]: Tammisola et al. (2011), ‘Effect of surface tension on global modes of confined wake flows’

constructed explicitly, and discretisation of the fluid phases is done on separate meshes, resulting in a conformal interface representation that is aligned with the mesh boundary, separating the domains. Along the interface, velocity and stress conditions are enforced to couple the domains. The base flow is computed using a single-phase spectral element code, and the fluid interface is extracted *a posteriori* as a streamline to obtain an artificial two-phase base flow.

In the present work, we explore a different approach, by developing a framework which allows for computation of global modes by means of time-stepping with a linearised DNS solver with an Eulerian interface representation, capable of computing two-phase flows. The benefits of a successful realisation of this approach are readily seen: base flow and perturbation computations are obtained using the same numerical schemes, so that no grid mapping or interpolation is necessary. Further, resource requirements for perturbation computations scale similarly to nonlinear simulations, such that analysis of three-dimensional base flows is possible. Finally, the utilisation of an available, highly optimised, nonlinear solver obviates the need for re-implementing the required schemes in a new solver.

For our study, we choose the open-source framework BASILISK, developed by Stéphane Popinet (<http://basilisk.fr>), which offers a geometrical Volume-Of-Fluid (VOF) interface representation, combined with a well-balanced surface tension scheme.

The aim of this article is two-fold: First, we give a detailed presentation of the derivation of the novel method for the computation of linear global modes of two-phase flows. Second, we revisit the wake flows investigated by [24], this time using nonlinear simulations and our linear solver, thereby shedding more light on the nonlinear dynamics of the flow and providing a rigorous validation.

In the remainder of this article, we first give an overview of the schemes implemented in BASILISK and outline the necessary modifications to the solver for computing linear global modes. We then proceed by presenting nonlinear results of the wake flow configurations of [24], and compare them with the linear results obtained with the present method. Finally, we discuss some of the differences between the studies of [24] and [91].

[24]: Tammisola et al. (2012), ‘Surface tension-induced global instability of planar jets and wakes’

[91]: Biancofiore et al. (2014), ‘Direct numerical simulations of two-phase immiscible wakes’

## 3.2 Numerical methods for two-phase flows

### 3.2.1 Governing equations for interfacial two-phase flow

As the stability computations are facilitated using the same numerical methods as the nonlinear solver, a recapitulation of the discretisation and schemes used in this work is given here. From a physical viewpoint, it is assumed that both fluid phases are separated by an interface of negligible thickness. The molecular imbalance of cohesive forces between both fluids is modelled as a surface tension force, acting on the interface. The numerical representation of the phases and the interface can be either Lagrangian or Eulerian. Current nonlinear solvers usually use the level set

[39]: Sussman et al. (1994), 'A level set approach for computing solutions to incompressible two-phase flow'

[38]: Scardovelli et al. (1999), 'Direct numerical simulation of free-surface and interfacial flow'

method [39], the Volume-Of-Fluid method (VOF) (e.g. [38]) or methods derived thereof, all of which use an Eulerian representation, resulting in a non-conformal interface representation of finite thickness. The incompressible continuity and momentum equations, including variable density and surface tension, are given in unified form as

$$\partial_t \rho + \mathbf{u} \cdot \nabla \rho = 0, \quad (3.1a)$$

$$\rho(\partial_t \mathbf{u} + \mathbf{u} \cdot \nabla \mathbf{u}) = -\nabla p + \nabla \cdot (\mu D) + \sigma \kappa \mathbf{n} \delta(\mathbf{x} - \mathbf{x}_s) \quad (3.1b)$$

with  $\mathbf{u} = (u, v, w)^T$  the velocity vector,  $\rho$  the density,  $\mu$  the dynamic viscosity,  $p$  the pressure and  $\mathbf{x}_s$  being the position of the interface. The deformation tensor is  $D = \nabla \mathbf{u} + \nabla^T \mathbf{u}$ . Density and viscosity differ between the phases but are constant within each phase. The rightmost term in equation (3.1b) represents the surface tension force along the interface, and is composed of the surface tension coefficient  $\sigma$ , the local interface curvature  $\kappa$ , the unit normal vector of the interface  $\mathbf{n}$  and  $\delta$ , the Dirac  $\delta$ -function that is non-zero on the interface. Using a Heaviside function  $H(\mathbf{x} - \mathbf{x}_s)$ , that is 1 in phase 1 and 0 in phase 2,  $\rho$  and  $\mu$  can be expressed as

$$\rho = \rho_2 + H(\rho_1 - \rho_2), \quad (3.2a)$$

$$\mu = \mu_2 + H(\mu_1 - \mu_2). \quad (3.2b)$$

### 3.2.2 Interface representations

Numerically,  $H$  and  $\delta$  are approximated as  $H_\epsilon$  and  $\delta_\epsilon$  where  $\epsilon$  is a characteristic length scale related to the local grid size  $\Delta$ . The method of computing the surface tension term is closely related to the immersed boundary method, introduced by [97] where we find a volumetric representation of the surface force as

$$\sigma \kappa \mathbf{n} \delta(\mathbf{x} - \mathbf{x}_s) = \sigma \kappa \nabla H_\epsilon(\mathbf{x} - \mathbf{x}_s). \quad (3.3)$$

While several numerical representation of  $H_\epsilon$  are possible, we will focus on two variants of the continuum surface force method (CSF) [41]. In the CSF method, combined with the Volume of Fluid method we set

$$H_\epsilon(\mathbf{x} - \mathbf{x}_s) = c(\mathbf{x}) = \begin{cases} 0, & \text{for } \mathbf{x} \text{ in the phase 1,} \\ 1, & \text{for } \mathbf{x} \text{ in the phase 2,} \\ 0.5, & \text{for } \mathbf{x} \text{ at the interface,} \end{cases} \quad (3.4)$$

where  $c$  is the volume fraction field and  $\epsilon = \Delta$ , the grid size. We then find  $\mathbf{n} \delta = \nabla c$ . Similarly, when combining the CSF method with a level set method, we can find a smooth approximation

[97]: Peskin (1972), 'Flow patterns around heart valves: a numerical method'

[41]: Brackbill et al. (1992), 'A continuum method for modeling surface tension'

$$H_\epsilon(\mathbf{x} - \mathbf{x}_s) = H_\epsilon(\phi(\mathbf{x})) = \begin{cases} 0, & \text{if } \phi < -\epsilon, \\ 1, & \text{if } \phi > \epsilon, \\ \frac{1+\phi/\epsilon+\sin(\pi\phi/\epsilon)/\pi}{2}, & \text{otherwise.} \end{cases} \quad (3.5)$$

where  $\phi$  is usually chosen as a signed distance function with respect to the interface:

$$\phi(\mathbf{x}) = \begin{cases} \phi > 0, & \text{for } \mathbf{x} \text{ in the phase 1,} \\ \phi < 0, & \text{for } \mathbf{x} \text{ in the phase 2,} \\ \phi = 0, & \text{for } \mathbf{x} \text{ at the interface.} \end{cases} \quad (3.6)$$

Here, we find  $\mathbf{n}\delta = \nabla\phi/|\nabla\phi|\delta_\epsilon$  where the smooth Delta function can be obtained as  $\delta_\epsilon = dH_\epsilon(\phi)/d\phi$ . Both methods usually lead to a characteristic interface thickness of  $O(\Delta)$  [98]. Since  $\rho$  is directly coupled to  $c$  or  $\phi$ , respectively, equation (3.1a) is equivalent to the advection of  $c$  or  $\phi$ :

[98]: Popinet (2018), ‘Numerical models of surface tension’

$$\partial_t c + \nabla \cdot (\mathbf{c}\mathbf{u}) = 0 \quad (3.7a)$$

$$\partial_t \phi + \nabla \cdot (\phi\mathbf{u}) = 0. \quad (3.7b)$$

In BASILISK, the CSF method in combination with a VOF interface representation is used. However, for reasons described in §3.3.3, we will adopt aspects of the level set method for the derivation and solution of the linearised code.

The discretisation of (3.3) warrants special attention as *well-balanced* schemes have to be used which are able to recover equilibrium solutions of certain continuous problems, thus avoiding the problem of so-called parasitic currents [66]. An extensive discussion of this matter is given in [98]. An essential requirement is that the same discrete operators are used for the gradients of the pressure  $p$  and the Heaviside function  $H_\epsilon$ . The computation of the normals and curvature depends on the method used for the interface representation. Since for the level set method,  $\phi$  is a continuous function, the curvature is easily computed as

[66]: Harvie et al. (2006), ‘An analysis of parasitic current generation in volume of fluid simulations’

$$\mathbf{n} = \frac{\nabla\phi}{|\nabla\phi|}, \quad (3.8a)$$

$$\kappa = \nabla \cdot \mathbf{n}. \quad (3.8b)$$

However, for the VOF-CSF method, direct derivation of  $c$  leads to problematic curvature estimates because of its discontinuity. Therefore BASILISK, uses a height-function method that gives second-order accurate curvature estimates [68].

[68]: Cummins et al. (2005), ‘Estimating curvature from volume fractions’

For illustration, in two dimensions a close-to-horizontal interface can be described by  $y = h_y(x)$ , where  $h_y$  is the vertical distance to the interface at a given  $x$ . The normals and curvature of this interface are then computed as

$$\mathbf{n} = \frac{(h'_y, 1)}{(1 + h_y^2)^{1/2}} \quad (3.9a)$$

$$\kappa = \frac{h''_y}{(1 + h_y'^2)^{3/2}}. \quad (3.9b)$$

[26]: Popinet (2009), ‘An accurate adaptive solver for surface-tension-driven interfacial flows’

For an interface  $x = h_x(y)$  the procedure is similar. An extension to three dimensions is straight forward and described in [26].

### 3.2.3 Discretisation in Basilisk

[25]: Popinet (2003), ‘Gerris: a tree-based adaptive solver for the incompressible Euler equations in complex geometries’

The equation system (3.1) is discretised on regular Cartesian grids using a staggered-in-time discretisation, which is second-order accurate, yielding the following velocity and volume fraction update at every time step [25],[26].

$$\mathbf{u}^{n+1} = \mathbf{u}^n + \Delta t \left( -\mathbf{u}^{n+1/2} \cdot \nabla \mathbf{u}^{n+1/2} - \nabla p^{n+1} / \rho_{n+1/2} + \nabla \cdot [2(\mu/\rho)_{n+1/2}(D_n + D_{n+1})] + [\sigma/\rho\kappa\nabla c]_{n+1/2} \right), \quad (3.10a)$$

$$c^{n+1/2} = c^{n-1/2} - \Delta t \nabla \cdot (c^n \mathbf{u}^n). \quad (3.10b)$$

[99]: Chorin (1969), ‘On the convergence of discrete approximations to the Navier-Stokes equations’

[100]: Bell et al. (1989), ‘A second-order projection method for the incompressible Navier-Stokes equations’

Pressure and velocity are decoupled using a standard time-splitting projection scheme [99]. The advection term is computed using the Bell-Colella-Glaz (BCG) second-order unsplit upwind scheme [100], as will be described in §3.3.2. A geometric VOF method is used to advect the volume fraction in equation (3.7a). The advection of a level set function  $\phi$  is equivalent to the advection of a passive scalar which is advected using

$$\phi^{n+1/2} = \phi^{n-1/2} - \Delta t \nabla \cdot (\phi^n \mathbf{u}^n). \quad (3.11)$$

## 3.3 Linearisation procedure

### 3.3.1 Derivation of the linearised equations

In order to obtain the linearised equations, we first non-dimensionalise the nonlinear equations (3.1b) with respect to  $\rho_1$ ,  $\mu_1$  and a suitable reference length and velocity scale, thus obtaining

$$[\tilde{\rho} + H_\epsilon(\phi)(1 - \tilde{\rho})](\partial_t \mathbf{u} + \mathbf{u} \cdot \nabla \mathbf{u}) = -\nabla p + \frac{1}{Re} \nabla \cdot [(\tilde{\mu} + H_\epsilon(\phi)(1 - \tilde{\mu}))(\nabla \mathbf{u} + \nabla^T \mathbf{u})] + \frac{1}{We} \kappa \mathbf{n} \delta_\epsilon(\phi), \quad (3.12a)$$

where we have used the level set methodology to account for the two phases. The Reynolds number is  $Re = \rho_1 U_{\text{ref}} D_{\text{ref}} / \mu_1$ , the Weber number is  $We = \rho_1 U_{\text{ref}}^2 D_{\text{ref}} / \sigma$ ,  $\bar{\rho} = \rho_2 / \rho_1$  and  $\bar{\mu} = \mu_2 / \mu_1$ . Note that, from equation (3.12) onward, all quantities are assumed to be dimensionless.

Starting point for the assessment of linear stability is the decomposition of the flow into a basic state and an infinitesimal perturbation,  $\mathbf{u} = \mathbf{U} + \zeta \mathbf{u}'$  and  $p = P + \zeta p'$  for the velocity and pressure respectively, with  $\zeta \ll 1$ . A similar linearisation is done for the level set function  $\phi = \Phi + \zeta \phi'$ . Therewith associated are a perturbed curvature  $\kappa = K + \zeta \kappa'$  and a normal vector  $\mathbf{n} = \mathbf{N} + \zeta \mathbf{n}'$ . We also make use of the base flow volume fraction  $C$  but, as will be described in §3.3.3, the use of a perturbation volume fraction poses several challenges and is thus avoided.

We insert the respective decompositions into equations (3.12, 3.7b) and retain only leading-order terms in  $\zeta$ . Dropping  $\zeta$  for convenience, we arrive at

$$\begin{aligned} & [\bar{\rho} + H_\epsilon(\Phi)(1 - \bar{\rho})](\partial_t \mathbf{u}' + \mathbf{u}' \cdot \nabla \mathbf{U} + \mathbf{U} \cdot \nabla \mathbf{u}') + 2[\delta_\epsilon(\Phi)\phi'(1 - \bar{\rho})](\mathbf{U} \cdot \nabla \mathbf{U}) \\ &= -\nabla p' + \frac{1}{Re} \nabla \cdot [(\bar{\mu} + H_\epsilon(\Phi)(1 - \bar{\mu}))(\nabla \mathbf{u}' + \nabla^T \mathbf{u}')] \\ &+ \frac{1}{Re} \nabla \cdot [(\delta_\epsilon(\Phi)\phi'(1 - \bar{\mu}))(\nabla \mathbf{U} + \nabla^T \mathbf{U})] + \mathbf{F}_s(\Phi, \phi'), \end{aligned} \quad (3.13a)$$

$$\partial_t \phi' + \nabla \cdot (\Phi \mathbf{u}') + \nabla \cdot (\phi' \mathbf{U}) = 0, \quad (3.13b)$$

where we have used the fact that  $\delta_\epsilon(\Phi)$  is obtained as the distributional derivative of  $H_\epsilon(\Phi)$ , during linearisation of terms involving  $H_\epsilon(\phi)$ . We further note that, as described in §3.2.2,  $H_\epsilon(\Phi)$  can be replaced by  $C$ . Thereby, we retain an interface thickness of  $O(\Delta)$ . Due to the involvement of two immiscible phases, the linearised equations contain a number of additional terms, compared to the linearised incompressible equations of a single fluid phase: The transport of the perturbation velocity by the base flow velocity and vice versa is scaled by the base flow density field. Additionally, a new advective term, composed only of the base flow velocity, appears that is acted upon by the perturbation density field. When comparing to a usual multi-domain approach of Navier-Stokes or Orr-Sommerfeld equations, where the interface height appears as a variable, this term corresponds to multiplication of the same base flow terms with a perturbation of the interface height. Similarly, a scaling of the perturbation velocity diffusion by the base flow viscosity field is introduced and a new term, representing the action of the perturbation viscosity field on the base flow velocity diffusion, appears.

The linearised surface tension force is given as

$$\mathbf{F}_s(\Phi, \phi') = \frac{1}{We} [\kappa' \mathbf{N} \delta_\epsilon(\Phi) + K \mathbf{n}' \delta_\epsilon(\Phi) + K \mathbf{N} \phi' \partial_\Phi \delta_\epsilon(\Phi)], \quad (3.14)$$

where  $\partial_\Phi$  in the rightmost term denotes the functional derivative with respect to  $\Phi$ , and  $f(\partial_\Phi \delta_\epsilon(\Phi)) = (\partial_\Phi f) \delta_\epsilon(\Phi)$  for some test function  $f$ . As long as  $\Phi$  has signed distance, we can make use of the fact that, at the

interface, any change of  $\Phi$  is along the normal  $\mathbf{N}$ , such that  $\partial_{\mathbf{N}}\Phi = 1$ . Hence, we have

$$\partial_{\Phi}(K\mathbf{N}\phi')\delta_{\epsilon}(\Phi) = \partial_{\mathbf{N}}(K\mathbf{N}\phi')(\partial_{\Phi}\mathbf{N})\delta_{\epsilon}(\Phi) = \partial_{\mathbf{N}}(K\mathbf{N}\phi')\delta_{\epsilon}(\Phi). \quad (3.15)$$

Consequently, we can write

$$K\mathbf{N}\phi'\partial_{\Phi}\delta_{\epsilon}(\Phi) = \mathbf{N} \cdot \nabla(K\mathbf{N}\phi')\delta_{\epsilon}(\Phi). \quad (3.16)$$

The three terms representing the linearised surface tension force account for the action of the perturbation curvature on the basic state normal at the unperturbed interface and vice versa, as well as the action of the perturbed interface on the basic state curvature and normal. Similar terms can be identified in the linearised multi-domain formulation, there multiplied with the perturbation of the interface height [24].

[24]: Tammissola et al. (2012), ‘Surface tension-induced global instability of planar jets and wakes’

### 3.3.2 Implementation of linearised advection and diffusion terms

The computation of the linearised advection terms is facilitated using a slightly modified version of the numerical scheme that is used for the nonlinear advection in BASILISK. Here, we give a general overview of the scheme and necessary modifications. For the calculation of the nonlinear advection term  $\mathbf{u}^{n+1/2} \cdot \nabla \mathbf{u}^{n+1/2}$  in equation (3.10a), a prediction of the velocity on the cell faces  $\mathbf{u}_f^{n+1/2}$  is computed with a variant of the BCG scheme [100], using the pressure gradient and body forces at  $t = n$ . Solenoidality of the predicted velocity is enforced in a projection step. The advection step itself is performed by an isolated function which takes, two arguments, a scalar field, in this case the cell centred velocity field  $\mathbf{u}^n$ , as well as  $\mathbf{u}_f^{n+1/2}$ , to compute the advection fluxes of  $\mathbf{u}$ .

[100]: Bell et al. (1989), ‘A second-order projection method for the incompressible Navier–Stokes equations’

For the linearised advection step, a prediction of the basic state velocity is not needed, since it is either stationary or known at all time steps (in case of a time-periodic base flow). Thus, the two linear advection terms can be computed by calling the advection routine twice, using  $\mathbf{u}'^n$  and  $\mathbf{U}_f^{n+1}$ , or  $\mathbf{U}^{n+1}$  and  $\mathbf{u}_f^{n+1/2}$ . A small technicality is involved when advecting  $\mathbf{U}^{n+1}$ . The advection routine is implemented so that it by default adds the action of the advection to the tracer fields that are advected, i.e.  $\mathbf{U}^{n+1}$ . However, for both advection terms, the action needs to be added to  $\mathbf{u}'^n$ . To ensure this, minor modifications of the routine are necessary.

The second advection term, stemming from the density variation between the fluids, is computed again using the same BCG scheme. The diffusion term is added explicitly, as it only contains the basic state velocity.

### 3.3.3 Implementation of linearised interface advection

An adaptation of BASILISK’s geometric VOF scheme for linear perturbation analysis is not straightforward. A naive linearisation of the volume fraction transport equation and the associated interface fluxes, as well as

the geometric interface reconstructions would retain the scheme's inherent property of computing finite amplitude waves. The reason is rooted in the way the interface location is defined in VOF methods. As seen from equation (3.4), a cell where  $0 < c < 1$  contains an interface segment. As soon as this cell becomes either full ( $c = 1$ ) or empty ( $c = 0$ ), the interface segment moves to one of the neighbouring cells. Thus, without further modifications of the schemes, a growing disturbance  $c'$  in a cell would eventually lead to  $c' = 1$  and the disturbed interface would move to an adjacent cell, producing a finite movement of the perturbed interface with respect to the basic state interface and makes a evaluation of the interface displacement difficult. As the level set function  $\phi$  is not bounded between  $0 < \phi < 1$ , a disturbance  $\phi'$  can grow to any value. Its interpretation is therefore more straight forward: the value of a disturbance  $\phi'$  along the basic state interface is a measure for its displacement.

Another aspect that complicates the use of a linearised VOF method is the height-function-based curvature computation in BASILISK. Depending on the orientation of the interface, case distinctions are needed, regarding the choice of the component of the height functions for computing the curvature (i.e. horizontal or vertical heights in a 2D problem). The introduction of perturbed height functions, to calculate the curvature of the perturbed interface, would add further case distinctions and complexity. By using a level set representation of the interface, as introduced above, these problems are avoided.

Since the VOF method is used for the computation of the base flow volume fraction  $C$ , an accurate reconstruction of the basic state level set field  $\Phi$  from  $C$  is needed. In general, one would need to compute the interface segments in each interfacial cell, where  $0 < C < 1$ , in order to compute the distance to the interface in each cell throughout the domain. However, in the present study the basic state interface is close to horizontal, and thus is consistently described by the height function field  $h_y(x)$ , used to compute the basic state curvature (see §3.2.2). Therefore, we can use  $\Phi_s = h_y(x)$  as an initial, shifted level set function, which is re-distanced by solving a Hamilton-Jacobi-type equation

$$\begin{cases} \frac{\partial \Phi}{\partial t^+} = \text{sgn}(\Phi_s)(1 - |\nabla \Phi|) \\ \Phi(\mathbf{x}, t^+ = 0) = \Phi_s \end{cases} . \quad (3.17)$$

The shifted level set is integrated in a pseudo time  $t^+$  until a steady state is reached. The resulting level set  $\Phi$  is a signed distance function, such that  $|\nabla \Phi| = 1$ . Note that, for the nonlinear case,  $\phi$  loses its signed distance properties during advection. Thus, it needs to be re-distanced every few time steps. In principle, this carries over to  $\phi'$  in the linear computations. Thus a linearised re-distancing function

$$\begin{cases} \frac{\partial \phi'}{\partial t^+} = -\Phi \left( \frac{\partial \phi'}{\partial x} \frac{\partial \Phi}{\partial x} + \frac{\partial \phi'}{\partial y} \frac{\partial \Phi}{\partial y} \right) \\ \phi'(\mathbf{x}, t^+ = 0) = \phi'_s \end{cases} \quad (3.18)$$

can be used to re-distance  $\phi'_s$ . The resulting  $\phi'$  has zero gradient in the base flow surface-normal direction. Since the perturbed level set field

corresponds to a displacement of the basic state level set contours, after re-distancing, all level set contours are displaced equally. However, we have found that re-distancing has no discernible influence on the results of the present linear computations. In the nonlinear case, there are several reasons for re-distancing  $\phi$ . One aspect is that the delta function, defining the interface, is calculated from  $\phi$ . Consequently, as  $\phi$  loses its signed distance properties, the computation of the interface location becomes inaccurate. Here, the linearised level set is only used to compute the perturbed normal vector and curvature, since the base flow interface is known *a priori*. Both computations were not affected by the re-distancing in our tests. Another reason is the possible degeneration of numerical gradients if  $\phi$  deviates significantly from a signed distance function. Again, we have not found this to be a source of error in our computations.

### 3.3.4 Implementation of the linearised surface tension force

For computing the linearised surface tension force, we utilise the volume fraction  $C$  of the basic state interface as well as the level set functions  $\Phi$  and  $\phi'$ . In 2D, the normal vectors are computed using the level sets as

$$\mathbf{N} = \frac{\nabla\Phi}{|\nabla\Phi|} = \frac{\left(\frac{\partial\Phi}{\partial x}, \frac{\partial\Phi}{\partial y}\right)}{\sqrt{\left(\frac{\partial\Phi}{\partial x}\right)^2 + \left(\frac{\partial\Phi}{\partial y}\right)^2}}, \quad (3.19a)$$

$$\zeta\mathbf{n}' = \frac{\left(\frac{\partial\zeta\phi'}{\partial x}, \frac{\partial\zeta\phi'}{\partial y}\right)}{\sqrt{\left(\frac{\partial\phi'}{\partial x}\right)^2 + \left(\frac{\partial\phi'}{\partial y}\right)^2}} - \left(\frac{\partial\Phi}{\partial x}, \frac{\partial\Phi}{\partial y}\right) \frac{\left(\frac{\partial\zeta\phi'}{\partial x} \frac{\partial\Phi}{\partial x} + \frac{\partial\zeta\phi'}{\partial y} \frac{\partial\Phi}{\partial y}\right)}{\left[\left(\frac{\partial\Phi}{\partial x}\right)^2 + \left(\frac{\partial\Phi}{\partial y}\right)^2\right]^{3/2}}. \quad (3.19b)$$

Note that, although  $|\nabla\Phi| = 1$ , we include the corresponding terms in the computation of the normal vectors, as this leads to smoother numerical approximations. A detailed derivation of  $\mathbf{n}'$  is given in appendix 3.7.1.

The basic state curvature  $K$  is computed similarly to  $\kappa$  in the nonlinear case using height functions as described in §3.2.2. The curvature of the perturbed interface is computed from  $\Phi$  and  $\phi'$  as

$$\kappa' = \nabla \cdot (\zeta\mathbf{n}'). \quad (3.20)$$

The full expansion of  $\kappa'$  is given in appendix 3.7.1. Further, we make use of the fact that

$$\mathbf{N}\delta(\Phi) = \nabla C \quad \text{and} \quad \delta(\Phi) = |\nabla C|, \quad (3.21)$$

to compute terms which involve either  $\mathbf{N}\delta(\Phi)$  or  $\delta(\Phi)$ . Consistently with the replacement of  $H_\varepsilon(\Phi)$  by  $C$  in §3.3.1, this choice as well retains an interface thickness of  $O(\Delta)$ .

## 3.4 Formulation and solution of the eigenvalue problem

### 3.4.1 Eigenvalue Problem

The linear system (3.13) is rewritten in compact form as

$$\frac{\partial \mathbf{q}'}{\partial t} = L(\mathbf{Q})\mathbf{q}', \quad (3.22)$$

where  $\mathbf{q}' = (\mathbf{u}', \phi')^T$ , and  $L(\mathbf{Q})$  is the linearised Navier-Stokes operator, which might be stationary or instationary, depending on the base flow  $\mathbf{Q} = (\mathbf{U}, \Phi)^T$ . For the former case, we then seek eigenmodes of  $L$  of the form

$$\mathbf{q}'(x, y, z, t) = \exp(\lambda_j t) \hat{\mathbf{q}}_j(x, y, z), \quad (3.23)$$

where both  $\lambda_j$  and  $\hat{\mathbf{q}}_j$  are generally complex-valued. The corresponding eigenvalue problem may be written as

$$L\hat{\mathbf{q}}_j = \lambda_j \hat{\mathbf{q}}_j. \quad (3.24)$$

This eigenvalue problem could in principle be solved directly, to give all eigenvalues, or via various time-stepping techniques, which would yield one or several of the dominant eigenvalues of the system, i.e. those of largest magnitude. However, the eigenvalues determining the stability of the system are the leading eigenvalues, which have the largest real part, that in turn might be close to zero near a bifurcation point. Following [46], the dominant eigenvalue can be extracted with the *exponential power method*.

[46]: Tuckerman et al. (2000), 'Bifurcation analysis for timesteppers'

The general solution to (3.22) is

$$\mathbf{q}'(t + \tau) = \mathbf{A}\mathbf{q}'(t) = \exp(L\tau)\mathbf{q}'(t), \quad (3.25)$$

where the dominant eigenvalues of  $\mathbf{A}$  are the leading eigenvalues of  $L$ . Thus, we obtain an alternative eigenvalue problem

$$\mathbf{A}\hat{\mathbf{q}}_j = \mu_j \hat{\mathbf{q}}_j, \quad \mu_j = \exp(\lambda_j \tau). \quad (3.26)$$

For a stationary base flow, the frequency of an eigenmode is given by the imaginary part of the eigenvalue  $\text{Im}(\lambda_j)$  whereas its growth rate is given by the real part  $\text{Re}(\lambda_j)$ . Consequently, the system is linearly unstable when any  $\text{Re}(\lambda_j)$  is positive. Since for a stationary  $\mathbf{Q}$ , the stability is determined by the long-time behaviour of a perturbation,  $\tau$  is an arbitrary value, which however should allow for a reasonable evolution of the perturbation [47].

[47]: Barkley et al. (2008), 'Direct optimal growth analysis for timesteppers'

### 3.4.2 Iterative Solution

[48]: Saad (2011), *Numerical Methods for Large Eigenvalue Problems: Revised Edition*

Besides the *power method* which is able to recover the single most dominant eigenvalue, the *Arnoldi method* [48] is a suitable choice to recover a number of dominant eigenvalues.

The method utilises a standard orthogonal projection of  $\mathbf{A}$  onto a lower dimensional Krylov subspace that allows for an approximate direct evaluation of  $\mathbf{A}$ . To this end, we construct a sequence

$$\mathbf{K}_n(\mathbf{A}, \mathbf{q}_0) = [\mathbf{q}_0, \mathbf{A}\mathbf{q}_0, \dots, \mathbf{A}^{n-1}\mathbf{q}_0] \quad (3.27)$$

which spans the Krylov subspace on which  $\mathbf{A}$  is projected. In practice, a direct construction of  $\mathbf{A}$  is not needed in order to build  $\mathbf{K}_n$ . We only need to be able to compute the repeated action of  $\mathbf{A}$  on  $\mathbf{q}_0$  which is precisely described by equation (3.25). The Krylov sequence can thus be updated by repeated time-stepping of the linearised solver. The methodology to construct  $\mathbf{K}_n$  and to compute the corresponding eigenpairs is that of the standard Arnoldi method with a modified Gram-Schmidt orthogonalisation. Following [47], the part of the initial vector  $\mathbf{q}_0$  concerning the velocities is prescribed as random fluctuations and solenoidality is enforced through the linearised solver. We do not impose any initial fluctuations on the level set field, instead we let the perturbation velocity generate those fluctuations consistently through equation (3.13b).

[47]: Barkley et al. (2008), 'Direct optimal growth analysis for timesteppers'

## 3.5 Global modes of a planar wake under the influence of surface tension

[24]: Tammissola et al. (2012), 'Surface tension-induced global instability of planar jets and wakes'

To validate the derived framework, we revisit the work of [24]. As noted above, this is one of very few works which study linear global modes of interfacial flows without further simplifications of the linearised equations, contrary to what has been done for instance in [101]. There, gravitational jets are studied based on a 1-D long-wave model, derived by [102].

[101]: Rubio-Rubio et al. (2013), 'On the thinnest steady threads obtained by gravitational stretching of capillary jets'

[102]: Eggers et al. (1994), 'Drop formation in a one-dimensional approximation of the Navier-Stokes equation'

The flows studied in [24] are planar, coflowing shear flows which resemble jets and wakes, depending on the velocity ratio between inner and outer flow. All configurations are confined flows, and for all but one flow condition, the flows are reported to be globally stable in the absence of surface tension. Only in the presence of rather strong surface tension, a regime of global instability occurs.

### 3.5.1 Nonlinear simulation

In the study of [24] no numerical or experimental validation of the studied configurations is performed. Therefore, it remains to be shown whether the computed linear modes really are present in the nonlinear flow, and if so, whether their shapes and frequencies are accurately predicted by linear theory. We therefore present nonlinear results for selected configurations of their study, with a focus on wake-type flows.

All flows are computed in a long channel with a half-channel height  $h_1 + h_2 = 2$  where  $h_1 = h_2 = 1$  are the heights of the respective fluid streams in the half-channel at the inlet, and subscripts 1,2 refer to the inner and outer fluid stream, respectively. The resulting confinement ratio is  $h = h_2/h_1 = 1$ . The plug flow velocity ratio of both streams at the inlet is  $\Lambda^{-1} = (U_1 + U_2)/(U_1 - U_2) = -1.4$ . The density and viscosity ratios are  $\rho_2/\rho_1 = 1$  and  $\mu_2/\mu_1 = 1$ . The configuration and flow field at subcritical conditions are shown in figure 3.1. Upon nondimensionalisation of the linearised equations, using  $U_2$  and  $h_2$ , the Reynolds number  $Re$  and the Weber number  $We$  are given as

$$Re = \frac{\rho_2 U_2 h_2}{\mu_2}, \quad We = \frac{\rho_2 U_2^2 h_2}{\sigma}. \quad (3.28)$$

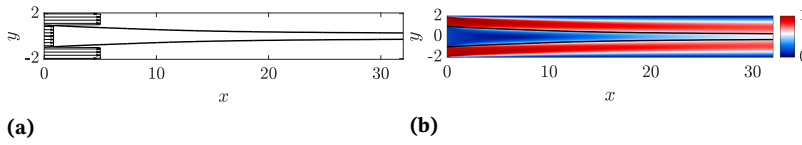


**Figure 3.1:** (a) Velocity profile at the inlet and interface separating the fluid phases at subcritical conditions ( $We = \infty$ ). (b) Velocity field  $u$  and interface at the same conditions.

We fix  $Re = 316$  and vary  $We$  to track the behaviour of the computed instabilities.

For the simulations, we use a uniformly spaced grid of  $N_x \times N_y = 1024 \times 128$  mesh points, corresponding to 10 levels of refinement in stream wise direction and spanning a nondimensional area of  $L_x \times L_y = 32 \times 4$ .

The domain is initialised with  $\mathbf{u} = 0$  and  $c = 0$ . At the left domain boundary  $\Omega_1$  an inlet velocity is imposed such that

$$u|_{\Omega_1} = \begin{cases} 1, & \text{if } |y| > 1 \\ \frac{1+\Lambda}{1-\Lambda}, & \text{if } |y| \leq 1 \end{cases}, \quad (3.29a)$$

$$\frac{\partial p}{\partial x}|_{\Omega_1} = 0, \quad (3.29b)$$

$$c|_{\Omega_1} = \begin{cases} 0, & \text{if } |y| > 1 \\ 1, & \text{if } |y| \leq 1 \end{cases}. \quad (3.29c)$$

For the right boundary  $\Omega_2$ , a standard outflow condition

$$\frac{\partial u}{\partial x}|_{\Omega_2} = 0, \quad (3.30a)$$

$$p|_{\Omega_2} = 0, \quad (3.30b)$$

$$\frac{\partial c}{\partial x}|_{\Omega_2} = 0 \quad (3.30c)$$

is used. The top and bottom boundaries  $\Omega_3$  are equipped with no-slip conditions. Time stepping is adaptive, based on a Courant condition

$$\Delta t \leq 0.5 \min \left\{ \frac{\Delta}{u}, \sqrt{\frac{\rho_1 \Delta^3}{\pi \sigma}} \right\} \quad (3.31)$$

[103]: Rowley et al. (2009), ‘Spectral analysis of nonlinear flows’

[104]: Schmid (2010), ‘Dynamic mode decomposition of numerical and experimental data’

[105]: Chen et al. (2012), ‘Variants of dynamic mode decomposition: boundary condition, Koopman, and Fourier analyses’

[24]: Tammisola et al. (2012), ‘Surface tension-induced global instability of planar jets and wakes’

where  $\Delta$  denotes the grid spacing. The second term inside the braces accounts for the propagation of capillary waves along the interface. Note that, especially for high surface tensions and small cell sizes, this term is significantly more restrictive than the first term. We monitor the energy of the system via the Euclidean norm  $\|\mathbf{u}^2\|_2$  to check whether a steady state or a stable limit cycle has been reached. In the latter case a Dynamic Mode Decomposition (DMD) is used for a modal decomposition of the flow field [103, 104]. The DMD yields an approximation of the Koopman operator, a linear infinite dimensional operator describing a nonlinear dynamical system. As a consequence, the frequencies associated with the DMD modes correspond to the modal frequencies of the dynamical system. Further, with the mean flow subtracted, the DMD modes are equivalent to modes of a Discrete Fourier Transformation (DFT), but they usually require a lot less samples [105]. A sequence composed of 2000 consecutive snapshots  $\mathbf{u}$  and  $c$  every  $\Delta t = 0.5$  for  $t > 1000$  is used for computation of the Ritz values  $\lambda_j$ . The dependence of the dominant DMD mode on the grid resolution is given exemplarily in table 3.2 for  $We = 12.5$

Following [24], we compute the nonlinear flow for a variety of Weber numbers ranging from  $We = 3.\bar{3}$  to  $We = 16.\bar{6}$ . In figure 3.2, the spectra obtained from the DMD and the corresponding mode shapes with the largest amplitude that dominate the flow are displayed for several investigated  $We$  where an unsteady solution is found. The interface amplitude is overlaid on the modes. These are the same Weber numbers that are presented in [24].

For Weber numbers larger than  $We \approx 16$ , all disturbances decay, and the flow settles to a steady solution. For  $We = 12.5$ , a periodic solution is seen that gives rise to a sinuous mode with its amplitude maximum located around  $x = 8$ . For increasing surface tension, at  $We = 10$ , three sinuous modes are observed. One mode is the same as seen for  $We = 12.5$ , which has moved slightly upstream (amplitude maximum  $x = 7.5$ ) and has a lower frequency and amplitude. The second and third mode show a short-wave structure in the vicinity of the inlet, with the amplitude maximum located at around  $x = 1.9$ , and a long-wave structure located further downstream with an amplitude maximum around  $x = 13$ . These modes have a higher (almost similar) frequency and a generally larger amplitude than the first mode. Further, both of these modes display opposite slight asymmetries in the amplitude in the short wave structure in the vicinity of the inlet. Note, that in figure 3.2b only one of these modes is shown. For  $We = 6.\bar{6}$  three modes are found. The most energetic mode has a varicose structure with an amplitude maximum located at around  $x = 4$ . The other modes are the sinuous modes, observed for  $We = 12.5$  and  $We = 10$ , with their amplitude maximum shifted far upstream. At  $We = 5$  a single varicose mode with its amplitude maximum close to the inlet at around  $x = 2.6$  is found. For even higher surface tension the flow becomes globally stable again, so that for  $We = 3.\bar{3}$  a steady solution is obtained.

To give a broader overview over the complexity of the dynamics in the flow and see in which Weber number regime the dominant modes are unstable, their frequencies are plotted versus the respective Weber numbers in figure 3.3a. Additionally, in figure 3.3b a bifurcation diagram is shown by plotting the local minima and maxima of the transversal velocity  $v$  at  $(x, y) = (5, 0)$ , within the time period after the saturation. From the above presentation

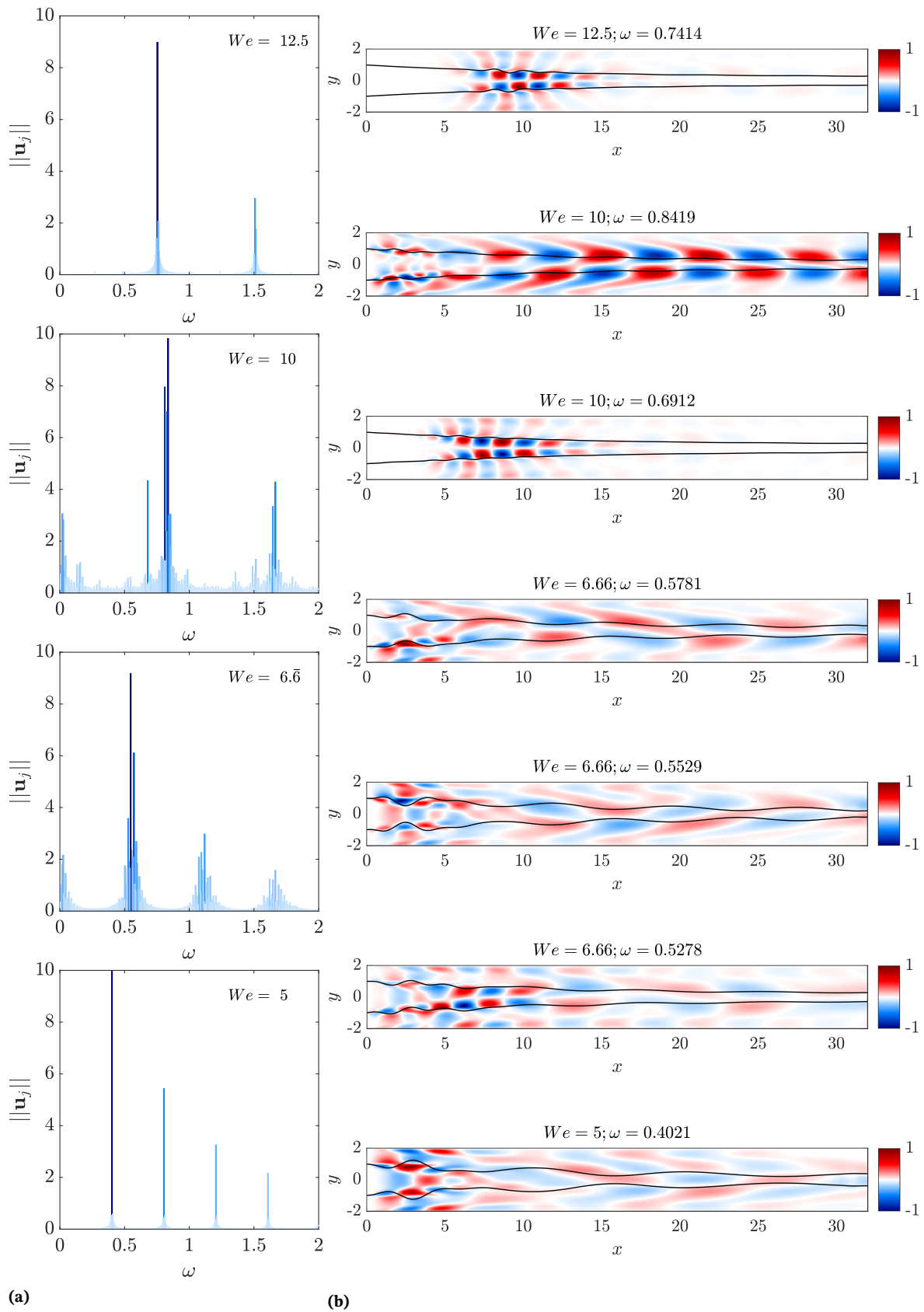


**Figure 3.2:** (a) Magnitude of the DMD modes at each frequency, extracted from the nonlinear simulation. (b) Shapes of the dominant modes at the respective Weber numbers.

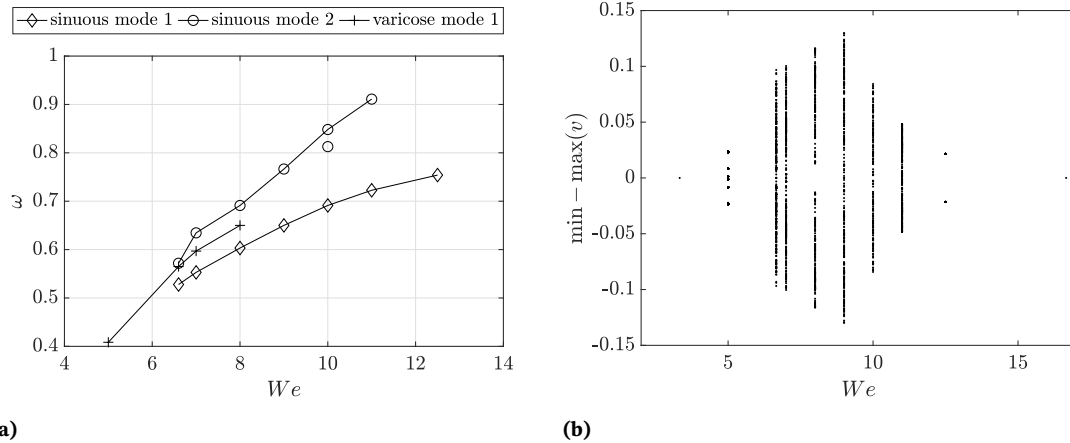


**Figure 3.3:** (a) Dominant frequencies of the appearing modes extracted from the DMD in the flow for all investigated Weber numbers. (b) Bifurcations illustrated by the min-max values of  $v$  at  $(x, y) = (5, 0)$

it is seen that, under the influence of surface tension, the flow undergoes a series of bifurcations that gives rise to an increasingly complex modal interplay that governs the flow dynamics. Starting from a stable fixed point solution, a first Hopf bifurcation occurs between  $We = 16.\bar{6}$  and  $We = 12.5$  where the flow reaches a stable limit cycle, governed by a periodic oscillation produced by sinuous mode 1. In figure 3.3b, this is characterised by a distinct minimum and maximum of  $v$ . A second mode, sinuous mode 2 bifurcates between  $We = 12$  and  $We = 11$ . Both sinuous modes have incommensurate frequencies, resulting in a quasiperiodic motion and thus the limit cycle loses its stability to a torus. As noted above, a separate mode very similar to sinuous mode 2, with a slightly lower frequency is observed at  $We = 10$ . Both modes, sinuous mode 1 and 2, are still active at  $We = 6.\bar{6}$  and vanish between  $We = 6.\bar{6}$  and  $We = 5$ . Between  $We = 9$  and  $We = 8$  a third mode with an incommensurate frequency, varicose mode 1, emerges that governs the dynamics until the flow returns to a stable fixed point again between  $We = 5$  and  $We = 3.\bar{3}$ . Additionally, as is seen in 3.2a for  $We = 10$  and  $We = 6.\bar{6}$ , a dense set of frequency peaks around the dominating peaks, as well as some very low frequencies are seen in the spectra. While not shown, this behaviour is also visible in the spectra for other intermediate Weber numbers. Furthermore, for  $We = 12.5$ , a more pronounced influence of the first harmonic mode is seen as compared to the other presented  $We$ . While a thorough investigation of these additional modes and their dynamics is beyond the scope of this work, they are likely the result of nonlinear interactions between the described modes and/or higher harmonics. As a result of the presence of several competing modes for  $11 \leq We \leq 6.\bar{6}$ , in this regime, the flow is attracted towards higher-dimensional states, characterised by quasiperiodic or chaotic oscillations. This is characterised in figure 3.3b by an increasingly dense variety of minima and maxima at the respective Weber numbers. In §3.5.4 we will compare linear and nonlinear dynamics.

### 3.5.2 Base flows

For the validation of the linear solver, we choose the basic state solution obtained for  $We_{\text{base}} = \infty$ , as it bears closest resemblance to the results of

[24] who obtained the base flow by computing a single phase flow without interface and surface tension, exploiting the fact that in the absence of surface tension the flow is globally stable. The interface was introduced *a posteriori* by computing a streamline from  $\mathbf{x} = (0, 1)^T$ . It was argued that, for this particular configuration, the curvature of the unperturbed interface is generally small, except for a small region very close to the inlet ( $x < 0.1$ ), and thus surface-tension induced pressure gradients are probably negligible even for very high surface tension.

We have verified this assumption by computing the steady state solution at  $We_{\text{base}} = \infty$ , where the flow is globally stable, and  $We_{\text{base}} = 12.5$ , where the flow is only unstable for sinuous perturbations and thus can be obtained by imposing symmetry conditions at  $y = 0$ . Additionally, we have computed the interface as a streamline on the single phase base flow. The interface coordinates of the first two base flows are computed by reconstructing the piecewise linear interface segments from the respective volume fractions using the same routines that are used by the VOF advection scheme. The interface is plotted in figure 3.4a and the relative errors, with respect to the single phase flow, where a streamline is computed as interface, are given in table 1. For both,  $We_{\text{base}} = \infty$  and  $We_{\text{base}} = 12.5$ , the error is below 1 %. The remaining error between the streamline interface and the interface for  $We_{\text{base}} = \infty$  is probably rooted in the inaccuracy of the advection scheme as will be addressed in the next paragraph. The relative error of the base flow interface for increasing grid resolutions is shown in table 3.2. As is seen, the relative error between the highest and second highest resolution is again, below 1 %. For the present flow configuration it is therefore justified to use the base flow at  $We_{\text{base}} = \infty$  for the linear computations.

It has to be noted, that despite the marginal differences between the interfaces of the basic states, the convergence of the case  $We_{\text{base}} = 12.5$  is worse than for  $We_{\text{base}} = \infty$  or for the case of the single phase flow. While for the latter two cases an error  $\|\mathbf{u}^{n+1} - \mathbf{u}^n\|_{\infty} = O(10^{-16})$  is reached, for the former it remains above  $O(10^{-6})$ . The reason for this behaviour is probably the occurrence of spurious currents. These are generally not considered an issue for equilibrium solutions of interfacial flows without velocity of the background fluid, when employing well-balanced schemes for computing the surface tension term. However, in the dynamic case where the background fluid has non-zero velocity, the problem persists due to numerical errors of the interface advection. These induce curvature errors which, again, induce errors in the velocity. As demonstrated in [26] for a translating droplet, the induced error in the velocity field is relatively insensitive to increased mesh resolution (its  $L_{\infty}$  norm shows less than first order convergence) and scales approximately with  $We^{-1/2}$ . The implications are readily seen in the curvature plot in figure 3.4b. Since the  $\kappa$  involves the second derivative of the height function of the interface, the numerical errors of the advection scheme produce significant oscillations in the curvature for  $We_{\text{base}} = 12.5$ . These are especially pronounced close to the inlet where the shear of the fluid streams is largest. To a lesser degree, these oscillations are also seen for  $We_{\text{base}} = \infty$ , but since the surface tension force is zero, there is no two-way coupling between the curvature and the velocity. Consequently, the disturbances are weaker and the convergence of the velocity field is not affected.

In preliminary computations we have assessed the effect of using finite

[24]: Tammisola et al. (2012), ‘Surface tension-induced global instability of planar jets and wakes’

[26]: Popinet (2009), ‘An accurate adaptive solver for surface-tension-driven interfacial flows’

**Table 3.1:** Relative error of the basic state interface  $I$ . Errors are measured against the streamline-constructed interface of the single phase flow  $I_s$ . The Weber numbers of the respective two-phase solutions are stated as subscripts.

$\ I_s - I_\infty\ /\ I_s\ $	$\ I_s - I_{12.5}\ /\ I_s\ $
0.0078	0.0086

**Table 3.2:** Convergence of the nonlinear and linear flow for increasing level of refinement. Shown is the relative error of the basic state interface for  $We_{\text{base}} = \infty$ , the convergence of the frequency  $\text{Im}(\lambda)$  of the dominant DMD mode of the nonlinear simulation and of the most unstable eigenvalue  $\lambda$  of the linear analysis for  $We = 12.5$ .

Level	grid points ( $N_x \times N_y$ )	$\ I_{\infty, \text{Level}} - I_{\infty, 10}\ /\ I_{\infty, 10}\ $	$\text{Im}(\lambda)$ (DNS)	$\lambda$ (linear analysis)
8	$256 \times 32 = 8192$	0.0555	0.7392	$0.0039 + 0.7431i$
9	$512 \times 64 = 32768$	0.0068	0.7414	$0.0092 + 0.7416i$
10	$1024 \times 128 = 131072$	0	0.7414	$0.0093 + 0.7416i$

[27]: Abadie et al. (2015), ‘On the combined effects of surface tension force calculation and interface advection on spurious currents within Volume of Fluid and Level Set frameworks’

Weber number base flows, as the one for  $We_{\text{base}} = 12.5$ , for the linear computations. However, due to the spurious advection errors in the base flow, spurious modes occurred in our results that hampered a successful analysis. [27] have shown that advection of the interface using a level set method may lead to a reduction of dynamic spurious currents as opposed to the VOF method that is used here. This could be a possible avenue towards reducing the base flow curvature errors for finite Weber numbers in a future study.

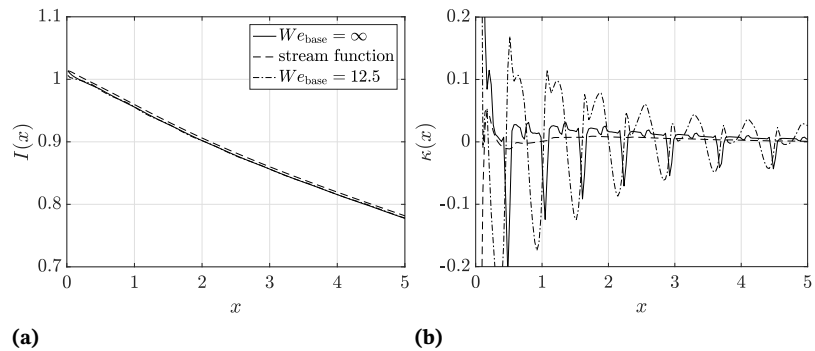


**Figure 3.4:** (a) Interface position and (b) curvature of the respective baseflows.

### 3.5.3 Computation of linear global modes

In section 3.5.1 we have seen that the action of surface tension on the base flow leads to complex dynamics, with often several distinct modes being visible in the flow. Here, we investigate whether linear analysis can successfully predict the destabilisation that gives rise to the observed nonlinear dynamics. Further, we aim to compare the present linear results with those of [24]. Therefore, we limit the analysis to the  $We$  investigated in their study.

[24]: Tammsola et al. (2012), ‘Surface tension-induced global instability of planar jets and wakes’

The computation of linear global modes is done by constructing a low-dimensional subspace representation of the linearised Navier-Stokes operator, using the Arnoldi method as outlined in §3.4.2. The Krylov vectors spanning the subspace are obtained by time-stepping of the linearised solver. The integration time  $\tau$  between two consecutive snapshots is arbitrary, however, in order to satisfy the Nyquist criterion, at least two sample points are needed to resolve the highest desired frequency. Furthermore, too small values of  $\tau$  may lead to insufficient temporal separation between

$We$	$We^{-1}$	$\lambda$ (present study)	$\lambda$ [24]	$\text{Im}(\lambda)$ (DNS)
16.6	0.06	-0.0042 + 0.7851i	-0.01 + 0.788i	stable
12.5	0.08	0.0093 + 0.7416i	0.005 + 0.743i	0.7414
10	0.1	0.0214 + 0.8422i	0.021 + 0.843i	0.8419
		0.0194 + 0.6946i	0.015 + 0.694i	0.6912
		0.0162 + 0.831i	-	0.8294
6.6	0.15	0.0250 + 0.6145i	0.02 + 0.63i	0.5781
		0.0243 + 0.5819i	-	0.5529
		0.0097 + 0.5653i	0.007 + 0.567i	0.5278
5	0.2	0.0161 + 0.4413i	0.017 + 0.453i	0.4021
3.3	0.3	-0.007 + 0.2896i	0.008 + 0.302i	stable

**Table 3.3:** Eigenvalues  $\lambda$  of the present linear analysis, the ones of [24] and frequencies  $\text{Im}(\lambda)$  of the dominant DMD modes of the nonlinear simulation at the respective Weber numbers.

consecutive Krylov vectors, thus hindering convergence of the method within a reasonable subspace dimension. In practice we choose  $\tau = 1.5$ . We have checked that the integration time, within the stated restrictions, does not influence the obtained results to a relevant degree. Arnoldi iterations are performed until a residual  $\|\mathbf{A}\hat{\mathbf{q}}_j - \mu_j \hat{\mathbf{q}}_j\| < 10^{-6}$  for all unstable eigenvalues is reached. The grid independence is demonstrated in table 3.2 for the unstable eigenvalue, computed for  $We = 12.5$ .

The computed growth rates  $\text{Re}(\lambda)$  and frequencies  $\text{Im}(\lambda)$  are given in figure 3.5 for the stated Weber numbers. Both are compared to the results of [24]. Further, the frequencies are compared to the mode frequencies obtained in the nonlinear simulation. The area within the dashed vertical lines corresponds to the range of Weber numbers where the nonlinear flow is unsteady. A direct comparison of the computed eigenvalues of the present study and those computed in [24] is given in table 3.3. Further, in figure 3.6a the growth rates, obtained from the linear analysis for  $We = 5, 6.6, 10, 12.5$ , are compared to the disturbance growth in the nonlinear simulation. In figure 3.6b, the shapes of the computed unstable modes are presented for each Weber number where the corresponding amplitude of the interface is plotted as black line and where the amplitude is chosen arbitrarily for suitable visualisation.

[24]: Tammiola et al. (2012), ‘Surface tension-induced global instability of planar jets and wakes’

The frequency values of the linear analysis and their nonlinear equivalents are very similar in all cases. They compare especially well in the upper regime of unstable Weber numbers, for  $We = 10$  and  $We = 12.5$ . In both cases, all unstable mode are sinuous. In line with the nonlinear simulation, sinuous mode 1 from  $We = 12.5$  is still unstable for  $We = 10$  and  $We = 6.6$  and the appearance of sinuous mode 2, that is the most unstable mode for  $We = 10$  and remains unstable for  $We = 6.6$ , is accurately predicted. The predicted mode shapes at both  $We$  show good agreement compared to the DMD modes in figure 3.2b, both in terms of shape and stream wise position of the amplitude maximum. For  $We = 6.6$ , the most unstable mode is varicose mode 1. In contrast to the computed DMD modes, the linear global modes at  $We = 6.6$  show a more regular and symmetric structure and their frequencies are slightly over-predicted. We believe this is not a shortcoming of the linear analysis but rather an indication that the quasiperiodicity of the dynamics induces non-negligible nonlinear interactions in the flow that lead to a departure of from the linear dynamics presented here. For  $We = 5$ , varicose mode 1 is the only unstable mode predicted. Its frequency is, again, slightly over-predicted which again can be attributed to a non-negligible nonlinearity in the flow dynamics.

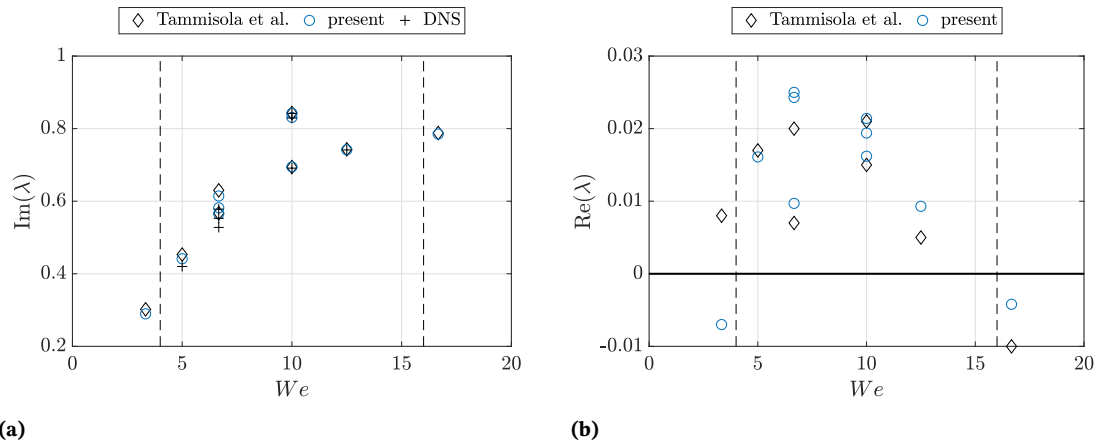


**Figure 3.5:** (a) Comparison of the mode frequencies and (b) growth rates at the respective Weber numbers.

Turning to the growth rates, in figure 3.6a a comparison of the present growth rates with the energy growth of the nonlinear simulation is shown. Therefore, we initialise the nonlinear flow from the steady base flow with  $We_{\text{base}} = \infty$  and monitor the disturbance growth via the  $v$  component of the velocity at  $(x, y) = (5, 0)$  where  $V = 0$ . The plotted time series of the nonlinear energy growth is obtained by computing the logarithm of the envelope of the modulus of the monitored velocity signal. The lines representing the growth rates of the linear analysis are shifted for suitable alignment with the nonlinear time series. For  $We = 12.5$ , a sufficiently long time interval of approximately exponential growth is seen that is in agreement with the obtained growth rates. For  $We = 10$  and  $We = 6.6$ , intervals of exponential growth are less clear which may be due to the competing modes that are observed at this Weber numbers and that prevent a clear exponential growth of a single mode from being observed. Furthermore it could be hypothesised that transient growth leads to short time amplification of additional modes that further influence the observed energy growth. Nevertheless, the modal growth rates obtained in the linear analysis agree reasonably well with the overall energy growth, observed in the nonlinear flow at  $We = 10, 6.6$ . For  $We = 5$ , an interval of clear exponential growth is seen that is in good agreement with the predicted growth rate of the linear analysis.

[24]: Tammisola et al. (2012), ‘Surface tension-induced global instability of planar jets and wakes’

Comparing the present results to the study of [24], good agreement is seen between the computed mode frequencies and those of [24]. In particular, both linear analyses show similar over-predictions of the frequencies for  $We = 5, 6.6$ . On the other hand, the present growth rates show notable deviations, compared to their results. For  $We = 6.6, 10, 12.5, 16.6$  the present growth rates are always higher, up to almost a factor of 2, whereas for  $We = 3.3$  they are notably lower. The prediction of the bifurcation points also differs. For  $We = 3.3$ , [24] still predict an unstable eigenvalue, while in the present study, the flow is already linearly stable, consistent with the nonlinear simulation. Several reasons for the different growth rates in both studies may be found. Generally, the growth rates obtained in both analyses are rather small for all computed Weber numbers. Therefore, slight differences in the employed numerical schemes may lead to large relative changes in the growth rates. From a numerical perspective, the treatment of the interface and surface tension via separate domains and

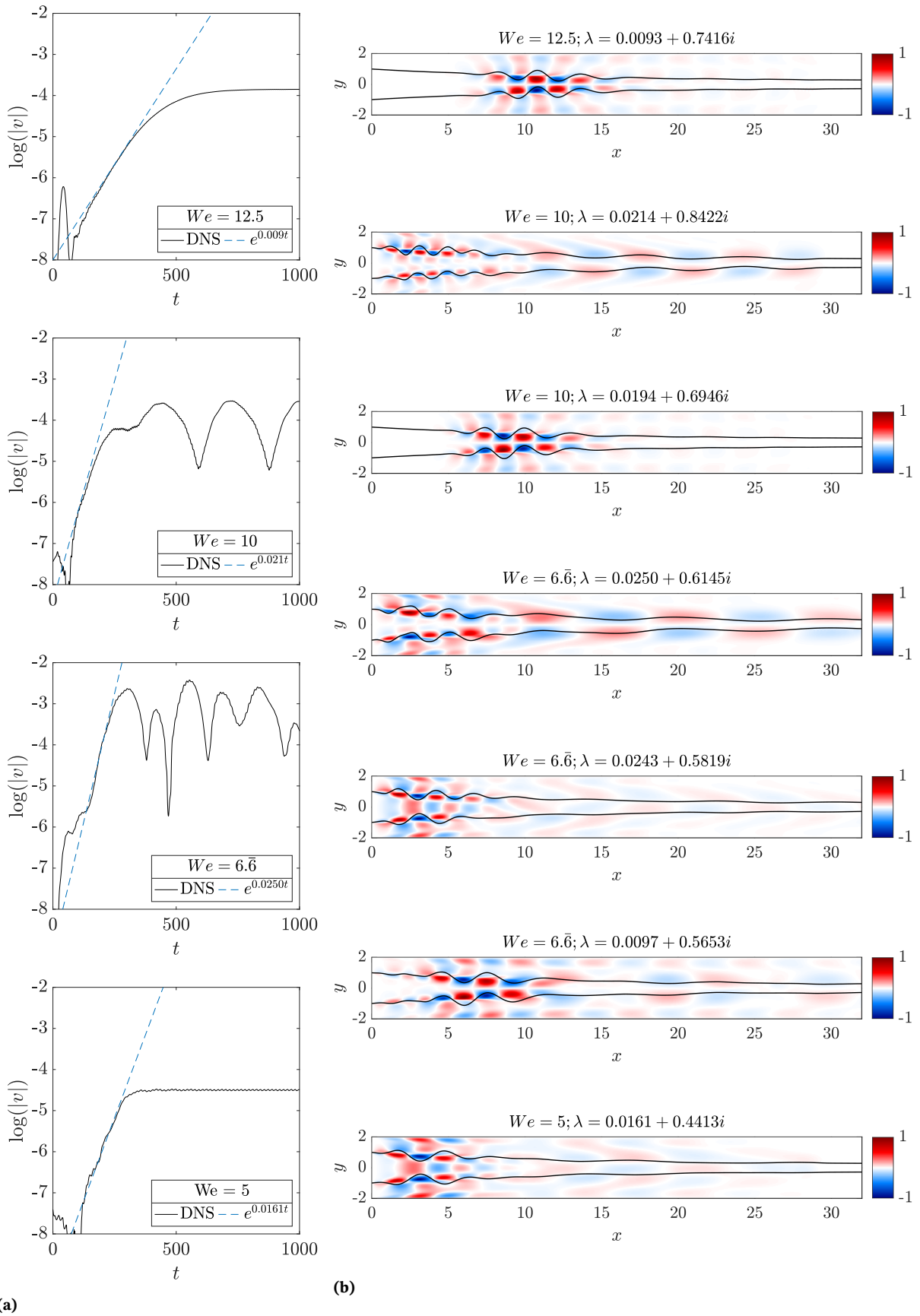


**Figure 3.6:** (a) Comparison of the velocity disturbance growth of the nonlinear simulation  $v$  at  $(x, y) = (5, 0)$  and the exponential growth rate of the most unstable linear global modes of the present analysis. (b) Mode shapes of the respective eigenmodes. The corresponding eigenvalue  $\lambda$  is given for each mode.

[24]: Tammisola et al. (2012), ‘Surface tension-induced global instability of planar jets and wakes’

coupling conditions in [24] might be a source for differences. Further, the use of Chebyshev polynomials in their study, while spectrally accurate, introduces a non-uniform grid spacing which leads to a reduced resolution in the centre of the respective domains. Another possible reason is the use of a streamline-based reconstruction of the interface which is shown to result in a slightly smaller interface curvature, as seen in figure 3.4b. These differences are especially prominent close to the inlet, where the global mode at this Weber number is localised.

### 3.5.4 Comparison of nonlinear and linear dynamics

In §3.5.1 and §3.5.3 we have analysed the nonlinear and linear dynamics of plane wakes under the influence of surface tension and have found that the linear analysis reliably predicts the dominant modes, seen in the nonlinear flow, to be linearly unstable. However, from figure 3.2a it is as well seen that for the intermediate Weber numbers studied there, the nonlinear dynamics contain significantly more modes than the linear analysis predicts. Hence, these modes are the result of nonlinear harmonic interactions resulting from the quadratic nonlinearity of the advection term or the higher order geometric nonlinearity of the surface tension term. It is therefore worthwhile to shed more light on the validity of the linear dynamics to approximate the nonlinear flow. To this end, we use the dominant DMD modes that are shown in figure 3.2b, and which we have seen to closely correspond to the linear modes presented figure 3.6b and table 3.3, to construct a low dimensional approximation of the nonlinear dynamics of the flow.

[62]: Barkley (2006), ‘Linear analysis of the cylinder wake mean flow’

[63]: Oberleithner et al. (2014), ‘Mean flow stability analysis of oscillating jet experiments’

[83]: Boujo et al. (2018), ‘Saturation of a turbulent mixing layer over a cavity: response to harmonic forcing around mean flows’

[106]: Schmidt et al. (2020), ‘Instability of forced planar liquid jets: mean field analysis and nonlinear simulation’

The departure of the linear dynamics towards the full nonlinear dynamics can be analysed by employing the time-averaged mean flow as has been shown in various works in recent times (e.g. [62, 63, 83, 106]). According to the theory established therein, the nonlinear saturation process is driven by the interaction of higher harmonics with their complex conjugates through the Reynolds stress divergence that modifies the base flow towards the mean flow. As a consequence, eigenmodes that are unstable with respect to the base flow become marginally stable on the mean flow. Simultaneously, the mean flow modification may alter the structure and frequency of the eigenmodes through the linear perturbation equation. The remaining difference to the full nonlinear flow is accounted for by nonlinear interactions between different harmonics. In the present work, the frequencies of the linear modes are in close correspondence to their equivalent nonlinear modes which indicates that these modes are not significantly affected by the mean flow modification. Hence, the constructed model can be seen as a representation of the linear dynamics around the mean flow. The difference between the reduced and full dynamics are the nonlinear interactions between different harmonics and thus, it is reasonable to assume that a comparison of the reconstructed and full dynamics yields an appropriate qualitative picture of how far linear and nonlinear dynamics are apart.

In figure 3.7, we present velocity phase trajectories of the full and reconstructed dynamics using probes located at the approximate stream wise location of the respective amplitude maxima of the oscillation of the nonlinear flow. For a clean visual representation, we plot the velocity histories using a time lag of one period  $\tau = 1/\text{Im}(\lambda)$  where  $\text{Im}(\lambda)$  is chosen as the

frequency of the mode with the largest amplitude for each respective Weber number (i.e. sinuous mode 1 ( $We = 12.5$ ), sinuous mode 2 ( $We = 10$ ), varicose mode 1 ( $We = 6.\bar{6}$ , 5)). To get a better view of the cross-sections of the phase space we plot a variant of Poincaré sections in figure 3.8. The section is chosen such that the phase trajectory crosses it every completed cycle  $n$ , established by the period  $\tau$ .

As is expected from the analysis in §3.5.1, for  $We = 12.5$  and  $We = 5$ , the full nonlinear dynamics are represented by a limit cycle. Thus a closed orbit is seen in figure 3.7 which, however, shows a notable deformation, caused by higher harmonic modes. The reconstructed mono-frequent dynamics lack this higher harmonic influence which results in a slightly smaller orbit and thus a reduced velocity amplitude. As expected for a limit-cycle solution, both trajectories cross the section plane at a fixed point in figure 3.8. For  $We = 10$  and  $We = 6.\bar{6}$ , the trajectories of the full nonlinear dynamics show complex patterns and the orbits fill a closed region in the phase space, possibly indicating chaotic behaviour. The reconstructed dynamics each consist of three incommensurate frequencies, thus forming a quasiperiodic cycle on a 3-torus. The reconstruction shows a significantly different behaviour compared to the full dynamics and particularly for  $We = 10$  results in an overall lower amplitude oscillation. For both Weber numbers, the section plots in figure 3.8 show the trajectory crossings clustered broadly around the fixed points, observed for  $We = 12.5, 5$ . While the crossings of the reconstructed dynamics show regular closed paths, indicative of quasiperiodicity, the full dynamics do not exhibit clear paths, again suggesting a chaotic behaviour.

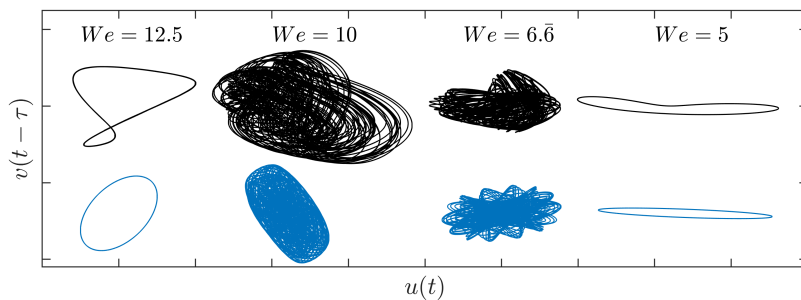


**Figure 3.7:** Qualitative representation of the velocity phase trajectories at  $(x, y) = (8, 0)$  ( $We = 12.5$ ),  $(x, y) = (8, 0)$  ( $We = 10$ ),  $(x, y) = (6, 0)$  ( $We = 6.\bar{6}$ ) and  $(x, y) = (4, 0)$  ( $We = 5$ ). The upper row in black shows the full dynamics and the lower row in blue the reconstructed dynamics. All plots are equally scaled.

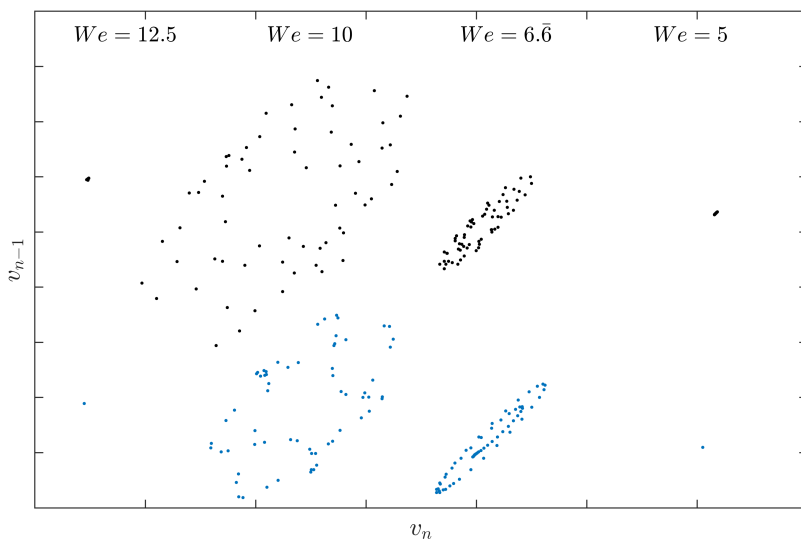


**Figure 3.8:** Qualitative Poincaré sections of the trajectories presented in figure 3.7. Sections are chosen such that trajectories cross every completed cycle  $n$ . The upper row in black shows the full dynamics and the lower row in blue the reconstructed dynamics. All plots are equally scaled.

### 3.5.5 Discussion and relations to other studies

[24]: Tammisola et al. (2012), ‘Surface tension-induced global instability of planar jets and wakes’

[17]: Squire (1953), ‘Investigation of the instability of a moving liquid film’

[19]: Hagerty et al. (1955), ‘A study of the stability of moving liquid film’

[94]: Rees et al. (2009), ‘The effect of surface tension on the stability of unconfined and confined planar jets and wakes’

[107]: Biancofiore et al. (2010), ‘Influence of confinement on temporal stability of plane jets and wakes’

The linear stability results obtained by [24] are counter-intuitive, in so far as they find surface tension to be destabilising in a plane two-dimensional flow, contrary to its common stabilising tendency in plane flows [17, 19]. Furthermore, at the studied Reynolds number, the velocity ratio of the adjacent fluid streams is too low to trigger the Bénard-von Kármán instability which is typically present in wake flows at higher Reynolds number or velocity ratio. As a result, the flow is globally stable in the absence of surface tension. Viscosity and density being equal across the fluids in the present configuration, the only possible destabilizing force is surface tension. In fact, a prospect of a destabilizing surface tension force in plane flows is given in studies by [94] and [107], based on inviscid local stability analyses, suggesting that such effect, induced by a top-hat velocity profile, exists in the high- $Re$  limit. It was found that for certain configurations, moderate surface tensions both, wakes and jets, are significantly more unstable than without surface tension. To further explore this topic, we have conducted detailed nonlinear and linear computations of this configuration.

The linear analysis is able to predict all dominant modes present in the nonlinear flow, even for  $We$  where several competing modes govern the dynamics. As a consequence, for the investigated Weber numbers close to the bifurcation points, i.e.  $We = 12.5, 5$ , the linear and nonlinear dynamics are in close correspondence. However, for intermediate Weber numbers, e.g.  $We = 10, 6.6$ , the full nonlinear dynamics have been shown to be significantly more complex, involving significant nonlinear harmonic interactions. Therefore, in these regimes, discrepancies between linear and nonlinear dynamics are found.

The presently obtained linear modes are also in very good agreement with the results of the linear stability analysis of [24]. On the other hand, the computed growth rates show notable differences between both analyses. However, the comparison of nonlinear and linear analysis suggests that the presently obtained growth rates are plausible. In the study of [24], the bifurcation occurring between  $We = 16.6$  and  $We = 12.5$  is well captured, as it is in the present results. The stabilisation of the global mode at  $We = 3.3$  is only captured in the present analysis, whereas in their work the linear analysis still shows a slightly unstable mode. Possible reasons for this discrepancy have been given in §3.5.3.

Comparing the present results to the stability maps for the uniform density case of [94] (Figs. 7 and 8 in their work), it is seen that our configuration is in a region of absolute instability for  $We^{-1} > 0.1$  (varicose modes) and  $0.1 < We^{-1} < 10$  (sinuous modes). Note, that maps for  $We^{-1} < 0.1$  are not considered in [94] but the inviscid stability limits should approximately remain similar as  $We^{-1}$  tends to zero, as is also seen in Fig. 9 of [107]. While their inviscid results cannot be expected to translate accurately to the present viscous flow results, the general trend of varicose modes remaining unstable for higher surface tensions, while sinuous modes becoming stable again, persists. The dampening effect of viscosity in the present flow eventually leads to stabilisation of also varicose modes below  $We \approx 3.3$ . Similarly, viscosity renders the flow stable above  $We \approx 16.6$ , while in the inviscid limit it remains unstable.

The physical mechanism of surface tension-induced instability of plane

[108]: Biancofiore et al. (2015), ‘Interaction between counterpropagating Rossby waves and capillary waves in planar shear flows’

[109]: Biancofiore et al. (2017), ‘Understanding the destabilizing role for surface tension in planar shear flows in terms of wave interaction’

shear flows has been explored in [108, 109] from a Kernel wave perspective. The resulting system consists of two counter-propagating inertial and capillary waves. As a general concept, the vorticity perturbation of each wave induces an effect on its counter-propagating wave. Depending on their phase angle (and speed) a dampening or amplification is observed. Without surface tension the studied system showed a single, purely inertial, unstable mode at large wavelengths. With the inclusion of surface tension a second mode appeared, acting at smaller wavelengths. It was further found, that at large wavelengths influence was mainly due to an interaction of the inertial waves, while for small wave numbers interaction was between one inertial wave and its counter-propagating capillary wave. This was explained using a phase-locking of the two counter-propagating waves, resulting in a continuous amplification. Contrastingly, at smaller wavelengths, the phase speed was found too high for prolonged interaction to take place effectively, thus limiting the capillary-inertial interaction to small wavelengths. For an increasing surface tension, the phase speed reduces and the upper cutoff wavelength is shifted towards larger wavelengths. Although their studied configurations do not match the present one, these findings translate conclusively to the present results: The long-wave sinuous mode 1 corresponds to an inertial wave interaction, likely a von Kármán mode, modified by surface tension to become unstable. Similarly, the short-wave sinuous mode 2 as well as the varicose mode 1 correspond to an inertial-capillary wave interaction with increasing wavelength for increasing surface tension.

In light of the present results, it is important to discuss the results of another related study by [91], which investigated the same flow configuration with direct numerical simulation, using a finite element method in conjunction with a level set method for interface capturing. Their study confirms the global stability of the flow in the absence of surface tension and shows comparable results for some of the cases studied in the present work. In particular, for  $We = 10$ , they detect a clear sinuous disturbance with a velocity amplitude of  $10^{-2}$  which is localised between  $5 < x < 15$ . The periodicity of this oscillation is  $T = 9$  which corresponds to a mode frequency  $\omega = 0.698$ . The spatial appearance and frequency of this instability are close to the sinuous mode 1 computed at this Weber number in the present study and by [24]. In contrast, for  $We = 12.5$ , they detect a weak sinuous disturbance in form of an intermittent, transient wave packet that has a disturbance amplitude of the velocity of about  $10^{-4}$  and a disturbance amplitude of the interface of about  $10^{-8}$ . Although it is not explicitly mentioned, the transient character of this disturbance leads to the conclusion that this is a convective instability. The flow at this Weber number still appears to be globally stable. For  $We = 5$ , a very weak disturbance in close vicinity of the inlet is detected, which, however, seems to have insufficient amplitude for a reliable frequency estimation. Moreover, it seems only detectable when axial symmetry is imposed along the channel axis.

[91] argue that the differences might stem from the fact that a single phase flow without surface tension was computed for the basic states used in [24], neglecting pressure modifications due to surface tension. In particular, they point out that the incompatibility of the plug flow inlet condition for the velocity with the wall boundaries leads to a very localised contraction of the interface immediately behind the inlet. The resulting curvature

[91]: Biancofiore et al. (2014), 'Direct numerical simulations of two-phase immiscible wakes'

[24]: Tammisola et al. (2012), 'Surface tension-induced global instability of planar jets and wakes'

[24]: Tammisola et al. (2012), ‘Surface tension-induced global instability of planar jets and wakes’

[91]: Biancofiore et al. (2014), ‘Direct numerical simulations of two-phase immiscible wakes’

thus induces a non-negligible pressure gradient. While we agree with this rationale, the present nonlinear results suggest that this pressure gradient is not the cause for the observed differences since the modes predicted in [24] are clearly present in our nonlinear simulations which account for the pressure gradient. It is not entirely clear what causes the differences in the results of [91]. However, one might speculate that, for instance, numerical diffusion caused by the employed numerical schemes or insufficient mesh resolution could attenuate some of the observed modes, leaving only the sinuous mode 1 unstable. Additionally, this could cause the bifurcation points of the detected unstable mode to move close together such that the flow remains only unstable around  $We = 10$ .

### 3.6 Conclusions

In this paper we have accomplished three objectives.

First, we have presented a framework for the computation of linear global modes of interfacial flow, by means of time-stepping of a linearised Navier-Stokes solver. The effects of surface tension, density and viscosity differences between the different phases are fully accounted for, thereby avoiding a few simplifications that were made in previous studies of similar interfacial flow situations. The matrix-free time-stepper-based method also avoids excessive memory requirements, so that the approach is fairly straightforward to apply to more complex geometries or to three-dimensional flow. As a perspective for future improvements, robust computations of finite Weber number or non-uniform viscosity or density base flows are needed. This includes the stabilisation of the unstable flow by methods like Newton iterations or selective frequency damping as well as a reduction of spurious advection errors by improved numerical schemes.

Second, we have revisited the work of [24] and conducted nonlinear simulations to rigorously validate the results of their global linear stability analysis. Further, we have reproduced the computations with the developed linear solver. The present linear analysis is in very good agreement with the results of [24] and both linear predictions are confirmed by the present nonlinear simulations. The present method accurately captures the bifurcation points as deduced from the nonlinear analysis and growth rates show good agreement with the initial disturbance growth found in the nonlinear simulation.

Third, our validation of the configuration provides clarity that a surface-tension-induced destabilisation of plane wakes can indeed be observed in the nonlinear flow. It is shown that, in the studied flow regimes, surface tension can induce both, varicose and sinuous oscillations of the flow which may be present simultaneously at several  $We$ , thus leading to complex quasiperiodic or chaotic dynamics.

## 3.7 Appendix

### 3.7.1 Derivation of the linearised normal vector and curvature

Here we give a detailed derivation of the linearised normal vector and curvature, based on the level set function  $\phi$ . the nonlinear normal vector is given as

$$\mathbf{n} = \frac{\nabla\phi}{|\nabla\phi|} = \frac{\left(\frac{\partial\phi}{\partial x} + \zeta \frac{\partial\phi'}{\partial x}, \frac{\partial\phi}{\partial y} + \zeta \frac{\partial\phi'}{\partial y}\right)}{\left[\left(\frac{\partial\phi}{\partial x} + \zeta \frac{\partial\phi'}{\partial x}\right)^2 + \left(\frac{\partial\phi}{\partial y} + \zeta \frac{\partial\phi'}{\partial y}\right)^2\right]^{1/2}}. \quad (3.32)$$

Then the basic state normal is

$$\mathbf{N} = \frac{\nabla\Phi}{|\nabla\Phi|} = \frac{\left(\frac{\partial\Phi}{\partial x}, \frac{\partial\Phi}{\partial y}\right)}{\left[\left(\frac{\partial\Phi}{\partial x}\right)^2 + \left(\frac{\partial\Phi}{\partial y}\right)^2\right]^{1/2}}, \quad (3.33)$$

and the perturbed normal vector is found by linear Taylor expansion of  $\mathbf{n}$  around  $\epsilon = 0$  as

$$\begin{aligned} \zeta \mathbf{n}' &= \zeta \left. \left( \frac{\partial \mathbf{n}}{\partial \zeta} \right) \right|_{\zeta=0} \quad (3.34) \\ &= \zeta \left( \frac{\partial\phi'}{\partial x}, \frac{\partial\phi'}{\partial y} \right) \left[ \left( \frac{\partial\phi}{\partial x} \right)^2 + \left( \frac{\partial\phi}{\partial y} \right)^2 \right]^{-1/2} + \\ &\zeta \left( \frac{\partial\phi}{\partial x}, \frac{\partial\phi}{\partial y} \right) \frac{\partial}{\partial \zeta} \left[ \left( \frac{\partial\phi}{\partial x} + \zeta \frac{\partial\phi'}{\partial x} \right)^2 + \left( \frac{\partial\phi}{\partial y} + \zeta \frac{\partial\phi'}{\partial y} \right)^2 \right]^{-1/2} \Bigg|_{\zeta=0} \\ &= \left( \frac{\partial\zeta\phi'}{\partial x}, \frac{\partial\zeta\phi'}{\partial y} \right) \left[ \left( \frac{\partial\phi}{\partial x} \right)^2 + \left( \frac{\partial\phi}{\partial y} \right)^2 \right]^{-1/2} + \\ &\left( \frac{\partial\phi}{\partial x}, \frac{\partial\phi}{\partial y} \right) \left( \frac{\partial\zeta\phi'}{\partial x} \frac{\partial\phi}{\partial x} + \frac{\partial\zeta\phi'}{\partial y} \frac{\partial\phi}{\partial y} \right) \left[ \left( \frac{\partial\phi}{\partial x} \right)^2 + \left( \frac{\partial\phi}{\partial y} \right)^2 \right]^{-3/2}. \end{aligned}$$

If we introduce

$$f(\Phi) = \left[ \left( \frac{\partial\Phi}{\partial x} \right)^2 + \left( \frac{\partial\Phi}{\partial y} \right)^2 \right]^{-1/2}, \quad (3.35a)$$

$$g(\Phi) = - \left( \frac{\partial\zeta\phi'}{\partial x} \frac{\partial\Phi}{\partial x} + \frac{\partial\zeta\phi'}{\partial y} \frac{\partial\Phi}{\partial y} \right), \quad (3.35b)$$

we can write the perturbed normal vector as

$$\zeta \mathbf{n}' = \left( \frac{\partial \zeta \phi'}{\partial x} f, \frac{\partial \zeta \phi'}{\partial y} f \right) + \left( g f^3 \frac{\partial \Phi}{\partial x}, g f^3 \frac{\partial \Phi}{\partial y} \right). \quad (3.36)$$

The curvature is the divergence of the normal vector. Consequently, the curvature of the basic state is given as

$$K = \nabla \cdot \mathbf{N} = \frac{\frac{\partial^2 \Phi}{\partial x^2} \left( \frac{\partial \Phi}{\partial y} \right)^2 - 2 \frac{\partial^2 \Phi}{\partial x \partial y} \frac{\partial \Phi}{\partial x} \frac{\partial \Phi}{\partial y} + \frac{\partial^2 \Phi}{\partial y^2} \left( \frac{\partial \Phi}{\partial x} \right)^2}{\left[ \left( \frac{\partial \Phi}{\partial x} \right) + \left( \frac{\partial \Phi}{\partial y} \right) \right]^{3/2}}. \quad (3.37)$$

Similarly, the curvature of the perturbed state is found as

$$\kappa' = \nabla \cdot \zeta \mathbf{n}' \quad (3.38)$$

$$\begin{aligned} &= \frac{\partial f}{\partial x} \frac{\partial \zeta \phi'}{\partial x} + f \frac{\partial^2 \zeta \phi'}{\partial x^2} + \frac{\partial f}{\partial y} \frac{\partial \zeta \phi'}{\partial y} + f \frac{\partial^2 \zeta \phi'}{\partial y^2} \\ &\quad + \frac{\partial g}{\partial x} f^3 \frac{\partial \Phi}{\partial x} + g 3 f^2 \frac{\partial f}{\partial x} \frac{\partial \Phi}{\partial x} + g f^3 \frac{\partial^2 \Phi}{\partial x^2} \\ &\quad + \frac{\partial g}{\partial y} f^3 \frac{\partial \Phi}{\partial y} + g 3 f^2 \frac{\partial f}{\partial y} \frac{\partial \Phi}{\partial y} + g f^3 \frac{\partial^2 \Phi}{\partial y^2} \end{aligned}$$

where

$$\frac{\partial f}{\partial x} = -f^3 \left( \frac{\partial \Phi}{\partial x} \frac{\partial^2 \Phi}{\partial x^2} + \frac{\partial \Phi}{\partial y} \frac{\partial^2 \Phi}{\partial x \partial y} \right), \quad (3.39)$$

$$\frac{\partial f}{\partial y} = -f^3 \left( \frac{\partial \Phi}{\partial x} \frac{\partial^2 \Phi}{\partial x \partial y} + \frac{\partial \Phi}{\partial y} \frac{\partial^2 \Phi}{\partial y^2} \right), \quad (3.40)$$

$$\frac{\partial g}{\partial x} = - \left( \frac{\partial \zeta \phi'}{\partial x} \frac{\partial^2 \Phi}{\partial x^2} + \frac{\partial^2 \zeta \phi'}{\partial x^2} \frac{\partial \Phi}{\partial x} + \frac{\partial \zeta \phi'}{\partial y} \frac{\partial^2 \Phi}{\partial x \partial y} + \frac{\partial^2 \zeta \phi'}{\partial x \partial y} \frac{\partial \Phi}{\partial y} \right), \quad (3.41)$$

$$\frac{\partial g}{\partial y} = - \left( \frac{\partial \zeta \phi'}{\partial y} \frac{\partial^2 \Phi}{\partial y^2} + \frac{\partial^2 \zeta \phi'}{\partial y^2} \frac{\partial \Phi}{\partial y} + \frac{\partial \zeta \phi'}{\partial x} \frac{\partial^2 \Phi}{\partial y \partial x} + \frac{\partial^2 \zeta \phi'}{\partial y \partial x} \frac{\partial \Phi}{\partial x} \right). \quad (3.42)$$

# Triadic resonance of single and double helical global modes in a variable viscosity two-phase swirling flow

# 4

## Abstract

The dynamics and interaction of two harmonically related global modes in a laminar, immiscible two-phase swirling flow with varying viscosity are investigated. We perform axisymmetric nonlinear simulations and linear global stability analysis of the fully three-dimensional flow for several swirl numbers  $S$ . They are accompanied by nonlinear three-dimensional simulations and subsequent modal analysis using the Bispectral Mode Decomposition, recently introduced by [110]. We find a pronounced destabilising effect of the viscosity stratification on both, the onset of axisymmetric vortex breakdown and helical instability. Consequently, destabilisation is shifted to lower  $S$  as compared to an equivalent flow with uniform viscosity. Further, the stability analysis reveals the simultaneous destabilisation of two global modes with wavenumbers  $m = 1$  and  $m = 2$  that have harmonic frequencies. The analysis of the nonlinear flow reveals a strong triadic resonance between these modes that governs the nonlinear dynamics and leads to a rapid departure from the linear dynamics. At larger swirl, the bifurcation of additional modes initiates an interaction cascade by means of triadic resonance which is elucidated by the bispectral analysis. It leads to the emergence of a variety of additional modes in the nonlinear flow. The existence and coupling of two global modes as in the present study may have implications for the analysis of other swirling flows where the existence of an  $m = 2$  global mode may easily be mistaken as being a purely higher harmonic. Consequently, flow control applications may have to account for the existence of this second global mode.

4.1	Introduction . . . . .	84
4.2	Numerical simulation and modal decomposition methods . . . . .	86
4.3	Steady axisymmetric breakdown states . . . . .	93
4.4	Linear global modes . . . . .	96
4.5	Analysis of helical instability in the nonlinear flow . . . . .	98
4.6	Discussion . . . . .	108
4.7	Conclusions . . . . .	111
4.8	Appendix . . . . .	111

[110]: Schmidt (2020), 'Bispectral mode decomposition of nonlinear flows'

The contents of this chapter have been **submitted** to the *Journal of Fluid Mechanics*.

This version is published under a Creative Commons CC-BY-NC-ND. No commercial re-distribution or re-use allowed. Derivative works cannot be distributed. ©copyright holder.

## 4.1 Introduction

Swirling flows are highly relevant for many technical applications. Swirl is used for flame stabilisation and mixing enhancement in modern lean-premixed gas turbine combustors, they occur in the wake of wind turbines, and they play an important role in the stability of Francis turbines. From an academic perspective, swirling flows are interesting as they support a variety of instabilities mechanisms, including axial and azimuthal shear instabilities, centrifugal instabilities, inertial waves and global instabilities. This again is important for the engineering context as these instabilities give rise to large-scale coherent structures that tremendously impact the efficiency and operationability of the technical system.

Swirling flows at high swirl are known to undergo an abrupt structural change in the flow, named vortex breakdown. It manifests in the appearance of a stagnation point at the jet centre. While a number of different manifestations of vortex breakdown have been identified in literature (see e.g. the review of [111]), the two most common types are the axisymmetric breakdown and the spiral breakdown. Axisymmetric breakdown is characterised by the formation of a steady or unsteady recirculating bubble that acts as a bluff body to the upstream fluid, thus inducing a wake-like flow profile downstream of the bubble. In contrast, spiral breakdown is a manifestation of the flows' susceptibility to helical instabilities which leads to the formation of spiralling coherent structures in the flow. Various forms of spiral breakdown have been observed in literature which may occur as single or double helical structures in the flow. A comprehensive experimental study to characterise the different states was conducted by e.g. [112] or [113].

Regarding the underlying physical mechanism of vortex breakdown, no generally accepted explanation is available, despite multiple theories. However, current literature (e.g. [7, 114, 115]) generally acknowledges the theory of [116], who interprets vortex breakdown to be the result of a supercritical to subcritical flow transition. The upstream supercritical flow is unable to support standing waves while the downstream subcritical flow is, resulting in a stagnation point and the formation of a breakdown bubble.

With the rise of global stability theory in the last two decades, our understanding of the dominant flow instabilities of swirling flows has substantially improved. The numerical study of laminar swirling flows, based on the Grabowski-Berger profile [117], conducted by [7] and the experimental study by [118] have suggested that the single and double helical structures are manifestations of global modes becoming unstable through a supercritical Hopf bifurcation. This view has been confirmed by [8] who performed a local stability analysis using a similar flow configuration to that of [7] and identified a single helical unstable global mode. Considering a turbulent swirling jet with vortex breakdown, [10] applied local stability analysis using the time-averaged mean flow and successfully identified a single helical global mode whose mode shape was in close correspondence to the respective experimental measurements. The destabilisation of double helical global modes and their coexistence with single helical modes was shown by [9], using the Grabowski-Berger profile as in [7] and [8]. At one combination of swirl and Reynolds number, a codimension-two point, the frequencies of these modes were approximately harmonic, thus

[111]: Lucca-Negro et al. (2001), 'Vortex breakdown: a review'

[112]: Escudier et al. (1982), 'Vortex-flow regimes'

[113]: Billant et al. (1998), 'Experimental study of vortex breakdown in swirling jets'

[7]: Ruith et al. (2003), 'Three-dimensional vortex breakdown in swirling jets and wakes: direct numerical simulation'

[114]: Oberleithner et al. (2012), 'Formation of turbulent vortex breakdown: intermittency, criticality, and global instability'

[115]: Vanierschot (2017), 'On the dynamics of the transition to vortex breakdown in axisymmetric inviscid swirling flows'

[116]: Benjamin (1962), 'Theory of the vortex breakdown phenomenon'

[117]: Grabowski et al. (1976), 'Solutions of the Navier-Stokes equations for vortex breakdown'

[118]: Liang et al. (2005), 'An experimental investigation of swirling jets'

[8]: Gallaire et al. (2006), 'Spiral vortex breakdown as a global mode'

[10]: Oberleithner et al. (2011), 'Three-dimensional coherent structures in a swirling jet undergoing vortex breakdown: stability analysis and empirical mode construction'

[9]: Meliga et al. (2012), 'A weakly nonlinear mechanism for mode selection in swirling jets'

[7]: Ruith et al. (2003), 'Three-dimensional vortex breakdown in swirling jets and wakes: direct numerical simulation'

enabling resonant behaviour. They further identified a weakly nonlinear interaction mechanism of these modes to drive the observed selection of global modes in the DNS study of [7]. Nonlinear interaction of global modes in a Grabowski-Berger vortex has been studied by [119] where the appearance of a second global mode with incommensurate frequency to the primary mode led to the emergence of quasi-periodic and chaotic dynamics. Additional evidence on the coexistence of multiple global modes in turbulent swirling flows has been given very recently by [120] who found a single and double helical mode located in separate regions of the flow. Both modes had separate wavemakers and, despite their frequencies being harmonically related, no nonlinear interactions between them was observed.

Swirling flows involving two immiscible fluid phases with varying density or viscosity, separated by an interface, have not found wider attention, yet. The available literature is mostly focused on experimental and theoretical studies of swirling liquid columns or jets in a gaseous environment (see e.g. [31, 121]). Nevertheless, two-phase swirling flows are relevant for a number of technical applications such as industrial cyclone separators or as a manifestation of cavitation in hydro-turbines or swirl atomisers ( e.g. [4, 122, 123]). In these examples the inner fluid is generally considered to be lighter (i.e. less viscous and/or dense) than the outer fluid.

The potentially destabilising nature of a viscosity stratification in two-phase flows has been highlighted in the seminal work of [18], who found a fundamental mechanism which renders all confined interfacial shear flows with viscosity stratification linearly unstable. Similar destabilisations have been identified, among others, by [124] and [125]. The introduction of a two-fluid flow with such stratification may therefore be expected to have considerable effects on the already complex linear and nonlinear dynamics of swirling flows.

The reviewed studies on (single-phase) swirling flows have shown that the existence of multiple global modes in swirling flows potentially allows for nonlinear interaction between them and as a consequence to complex dynamics of the nonlinear flow. Interactions may take place through triadic resonance fed by the quadratic nonlinearity of the convective term of the Navier-Stokes equation. Among various studies, triadic interaction have been identified to play an important role in frequency excitation in the energy cascade of homogeneous turbulence (e.g [126]). Additionally, triadic interactions between Tollmien-Schlichting waves can drive the laminar-turbulent transition process in wall-bounded shear layers as has been shown by [127]. In the context of linear stability analysis, the strength of triadic interactions plays a role for the applicability and validity of mean flow stability analysis, as strong nonlinear coupling of fundamental and harmonic waves can severely impact accuracy of the analysis (e.g. [52, 83, 106]).

From a data-driven perspective, triadic interactions of general one-dimensional signals can be identified by higher-order statistical analysis, namely the bispectrum. A recently introduced method by [110], the bispectral mode decomposition (BMD), allows for the identification and analysis of triadic interactions of multidimensional signals and thus is ideally suited for the identification of these interactions in three-dimensional flows such as considered in this study.

[7]: Ruith et al. (2003), ‘Three-dimensional vortex breakdown in swirling jets and wakes: direct numerical simulation’

[119]: Pasche et al. (2018), ‘Onset of chaos in helical vortex breakdown at low Reynolds number’

[120]: Vanierschot et al. (2020), ‘Single- and double-helix vortex breakdown as two dominant global modes in turbulent swirling jet flow’

[31]: Kubitschek et al. (2007), ‘Helical instability of a rotating viscous liquid jet’

[121]: Kubitschek et al. (2007), ‘The effect of viscosity on the stability of a uniformly rotating liquid column in zero gravity’

[4]: Alligne et al. (2014), ‘Cavitation surge modelling in Francis turbine draft tube’

[122]: Hreiz et al. (2014), ‘Hydrodynamics and velocity measurements in gas-liquid swirling flows in cylindrical cyclones’

[123]: Maly et al. (2021), ‘Internal flow dynamics of spill-return pressure-swirl atomizers’

[18]: Yih (1967), ‘Instability due to viscosity stratification’

[124]: Hickox (1971), ‘Instability due to viscosity and density stratification in axisymmetric pipe flow’

[125]: Hooper et al. (1983), ‘Shear-flow instability at the interface between two viscous fluids’

[126]: Kraichnan (1967), ‘Inertial ranges in two-dimensional turbulence’

[127]: Craik (1971), ‘Non-linear resonant instability in boundary layers’

[52]: Turton et al. (2015), ‘Prediction of frequencies in thermosolutal convection from mean flows’

[83]: Boujo et al. (2018), ‘Saturation of a turbulent mixing layer over a cavity: response to harmonic forcing around mean flows’

[106]: Schmidt et al. (2020), ‘Instability of forced planar liquid jets: mean field analysis and nonlinear simulation’

[110]: Schmidt (2020), ‘Bispectral mode decomposition of nonlinear flows’

[128]: Schmidt et al. (2021), 'Global stability and nonlinear dynamics of wake flows with a two-fluid interface'

In this work we aim to extend the body of existing studies on global mode interactions in swirling flows and shed light on the resonant triadic interactions of global modes in two-phase swirling flows with a variable viscosity where the inner fluid is less viscous than the outer one. The addition of an interface and variable viscosities aims to aid destabilisation of the flow and to potentially promote modal interactions in accordance to the reviewed studies on viscosity stratified flows. The employed flow profile is that of the Grabowski-Berger vortex, extended to two fluid phases. The linear stability of the investigated flows is assessed through a framework recently introduced by [128] which allows for the computation of global modes of interfacial flows by time-stepping of a linearised DNS solver. We show that the introduction of a variable viscosity flow indeed promotes destabilisation of the flow, leading to the emergence of two global modes which notably oscillate at harmonic frequencies. Subsequent bispectral analysis of the nonlinear dynamics reveals strong triadic resonance to take place in the flow at increased swirl which is rooted in the interaction of the two harmonic global modes. This leads to the emergence of multiple ultraharmonic frequencies that alter the flows periodicity. The dynamics of the investigated swirling flow may be seen as a prototype for various other single or two-phase swirling flows where a similar destabilisation and interaction of two global modes may be observed.

The remainder of the paper is structured as follows: In §4.2, we give a brief overview of the governing equations and numerical methodology to perform nonlinear and linear computations of immiscible two-phase flows. In §4.3 we then compute nonlinear axisymmetric solutions for various flow parameters to get a general overview how the viscosity contrast of the phases affects vortex breakdown and compare the results to those of previous studies. The axisymmetric flow states constitute the basis for the linear stability analysis which is conducted in §4.4 to compute the aforementioned global modes. The linear computations are supplemented by fully three-dimensional nonlinear simulations to analyse the effect of the nonlinear triadic interaction of the unstable global modes (§4.5). Finally, a discussion of the presented results is conducted in §4.6.

## 4.2 Numerical simulation and modal decomposition methods

### 4.2.1 Nonlinear simulation

The governing equations for an incompressible and immiscible two-phase flow are derived from their single-phase equivalents by assuming an interface of negligible thickness that separates both phases. The molecular imbalance of cohesive forces between both fluids is modelled as a surface tension force, located at the interface. The continuity and momentum equations, respectively, are given in a unified form over both fluid phases as

$$\partial_t \rho + \mathbf{u} \cdot \nabla \rho = 0, \quad (4.1a)$$

$$\rho(\partial_t \mathbf{u} + \mathbf{u} \cdot \nabla \mathbf{u}) = -\nabla p + \nabla \cdot (\mu \mathbf{D}) + \sigma \kappa \mathbf{n} \delta(\mathbf{x} - \mathbf{x}_s) \quad (4.1b)$$

$$\nabla \cdot \mathbf{u} = 0 \quad (4.1c)$$

with  $\mathbf{u} = (u, v, w)^T$  the velocity vector,  $\rho$  the density,  $\mu$  the dynamic viscosity,  $p$  the pressure and  $\mathbf{x}_s$  being the position of the interface. The deformation tensor is  $\mathbf{D} = \nabla \mathbf{u} + \nabla^T \mathbf{u}$ . Density and viscosity are represented by a Heaviside function  $H(\mathbf{x} - \mathbf{x}_s)$ , that is 1 in phase 1 and 0 in phase 2 such that

$$\rho = \rho_2 + H(\rho_1 - \rho_2), \quad (4.2a)$$

$$\mu = \mu_2 + H(\mu_1 - \mu_2). \quad (4.2b)$$

The rightmost term in 4.1b constitutes the surface tension where  $\sigma$  is the surface tension coefficient,  $\kappa$  is the interface curvature,  $\mathbf{n}$  is the unit normal vector of the interface and  $\delta$  is the Dirac  $\delta$ -function that is non-zero on the interface. The surface tension is a surface force but may be converted into a volumetric force as

$$\sigma \kappa \mathbf{n} \delta(\mathbf{x} - \mathbf{x}_s) = \sigma \kappa \nabla H(\mathbf{x} - \mathbf{x}_s). \quad (4.3)$$

From a numerical perspective, approximations of  $\delta$  and  $H$  are given as  $\delta_\epsilon$  and  $H_\epsilon$ , respectively, where  $\epsilon$  is a characteristic length scale, related to the local grid size  $\Delta$ .

Various numerical approximation for  $H_\epsilon$  may be found which are based on the the continuum surface method (CSF) [41] where we set  $H_\epsilon = c$  with  $c$  being the volume fraction. This is the methodology applied in the Volume-Of-Fluid method (VOF) (e.g. [38]). Similarly, for level-set methods (LS) [39] some smooth representation  $H_\epsilon = f(\phi)$ , based on the signed-distance function  $\phi$  is used.

The advection of  $\rho$  in equation (4.1a) is equivalent to the advection of  $c$  or  $\phi$ , respectively and thus may be replaced by

$$\partial_t \psi + \nabla \cdot (\psi \mathbf{u}) = 0 \quad \begin{cases} \psi = c & \text{if VOF} \\ \psi = \phi & \text{if LS} \end{cases} . \quad (4.4a)$$

The system of equations 4.1 is solved with the Basilisk solver (<http://basilisk.fr>), using the CSF and VOF method. We will not go into the details of computing the nonlinear surface tension term but refer to [25, 26, 98] where these topics are discussed extensively alongside their numerical implementations in Basilisk.

[41]: Brackbill et al. (1992), ‘A continuum method for modeling surface tension’

[38]: Scardovelli et al. (1999), ‘Direct numerical simulation of free-surface and interfacial flow’

[39]: Sussman et al. (1994), ‘A level set approach for computing solutions to incompressible two-phase flow’

[25]: Popinet (2003), ‘Gerris: a tree-based adaptive solver for the incompressible Euler equations in complex geometries’

[26]: Popinet (2009), ‘An accurate adaptive solver for surface-tension-driven interfacial flows’

[98]: Popinet (2018), ‘Numerical models of surface tension’

### 4.2.2 Linear stability analysis

In the context of linear stability theory, sustained coherent structures appearing in a flow may be analysed by the exponential growth of infinitesimal disturbances on a basic state flow field. To this end, the derivation of the linearised form of equation (4.1) follows verbatim the description in [128]. Upon non-dimensionalisation, using  $\rho_1$ ,  $\mu_1$  and suitable length and velocity scales we obtain

[128]: Schmidt et al. (2021), ‘Global stability and nonlinear dynamics of wake flows with a two-fluid interface’

$$[\bar{\rho} + H_\epsilon(\phi)(1 - \bar{\rho})](\partial_t \mathbf{u} + \mathbf{u} \cdot \nabla \mathbf{u}) = -\nabla p + \frac{1}{Re} \nabla \cdot [(\bar{\mu} + H_\epsilon(\phi)(1 - \bar{\mu}))(\nabla \mathbf{u} + \nabla^T \mathbf{u})] + \frac{1}{We} \kappa \mathbf{n} \delta_\epsilon(\phi), \quad (4.5)$$

where the Reynolds number is  $Re = \rho_1 U_{\text{ref}} D_{\text{ref}} / \mu_1$ , the Weber number is  $We = \rho_1 U_{\text{ref}}^2 D_{\text{ref}} / \sigma$ ,  $\bar{\rho} = \rho_2 / \rho_1$  and  $\bar{\mu} = \mu_2 / \mu_1$ . Further we define the vector  $\mathbf{q} = (\mathbf{u}, p, \psi)^T$ , containing the flow variables, where  $\psi$  may denote either  $c$  or  $\phi$  as required.

The quantities in equation (4.5) are expanded as,  $\mathbf{q} = \mathbf{Q} + \zeta \mathbf{q}'$ , where  $\mathbf{Q} = (\mathbf{U}, \Psi)^T$  is the basic state and  $\mathbf{q}' = (\mathbf{u}', p', \psi')^T$  is a disturbance, with  $0 < \zeta \ll 1$ . The disturbances are composed of normal modes

$$\mathbf{q}'(x, y, z, t) = \hat{\mathbf{q}}_j(x, y, z) e^{\lambda_j t} + \text{c.c.} \quad (4.6)$$

where c.c. denotes the complex conjugate. At leading order, the resulting linear disturbance equations in a level-set formulation are then given as

$$\begin{aligned} & [\bar{\rho} + H_\epsilon(\Phi)(1 - \bar{\rho})](\partial_t \mathbf{u}' + \mathbf{u}' \cdot \nabla \mathbf{U} + \mathbf{U} \cdot \nabla \mathbf{u}') + 2[\delta_\epsilon(\Phi)\phi'(1 - \bar{\rho})](\mathbf{U} \cdot \nabla \mathbf{U}) \\ & = -\nabla p' + \frac{1}{Re} \nabla \cdot [(\bar{\mu} + H_\epsilon(\Phi)(1 - \bar{\mu}))(\nabla \mathbf{u}' + \nabla^T \mathbf{u}')] \\ & + \frac{1}{Re} \nabla \cdot [(\delta_\epsilon(\Phi)\phi'(1 - \bar{\mu}))(\nabla \mathbf{U} + \nabla^T \mathbf{U})] + \mathbf{F}_s(\Phi, \phi'), \end{aligned} \quad (4.7a)$$

$$\partial_t \phi' + \nabla \cdot (\Phi \mathbf{u}') + \nabla \cdot (\phi' \mathbf{U}) = 0, \quad (4.7b)$$

$$\nabla \cdot \mathbf{u}' = 0. \quad (4.7c)$$

The linearised momentum equation (4.7a) for interfacial two-phase flows contains several additional terms, as compared to the equation for single-phase flow which stem from the disturbances of the viscosity and density, as well as the linearised surface tension force  $\mathbf{F}_s(\Phi, \phi')$ . These terms are described in detail in [128].

The linear system (4.7) is stated in compact form as

$$\frac{\partial \mathbf{q}'}{\partial t} = \mathcal{L}(\mathbf{Q}) \mathbf{q}', \quad (4.8)$$

[46]: Tuckerman et al. (2000), ‘Bifurcation analysis for timesteppers’

[47]: Barkley et al. (2008), ‘Direct optimal growth analysis for timesteppers’

where  $\mathcal{L}(\mathbf{Q})$  is the linearised Navier-Stokes operator. Following [46] and [47], the system (4.8) may be reformulated as an eigenvalue problem where

$\lambda_j$  and  $\hat{\mathbf{q}}_j$  are the complex-valued eigenvalues and eigenmodes, respectively, and solved iteratively with an Arnoldi method.

In practice, the construction of the subspace in the Arnoldi method amounts to time-stepping of the linearised equations (4.7) to obtain each Krylov vector. Following [128], the equations (4.7) are discretised in Basilisk, similarly to the nonlinear equations. As a consequence, both the nonlinear and linear computations are facilitated using the same numerical schemes and on the same computational grid.

[128]: Schmidt et al. (2021), ‘Global stability and nonlinear dynamics of wake flows with a two-fluid interface’

### 4.2.3 Flow configuration

The three-dimensional nonlinear and linear equations, (4.1) and (4.7) respectively, are solved in cartesian coordinates on an octree-discretised grid in a cuboid domain. The total domain edge length is  $L_{tot} = 128$  and a cylindrical region with  $0 \leq z \leq 64$  and  $0 \leq r \leq 8$  is statically refined with a cell edge length of  $\Delta = 0.0625$  (The convergence of the employed mesh for the linear and nonlinear analysis is demonstrated in Appendix 4.8.1). The domain outside the refined cylinder is successively coarsened and indirectly acts as a sponge layer in downstream direction, by numerically diffusing vorticity and ensuring an approximately vorticity-free outflow. All length scales are nondimensionalised with respect to the interface position at the inlet as given in equation (4.10). A schematic view of the domain is provided in figure 4.1.

For the nonlinear flow, the parameterized Grabowski-Berger profile [117], with the velocity stated in cylindrical coordinates as  $\mathbf{u} = (u_z, u_r, u_\theta)^T$ , is given as

[117]: Grabowski et al. (1976), ‘Solutions of the Navier-Stokes equations for vortex breakdown’

$$u_z = \begin{cases} \alpha + (1 - \alpha)r^2(6 - 8r + 3r^2) & \text{if } r \leq 1 \\ 1 & \text{if } r > 1 \end{cases} \quad (4.9a)$$

$$u_\theta = \begin{cases} Sr(2 - r^2) & \text{if } r \leq 1 \\ S/r & \text{if } r > 1 \end{cases} \quad (4.9b)$$

$$u_r = 0, \quad (4.9c)$$

where  $S$  is the nondimensional swirl number which is defined as the azimuthal velocity at  $r = 1$ , relative to the axial free-stream velocity:  $S = u_\theta(r = 1)/u_{z,\infty}$ . The parameter  $\alpha$  blends between jet ( $\alpha > 1$ ) and wake-like ( $\alpha < 1$ ) profiles of the core region  $r \leq 1$  and is defined as  $\alpha = u_z(r = 0)/u_{z,\infty}$ . Throughout this work, we only consider  $\alpha = 1$ , i.e. a constant axial flow profile.

The Grabowski-Berger profile was initially introduced for single-phase flow, so the extension to interfacial flow requires the definition of an interface position. Derived from the parameterization of the  $u_z$  component, a natural choice is the radial limit of the inner core region at  $r = 1$ . Consequently, we define the following profiles for the volume fraction  $c$ , as well as for a level-set-like passive scalar  $\phi$ , that is co-advected alongside  $c$ :

$$c = \begin{cases} 0 & \text{if } r \leq 1 \\ 1 & \text{if } r > 1 \end{cases}, \quad \phi = r - 1. \quad (4.10a)$$

[7]: Ruith et al. (2003), ‘Three-dimensional vortex breakdown in swirling jets and wakes: direct numerical simulation’

[129]: Ruith et al. (2004), ‘Development of boundary conditions for direct numerical simulations of three-dimensional vortex breakdown phenomena in semi-infinite domains’

The profile is prescribed in cartesian coordinates at the inlet  $\Omega_1$ , located on the left hand side of the domain. Previous studies (e.g. [7, 129]) have discussed the sensitivity of lateral and outflow boundary conditions on the dynamics of laminar swirling flows. Therein, convective boundary conditions are advocated to avoid reflections at the boundaries that affect the flow in the interior of the domain. However, given the grid coarsening in downstream direction for  $z > 45$  and  $r > 8$ , in combination with a sufficiently large total domain size, we have found it sufficient to employ a standard outflow condition,

$$\partial \mathbf{q} / \partial \mathbf{n}_\Omega = 0, \quad p = 0, \quad (4.11a)$$

imposed on the right hand side boundary of the domain  $\Omega_2$  where  $\mathbf{n}_\Omega$  is the unit normal vector at the domain boundary. On the lateral domain boundaries  $\Omega_3$  we employ symmetry conditions

$$\mathbf{u} \cdot \mathbf{n}_\Omega = 0, \quad \partial \psi / \partial \mathbf{n}_\Omega = 0, \quad \partial(\mathbf{u} \cdot \mathbf{t}_\Omega) / \partial \mathbf{n}_\Omega = 0, \quad (4.12a)$$

where  $\mathbf{t}_\Omega$  is the unit tangent vector.

For the linear flow, vanishing disturbances  $\hat{\mathbf{q}} = 0$  are enforced at  $\Omega_1$  and  $\Omega_2$ , as well as  $\partial \hat{\mathbf{p}} / \partial \mathbf{n}_\Omega = 0$ . The boundary conditions for disturbances along  $\Omega_3$  are similar to the nonlinear flow. Additionally, for  $z > 64$ , a damping volume force is added such that in this region the disturbances are of the form  $\tilde{\mathbf{q}} = \hat{\mathbf{q}}(1 - \eta(z))$ . The damping function is formulated as

$$\eta(z) = \frac{1}{2} + \frac{1}{2} \tanh\left(\frac{z - z_0}{l}\right), \quad (4.13)$$

with  $z_0 = 1.25 \cdot 64$  and  $l = 4$  as scaling parameters.

The basic state flow fields  $\mathbf{Q}$  required for the linear analysis are obtained with axisymmetric nonlinear simulations including swirl. The simulations are advanced towards steady state solutions until convergence with a residual  $\|\mathbf{u}^{n+1} - \mathbf{u}^n\|_\infty = O(10^{-8})$ . The axisymmetric fields are then rotated and cubically interpolated on the three-dimensional cartesian grid, used for the linear analysis.

## 4.2.4 Modal decomposition of the nonlinear flow

### Azimuthal Fourier decomposition

Given the rotational character of the flow, the computed time-resolved fields are cubically interpolated from the computational grid in cartesian

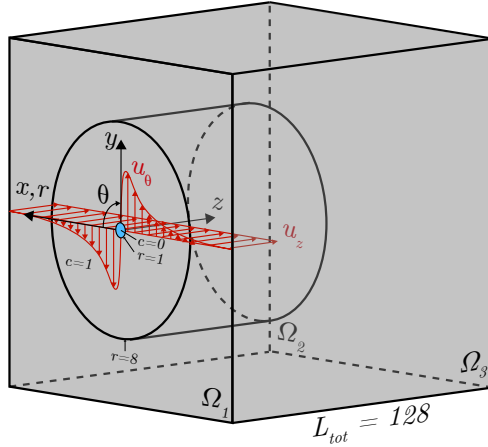


**Figure 4.1:** Schematic view of the computational domain.

coordinates  $(x, y, z)^T$  onto a cylindrical grid  $(r, \theta, z)^T$ . The interpolated fields are then decomposed into azimuthal Fourier modes

$$\mathbf{q}'(r, \theta, z, t) = \sum_{m=-\infty}^{\infty} \hat{\mathbf{q}}_m(r, m, z, t) e^{im\theta}, \quad (4.14)$$

with  $m$  being the azimuthal wavenumber, prior to subsequent analysis. The azimuthal wavenumbers aid in the characterisation of the structures observed in the swirling flow. Structures with  $m = 0$  are axisymmetric whereas  $|m| > 1$  correspond to helical structures. The helical structures further, can be characterised by their sense of rotation and winding with respect to the orientation of the coordinate system or the direction of the imposed swirl. Consequently, four different combinations of helical structures may be observed: co-rotating and co-winding, co-rotating and counter-winding, counter-rotating and co-winding or counter-rotating and counter-winding.

In the present flow configuration a positive  $\theta$  points in clock-wise direction (figure 4.1). Together with the definition (4.14),  $m > 0$  and  $m < 0$  correspond to a clock-wise and counter-clockwise rotation, respectively. The rotation sense of the swirl, imposed at the inlet is positive, thus oriented in clock-wise direction. The winding sense of the helices in the simulated flow is deduced visually. In line with previous studies (e.g. [7, 112, 130]), the observed structures in the flow are identified to be co-rotating and counter-winding with respect to the imposed swirl and the direction of positive  $\theta$ . Therefore, positive azimuthal wavenumbers  $m > 0$  are used throughout this work to distinguish the different helical structures.

### Dynamic mode decomposition

For analysis of the overall flow dynamics, the flow is decomposed into temporal modes using the Dynamic mode decomposition (DMD) [131, 132]. The resulting decomposition is an approximation of the Koopman operator, which is a linear infinite dimensional operator describing a nonlinear dynamical system. Given a set of  $n$  snapshots of the flow  $\mathbf{q}'^n$ , the DMD yields a decomposition

[7]: Ruith et al. (2003), ‘Three-dimensional vortex breakdown in swirling jets and wakes: direct numerical simulation’

[112]: Escudier et al. (1982), ‘Vortex-flow regimes’

[130]: Oberleithner et al. (2014), ‘On the impact of swirl on the growth of coherent structures’

[131]: Rowley et al. (2009), ‘Spectral analysis of nonlinear flows’

[132]: Schmid (2010), ‘Dynamic mode decomposition of numerical and experimental data’

$$\mathbf{q}'^n = \sum_{j=1}^{M-1} \lambda_j^n \hat{\mathbf{q}}_j + \mathbf{r}, \quad (4.15)$$

where  $\lambda_j^n$  and  $\hat{\mathbf{q}}_j$  are the Ritz values and vectors that approximate the Koopman modes of the dynamical system. The residual  $\mathbf{r}$  is the result of the projection onto the subspace, spanned by  $\mathbf{q}'^n$ .

### Bispectral mode decomposition

[110]: Schmidt (2020), 'Bispectral mode decomposition of nonlinear flows'

Additionally, we employ the Bispectral mode decomposition (BMD) which has recently been introduced by [110] and is briefly summarised here, given its novelty. The BMD allows for the identification of nonlinear triadic interactions that result from a quadratic phase-coupling of two frequencies. For illustration, we write equation (4.1) in compact form with disturbances as in equation (4.6),

$$\frac{\partial \mathbf{q}'}{\partial t} = \mathcal{L}(\mathbf{Q})\mathbf{q}' + \mathcal{Q}(\mathbf{q}', \mathbf{q}') + \mathcal{C}(\mathbf{q}', \mathbf{q}', \mathbf{q}') + \mathcal{S}(\mathbf{q}'), \quad (4.16)$$

and identify four groups of terms on the right hand side. The first term is the linear interaction between the base flow terms and a single disturbance quantity, the second term contains quadratic nonlinearities of the velocity disturbances with itself and interactions of the velocity and density or viscosity disturbances, as well as the quadratic nonlinear part of the surface tension term. The third term contains cubic interactions of the velocity and density disturbances, as well as the cubic nonlinear part of the surface tension term. The last term contains the remaining higher-order nonlinearities of the surface tension term. Consequently, triadic interactions are driven by  $\mathcal{Q}(\mathbf{q}', \mathbf{q}')$ .

A triad is described by the frequency triplet  $(\omega_x, \omega_y, \omega_{x+y})$  where the frequencies  $\omega_x$  and  $\omega_y$  interact to form a third frequency  $\omega_{x+y}$ , obeying the condition  $\omega_x \pm \omega_y \pm \omega_{x+y} = 0$ .

The BMD constitutes an analogy to the classical bispectrum for multi-dimensional signals. Given a signal  $q(t)$  and the third-order moment  $R_{qqq} = E[q(t)q(t - \tau_x)q(t - \tau_y)]$  where  $E[\cdot]$  is the expectation value, the bispectrum is defined as the double Fourier transform of  $R_{qqq}$ ,

$$\begin{aligned} S_{qqq}(\omega_x, \omega_y) &= \int_{-\infty}^{\infty} \int_{-\infty}^{\infty} R_{qqq}(\tau_x, \tau_y) e^{-i(\omega_x \tau_x + \omega_y \tau_y)} d\tau_x d\tau_y \\ &= \lim_{T \rightarrow \infty} \frac{1}{T} E[\hat{q}(\omega_y)^* \hat{q}(\omega_x) \hat{q}(\omega_y + \omega_x)], \end{aligned} \quad (4.17)$$

where  $(\cdot)^*$  is the complex conjugate and  $\hat{q}(\omega_x)$  and  $\hat{q}(\omega_y)$  are the  $x$ -th and  $y$ -th frequency component of the Fourier transform of  $\hat{q}$ .

The BMD, for a multidimensional signal  $\mathbf{q}(\mathbf{x}, t)$ , is derived from the bispectrum as the expectation value of the spatial integral of the Fourier transforms  $\hat{\mathbf{q}}_x = \hat{\mathbf{q}}(\mathbf{x}, \omega_x)$ ,  $\hat{\mathbf{q}}_y = \hat{\mathbf{q}}(\mathbf{x}, \omega_y)$  and  $\hat{\mathbf{q}}_{x+y} = \hat{\mathbf{q}}(\mathbf{x}, \omega_{x+y})$ ,

$$b(\omega_x, \omega_y) \equiv E \left[ \int_{\Omega} \hat{\mathbf{q}}_x \circ \hat{\mathbf{q}}_y \circ \hat{\mathbf{q}}_{x+y} \, d\mathbf{x} \right], \quad (4.18)$$

where  $\circ$  denotes the element-wise product. Now, taking a number of  $N_{\text{blk}}$  realisations of the Fourier transform  $\hat{\mathbf{q}}$ , the bispectral modes, representing the spatial structure of the triadic interaction, are defined as

$$\phi_{x+y}^{[i]}(\mathbf{x}, f_{x+y}) = \sum_{j=1}^{N_{\text{blk}}} a_{ij}(f_{x+y}) \hat{\mathbf{q}}_{x+y}^{[j]}. \quad (4.19)$$

The cross-frequency fields, which quantify the phase-alignment of two frequencies, are given as

$$\phi_{xoy}^{[i]}(\mathbf{x}, f_x, f_y) = \sum_{j=1}^{N_{\text{blk}}} a_{ij}(f_{x+y}) \hat{\mathbf{q}}_{xoy}^{[j]}, \quad (4.20)$$

where  $\hat{\mathbf{q}}_{xoy} = \hat{\mathbf{q}}_x \circ \hat{\mathbf{q}}_y$ . The bispectral modes are therefore linear combinations of the Fourier modes  $\hat{\mathbf{q}}$  whereas the cross-frequency fields are maps of phase-alignment. The mode bispectrum (4.18) is derived from the spatial integration of the element-wise product

$$\psi_{x,y}(\mathbf{x}, \omega_x, \omega_y) = |\hat{\mathbf{q}}_{xoy} \circ \hat{\mathbf{q}}_{x+y}|, \quad (4.21)$$

which is a measure of the local biconrelation of  $\omega_x$  and  $\omega_y$  and hence we may call  $\psi$  an interaction map.

The goal then is to find the coefficients  $a_{ij}$  such that the modulus of  $b(\omega_x, \omega_y)$  in equation (4.18) is maximised. The result is the complex mode spectrum  $\lambda_1(\omega_x, \omega_y)$  which quantifies the triadic interaction of the frequency triplet  $(\omega_x, \omega_y, \omega_{x+y})$ . Details on the exact algorithm may be found in Schmidt (2020).

Similar to the bispectrum of a single signal,  $S_{qqq}(\omega_x, \omega_y)$ , the cross-bispectrum of up to three different signals is given as  $S_{qrs}(\omega_x, \omega_y)$ . It identifies triadic interactions acting across the involved signals. In similar fashion, the cross-BMD of three different fields  $\mathbf{q}, \mathbf{r}, \mathbf{s}$  may be computed.

### 4.3 Steady axisymmetric breakdown states

The governing equations for interfacial flows, as derived in §4.2, lead to a notably larger parameter space as compared to a single-phase flow. While a comprehensive parameter study of interfacial swirling flows is beyond the scope of this work, it is instructive to map out some parameter combinations for axisymmetric configurations to get a clear picture when axisymmetric breakdown is promoted or inhibited.

For the rest of this work we fix  $Re = 200$ , and since we are interested in the isolated effect of the viscosity variation, we assume equal densities of both phases (i.e.  $\bar{\rho} = 1$ ) and neglect the influence of surface tension ( $We = \infty$ ).

Further, we assume the inner phase to be equally or less viscous than the outer phase ( $\tilde{\mu} \leq 1$ ). The remaining parameters then are  $S$  and  $\tilde{\mu}$ .

In figure 4.2a the dependence of the critical swirl  $S_c$  in relation to  $\tilde{\mu}$  is plotted (blue line). For each  $\tilde{\mu}$ , indicated by a dot in the plot, flows are computed with varying  $S$  in increments of 0.1. The plotted values of  $S_c$  are the smallest ones for which a stagnation point forms in the flow which leads to vortex breakdown. It is seen that a reduction of  $\tilde{\mu}$ , i.e. a decrease of the viscosity of the inner fluid, leads to a decrease of  $S_c$  thus making the flow more susceptible to axisymmetric breakdown.

For further illustration of the flow at pre- and post-breakdown states, contour plots of the axial velocity field  $u_z$  for the dots along the black lines in figure 4.2a are presented in figures 4.3a and 4.3b. The interface is shown as a solid white line and the  $u_z = 0$  contour, indicating reverse flow, as a dashed line. The location of the minimum of  $u_z$  is shown as a red dot. Additionally, for the presented configurations, the minimum axial velocity is plotted along  $z$  in figures 4.2b (corresponding to the horizontal dots in figure 4.2a) and 4.2c (corresponding to the vertical dots in figure 4.2a).

Fixing the swirl at  $S = 0.8$  (thus moving along the dashed horizontal line in figure 4.2a), the flow at  $\tilde{\mu} = 0.75$  is located in the pre-breakdown region, consequently the axial velocity remains positive and no reverse flow occurs. For  $\tilde{\mu} = 0.5$ , axisymmetric breakdown has just occurred, and a single, small breakdown bubble, centred around  $z = 5$ , is formed. For  $\tilde{\mu} = 0.25, 0.1$ , the strength of the reverse flow increases, as the bubble grows and forms a ring while moving upstream. Additionally, a second and third recirculation area form downstream of the first bubble. As a consequence of the bubble formations, the interface is pushed outwards in radial direction.

Now fixing  $\tilde{\mu} = 0.5$ , breakdown occurs for all presented configurations. For increased swirl, the single breakdown bubble present at  $S = 0.8$  shows a similar behaviour as when decreasing  $\tilde{\mu}$ . It appears, however, that it converges towards a fixed size and generally remains smaller. Similarly, a second breakdown bubble forms downstream of the first one that is elongated when increasing  $S$  until it extends over the full length of the considered domain. As a consequence, no third breakdown bubble is formed.

For completing the picture, a comparison of the two-phase ( $\tilde{\mu} = 0.5$ ) and single-phase flow ( $\tilde{\mu} = 1$ ) is shown for  $S = 0.9, 1.3$  in figure 4.2d. The plots for  $\tilde{\mu} = 1$  are similar to those analysed by [7]. Similar to their analysis, a first breakdown has just occurred for  $S = 0.9$  and a second breakdown region is formed for  $S = 1.3$ .

It is seen that the introduction of a low-viscosity inner fluid phase promotes the formation and growth of axisymmetric breakdown bubbles such that in comparison to a single-phase flow, the breakdown regions are larger and the reverse flow is stronger in case of a two-phase flow. The relevance of multiple breakdowns as seen here, however, is questionable for the three-dimensional flow as has been pointed out by [7]. It is likely that the downstream bubbles are quickly overcome by helical instability and thus do not prevail in the three-dimensional flow.

[7]: Ruith et al. (2003), ‘Three-dimensional vortex breakdown in swirling jets and wakes: direct numerical simulation’

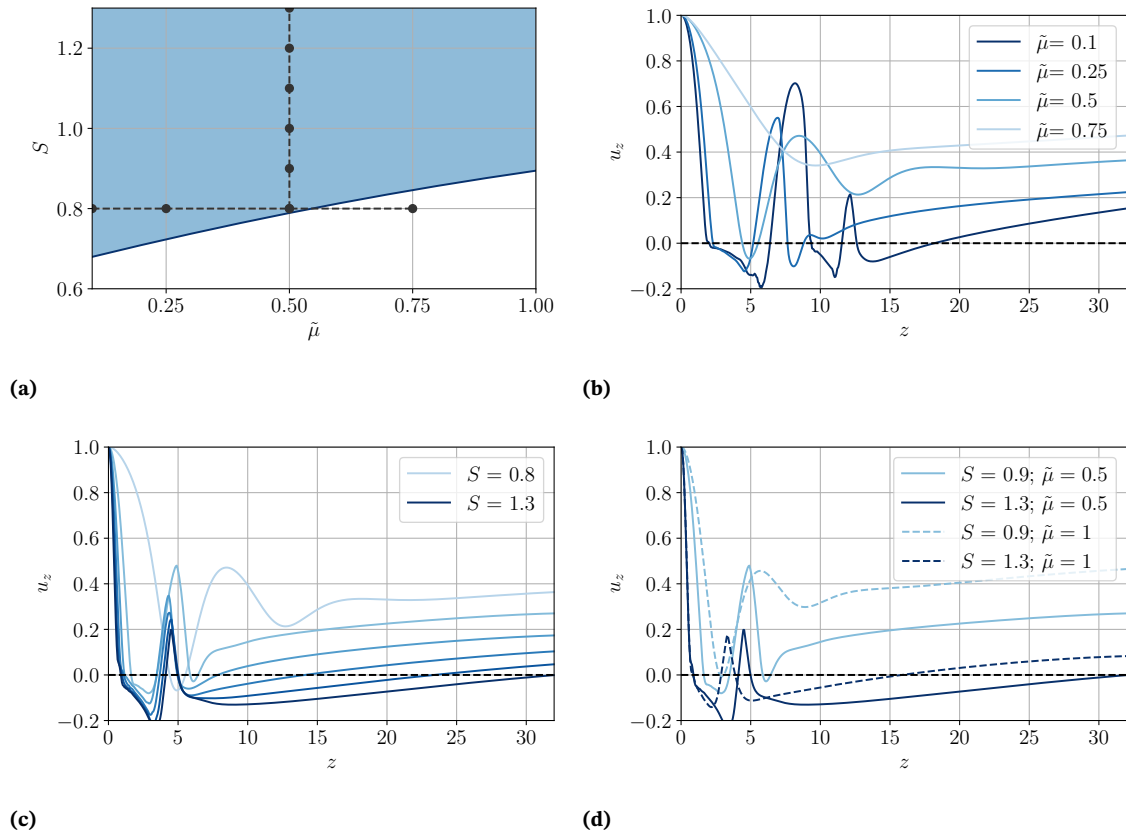


**Figure 4.2:** (a) In blue: Critical swirl  $S_c$  in relation to  $\tilde{\mu}$  above which axisymmetric breakdown is observed. As black dots: configurations plotted in figures 4.2b, 4.2c and 4.3a, 4.3b. (b) Minimum axial velocity at every stream-wise location for  $S = 0.8$  and varying  $\tilde{\mu}$ . (c) Similar plot for  $\tilde{\mu} = 0.5$  and varying  $S$ . (d) Comparison of single-phase ( $\tilde{\mu} = 1$ ) and two-phase flow ( $\tilde{\mu} = 0.5$ ) for varying  $S$ .

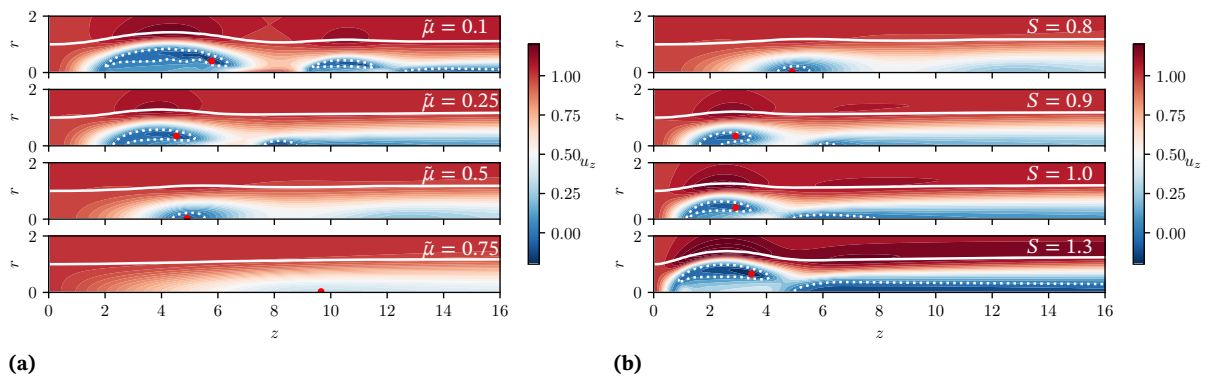


**Figure 4.3:** Contour plots of  $u_z$  of axisymmetric flows for  $S = 0.8$  and varying  $\tilde{\mu}$  (a) and  $S$  (b) (for the grey dots in figure 4.2b). The interface is shown as solid white line and the  $u_z = 0$  contour, indicating reverse flow, as dashed line. The location of the minimum of  $u_z$  is shown as red dot.

## 4.4 Linear global modes

Continuing from the analysis of the axisymmetric flow, the obtained steady breakdown states are used as a base flow to compute linear global modes of the respective flow configurations. In previous studies of single-phase swirling flows, helical destabilisation has been successfully explained through the instability of the Navier-Stokes operator, linearised around a stationary basic state (e.g. [9, 133]). It was shown that the flow undergoes a supercritical Hopf bifurcation through the destabilisation of a single helical global mode. In order to investigate the global linear stability of the present interfacial flow, we employ the solution procedure described in §4.2.2 to compute the most unstable global modes for a selection of swirl numbers above  $S_c = 0.79$  with  $\tilde{\mu} = 0.5$  (corresponding to the vertical dots in figure 4.2a).

The growth rates  $\text{Re}(\lambda)$  and frequencies  $\text{Im}(\lambda)$  of the computed eigenvalues at each swirl number, ranging from  $S = 0.78$  to  $S = 1$  are shown in figure 4.4a where increments of 0.01 are used to compute solutions between  $0.78 \leq S \leq 0.81$ . The grey shaded area marks the regime where the nonlinear flow which will be analysed in §4.5, converges towards a stationary solution. Additionally, tabulated values for growth rates and frequencies of the computed eigenvalues of the linear analysis for  $S = 0.8, 0.9, 1.0$  are given in table 4.1, as well as the frequencies of the equivalent modes from the nonlinear flow.

As is seen, the flow remains linearly stable to perturbations for  $S \leq 0.78$  but becomes unstable to two global modes,  $\omega_1^l$  and  $\omega_2^l$  that bifurcate simultaneously at  $S \approx 0.79$ . Their frequencies are related harmonically as  $\omega_2^l \approx 2\omega_1^l$ . For the largest investigated swirl,  $S = 1.0$ , a destabilisation of two additional modes,  $\omega_l^l$  and  $\omega_m^l$  is observed. Their nomenclature here, is chosen in accordance to the analysis of the nonlinear flow in §4.5.3 where two modes,  $\omega_l, \omega_m$  are found that bear close resemblance to these linear modes. When comparing the boundary curve in figure 4.2a, which separates regions of columnar flow and vortex breakdown, with the point of neutral stability at  $S \approx 0.79$  in figure 4.4a, it is seen that they essentially coincide. Therefore, the topological change from a columnar state to a breakdown state is a prerequisite for global instability in the present configurations. The simultaneous onset of axisymmetric breakdown and global instability is in contrast to previous studies of the single-phase Grabowski-Berger vortex where usually a notable regime exists where the flow, despite axisymmetric breakdown, remains stable (e.g. [7], [9]).

A direct comparison of the frequencies of  $\omega^l$  predicted by the linear analysis with the dominant frequencies found in the nonlinear flow is shown in figure 4.4b. As can be seen, the agreement is excellent up to  $S = 0.9$ . For  $S = 1.0$  on the other hand, a notable deviation of the frequencies of  $\omega_1^l$  and  $\omega_2^l$  is found whereas the agreement of the newly bifurcated modes  $\omega_l^l$  and  $\omega_m^l$  with their nonlinear equivalents remains good.

The three-dimensional mode shapes of the linear modes for  $S = 0.8, 0.9, 1.0$  are plotted as velocity and level-set disturbances,  $\text{Re}(\hat{u}_\theta^l)$  and  $\text{Re}(\hat{\phi}^l)$  in figure 4.5. Additionally, each mode is decomposed into its azimuthal wavenumbers using the conventions described in §4.2.4 and the energy contained in each wavenumber is calculated via the standard  $L_2$  norm.

[9]: Meliga et al. (2012), ‘A weakly nonlinear mechanism for mode selection in swirling jets’

[133]: Qadri et al. (2013), ‘Structural sensitivity of spiral vortex breakdown’

[7]: Ruith et al. (2003), ‘Three-dimensional vortex breakdown in swirling jets and wakes: direct numerical simulation’

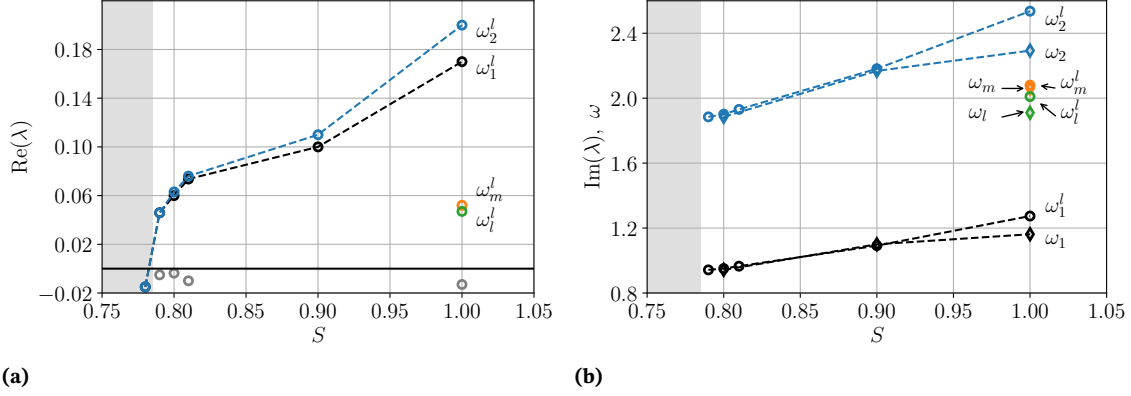


**Figure 4.4:** (a) Plot of the growth rates  $\text{Re}(\lambda)$  of the unstable linear global modes  $\omega^l$ , obtained from the linear analysis, over several  $S$ . The grey circles denote stable modes. (b) Comparison of the frequencies  $\text{Im}(\lambda)$  of the linear global modes  $\omega^l$  (denoted by  $\circ$ ) with the limit cycle oscillations  $\omega$  (denoted by  $\diamond$ ) of the nonlinear flow in §4.5. The dashed lines connecting the data points are printed for improved readability and should not be interpreted as a linear variation of the data.

$S$		$\text{Re}(\lambda)$	$\text{Im}(\lambda)$	$\omega$
0.8	$\omega_2^l$ :	0.06	1.9	$\omega_2$ : 1.91
	$\omega_1^l$ :	0.06	0.95	$\omega_1$ : 0.96
0.9	$\omega_2^l$ :	0.11	2.18	$\omega_2$ : 2.22
	$\omega_1^l$ :	0.10	1.09	$\omega_1$ : 1.1
1.0	$\omega_2^l$ :	0.20	2.53	$\omega_2$ : 2.37
	$\omega_1^l$ :	0.17	1.27	$\omega_1$ : 1.19
	$\omega_m^l$ :	0.05	2.08	$\omega_m$ : 2.08
	$\omega_l^l$ :	0.04	2.01	$\omega_l$ : 1.93

**Table 4.1:** Tabulated values of growth rates  $\text{Re}(\lambda)$  and frequencies  $\text{Im}(\lambda)$  of the linear modes  $\omega^l$ . The corresponding frequencies  $\omega$ , obtained from the nonlinear flow in §4.5 are shown for comparison.

A pictographic bar chart is given that shows the mode's relative energy content per azimuthal wavenumber  $m = 0, 1, 2, 3$ .

The mode shapes for  $S = 0.8$  reveal that the two unstable global modes have different azimuthal wavenumbers, where  $\omega_1^l$  has  $m = 1$  and  $\omega_2^l$  has  $m = 2$ . This also is seen from the single and double spiralling shape of the respective modes. Both modes are active in the wake of the breakdown bubble. For  $S = 0.9$ , the results are qualitatively similar but the modes are shifted upstream, closer to the breakdown bubble. For  $S = 1.0$ , the mode shapes of  $\omega_1^l$  and  $\omega_2^l$  are concentrated in the immediate vicinity of the breakdown bubble. Conversely, the newly bifurcated modes  $\omega_l^l$  and  $\omega_m^l$  are located in the far wake region of the flow. Both modes are double helical ( $m = 2$ ). Following the sign convention for  $m$  made in §4.2.4, all modes shown in figure 4.5 are co-rotating and counter-winding with respect to the base flow swirl orientation.

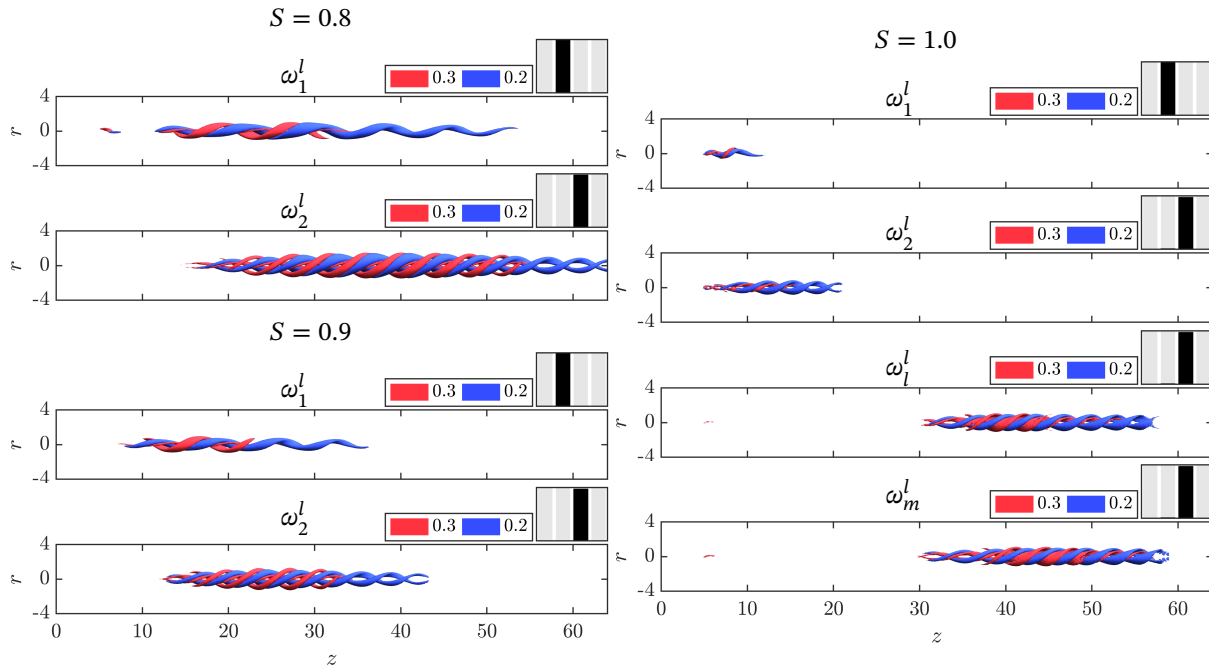


**Figure 4.5:** Shapes of the unstable linear global modes ( $\text{Re}(\hat{u}'_\theta)/\max[\text{Re}(\hat{u}'_\theta)]$  in red,  $\text{Re}(\hat{\phi}'^l)/\max[\text{Re}(\hat{\phi}'^l)]$  in blue) at the respective swirl numbers. The pictographic bar charts show the relative contributions of the respective wavenumbers  $m = 0, 1, 2, 3$  (from left to right) to each mode.

## 4.5 Analysis of helical instability in the nonlinear flow

The analysis of the axisymmetric breakdown in §4.3 and the linear stability analysis conducted in §4.4 have shown that the introduction of a second, less viscous fluid has a destabilising effect on the flow, resulting in vortex breakdown at lower swirl and also in an earlier destabilisation of helical global modes on the breakdown state. Further, the linear stability analysis has revealed the simultaneous destabilisation of two unstable global modes in the flow that have harmonic frequencies. It is thus to be expected that a strong synchronisation and resonance of these modes can be observed in the nonlinear flow. This is investigated in the following by performing nonlinear simulations of the flow and subsequent analysis of its dynamics.

### 4.5.1 Vortex dynamics

For the nonlinear simulations, we restrict the analysis to  $S > 0.79$  which is beyond the bifurcation point of the two identified helical global modes (refer to figure 4.4a). The three-dimensional simulations are initialised from the axisymmetric basic states, analysed in §4.3. After initialisation, disturbances develop in the flow and lead to a loss of axisymmetry. Consequently, a spiralling motion forms in the wake of the breakdown bubble, that deforms the interface.

For a phenomenological characterisation of the flow, the vortex dynamics of the three configurations  $S = 0.8, 0.9, 1.0$  are visualised via isosurfaces of the  $\lambda_2$ -criterion [134] together with the fluid interface in figure 4.6.

[134]: Jeong et al. (1995), ‘On the identification of a vortex’

For each configuration the initial unstable base flow is shown as well as a snapshot of the fully developed flow. At  $S = 0.8$ , the  $\lambda_2$  isosurfaces suggest the presence of a predominantly single-helical vortex in the low-viscosity core of the flow. In contrast, the illustration of the interface clearly shows a double-helical structure. Both spirals are synchronised in space. It therefore appears that there are two different structures, one single-helical and one double-helical, present in the flow which exist at harmonic frequencies as is predicted by the linear analysis. For  $S = 0.9$ , the appearance of the flow changes. The core region now leans towards a double helix whereas the overall interface deformation is single helical. The illustration of the flow at  $S = 1.0$  shows an overall similar appearance to that of  $S = 0.9$  but reveals a more complex dynamics with several new structures appearing and disappearing in downstream development of the flow.

### 4.5.2 Time traces and disturbance growth

To illustrate the temporally oscillating behaviour of the observed instabilities, both in the vicinity of the breakdown bubble and in its wake, the time signal of the disturbance velocity  $u'_\theta$  at monitor points located at  $(r, \theta, z) = (0.05, 0, 5)$  and  $(r, \theta, z) = (0.05, 0, 30)$  is shown in figure 4.7a for all three configurations. Additionally, in every plot, the insets show a detailed excerpt of the time signal of both monitor points once the oscillation amplitude has saturated. Starting from the initial undisturbed basic state, perturbations develop in the flow that initially grow exponentially in time before nonlinear saturation sets in. It should be noted that these time signals show the nonlinear disturbance development of the superposition of both linearly unstable global modes. For  $S = 0.8, 0.9$ , a periodic oscillation is seen in the saturated state which corroborates the synchronisation of the modes observed in figure 4.6 and §4.4. For  $S = 1.0$  on the other hand, the saturated state exhibits a more complex pattern, including multiple frequencies, which however seem to retain a certain periodicity as is seen from the monitor point in the far wake ( $z = 30$ ). The display of the time signals, thus, gives a first illustration of the nonlinear disturbance development, originating from the unstable global modes. For  $S = 0.8$ , close to the bifurcation point, the nonlinear dynamics have a clear periodicity and are close to the linear dynamics whereas for larger swirl a clear influence of nonlinear interactions leads to a departure from the initial periodic state.

In figure 4.7b, the growth rates of the dominant linear modes  $\omega_1^l, \omega_2^l$  are compared to the logarithm of the envelope of the initial disturbance growth in the nonlinear flow. To this end  $u'_\theta$  is azimuthally decomposed into  $\hat{u}_{\theta,m}$ . The initial disturbance growth  $\hat{u}_{\theta,1}$  then is compared to the growth rate of  $\omega_1^l$  while the growth  $\hat{u}_{\theta,2}$  is compared to the growth rate of  $\omega_2^l$ . For  $S = 0.8, 0.9$  it is seen, that the growth rates predicted by the linear analysis agree well with the initial exponential growth of the helical disturbances in the nonlinear flow. At higher swirl,  $S = 1.0$ , the growth of the  $m = 1$  disturbance still agrees reasonably well to the growth of  $\omega_1^l$  whereas the growth of the  $m = 2$  disturbance is significantly larger than that of  $\omega_2^l$  and does not show a clear exponential behaviour which may be attributed to increased nonlinear mechanisms driving the instability growth.

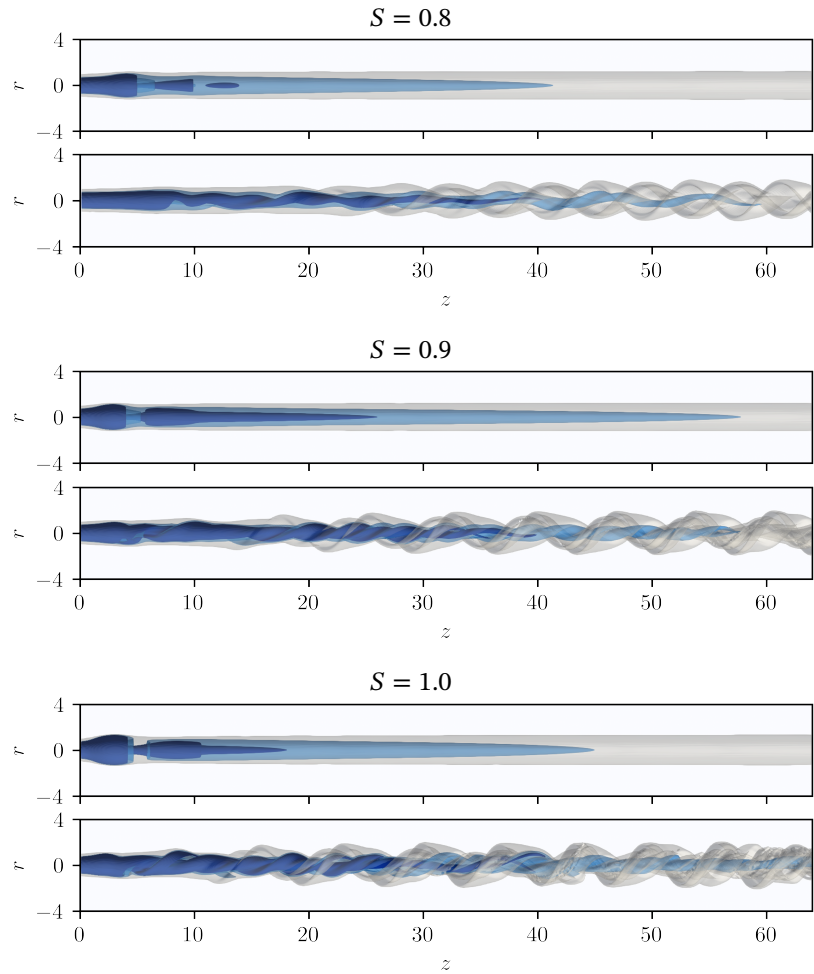


**Figure 4.6:** Visualisation of the instantaneous flow. The upper image shows the unstable axisymmetric basic state and the lower image the fully developed flow. Iso-surfaces: interface ( $c = 0.5$ , in translucent grey) and vortical structures ( $\lambda_2 = -0.5$ , in dark blue;  $\lambda_2 = -0.25$ , in light translucent blue).

### 4.5.3 Modal analysis

#### Global mode spectra

To gain more detailed insights on the nonlinear dynamics of the flow, a spectral analysis of the configurations  $S = 0.8, 0.9, 1.0$  using a DMD is performed. A sequence composed of  $n = 1024$  consecutive snapshots of  $\mathbf{q}'$  every  $\Delta t = 0.5$  is used for computation of the Ritz values  $\lambda_j^n$  once the flow has reached a stable limit cycle. The resulting amplitude spectra are presented in figure 4.8a. Further, a comparison of the frequencies of the linear modes  $\omega^l$  and the corresponding nonlinear modes  $\omega$  is given in table 4.1 and figure 4.4b.

The spectrum obtained for  $S = 0.8$  shows two dominant frequency peaks,  $\omega_1$  and  $\omega_2$  which are in close agreement with the global modes  $\omega_1^l$  and  $\omega_2^l$  found in the linear analysis. Both modes have similar amplitudes. For convenience, we denote this set of frequencies as  $\omega_l$  with  $l = 1, 2, 3, \dots$

Increasing the swirl number to  $S = 0.9$ , results in an overall similar spectrum where now, however,  $\omega_1$  is clearly the most energetic frequency. The analysis at  $S = 1.0$  reveals a significantly richer set of frequencies appearing in the spectrum. Apart from the frequencies contained in  $\omega_l$  multiple new peaks appear which are ultraharmonic frequencies with respect to  $\omega_l$  (their frequency ratios with respect to  $\omega_1$  may be found in

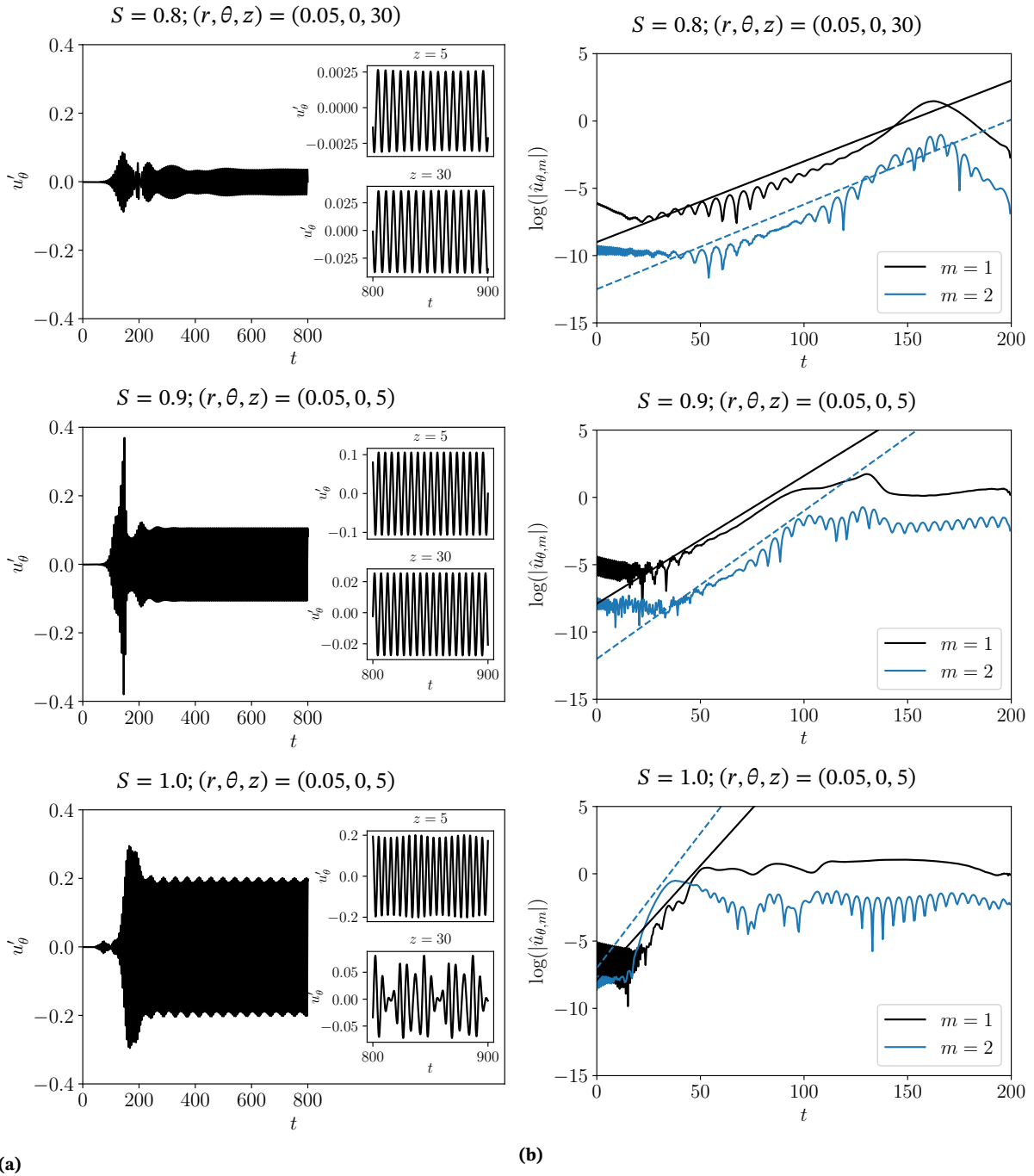


**Figure 4.7:** (a) Time signal  $u'_\theta$  of the monitor point as given in the title of each figure. The insets show a zoomed interval with  $z$ -position as annotated. (b) Disturbance growth of  $\hat{u}_{\theta,m}$ , for azimuthal wavenumbers  $m = 1$ ,  $m = 2$ , and exponential growth rate obtained from the linear analysis. The straight lines denoting the growth rate are shifted to align with the respective time signals.

Appendix 4.8.2). These are created through nonlinear interactions in the flow. We denote the resulting set as  $\omega_\kappa$  where  $\kappa = a, b, c, \dots, n$ . The mode  $\omega_1$  is again the most energetic mode.

### Stream-wise mode spectra and mode shapes

For further analysis of the spatial structure of the modes, the DMD is additionally performed in the  $r - \theta$  plane along several downstream stations of the flows for  $S = 0.8, 1.0$  (see figure 4.8b). Here, snapshots of the azimuthally decomposed vector  $\hat{\mathbf{q}}_m$  are used that allow for a separation of the involved wavenumbers in the spectrum plot. Consequently, at every stream-wise station, a spectrum for each azimuthal wavenumbers  $m = 0, 1, 2, 3$  is plotted. The mode shapes corresponding to the annotated modes are shown in figure 4.8c. They are computed from the full vector  $\mathbf{q}'$  and are illustrated via the azimuthal disturbance velocity  $u'_\theta$  and the interface level-set function  $\phi'$ . For each mode, a pictographic bar chart is given that shows the mode's relative energy content per azimuthal wavenumber  $m = 0, 1, 2, 3$ .

For  $S = 0.8$ , the energy of the mode  $\omega_1$  is almost exclusively contained in  $m = 1$  and the mode shape shows a single helix. Conversely,  $\omega_2$  has most contained in  $m = 2$  and thus displays a double spiralling structure.

The illustration of the mode structures for  $\omega_1$ , reveals a spatial separation of the velocity and interface disturbances. The former is prominent in the region around  $z = 10$ , which is shortly downstream of the axisymmetric breakdown bubble (near wake region). A second region, slightly detached from the first then extends throughout the downstream development of the flow (far wake region). This region is characterised by two separated spirals that wind concentrically but with a phase lag. In contrast, the interfacial disturbance only develops a significant amplitude in the far wake for  $z > 20$  which however keeps growing further downstream and coincides with the second activity region of the velocity disturbance. The  $m = 2$  mode corresponding to  $\omega_2$  is concentrated in the region  $z > 20$  and barely shows any activity upstream in the proximity of the breakdown bubble. For this mode, the velocity disturbance shows two concentrically winding double helices while the interface disturbance is composed of a single double helix. The comparison of the mode structures in figure 4.8 with the full nonlinear flow in figure 4.6 corroborates this description: The interfacial disturbances in the near wake are small and the instability is mainly driven by velocity disturbances of  $\omega_1$  in the core fluid. In the far wake, interfacial disturbances grow and are dominated by  $\omega_2$ , which produces the characteristic double helix. The velocity disturbances of the core fluid show the influence of both modes, with a dominance of  $\omega_1$ , yielding a predominantly single helical appearance.

For  $S = 1.0$ , the major part of the energy of  $\omega_1$  remains contained in  $m = 1$ . Similarly, most of the energy of  $\omega_2$  is contained in  $m = 2$ . In comparison to  $S = 0.8$ , however, the relative energy content in the respective wavenumbers diminishes as more energy is distributed to adjacent wavenumbers. Thus,  $\omega_1$  shows an increased activity in  $m = 2$ , whereas  $\omega_2$  is also active in  $m = 0$  and  $m = 3$ . The near wake appearance of the  $\omega_1$  velocity disturbance is similar to  $S = 0.8$ , but the activity in the far wake diminishes. In contrast to  $S = 0.8$ , the interfacial disturbance extends upstream into

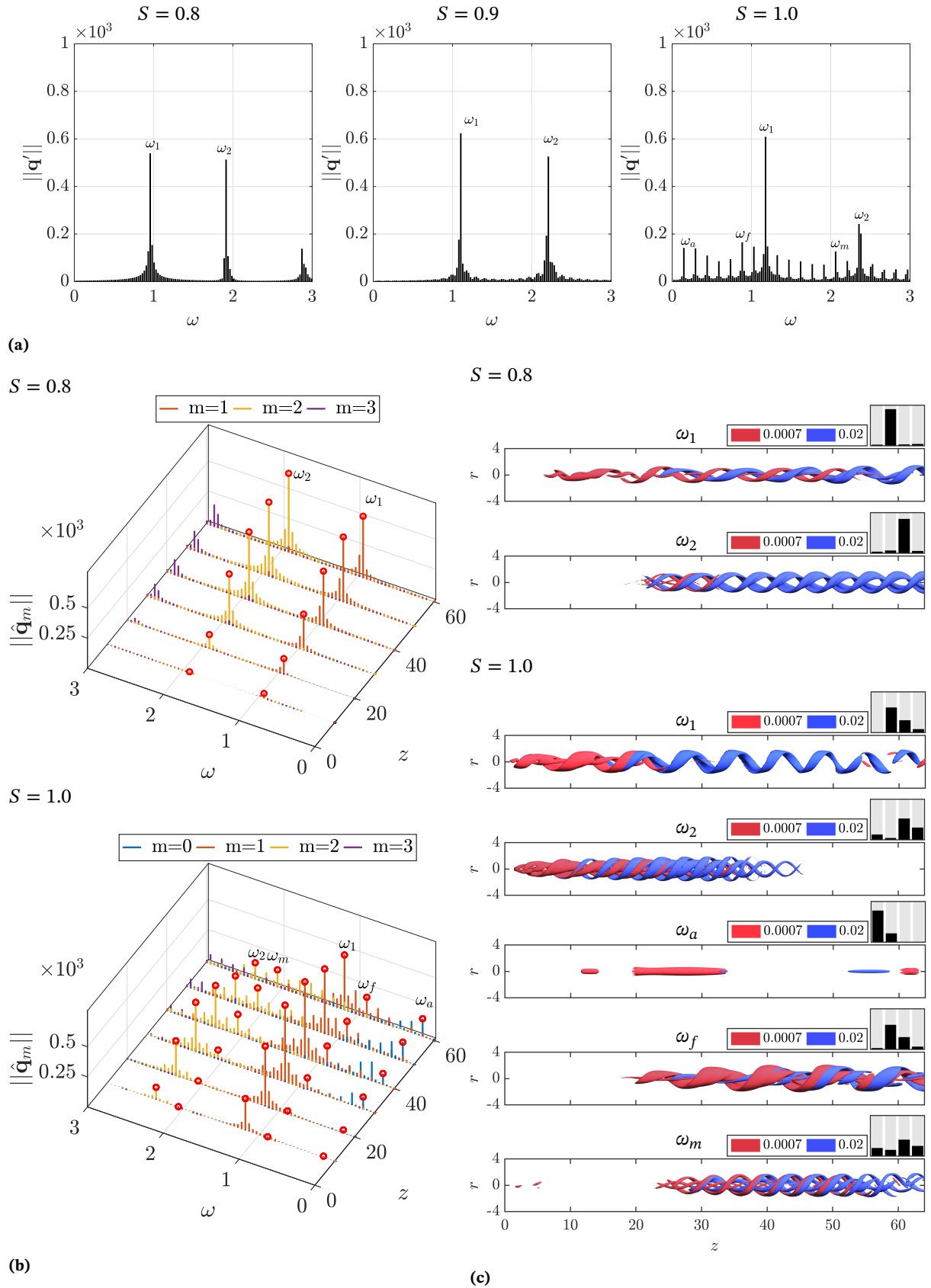


**Figure 4.8:** (a) Magnitude of the DMD modes per frequency, extracted from the nonlinear simulation. (b) Magnitude of the DMD modes per frequency and stream-wise stations every  $\Delta z = 10$ . The colours denote the different wavenumbers. The peaks of the annotated modes are marked by  $\circ$ . (c) The spatial mode shapes  $(\text{Re}(\hat{u}_\theta))$  in red,  $(\text{Re}(\hat{\phi}))$  in blue corresponding to the annotated modes in (a). The pictographic bar charts show the relative contributions of the respective wavenumbers  $m = 0, 1, 2, 3$  (from left to right) to each mode.

the near wake and the breakdown bubble. The amplitude maximum of the mode appears around  $z \approx 30$ . The mode  $\omega_2$  is significantly shifted upstream into near wake and attains in maximum amplitude for  $z \approx 25$ . Thereafter it diminishes. The far wake region at this swirl numbers is dominated by the modes corresponding to  $\omega_\kappa$  which spread across several wavenumbers. The most amplified frequencies, contained in  $\omega_\kappa$ , at each wavenumber  $m = 0, 1, 2$  are  $\omega_a$ ,  $\omega_f$  and  $\omega_m$ , respectively. The mode corresponding to  $\omega_f$  shows a strong velocity and interface disturbance covering the complete far wake region for  $z > 20$ . The mode corresponding to  $\omega_m$  shows a similar behaviour but appears double helical. Finally, the mode shape for  $\omega_a$  is axisymmetric, i.e.  $m = 0$ . It shows several pulsations in the near and far wake region of the flow. The fact that this mode (and other  $m = 0$  modes) does not appear in the axisymmetric simulations which converge towards steady states, indicates that its origin is rooted in a nonlinear mechanism not present in the axisymmetric flow.

The mode shapes obtained for  $S = 0.8$  from the linear analysis shown in figure 4.5 show a good agreement with the corresponding modes extracted from the nonlinear flow in figure 4.8c. In particular, the single and double helical structure of the respective modes is correctly captured as is the spatial wavelength which is represented through the helix pitch. A deviation is seen in the stream-wise amplitude distribution of the respective modes. For instance, the amplitude of the near wake velocity disturbance of the linear mode corresponding to  $\omega_1$  is smaller than the far wake disturbance which explains the absence of the upstream structure in figure 4.5.

The mode shapes of  $\omega_1^l$  and  $\omega_2^l$  for  $S = 1.0$  are very localised and concentrated in the immediate near wake-part of the flow and thus deviate significantly from their nonlinear equivalents. The location of the mode shape of  $\omega_m^l$  on the other hand agrees well with that of  $\omega_m$  (and so does  $\omega_l^l$  with  $\omega_l$  which is not reproduced here). The observed differences for  $S = 1.0$  may be attributed to the significant nonlinear interactions which have been shown to take part in the flow even at this swirl number and which leads to a departure of the actual dynamics from those represented by the linear analysis.

#### 4.5.4 Triadic mode interactions

##### Bispectrum

The amplitude spectra in figure 4.8 have shown a profound influence of the nonlinear modal interactions in and between the two sets of modes  $\omega_l$  and  $\omega_\kappa$  for  $S = 1.0$ . To shed light on these interactions and to identify dominant interaction mechanisms, higher order spectral analysis is leveraged. To this end, we apply the BMD to a sequence composed of  $n = 1024$  consecutive snapshots  $\mathbf{q}^l$  every  $\Delta t = 0.5$  and compare the configurations  $S = 0.8, 1.0$ . The interactions for  $S = 0.9$  are comparable to those of  $S = 0.8$  and are not further analysed here. For completeness, the BMD modes for  $S = 0.8$  are presented in Appendix 4.8.3, alongside the respective DMD modes and linear global modes.

The obtained magnitude mode bispectra are shown as a scatter plot in the top row of figure 4.9. The modulus  $|\lambda_1(\omega_x, \omega_y)|$  is the magnitude mode bispectrum which quantifies the interaction of the frequency doublet  $(\omega_x, \omega_y)$

and every dot in the plot represents such an interacting doublet. The dot diameters and colour coding are scaled with  $|\lambda_1|$ , such that small, bright dots correspond to weak interactions and large, dark dots to strong interactions. The dashed diagonal lines, overlaying the plots, denote doublets generating the same frequency, e.g.  $\omega_1$  or  $\omega_2$ . Additionally, for selected frequencies, the three most energetic contributions to this frequency, which lie on the dashed lines, are shown as a bar chart in the bottom row of figure 4.9.

The interpretation for  $S = 0.8$  then may be the following: Initially, we assume the existence of the two global modes  $\omega_1^l, \omega_2^l$  as the result of the linear instability mechanism addressed in §4.4. Their counterparts in the nonlinear flow are  $\omega_1, \omega_2$ . Nonlinear self-interaction  $\omega_1 + \omega_1 = \omega_2$  then takes place via the triad  $(\omega_1, \omega_1, \omega_2)$ , marked by  $\circ(\omega_1, \omega_1)$  in the plot. Subsequent interaction continues as  $(\omega_2, \omega_1, \omega_3), (\omega_2, \omega_2, \omega_4)$  and so forth. Simultaneously, the doublet  $(\omega_2, -\omega_1)$  feeds back on  $\omega_1$ . The interactions  $(\omega_1, -\omega_1, 0)$  and  $(\omega_2, -\omega_2, 0)$  produce the stationary mean flow correction and  $(\omega_1, 0, \omega_1), (\omega_2, 0, \omega_2)$  are the interactions of the respective modes with the mean flow. Hence, the latter approximately correspond to the linear dynamics of these modes around the mean flow. A comparison of the interaction of e.g.  $(\omega_1, 0, \omega_1)$  with  $(\omega_2, -\omega_1, \omega_1)$  then allows for an estimate of the strength of the nonlinear interaction responsible for sustaining  $\omega_1$ . Here,  $(\omega_2, -\omega_1, \omega_1) \gg (\omega_1, 0, \omega_1)$  and thus the energy contribution through nonlinear triadic interaction dominates over the energy contributed by the linear instability mechanism that is responsible for the initial appearance of  $\omega_1$ . A similar argument,  $(\omega_1, \omega_1, \omega_2) \gg (\omega_2, 0, \omega_2)$ , can be made for  $\omega_2$ .

Therefore, it is evident that the nonlinear flow at  $S = 0.8$  is already strongly influenced by triadic interactions which are enabled by the simultaneous destabilisation of  $\omega_1^l$  and  $\omega_2^l$ . The resulting dominant interactions are the self interaction of  $\omega_1$  that amplifies  $\omega_2$  and the reinforcement of  $\omega_1$  through interaction of its complex conjugate with  $\omega_2$ .

For  $S = 1.0$ , significantly more triadic interactions are observed. The bispectrum allows to clearly identify these appearing interactions in and between the sets  $\omega_l$  and  $\omega_\kappa$ . Again, we assume the linear global modes  $\omega_1^l, \omega_2^l$  as a starting point which are now accompanied by two additional modes  $\omega_l^l, \omega_m^l$ . This enables all four global modes to interact nonlinearly and to form new modes, thus accounting for the appearance of all the modes contained in the set  $\omega_\kappa$ . Regarding the analysis of these new modes, we will concentrate on the modes  $\omega_a, \omega_f$  and  $\omega_m$ . The interactions inside the set  $\omega_l$  are partly similar to the interactions for  $S = 0.8$ : The most energetic interactions are again the triads  $(\omega_1, \omega_1, \omega_2)$  and  $(\omega_2, -\omega_1, \omega_1)$ . However, both modes are now also influenced by various other triads such as  $(\omega_m, -\omega_f, \omega_1)$  or  $(\omega_i, \omega_f, \omega_2)$ . Within the set  $\omega_\kappa$ ,  $\omega_f$  is identified to be predominantly formed by the doublet  $(\omega_m, -\omega_1)$ , while  $\omega_a$  and  $\omega_m$  are formed by the doublets  $(\omega_b, -\omega_a)$  and  $(\omega_1, \omega_f)$ , respectively. A complete list of the dominant triadic interactions with respect to each frequency is given in Appendix 4.8.2.

In summary, the bispectral analysis shows that the simultaneous existence of the two unstable global modes  $\omega_1^l, \omega_2^l$  with harmonic frequencies allows for a triadic resonance of these modes in the nonlinear flow, resulting in the formation of higher harmonic modes as well as a reinforcement of

the global modes themselves. Through the appearance of two additional modes  $\omega_l^l$ ,  $\omega_m^l$  a triadic interaction between all four modes is possible which initiates an interaction cascade and leads to the emergence of a variety of additional modes.

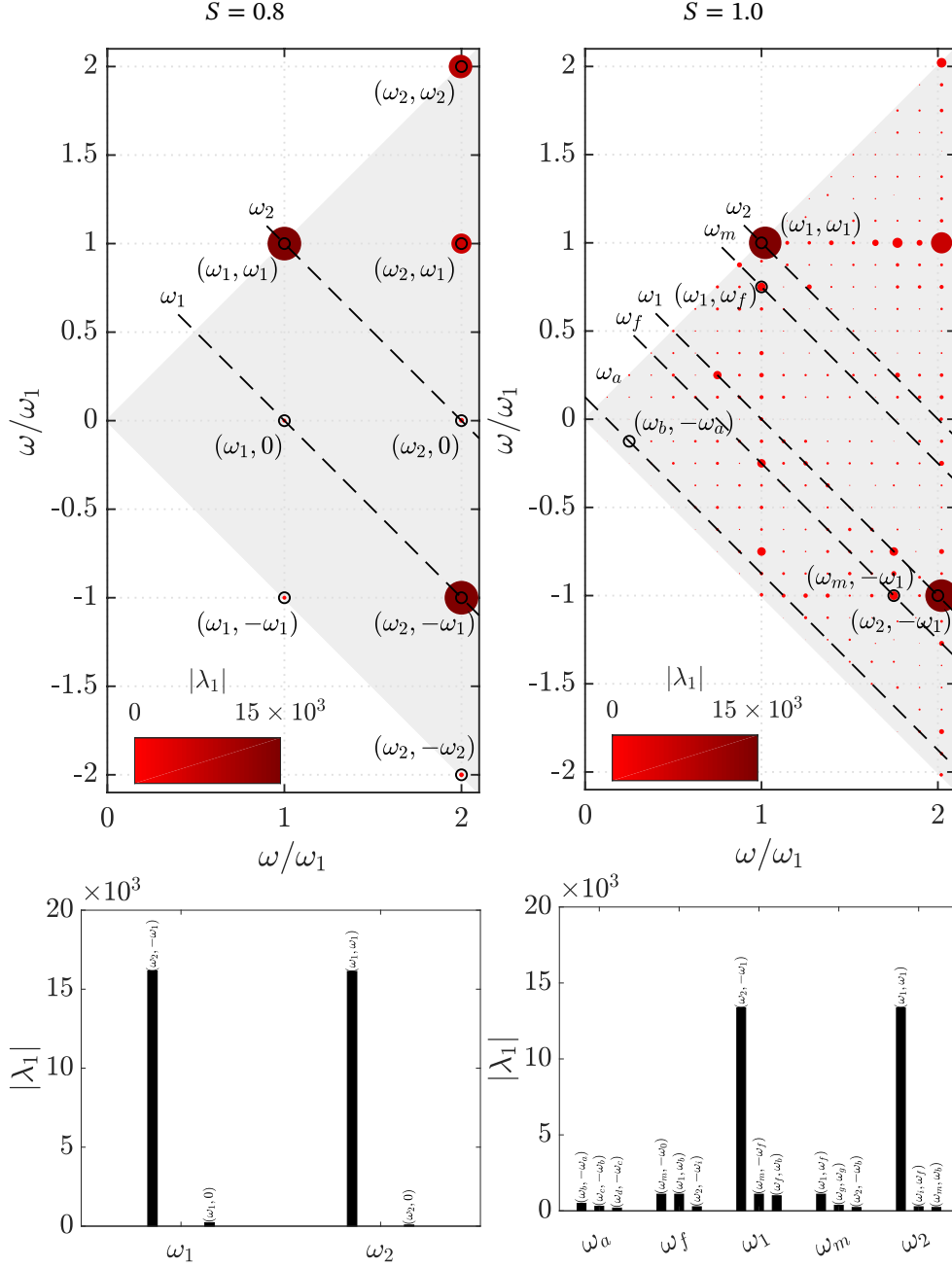


**Figure 4.9:** Upper row: Scatter plot of the local maxima of the mode bispectrum. The dashed diagonal lines denote triadic interactions forming the same frequency, as annotated at the respective lines. Relevant triadic interactions mentioned in the text are marked by  $\circ$ . The dot diameters and colour coding are scaled with  $|\lambda_1|$ , such that small, bright dots correspond to weak interactions and large, dark dots to strong interactions. Lower row: Bar chart showing the three most energetic interactions contributing to the denoted frequencies. Each bar is corresponding to a peak in the bispectrum above and the largest interaction for each frequency corresponds to the interactions marked by  $\circ$  in the bispectrum.

### Cross-Bispectrum

To attain additional insights on the triadic energy transfer across different azimuthal wavenumbers, the cross-BMD is computed for selected wavenumber triplets  $[m_p, m_q, m_{p+q}]$ . The respective bispectra are shown in figure 4.10, alongside bar charts of the three most energetic contributions to the wavenumbers  $m = 0, 1, 2$ . Similarly to before, triadic interaction between frequencies are identified, now however, with the additional constraint of a triadic interaction between the involved wavenumbers. Consequently, for each wavenumber doublet in figure 4.10, only frequency interactions that act across the involved wavenumbers are identified.

For  $S = 0.8$ , energy transfer is limited to the wavenumbers  $m = 1, m = 2$  where the wavenumber triads  $[2, -1, 1]$  and  $[1, 1, 2]$ , respectively, are the dominant interactions. From the respective bispectra, it is seen that the energy transfer for these wavenumber doublets is almost exclusively driven by the interaction of  $\omega_1$  and the complex conjugate of  $\omega_2$ , as well the self-interaction of  $\omega_1$ . This is in line with the wavenumber-divided DMD spectrum in figure 4.8, which identifies  $\omega_1$  having  $m = 1$  and  $\omega_2$  having  $m = 2$ . Consistently, the reinforcement of  $\omega_1$  through the interaction  $(\omega_2, -\omega_1)$  involves the negative wavenumber  $m = -1$ . Although there are no axisymmetric  $m = 0$  modes present in the flow at this swirl number, the cross-BMD identifies a small energy transfer to  $m = 0$  through interaction of the wavenumber doublets  $[1, -1]$  and  $[2, -2]$ . As explained before, this is the interaction producing the stationary mean flow correction.

For  $S = 1.0$ , again, the dominant energy transfer is to the wavenumbers  $m = 1, m = 2$ , similar to the flow at  $S = 0.8$ . Again, the interaction of  $\omega_1$  and  $\omega_2$  is the driving mechanism. However, there are now as well contributions of the other frequencies with wavenumbers  $|m| = 1, 2$  involved, such that the respective bispectra show a multitude of interactions. In contrast to  $S = 0.8$ , the interaction of  $\omega_1, \omega_2$  and other frequencies with their respective complex conjugate mode, leads to a more pronounced energy transfer from  $|m| = 1$  and  $|m| = 2$  to  $m = 0$ . The formation of these  $m = 0$  modes through triadic interaction at higher wavenumbers further provides an explanation why these modes are not observed in the axisymmetric solutions in §4.3. They are produced by helical waves interacting with their complex conjugate counterparts and thus are a consequence of helical instability in the three-dimensional flow.

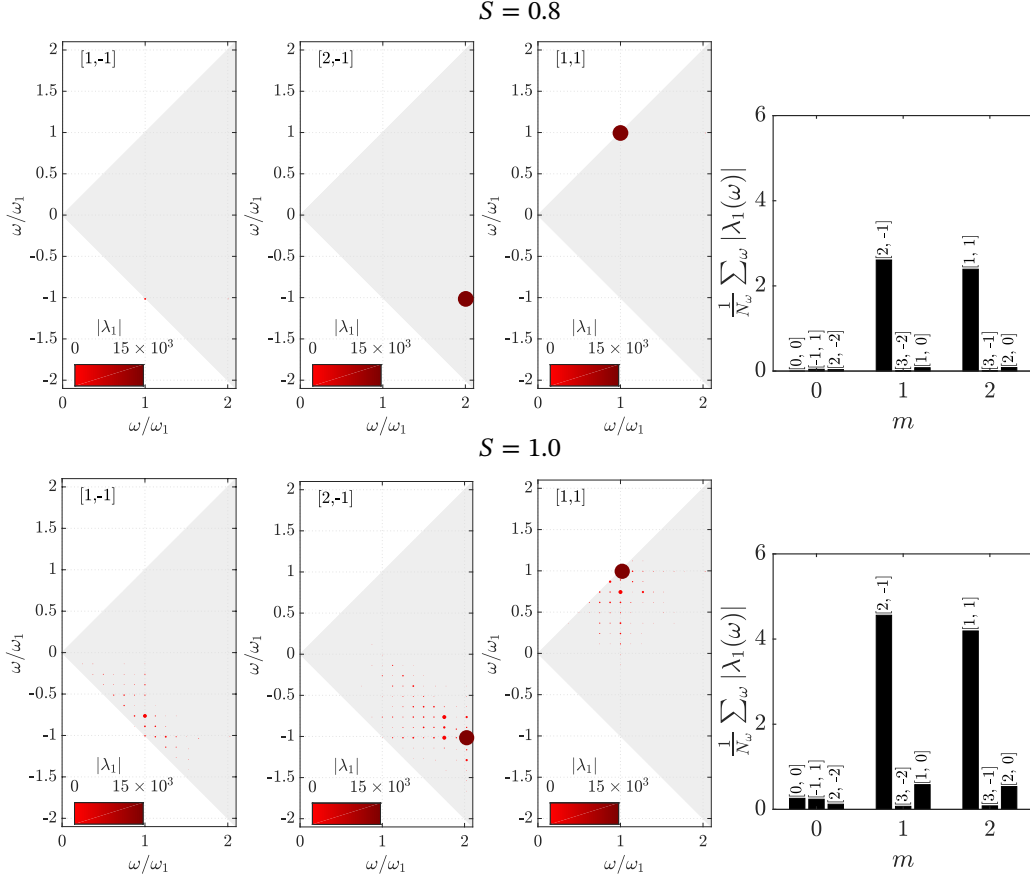


**Figure 4.10:** Left: The mode cross-bispectrum for the dominant azimuthal wavenumber interactions. The partaking wavenumber doublets  $[m_p, m_q]$  are denoted in the plots. Right: The three most energetic wavenumber interactions contributing to the denoted wavenumbers.

## 4.6 Discussion

We have investigated the linear and nonlinear dynamics of a two-phase swirling flow under the influence of a variable viscosity and have seen that the viscosity variation strongly affects the onset of vortex breakdown and helical instability. Further, the simultaneous destabilisation of two linear global modes has enabled the nonlinear flow to produce strong triadic interactions. Both of these findings are discussed here.

### 4.6.1 Impact of the viscosity variation on vortex breakdown and helical instability

The introduction of a two-phase flow with different viscosities that are separated by an interface has shown to significantly affect the dynamics of swirling flows, produced by the Grabowski-Berger profile. In particular, a viscosity ratio  $\tilde{\mu} < 1$  between outer and inner fluid significantly reduces the critical swirl  $S_c$  necessary to produce axisymmetric vortex breakdown. Considering the flow for  $\tilde{\mu}_r = 0.5$ , vortex breakdown occurs around  $S_c = 0.79$  in contrast to the corresponding single-phase flow with  $\tilde{\mu} = 1$  where  $S_c = 0.8799$  [7].

[7]: Ruith et al. (2003), ‘Three-dimensional vortex breakdown in swirling jets and wakes: direct numerical simulation’

Intuition would suggest that the introduction of a second phase with a lower viscosity destabilises the flow simply through the increase of the

maximum local Reynolds number in the less viscous phase which is given as  $Re_{\max} = Re/\tilde{\mu}$ . Consequently,  $S_c$  would lie somewhere between the respective values for  $Re$  and  $Re_{\max}$  for a flow with  $\tilde{\mu} = 1$ . However, this turns out to be not the case.

From [9] it is evident that for  $S = 0.79$  no breakdown is to be expected for any Reynolds number of the single-phase flows computed therein (up to  $Re = 300$ ). From figure 3a in their work it can further be assumed that the single-phase axisymmetric flow at this particular  $S$  never reaches criticality for any chosen  $Re$ . We have verified this assumption by computing the respective flow for  $\tilde{\mu} = 1$  and  $Re = 400$  which corresponds to  $Re_{\max}$  in the present flow. The result converges towards a stationary solution without vortex breakdown (not shown).

Similarly to the axisymmetric flow, the critical swirl for helical destabilisation of the three-dimensional flow is reduced to  $S \approx 0.79$  for  $\tilde{\mu} = 0.5$ , in contrast to  $S \approx 1.0$  for  $\tilde{\mu} = 1$  [7]. From figure 4a of [9] it is evident that helical destabilisation at low  $S$  and large  $Re$  can occur prior to axisymmetric breakdown. Therefore, a flow with  $\tilde{\mu} = 1$  and  $Re = 400$ , as computed for the axisymmetric case, could still be unstable to helical perturbations. However, as before, our computations show this flow to converge to a stationary solution (not shown). Thus, it is evident that the varying viscosity, separated by an interface, leads to stronger destabilisation than a constant viscosity flow at the largest local Reynolds number occurring in the two-phase flow.

As to the cause of the increased destabilisation, some insights can be gained from the existing literature on viscosity-stratified flows. [18] discovered a long-wave mechanism (Yih mode or interface mode) that destabilises all confined shear flows with a viscosity stratification. [125] equally, found a destabilisation of short waves in viscosity-stratified open Couette flow which originates in the vicinity of the interface. Similarly, for pipe flows with concentric viscosity-stratified fluids, [124], found a destabilisation for azimuthal wavenumbers  $m = 0$  and  $m = 1$ . In all of these studies the respective flows appear stable in the absence of a viscosity stratification. A physical explanation for the phenomenon was given by [135] who argued that due to the viscosity jump, the undisturbed velocity at the disturbed interface is discontinuous. In order to satisfy shear stress continuity at the interface, a velocity disturbance is required. This again induces vorticity disturbances on both sides of the interface where the vorticity of the less viscous layer drives the instability.

The present flow is obviously significantly more complex and a direct translation of the above mechanism is questionable especially in light of the fact that the observed instabilities are similar to those observed in single-phase swirling flows. Thus, the underlying mechanism remains the same. However, it may be hypothesised that similar effects that lead to a purely viscosity-induced destabilisation, play a role in the modification of the stability properties in the present flow. The introduction of a viscosity stratification to the columnar (pre-breakdown) flow promotes the supercritical-subcritical transition, leading to an earlier onset of axisymmetric breakdown. Concurring with the accepted view in literature [112], the properties of helical destabilisation are then a consequence of the axisymmetric breakdown state, altered by viscosity stratification.

[9]: Meliga et al. (2012), 'A weakly non-linear mechanism for mode selection in swirling jets'

[7]: Ruith et al. (2003), 'Three-dimensional vortex breakdown in swirling jets and wakes: direct numerical simulation'

[18]: Yih (1967), 'Instability due to viscosity stratification'

[125]: Hooper et al. (1983), 'Shear-flow instability at the interface between two viscous fluids'

[124]: Hickox (1971), 'Instability due to viscosity and density stratification in axisymmetric pipe flow'

[135]: Hinch (1984), 'A note on the mechanism of the instability at the interface between two shearing fluids'

[112]: Escudier et al. (1982), 'Vortex-flow regimes'

Some further insights are gained by performing the linear computations of a synthetic flow without viscosity stratification and perturbation (thus having a single viscosity) on the respective base flow with a viscosity stratification slightly above the stability limit of  $S \approx 0.79$ . This results in an unstable linear flow but with smaller growth rates than for the flow computed in §4.4. This indicates that the destabilisation of the flow investigated in this study is driven by both, the structural change of the base flow through axisymmetric breakdown, promoted by the viscosity stratification, as well as a promotion of helical instability itself by viscosity stratification.

#### 4.6.2 Resonant triadic interaction of the unstable global modes

The linear analysis has revealed that two unstable global modes,  $\omega_1^l$  and  $\omega_2^l$ , are present in the flow which bifurcate simultaneously at  $S \approx 0.79$ . Notably, both modes have harmonic frequencies where  $\omega_2^l \approx 2\omega_1^l$ . Such an occurrence of multiple unstable modes with increasing azimuthal wavenumbers has as well been observed by [9] in their systematic study of single-phase swirling flows in the  $Re$ - $S$  plane using linear and weakly nonlinear analysis to identify mechanisms of mode selection in the nonlinear flow. Starting from either an unstable  $m = 1$  or  $m = 2$  mode, they observe subsequent bifurcations of modes with higher wavenumbers if  $Re$  or  $S$  are increased. Moreover, they as well report the simultaneously bifurcation of an  $m = 1$  and  $m = 2$  mode at a particular  $S$ - $Re$  combination (codimension-two point) where the frequencies of both modes further show an approximate 2 : 1 resonance, similar to the present scenario.

The resonance of the unstable global modes in the present study has important implications for the nonlinear dynamics of the flow as it allows for an amplification of these modes through triadic interaction as well as the formation of additional ultraharmonic frequencies at larger swirl numbers.

The dynamics for the lowest computed swirl, at  $S = 0.8$ , is dominated by the two modes,  $\omega_1$  and  $\omega_2$  with azimuthal wavenumbers  $m = 1$  and  $m = 2$  whose frequencies are in close agreement with the linear global modes  $\omega_1^l$  and  $\omega_2^l$ . The fact that  $\omega_2$  is as well the first harmonic of  $\omega_1$ , enables both modes to triadically interact and reinforce each other, thus leading to a pronounced influence of nonlinear mode interactions already close to the linear stability boundary. Moreover, the bispectral analysis has also revealed that the energy portions stemming from the harmonic interactions are significantly larger than those coming from the mean field correction. Hence it may be concluded that the nonlinear dynamics is predominantly driven by harmonics generation and not by the mean field correction.

The triadic interactions are significantly increased if the swirl is increased to  $S = 1.0$  due to the destabilisation of two additional linear global modes,  $\omega_l^l$  and  $\omega_m^l$ . In the linear flow, the unstable global modes exist independently and therefore cannot influence each other. In the nonlinear flow, however, such interactions are possible and now lead to a synchronisation of  $\omega_l$  and  $\omega_m$  with respect to  $\omega_1$  and  $\omega_2$ , possibly through harmonic Reynolds stresses leading to a sufficiently large mean flow correction for

[9]: Meliga et al. (2012), 'A weakly nonlinear mechanism for mode selection in swirling jets'

$\omega_l$  and  $\omega_m$  having ultraharmonic frequency ratios with respect to  $\omega_1$  and  $\omega_2$ . As a result their interaction initiates an interaction cascade that manifests in the appearance of the mode set  $\omega_\kappa$  which contains ultraharmonic frequencies with respect to  $\omega_l$ . Consequently, the dynamics becomes much more complex but retains its periodicity since all frequencies are commensurate. The appearance of these strictly ultraharmonic modes differs from the observations made by [119] for single-phase swirling flows. There, the nonlinear dynamics are initiated by the appearance of an additional mode that is incommensurate with respect to the initially single unstable global mode, resulting in a transition from periodic to chaotic dynamics.

[119]: Pasche et al. (2018), 'Onset of chaos in helical vortex breakdown at low Reynolds number'

## 4.7 Conclusions

Two main conclusions are drawn from the present study of a two-phase swirling flow with a viscosity stratification:

First, the introduction of a less viscous core fluid acts destabilising on the flow, leading to an earlier onset of vortex breakdown and subsequent destabilisation of helical global modes in the flow at lower swirl numbers as compared to an equivalent single phase flow at the maximum local Reynolds number of the two-phase flow.

Second, the simultaneous destabilisation of two linear global modes at harmonic frequencies enables strong triadic interactions between these modes to take place in the nonlinear flow. At larger swirl, the destabilisation of additional modes leads to a cascade of triadic interactions and synchronisation of the newly formed modes. The resulting nonlinear dynamics become significantly more complex but remain periodic.

In consequence, the coexistence of two harmonic global modes acts as a catalyst for the onset of triadic resonance in the nonlinear flow, starting immediately after the bifurcation of these modes. As a result, the flow quickly departs from the linear dynamics that are observed at the bifurcation point. It is conceivable that these effects may also accelerate transition of the flow towards a turbulent state at larger swirl, through the continuing triadic interaction and formation of additional modes. The existence and coupling of two global modes as in the present study may also have implications for the analysis of other swirling flows where the existence of an  $m = 2$  global mode may easily be mistaken as being a purely higher harmonic. Further, the presence of two or more unstable global modes has implications for flow control applications such as the attenuation of helical instability. In the present flow, control approaches realised through the stabilisation of unstable eigenvalues would need to target all unstable global modes in order to be successful.

## 4.8 Appendix

### 4.8.1

In table 4.2 convergence of the linear solver on different meshes is demonstrated. For comparability with previous studies we compute linear solutions for the single-phase flow with  $Re = 200$ ,  $S = 1$ ,  $\tilde{\mu} = 1$ . As can be

**Table 4.2:** Convergence of the unstable eigenvalue for  $Re = 200$ ,  $S = 1$ ,  $\tilde{\mu} = 1$  on different meshes and comparison with previous studies. As the present computations are 3D in cartesian coordinates, radial measures  $r$  correspond to the respective measures in  $y$  and  $z$ . The mesh  $M_{\text{ref}}$  is used throughout the study.

	$L_z$	$L_r$	$n_z$	$n_r$	$\text{Re}(\lambda)$	$\text{Im}(\lambda)$
[7]	20	10	193	61	0.0359	1.18
[133]	20	8	513	127	0.0352	1.17
[9]	40	6	-	-	0.0335	1.17
$M_{\text{ref}}$	64	8	1024	128	0.0329	1.17
$M_1$	64	8	2048	256	0.0332	1.17
$M_2$	64	8	512	64	0.0242	1.18

seen, the meshes  $M_{\text{ref}}$  and  $M_1$  are in good agreement with the results of previous studies. Moreover, only marginal changes in the growth rate are seen between  $M_{\text{ref}}$  and the mesh  $M_1$  while doubling the resolution in each dimension. Therefore, the use of the mesh  $M_{\text{ref}}$  seems justified to avoid excessive computational resources.

### 4.8.2

The flow for  $S = 1.0$  exhibits a rich nonlinear dynamics. The frequencies occurring in the flow up to  $\omega_2$  are listed in table 4.3. The occurring ultra-harmonic frequencies can be expressed as fractions w.r.t.  $\omega_1$ . Further, the dominant triadic interaction partaking in the formation of each frequency is given.

**Table 4.3:** Frequencies occurring for  $S = 1.0$  and dominant triadic interaction forming them

	$\omega_a$	$\omega_b$	$\omega_c$	$\omega_d$	$\omega_e$	$\omega_f$	$\omega_g$	$\omega_1$
$\omega_1 \cdot ()$	1/8	2/8	3/8	4/8	5/8	6/8	7/8	1
$(\omega_x, \omega_y)$	$(\omega_b, -\omega_a)$	$(\omega_1, -\omega_f)$	$(\omega_a, \omega_b)$	$(\omega_1, -\omega_d)$	$(\omega_l, -\omega_1)$	$(\omega_m, -\omega_1)$	$(\omega_m, -\omega_g)$	$(\omega_2, -\omega_1)$
	$\omega_h$	$\omega_i$	$\omega_j$	$\omega_k$	$\omega_l$	$\omega_m$	$\omega_n$	$\omega_2$
	9/8	10/8	11/8	12/8	13/8	14/8	15/8	2
	$(\omega_1, \omega_a)$	$(\omega_2, -\omega_f)$	$(\omega_1, \omega_c)$	$(\omega_g, \omega_e)$	$(\omega_1, \omega_e)$	$(\omega_1, \omega_f)$	$(\omega_1, \omega_g)$	$(\omega_1, \omega_1)$

### 4.8.3

In figure 4.11 we compare the computed modes from the linear stability analysis (§4.4), the dynamic mode decomposition (§4.5.3) and the bispectral mode decomposition (§4.5.4) for  $S = 0.8$ . The respective modes are computed from  $u_\theta$  or  $u_\theta^l$  and the real part of the modes is shown. For the BMD, the bispectral modes  $\phi_{x+y}$  are shown which correspond to the mode shape of  $\omega_z$ , formed by the doublet  $(\omega_x, \omega_y)$ . Additionally, the interaction map  $\psi_{x,y}$  is plotted which identifies regions where  $\omega_x$  and  $\omega_y$  interact.

The DMD and BMD modes along each column of figure 4.11 appear virtually identical (apart from not being phase aligned) which is to be expected since they represent similar frequencies. The linear global modes resemble the overall structure of the nonlinear modes satisfactorily but exhibit differences in the amplitude distribution and the near wake structure. This is not unexpected since nonlinear interaction between the global modes is quite strong even for  $S = 0.8$  as has been shown in §4.5.4. The interaction maps show that the interaction of  $\omega_1$  with the mean field is limited to the core region in the near wake whereas that of  $\omega_2$  extends radially into the far wake region.

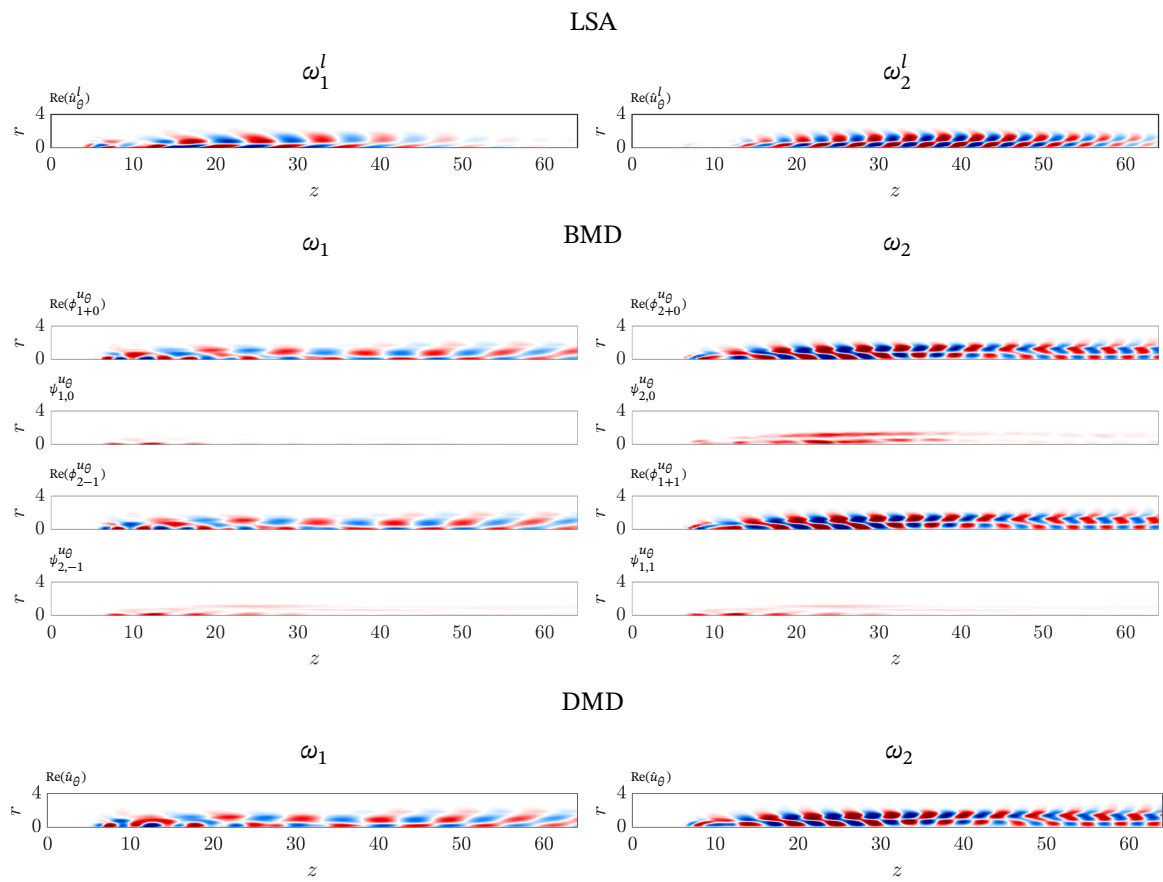


**Figure 4.11:** Comparison of the computed modes of the linear stability analysis (LSA), the bispectral mode decomposition (BMD) and the dynamic mode decomposition (DMD) for  $S = 0.8$ . All modes are computed from  $u_\theta$  or  $u_\theta^l$ . The real part of the respective modes is shown. For the BMD, the bispectral modes  $\phi$  as well as the interaction map  $\psi$  is displayed.



## 5.1 Summary and Discussion

The numerical modelling of two-phase flows is a challenging task that requires robust and accurate methods to be successful. In recent years, considerable advances have been made in developing such methods for the simulation of nonlinear flows. With the ever-increasing availability of computational power, it has become possible to facilitate accurate modelling of large-scale three-dimensional flows. Similarly, the linear analysis of large-scale single-phase flows by means of global linear stability analysis and related methods has benefited from the increased availability of computational power. However, the development of these methods for the linear analysis of two-phase flows lags behind. The overarching goal of this thesis is to take a step towards closing this gap between methods for single- and two-phase linear stability analysis. Additionally, new insights regarding the physical aspects of the flow configuration, selected for this thesis, are gained. In the following, the main findings of the three publications presented in the thesis are summarised and put into perspective.

### 5.1.1 Mean field stability analysis of two-phase flows

In **Publication 1** (Chapter 2), we have applied mean field stability analysis in a local framework to an externally forced two-phase jet. The externally forced flow used here serves as an example of a flow that does not possess a stationary solution and as such cannot be analysed meaningfully using a linear analysis of a base flow.

The time-averaged flow is formed as the result of the action of harmonic Reynolds stresses on the stationary base flow. Therefore, mean flow stability analysis is inherently accounting for the nonlinear modifications that produce the mean flow and thus is able to retrieve surprisingly accurate results for flows with limit cycle dynamics far away from the bifurcation point. While the time-averaged velocity field allows for a clear interpretation using the described mechanism, the application of the mean field approach to a two-phase flow has shown to introduce an ambiguity to the analysis.

In the study, we have shown that it is not *a priori* clear how to account for the interface position in the time-averaged flow as a simple time-averaging has proven to be not meaningful. This is mainly due to the fact, that the interface represents a discontinuity. In case of an approximately symmetric oscillation of the interface as in the current study, a simple time-average results in the cancellation of the oscillation in the mean flow and thus one obtains the interface position of the unperturbed flow. Consequently, the hypothetical time-averaged interface position becomes dislocated from

the mean flow shear layer. Therefore, instead of a simple time-averaging, we have developed a model to compute an interface position in the time-averaged flow, by requiring mass conservation of each phase in the time-averaged flow at every stream-wise position. This allows to compute an interface position that follows the mean flow shear-layer. With the resulting model, we have been able to accurately model the spatial disturbance growth in the forced flow for a low-amplitude forcing. Furthermore, using the time-averaged flow in conjunction with the proposed model, the accuracy of the analysis is notably improved as compared to either a base flow analysis of the unperturbed flow or a mean flow analysis with simple time-averaging of the interface position.

For stronger forcing, however, the analysis fails due to the strong non-parallelism of the flow as well as the influence of the nonlinear flow by non-negligible higher harmonic interaction through Reynolds stresses acting on the dynamics of the fundamental wave and those of the higher harmonics. As a consequence, the *a priori* assumption that the terms accounting for the quadratic nonlinear interaction in the dynamic equation of the fundamental wave are negligible, is violated. The flow configuration with the strong forcing therefore poses as an example of the limitations of mean flow analysis which have previously been highlighted, among others, in the works of [51] and [52]. It is worth noting that, given the strength of the external forcing of the flow, the nonlinear harmonic interactions appear unusually strong. This is especially seen in comparison to the oscillating single-phase jet experiments conducted in [63]. There, the nonlinear interactions remain significantly smaller at this level of forcing and a successful mean flow analysis can be performed even for notably larger forcing amplitudes before the linear model breaks down. It may therefore be hypothesised that the two-phase character of the flow amplifies nonlinear harmonic interactions in the flow. This would pose as a significant obstacle to the general applicability of mean flow analysis to this type of flow.

[51]: Sipp et al. (2007), ‘Global stability of base and mean flows: a general approach and its applications to cylinder and open cavity flows’

[52]: Turton et al. (2015), ‘Prediction of frequencies in thermosolutal convection from mean flows’

[63]: Oberleithner et al. (2014), ‘Mean flow stability analysis of oscillating jet experiments’

### 5.1.2 Global stability analysis of two-phase flows

In **Publication 2** (Chapter 3), we have developed a framework for the global stability analysis of two-phase flows in order to lift the restriction of a parallel base flow. To this end, a DNS solver for the computation of two-phase flows is linearised. The linearised two-phase flow is modelled using a combination of Volume-Of-Fluid and level-set methodology. This implies, that the fluid phases and interface position are represented in an Eulerian manner. The resulting matrix-free solver is able to compute stability properties of two- and three-dimensional flows with arbitrary interface topologies by time-stepping of the linearised equations. The framework uses the same numerical methods employed for the computation of the nonlinear flow and thus maintains their accuracy and efficiency with respect to discretisation and resource requirements. Base state computation and linear analysis can be performed ‘in-place’ without the necessity of interpolating fields or changing discretisations.

The methodology of the current framework, thus, has several advantages over previously employed Lagrangian methodologies for global linear stability analysis that use separate domains and boundary-fitted meshes for each phase [24]. In contrast to the present framework, these are usually

[24]: Tammisola et al. (2012), ‘Surface tension-induced global instability of planar jets and wakes’

implemented by explicitly constructing the linear operator, thus posing strict limits on the representable degrees of freedom through the availability of computer memory. Therefore, the analysis of three-dimensional flows with many degrees of freedom may not be possible. Further, for more complex flow configurations, base flows (or the unsteady flow, in case of a mean field analysis) have to be computed using a separate nonlinear solver which then requires the interpolation of the flow field on the mesh, constructed for the linear solver.

A potential challenge for the current approach is the accurate computation of interface positions and curvature values of basic states with large surface tensions. These are currently limited by the accuracy of the interface advection scheme. Additionally, while the the matrix-free approach avoids explicit construction of the linear operator, this comes at the expense of largely increased CPU time requirements. Thus, the method essentially exchanges memory requirements for computation time.

The developed framework has been applied to compute global modes of a two-fluid wake flow. This flow, previously investigated by [24], has shown to be destabilised solely through the action of surface tension. The flow configuration offers a rich dynamics and the surface tension-induced destabilisation requires for an accurate discretisation of the interface and linearised surface tension terms. The present results show an excellent agreement of the computed linear modes with previous linear computations as well as nonlinear results which have been computed concurrently. From a physical point of view, the study has confirmed the observations made by [24] and previously [94] that a purely surface tension-induced destabilisation of plane wake flows is possible. Further, it has revealed new insights into the nonlinear dynamics of this flow configuration.

As the surface tension force represents a higher-order geometric nonlinearity, it has the potential of inducing significantly more complex dynamics as compared to the quadratic nonlinearity of the advective term of the Navier-Stokes equations. Therefore, through the action of surface tension, a bifurcation of several global modes is provoked that lead to a rich dynamics in the nonlinear flow and the transition from a periodic (limit cycle) to quasi-periodic (torus) and chaotic oscillation.

In **Publication 3** (Chapter 4), the developed global stability solver has been used to investigate the linear dynamics of a laminar two-phase swirling flow with varying viscosity. The linear analysis is accompanied by nonlinear simulations and an in-depth analysis of the nonlinear dynamics by means of the BMD [110] to elucidate resonant triadic interactions in the flow.

The linear analysis has revealed a pronounced destabilising effect if a second, less viscous fluid is introduced in the core of the swirling flow. Consequently, axisymmetric vortex breakdown and subsequent helical destabilisation are shifted to lower swirl numbers. Furthermore, for the investigated configuration, the simultaneous destabilisation of two linear global modes with wavenumbers  $m = 1$  and  $m = 2$  is observed. Both modes are harmonically related which enables a strong triadic interaction in the nonlinear flow that again leads to a rapid departure from the linear dynamics already close to the bifurcation point. At larger swirl, the destabilisation of additional linear modes leads to an interaction cascade

[24]: Tammissola et al. (2012), ‘Surface tension-induced global instability of planar jets and wakes’

[94]: Rees et al. (2009), ‘The effect of surface tension on the stability of unconfined and confined planar jets and wakes’

[110]: Schmidt (2020), ‘Bispectral mode decomposition of nonlinear flows’

[9]: Meliga et al. (2012), 'A weakly nonlinear mechanism for mode selection in swirling jets'

[120]: Vanierschot et al. (2020), 'Single- and double-helix vortex breakdown as two dominant global modes in turbulent swirling jet flow'

in the nonlinear flow. In relation to previous studies, [9] and [120] both have reported the existence of multiple global modes in swirling flows. In the study of [9], additionally an approximate 2 : 1 resonance of the bifurcating modes (codimension-two point) was observed.

The present results are noteworthy insofar as a significant triadic resonance of global modes in a nonlinear swirling flow has not been reported yet. In perspective to the findings in Chapter 2, a similar tendency is observed regarding the influence of nonlinearities in the flow: In both studies, a pronounced influence of harmonic interactions is observed already in close proximity to the bifurcation point or at low forcing amplitudes, respectively. Additionally, in both cases these interaction are significantly stronger than those observed for comparable single-phase flows.

The destabilisation of multiple linear modes also has implications regarding control approaches which target the destabilisation of these modes. To be successful, all unstable global modes need to be suppressed. Further, through the harmonic relation of the two primary global modes, any one of them could easily be mistaken as being a purely higher harmonic or subharmonic mode of the other. The identification of both modes as being linearly unstable is only possible by means of linear analysis or a thorough analysis of the triadic interactions taking place in the nonlinear flow.

This study demonstrates the applicability of the developed framework to more complex, three-dimensional two-phase flows and thus may be viewed as an important step towards the linear modelling of industrial-scale flows in the future such as an idealised, cavitating flow inside the draft tube of a hydro turbine.

### 5.1.3 Comparing explicit and implicit interface representations

There are generally two common approaches to represent the fluid phases in two-phase flows and the interface separating them: An explicit, Lagrangian approach, as well as an implicit, Eulerian approach. In modern solvers for nonlinear flow simulations, the latter approach is usually preferred, as the associated methods, mainly the Volume-Of-Fluid method [67], level-set method [39] and phase field method [40], account intrinsically for topological changes of the interface. This includes large deformations as well as breakup of liquid structures into droplets and ligaments. Further, their numerical implementations are relatively straightforward. Specifically, these methods rely on the advection of a tracer field (a volume fraction, signed-distance function or a phase field function). The interface position and its properties (i.e. normal vector and curvature) are given implicitly by the tracer field. Consequently, fixed, unaligned computational grids, as in single-phase flow simulations may be used. Lagrangian methods, on the other hand, require for an explicit treatment of the interface. One possibility then is to align mesh and interface, such that the interface is represented by a fixed number of nodal points [36]. In the case of an instationary flow, this implies the use of a deformable mesh. Another possibility is the advection of marker particles that belong to either phase to track the phase movement. The interface is then explicitly computed using some continuous function with the boundary particles of the respective phases acting as nodes. This is the methodology used

[67]: Torrey et al. (1985), *NASA-VOF2D: A Computer Program for Incompressible Flows With Free Surfaces*

[39]: Sussman et al. (1994), 'A level set approach for computing solutions to incompressible two-phase flow'

[40]: Anderson et al. (1998), 'Diffuse-interface methods in fluid mechanics'

[36]: Fyfe et al. (1988), 'Surface tension and viscosity with Lagrangian hydrodynamics on a triangular mesh'

in Front-Tracking methods [37]. As a result, Lagrangian methods allow for a very accurate representation of interface, for moderately deformed interfaces. However, large deformations and breakup are problematic as they may require remeshing or the redistribution of marker particles.

Essentially all past studies of the linear stability of two-phase flows have employed a Lagrangian interface representation through the use of boundary fitted meshes (e.g. [17–24]). As the computations usually are performed in a local framework, the resulting grids are one dimensional and the interface is reduced to a single node. Consequently, the increased complexity of the discretisation is negligible. The resulting overall methodology is similar to equivalent single-phase computations with the addition of coupling conditions, imposed at the interface node. The linear operator is constructed explicitly and solved as an eigenvalue problem. While this procedure is probably the most straightforward and simplest one for a local analysis, its extension to global analysis with two- and three-dimensional meshes can be problematic as the complexity of the discretisation may significantly increase, depending on the topology of the base flow interface. Since for this approach often two different solvers and discretisation are employed, one to obtain the base flow and another one to compute the linear global modes, the meshes and interface for the stability solver have to be constructed *a posteriori* from the base flow. This requires interpolation and potentially introduces inaccuracies for large interface deformations. Most importantly, the usual explicit construction of the linear operator may quickly lead to prohibitive matrix sizes.

To alleviate either of these problems, two immediate approaches are conceivable. On the one hand, explicit construction of the linear operator can be avoided by employing a time-stepping formalism, leaving the discretisation of the base flow and perturbations untouched. On the other hand, one could follow an approach similar to that used in the majority of current nonlinear solvers and switch from a Lagrangian to an Eulerian interface representation. As Eulerian methods are naturally suited for time-stepping, this approach is promising. If the implementation of the linear stability solver is facilitated by leveraging an existing implementation of a nonlinear solver, this not only allows for the use of a single solver to compute base flow and perturbations but also greatly simplifies the implementation of the linear solver. In case of a level-set solver, the only modifications necessary are the linearisation of the advective terms in the momentum and tracer transport equation, the linearisation of the surface tension force, as well as the implementation of the two additional terms accounting for the action of the perturbed interface on the advective and diffusive term in the momentum equation. All schemes and solution strategies, employed by the nonlinear solver, are maintained, including its parallelisation. In case of a VOF method, as implemented in the current nonlinear solver, slightly more modifications are necessary, as the perturbation quantities and their evolution cannot be modelled in a straightforward manner using the VOF methodology. Therefore, the representation of these quantities is realised using a level-set formalism while the base flow representation remains that of the VOF method. This results in a mixed LS-VOF approach.

The gained flexibility of the Eulerian approach, however, comes at the expense of a reduced accuracy of the interface representation. While this remains uncritical for the cases studied in this thesis, it may lead to more significant inaccuracies for flows with large base flow curvatures or surface

[37]: Unverdi et al. (1992), ‘A front-tracking method for viscous, incompressible, multi-fluid flows’

[17]: Squire (1953), ‘Investigation of the instability of a moving liquid film’

[18]: Yih (1967), ‘Instability due to viscosity stratification’

[19]: Hagerly et al. (1955), ‘A study of the stability of moving liquid film’

[20]: Lin et al. (1990), ‘Absolute and convective instability of a liquid sheet’

[21]: Söderberg (2003), ‘Absolute and convective instability of a relaxational plane liquid jet’

[22]: Boeck et al. (2005), ‘Viscous versus inviscid instability of two-phase mixing layers with continuous velocity profile’

[23]: Tammissola et al. (2011), ‘Effect of surface tension on global modes of confined wake flows’

[24]: Tammissola et al. (2012), ‘Surface tension-induced global instability of planar jets and wakes’

tension. A possible solution to this problem could be the use of a linearised front-tracking solver which would result in a more accurate interface representation while retaining the benefits resulting from time-stepping and the avoidance of using multiple solvers. As the base flow is stationary, the treatment of interface topology changes would not be an issue.

Another problem are large density ratios between the phases (in case of water and air it is close to 800). These lead to problems for nonlinear solvers which translate to the linear solver as well. They are rooted in the solution of the poisson equation, used to enforce solenoidality of the velocity field in classic projection methods. As the density ratio increases, the discontinuity of the density fields becomes more pronounced which eventually leads to the equation being ill-conditioned [136]. As a result, inconsistent mass transfer across the interface occurs. Several strategies exist to alleviate this problem. While currently not employed, they could be adapted to the linear solver.

[136]: Desjardins et al. (2010), 'Methods for multiphase flows with high density ratio'

## 5.2 Perspectives

In this work, we have made two major contributions towards the development and application of current methods for the linear stability analysis of two-phase flows. We have investigated the potential of mean flow analysis to compute stability properties of a spatially developing two-phase flow, and we have developed a flexible framework for the global stability analysis of two-phase flows which can principally be applied to flows with arbitrary complexity in terms of interface topology and flow configuration. Still, several questions and potential avenues for further studies remain:

The mean flow analysis and interface model developed in this work are applied in a local stability framework, by assuming a parallel flow. A natural step would be the adaptation to a global framework, in order to, for instance, leverage the potential of mean flow analysis for a turbulent flow. It remains to be seen, whether the methodology for treating the interface in the local framework can be translated successfully to a global framework or if modifications or an alternative representation are necessary. Further, in case of a highly turbulent flow where breakup occurs, the question arises whether the assumption of a discrete interface position in the linear analysis is meaningful at all. As for such flows, the Weber number is typically very large and inertia dominates over surface tension. Therefore, a possible route towards mean flow stability analysis of such flows may be to model the two-phase character of the flow via the time-averaged density and viscosity fields only, thus neglecting the localised action of surface tension. A similar approach has been used successfully to model the global linear stability of reacting flows [72].

[72]: Terhaar et al. (2015), 'Key parameters governing the precessing vortex core in reacting flows: An experimental and analytical study'

The developed global stability framework has presently been used to solve the direct linearised Navier-Stokes equations for two-phase flows in a level-set framework. For future studies, the framework could be extended to also solve the adjoint equations in order to identify the so-called *wave maker* [137] or to investigate transient growth [47], associated with the non-normality of the Navier-Stokes operator. However, to our knowledge, the derivation of the required adjoint equations for two-phase flows has never been attempted and thus poses an individual research objective.

[137]: Chomaz (2005), 'Global instabilities in spatially developing flows: non-normality and nonlinearity'

[47]: Barkley et al. (2008), 'Direct optimal growth analysis for timesteppers'

In the context of Floquet analysis [138], the current framework can be used to compute the stability of time-periodic flows with minor modifications. Therefore, instead of loading a single base flow at the beginning of the linear time-stepping, at every time step an instantaneous base flow time slice is loaded or interpolated from a set of available time slices. The integration time to construct each Krylov vector corresponds to the period length  $\tau$  of the basic state. The wanted Floquet multipliers, determining the stability of the periodic orbit, are computed from the eigenvalues  $\lambda_j$  as  $\mu_j = \exp(\lambda_j \tau)$ . A similar time-stepping approach has been employed by [139] to model the subharmonic instability associated with vortex pairing in forced axisymmetric jets. In the context of two-phase flows, a potential application is the excitation of Faraday waves induced through a parametric excitation of a fluid interface. While these have been successfully modelled in a local framework, assuming flat or spherical interfaces [140, 141], computations for more complex interface topologies require the use global methods.

From a numerical point of view, several aspects could deserve further development.

First of all, a desirable improvement of the present framework lies in the computation of accurate base flows for arbitrary surface tension values which do not suffer from excessive spurious currents, thereby disturbing the interface position and leading to erroneous curvature values. This, however, is a problem not specific to the application of global stability analysis but to the numerical solution of the nonlinear equations in general. In order to alleviate this problem, improvements to the advection scheme of the volume fraction or level-set fields respectively and the coupling to the curvature computation have to be made. This remains an open field of research.

Another aspect concerns the convergence order of the employed schemes which currently result in an overall second-order accurate discretisation. A desirable property of matrix-forming approaches to linear stability analysis is the use of spectral discretisation methods (e.g. Chebyshev polynomials). Consequently, these methods provide excellent convergence properties and a high level of accuracy. In the context of matrix-free time-stepping solvers, a common approach for linear analysis of single-phase flows is the use of finite element methods with high-order polynomial basis function (Spectral Element Method) that achieve spectral-like accuracy (e.g. [142, 143]), in combination with a high-order temporal discretisation. In the present framework, an increase of the convergence order of the temporal discretisation, as well as the spatial discretisation of the advective and diffusive terms can be realised fairly straightforward, through the implementation of higher-order finite volume schemes (e.g. a Weighted Essentially Non Oscillatory (WENO) scheme [144]) or by compact finite difference schemes [145], in combination with, for instance, a fourth order Runge-Kutta scheme. To increase the convergence order of interface and curvature discretisations, higher-order polynomial schemes to compute distance functions [146] as well as higher-order height-function schemes have been proposed [147].

[138]: Floquet (1883), ‘Sur les équations différentielles linéaires à coefficients périodiques’

[139]: Shaabani-Ardali et al. (2019), ‘Vortex pairing in jets as a global Floquet instability: modal and transient dynamics’

[140]: Kumar et al. (1994), ‘Parametric instability of the interface between two fluids’

[141]: Adou et al. (2016), ‘Faraday instability on a sphere: Floquet analysis’

[142]: Karniadakis et al. (2013), *Spectral/hp element methods for computational fluid dynamics*

[143]: Peplinski et al. (2014), ‘Stability tools for the spectral-element code Nek5000: Application to jet-in-crossflow’

[144]: Harten et al. (1987), ‘Uniformly high order accurate essentially non-oscillatory schemes, III’

[145]: Lele (1992), ‘Compact finite difference schemes with spectral-like resolution’

[146]: Saye (2014), ‘High-order methods for computing distances to implicitly defined surfaces’

[147]: Sussman et al. (2006), ‘High-order techniques for calculating surface tension forces’



# Bibliography

Here are the references in citation order.

- [1] IEA. *World hydroelectricity production by region 1971-2019*. [Online; accessed 21-October-2021]. 2021 (cited on pages 1, 2).
- [2] IEA. *Renewable electricity generation by source (non-combustible), World 1990-2019*. [Online; accessed 21-October-2021]. 2021 (cited on pages 1, 2).
- [3] A. Favrel, A. Müller, C. Landry, K. Yamamoto, and F. Avellan. ‘Study of the vortex-induced pressure excitation source in a Francis turbine draft tube by particle image velocimetry’. In: *Experiments in Fluids* 56.12 (2015), pp. 1–15 (cited on page 2).
- [4] S. Alligne, C. Nicolet, Y. Tsujimoto, and F. Avellan. ‘Cavitation surge modelling in Francis turbine draft tube’. In: *Journal of Hydraulic Research* 52.3 (2014), pp. 399–411 (cited on pages 2, 85).
- [5] A. T. Favrel. ‘Dynamics of the cavitation precessing vortex rope for Francis turbines at part load operating conditions’. PhD thesis. EPFL, 2016 (cited on page 3).
- [6] U. Seidel, C. Mende, B. Hübner, W. Weber, and A. Otto. ‘Dynamic loads in Francis runners and their impact on fatigue life’. In: *IOP conference series: earth and environmental science*. Vol. 22. 3. IOP Publishing, 2014, p. 032054 (cited on page 3).
- [7] M. R. Ruith, P. Chen, E. Meiburg, and T. Maxworthy. ‘Three-dimensional vortex breakdown in swirling jets and wakes: direct numerical simulation’. In: *Journal of Fluid Mechanics* 486 (2003), pp. 331–378 (cited on pages 3, 84, 85, 90, 91, 94, 96, 108, 109, 112).
- [8] F. Gallaire, M. Ruith, E. Meiburg, J.-M. Chomaz, and P. Huerre. ‘Spiral vortex breakdown as a global mode’. In: *Journal of Fluid Mechanics* 549 (2006), pp. 71–80 (cited on pages 3, 84).
- [9] P. Meliga, F. Gallaire, and J.-M. Chomaz. ‘A weakly nonlinear mechanism for mode selection in swirling jets’. In: *Journal of Fluid Mechanics* 699 (2012), pp. 216–262 (cited on pages 3, 84, 96, 109, 110, 112, 118).
- [10] K. Oberleithner, M. Sieber, C. N. Nayeri, C. O. Paschereit, C. Petz, H.-C. Hege, B. R. Noack, and I. Wygnanski. ‘Three-dimensional coherent structures in a swirling jet undergoing vortex breakdown: stability analysis and empirical mode construction’. In: *Journal of Fluid Mechanics* 679 (2011), pp. 383–414 (cited on pages 3, 84).
- [11] O. Tammisola and M. P. Juniper. ‘Coherent structures in a swirl injector at  $Re=4800$  by nonlinear simulations and linear global modes’. In: *Journal of Fluid Mechanics* 792 (2016), pp. 620–657 (cited on page 3).
- [12] S. Pasche, F. Avellan, and F. Gallaire. ‘Part load vortex rope as a global unstable mode’. In: *Journal of Fluids Engineering* 139.5 (2017) (cited on page 3).
- [13] J. S. Müller, M. Sieber, I. Litvinov, S. Shtork, S. Alekseenko, and K. Oberleithner. ‘Prediction of vortex precession in the draft tube of a model hydro turbine using mean field stability theory and stochastic modelling’. In: *IOP Conference Series: Earth and Environmental Science*. Vol. 774. 1. IOP Publishing, 2021, p. 012003 (cited on page 3).
- [14] C. E. Brennen. *Cavitation and bubble dynamics*. Cambridge University Press, 2014 (cited on page 4).
- [15] D. Fuster. ‘A review of models for bubble clusters in cavitating flows’. In: *Flow, Turbulence and Combustion* 102.3 (2019), pp. 497–536 (cited on page 4).
- [16] A. Ferrari. ‘Fluid dynamics of acoustic and hydrodynamic cavitation in hydraulic power systems’. In: *Proceedings of the Royal Society A: Mathematical, Physical and Engineering Sciences* 473.2199 (2017), p. 20160345 (cited on page 4).

- [17] H. B. Squire. 'Investigation of the instability of a moving liquid film'. In: *British Journal of Applied Physics* 4.6 (1953), p. 167 (cited on pages 4, 20, 56, 78, 119).
- [18] C. Yih. 'Instability due to viscosity stratification'. In: *Journal of Fluid Mechanics* 27.2 (1967), pp. 337–352 (cited on pages 4, 20, 56, 85, 109, 119).
- [19] W. Hagerty and J. F. Shea. 'A study of the stability of moving liquid film'. In: *ASME Journal of Applied Mechanics* 22 (1955), pp. 509–514 (cited on pages 4, 20, 56, 78, 119).
- [20] S. P. Lin, Z. W. Lian, and B. J. Creighton. 'Absolute and convective instability of a liquid sheet'. In: *Journal of Fluid Mechanics* 220 (1990), pp. 673–689 (cited on pages 4, 20, 119).
- [21] L. D. Söderberg. 'Absolute and convective instability of a relaxational plane liquid jet'. In: *Journal of Fluid Mechanics* 493 (2003), pp. 89–119 (cited on pages 4, 11, 20, 29, 30, 33, 35, 40, 41, 49, 52, 119).
- [22] T. Boeck and S. Zaleski. 'Viscous versus inviscid instability of two-phase mixing layers with continuous velocity profile'. In: *Physics of fluids* 17.3 (2005), p. 032106 (cited on pages 4, 11, 20, 56, 119).
- [23] O. Tammisola, F. Lundell, and L. D. Söderberg. 'Effect of surface tension on global modes of confined wake flows'. In: *Physics of Fluids* 23.1 (2011), p. 014108 (cited on pages 4, 13, 56, 119).
- [24] O. Tammisola, F. Lundell, and L. D. Söderberg. 'Surface tension-induced global instability of planar jets and wakes'. In: *Journal of Fluid Mechanics* 713 (2012), pp. 632–658 (cited on pages 4, 13, 20, 55–57, 62, 66, 68, 71–74, 76, 78–80, 116, 117, 119).
- [25] S. Popinet. 'Gerris: a tree-based adaptive solver for the incompressible Euler equations in complex geometries'. In: *Journal of Computational Physics* 190.2 (2003), pp. 572–600 (cited on pages 5, 22, 60, 87).
- [26] S. Popinet. 'An accurate adaptive solver for surface-tension-driven interfacial flows'. In: *Journal of Computational Physics* 228.16 (2009), pp. 5838–5866 (cited on pages 5, 22, 60, 71, 87).
- [27] T. Abadie, J. Aubin, and D. Legendre. 'On the combined effects of surface tension force calculation and interface advection on spurious currents within Volume of Fluid and Level Set frameworks'. In: *Journal of Computational Physics* 297 (2015), pp. 611–636 (cited on pages 5, 72).
- [28] J. W. Hoyt and J. J. Taylor. 'Waves on water jets'. In: *Journal of Fluid Mechanics* 83.1 (1977), pp. 119–127 (cited on page 5).
- [29] S. Schmidt, O. Krüger, K. Göckeler, and C. O. Paschereit. 'Numerical investigation of the breakup behavior of an oscillating two-phase jet'. In: *Physics of Fluids* 30.7 (2018), p. 072101 (cited on pages 5, 20, 27).
- [30] X. D. Shi, M. P. Brenner, and S. R. Nagel. 'A cascade of structure in a drop falling from a faucet'. In: *Science* 265.5169 (1994), pp. 219–222 (cited on page 5).
- [31] J. P. Kubitschek and P. D. Weidman. 'Helical instability of a rotating viscous liquid jet'. In: *Physics of Fluids* 19.11 (2007), p. 114108 (cited on pages 5, 7, 85).
- [32] J. A. F. Plateau. *Statique expérimentale et théorique des liquides soumis aux seules forces moléculaires*. Vol. 2. Gauthier-Villars, 1873 (cited on page 6).
- [33] L. Rayleigh. 'On the capillary phenomena of jets'. In: *Proceedings of the Royal Society of London* 29.196-199 (1879), pp. 71–97 (cited on page 6).
- [34] P. Marmottant and E. Villermaux. 'On spray formation'. In: *Journal of Fluid Mechanics* 498 (2004), pp. 73–111 (cited on pages 7, 47).
- [35] G. Tryggvason, R. Scardovelli, and S. Zaleski. *Direct Numerical Simulations of Gas–Liquid Multiphase Flows*. Cambridge University Press, 2011 (cited on pages 7, 21).
- [36] D. E. Fyfe, E. S. Oran, and M. J. Fritts. 'Surface tension and viscosity with Lagrangian hydrodynamics on a triangular mesh'. In: *Journal of Computational Physics* 76.2 (1988), pp. 349–384 (cited on pages 8, 118).
- [37] S. O. Unverdi and G. Tryggvason. 'A front-tracking method for viscous, incompressible, multi-fluid flows'. In: *Journal of Computational Physics* 100.1 (1992), pp. 25–37 (cited on pages 8, 119).

- [38] R. Scardovelli and S. Zaleski. ‘Direct numerical simulation of free-surface and interfacial flow’. In: *Annual Review of Fluid Mechanics* 31.1 (1999), pp. 567–603 (cited on pages 8, 22, 58, 87).
- [39] M. Sussman, P. Smereka, S. Osher, et al. ‘A level set approach for computing solutions to incompressible two-phase flow’. In: *Journal of Computational Physics* 114.1 (1994), pp. 146–159 (cited on pages 8, 58, 87, 118).
- [40] D. M. Anderson, G. B. McFadden, and A. A. Wheeler. ‘Diffuse-interface methods in fluid mechanics’. In: *Annual Review of Fluid Mechanics* 30.1 (1998), pp. 139–165 (cited on pages 8, 118).
- [41] J. U. Brackbill, D. B. Kothe, and C. Zemach. ‘A continuum method for modeling surface tension’. In: *Journal of Computational Physics* 100.2 (1992), pp. 335–354 (cited on pages 9, 22, 58, 87).
- [42] R. J. Briggs. *Electron-stream interaction with plasmas*. MIT-Press, 1964 (cited on page 10).
- [43] P. Huerre and P. A. Monkewitz. ‘Local and global instabilities in spatially developing flows’. In: *Annual Review of Fluid Mechanics* 22.1 (1990), pp. 473–537 (cited on page 10).
- [44] M. Van Dyke. *An album of fluid motion*. Vol. 176. Parabolic Press Stanford, 1982 (cited on page 11).
- [45] O. Tammisola, A. Sasaki, F. Lundell, M. Matsubara, and L. D. Söderberg. ‘Stabilizing effect of surrounding gas flow on a plane liquid sheet’. In: *Journal of Fluid Mechanics* 672 (2011), pp. 5–32 (cited on pages 11, 20, 27, 29, 32, 33, 40, 41).
- [46] L. S. Tuckerman and D. Barkley. ‘Bifurcation analysis for timesteppers’. In: *Numerical methods for bifurcation problems and large-scale dynamical systems*. Springer, 2000, pp. 453–466 (cited on pages 13, 65, 88).
- [47] D. Barkley, H. M. Blackburn, and S. J. Sherwin. ‘Direct optimal growth analysis for timesteppers’. In: *International Journal for Numerical Methods in Fluids* 57.9 (2008), pp. 1435–1458 (cited on pages 13, 56, 65, 66, 88, 120).
- [48] Y. Saad. *Numerical Methods for Large Eigenvalue Problems: Revised Edition*. SIAM, 2011 (cited on pages 13, 66).
- [49] B. R. Noack, K. Afanasiev, M. Morzyński, G. Tadmor, and F. Thiele. ‘A hierarchy of low-dimensional models for the transient and post-transient cylinder wake’. In: *Journal of Fluid Mechanics* 497 (2003), pp. 335–363 (cited on pages 14, 28).
- [50] W. C. Reynolds and A. K. M. F. Hussain. ‘The mechanics of an organized wave in turbulent shear flow. Part 3. Theoretical models and comparisons with experiments’. In: *Journal of Fluid Mechanics* 54.2 (1972), pp. 263–288 (cited on pages 14, 28, 45).
- [51] D. Sipp and A. Lebedev. ‘Global stability of base and mean flows: a general approach and its applications to cylinder and open cavity flows’. In: *Journal of Fluid Mechanics* 593 (2007), pp. 333–358 (cited on pages 15, 21, 43, 49, 116).
- [52] S. E. Turton, L. S. Tuckerman, and D. Barkley. ‘Prediction of frequencies in thermosolutal convection from mean flows’. In: *Physical Review E* 91.4 (2015), p. 043009 (cited on pages 15, 43, 45, 49, 85, 116).
- [53] B. C. Bobusch, R. Woszidlo, J. M. Bergada, C. N. Nayeri, and C. O. Paschereit. ‘Experimental study of the internal flow structures inside a fluidic oscillator’. In: *Experiments in Fluids* 54.6 (2013), p. 1559 (cited on page 20).
- [54] O. Krüger, B. C. Bobusch, R. Woszidlo, and C. O. Paschereit. ‘Numerical modeling and validation of the flow in a fluidic oscillator’. In: *21st AIAA Computational Fluid Dynamics Conference*. 2013, p. 3087 (cited on page 20).
- [55] L. Rayleigh. ‘On The Instability Of Jets’. In: *Proceedings of the London Mathematical Society* s1-10.1 (1878), pp. 4–13 (cited on pages 20, 56).
- [56] P. G. Drazin and W. H. Reid. *Hydrodynamic Stability*. Cambridge Mathematical Library 1. Cambridge University Press, 2004 (cited on pages 20, 56).
- [57] X. Li and R. S. Tankin. ‘On the temporal instability of a two-dimensional viscous liquid sheet’. In: *Journal of Fluid Mechanics* 226 (1991), pp. 425–443 (cited on page 20).

- [58] X. Li. 'Spatial instability of plane liquid sheets'. In: *Chemical Engineering Science* 48.16 (1993), pp. 2973–2981 (cited on page 20).
- [59] H. Schlichting and K. Gersten. *Grenzschicht-Theorie*. Springer-Verlag, 2006 (cited on page 20).
- [60] J. M. Gordillo and M. Pérez-Saborid. 'Aerodynamic effects in the break-up of liquid jets: on the first wind-induced break-up regime'. In: *Journal of Fluid Mechanics* 541 (2005), pp. 1–20 (cited on pages 20, 30, 32, 33).
- [61] B. Pier. 'On the frequency selection of finite-amplitude vortex shedding in the cylinder wake'. In: *Journal of Fluid Mechanics* 458 (2002), pp. 407–417 (cited on pages 21, 30).
- [62] D. Barkley. 'Linear analysis of the cylinder wake mean flow'. In: *EPL (Europhysics Letters)* 75.5 (2006), p. 750 (cited on pages 21, 29, 76).
- [63] K. Oberleithner, L. Rukes, and J. Soria. 'Mean flow stability analysis of oscillating jet experiments'. In: *Journal of Fluid Mechanics* 757 (2014), pp. 1–32 (cited on pages 21, 30, 38, 42, 45, 46, 50, 76, 116).
- [64] C. W. Hirt and B. D. Nichols. 'Volume of fluid (VOF) method for the dynamics of free boundaries'. In: *Journal of Computational Physics* 39.1 (1981), pp. 201–225 (cited on page 22).
- [65] M. M. Francois, S. J. Cummins, E. D. Dendy, D. B. Kothe, J. M. Sicilian, and M. W. Williams. 'A balanced-force algorithm for continuous and sharp interfacial surface tension models within a volume tracking framework'. In: *Journal of Computational Physics* 213.1 (2006), pp. 141–173 (cited on page 22).
- [66] D. J. E. Harvie, M. R. Davidson, and M. Rudman. 'An analysis of parasitic current generation in volume of fluid simulations'. In: *Applied Mathematical Modelling* 30.10 (2006), pp. 1056–1066 (cited on pages 22, 59).
- [67] M. D. Torrey, L. D. Cloutman, R. C. Mjolsness, and C. W. Hirt. *NASA-VOF2D: A Computer Program for Incompressible Flows With Free Surfaces*. Tech. rep. Los Alamos National Lab., 1985 (cited on pages 22, 118).
- [68] S. J. Cummins, M. M. Francois, and D. B. Kothe. 'Estimating curvature from volume fractions'. In: *Computers & Structures* 83.6 (2005), pp. 425–434 (cited on pages 22, 59).
- [69] J. A. van Hooft, S. Popinet, C. C. van Heerwaarden, S. J. A. van der Linden, S. R. de Roode, and B. J. H. van de Wiel. 'Towards adaptive grids for atmospheric boundary-layer simulations'. In: *Boundary-Layer Meteorology* 167.3 (2018), pp. 421–443 (cited on page 24).
- [70] J. Cohen and I. Wygnanski. 'The evolution of instabilities in the axisymmetric jet. Part 1. The linear growth of disturbances near the nozzle'. In: *Journal of Fluid Mechanics* 176 (1987), pp. 191–219 (cited on page 30).
- [71] K. Oberleithner, C. O. Paschereit, and I. Wygnanski. 'On the impact of swirl on the growth of coherent structures'. In: *Journal of Fluid Mechanics* 741 (2014), pp. 156–199 (cited on page 30).
- [72] S. Terhaar, K. Oberleithner, and C. O. Paschereit. 'Key parameters governing the precessing vortex core in reacting flows: An experimental and analytical study'. In: *Proceedings of the Combustion Institute* 35.3 (2015), pp. 3347–3354 (cited on pages 30, 120).
- [73] B. Emerson, T. Lieuwen, and M. P. Juniper. 'Local stability analysis and eigenvalue sensitivity of reacting bluff-body wakes'. In: *Journal of Fluid Mechanics* 788 (2016), pp. 549–575 (cited on page 30).
- [74] D. G. Crighton and M. Gaster. 'Stability of slowly diverging jet flow'. In: *Journal of Fluid Mechanics* 77.2 (1976), pp. 397–413 (cited on page 30).
- [75] T. Herbert. 'Parabolized stability equations'. In: *Annual Review of Fluid Mechanics* 29.1 (1997), pp. 245–283 (cited on page 30).
- [76] L. C. Cheung and T. A. Zaki. 'Linear and nonlinear instability waves in spatially developing two-phase mixing layers'. In: *Physics of Fluids* 22.5 (2010), p. 052103 (cited on page 30).
- [77] S. Beneddine, D. Sipp, A. Arnault, J. Dandois, and L. Lesshafft. 'Conditions for validity of mean flow stability analysis'. In: *Journal of Fluid Mechanics* 798 (2016), pp. 485–504 (cited on page 30).

- [78] J. J. Dongarra, B. Straughan, and D. W. Walker. ‘Chebyshev tau-QZ algorithm methods for calculating spectra of hydrodynamic stability problems’. In: *Applied Numerical Mathematics* 22.4 (1996), pp. 399–434 (cited on pages 32, 51).
- [79] P. A. M. Boomkamp and R. H. M. Miesen. ‘Classification of instabilities in parallel two-phase flow’. In: *International Journal of Multiphase Flow* 22 (1996), pp. 67–88 (cited on pages 35, 52).
- [80] T. Otto. ‘Spatio-Temporal Stability Analysis in Two-Phase Mixing Layers’. PhD thesis. Technische Universität Ilmenau, 2012 (cited on pages 35, 52).
- [81] S. A. Orszag and S. C. Crow. ‘Instability of a vortex sheet leaving a semi-infinite plate’. In: *Studies in Applied Mathematics* 49.2 (1970), pp. 167–181 (cited on page 38).
- [82] I. Delbende, J. Chomaz, and P. Huerre. ‘Absolute/convective instabilities in the Batchelor vortex: a numerical study of the linear impulse response’. In: *Journal of Fluid Mechanics* 355 (1998), pp. 229–254 (cited on page 38).
- [83] E. Boujo, M. Bauerheim, and N. Noiray. ‘Saturation of a turbulent mixing layer over a cavity: response to harmonic forcing around mean flows’. In: *Journal of Fluid Mechanics* 853 (2018), pp. 386–418 (cited on pages 43, 76, 85).
- [84] V. Mantič-Lugo, C. Arratia, and F. Gallaire. ‘Self-consistent mean flow description of the nonlinear saturation of the vortex shedding in the cylinder wake’. In: *Physical Review Letters* 113.8 (2014), p. 084501 (cited on page 43).
- [85] P. Yecko and S. Zaleski. ‘Transient growth in two-phase mixing layers’. In: *Journal of Fluid Mechanics* 528 (2005), pp. 43–52 (cited on page 46).
- [86] L. De Luca. ‘Non-modal growth of disturbances in free-surface flows’. In: *Proceedings of International Conference RDAMM-2001*. Vol. 6. 2. 2001 (cited on page 46).
- [87] C. Mehring and W. A. Sirignano. ‘Nonlinear capillary wave distortion and disintegration of thin planar liquid sheets’. In: *Journal of Fluid Mechanics* 388 (1999), pp. 69–113 (cited on page 46).
- [88] C. J. Clark and N. Dombrowski. ‘Aerodynamic instability and disintegration of inviscid liquid sheets’. In: *Proceedings of the Royal Society of London. A. Mathematical and Physical Sciences* 329.1579 (1972), pp. 467–478 (cited on page 46).
- [89] D. Jarrabhashi and W. A. Sirignano. ‘Vorticity dynamics for transient high-pressure liquid injection’. In: *Physics of Fluids* 26.10 (2014), p. 73 (cited on page 47).
- [90] A. Zandian, W. A. Sirignano, and F. Hussain. ‘Understanding liquid-jet atomization cascades via vortex dynamics’. In: *Journal of Fluid Mechanics* 843 (2018), pp. 293–354 (cited on page 47).
- [91] L. Biancofiore, F. Gallaire, P. Laure, and E. Hachem. ‘Direct numerical simulations of two-phase immiscible wakes’. In: *Fluid Dynamics Research* 46.4 (2014), p. 041409 (cited on pages 56, 57, 79, 80).
- [92] P. J. Schmid and D. S. Henningson. *Stability and transition in shear flows*. Vol. 142. Springer Science & Business Media, 2012 (cited on page 56).
- [93] L. D. Söderberg. ‘Absolute and convective instability of a relaxational plane liquid jet’. In: *Journal of Fluid Mechanics* 493 (2003), p. 89 (cited on page 56).
- [94] S. J. Rees and M. P. Juniper. ‘The effect of surface tension on the stability of unconfined and confined planar jets and wakes’. In: *Journal of Fluid Mechanics* 633 (2009), p. 71 (cited on pages 56, 78, 117).
- [95] A. Sevilla. ‘The effect of viscous relaxation on the spatiotemporal stability of capillary jets’. In: *Journal of Fluid Mechanics* 684 (2011), pp. 204–226 (cited on page 56).
- [96] O. Tammisola, J.-C. Loiseau, and L. Brandt. ‘Effect of viscosity ratio on the self-sustained instabilities in planar immiscible jets’. In: *Physical Review Fluids* 2 (3 Mar. 2017), p. 033903 (cited on page 56).
- [97] C. S. Peskin. ‘Flow patterns around heart valves: a numerical method’. In: *Journal of Computational Physics* 10.2 (1972), pp. 252–271 (cited on page 58).
- [98] S. Popinet. ‘Numerical models of surface tension’. In: *Annual Review of Fluid Mechanics* 50 (2018), pp. 49–75 (cited on pages 59, 87).

- [99] A. J. Chorin. ‘On the convergence of discrete approximations to the Navier–Stokes equations’. In: *Mathematics of Computation* 23.106 (1969), pp. 341–353 (cited on page 60).
- [100] J. B. Bell, P. Colella, and H. M. Glaz. ‘A second-order projection method for the incompressible Navier–Stokes equations’. In: *Journal of Computational Physics* 85.2 (1989), pp. 257–283 (cited on pages 60, 62).
- [101] M. Rubio-Rubio, A. Sevilla, and J. M. Gordillo. ‘On the thinnest steady threads obtained by gravitational stretching of capillary jets’. In: *Journal of Fluid Mechanics* 729 (2013), pp. 471–483 (cited on page 66).
- [102] J. Eggers and T. F. Dupont. ‘Drop formation in a one-dimensional approximation of the Navier–Stokes equation’. In: *Journal of Fluid Mechanics* 262 (1994), pp. 205–221 (cited on page 66).
- [103] C. W. Rowley, I. Mezić, S. Bagheri, P. Schlatter, and D. S. Henningson. ‘Spectral analysis of nonlinear flows’. In: *Journal of Fluid Mechanics* 641 (2009), pp. 115–127 (cited on page 68).
- [104] P. J. Schmid. ‘Dynamic mode decomposition of numerical and experimental data’. In: *Journal of Fluid Mechanics* 656 (2010), pp. 5–28 (cited on page 68).
- [105] K. K. Chen, J. H. Tu, and C. W. Rowley. ‘Variants of dynamic mode decomposition: boundary condition, Koopman, and Fourier analyses’. In: *Journal of Nonlinear Science* 22.6 (2012), pp. 887–915 (cited on page 68).
- [106] S. Schmidt and K. Oberleithner. ‘Instability of forced planar liquid jets: mean field analysis and nonlinear simulation’. In: *Journal of Fluid Mechanics* 883 (2020) (cited on pages 76, 85).
- [107] L. Biancofiore and F. Gallaire. ‘Influence of confinement on temporal stability of plane jets and wakes’. In: *Physics of Fluids* 22.1 (2010), p. 014106 (cited on page 78).
- [108] L. Biancofiore, F. Gallaire, and E. Heifetz. ‘Interaction between counterpropagating Rossby waves and capillary waves in planar shear flows’. In: *Physics of Fluids* 27.4 (2015), p. 044104 (cited on pages 78, 79).
- [109] L. Biancofiore, E. Heifetz, J. Hoepffner, and F. Gallaire. ‘Understanding the destabilizing role for surface tension in planar shear flows in terms of wave interaction’. In: *Physical Review Fluids* 2.10 (2017), p. 103901 (cited on pages 78, 79).
- [110] O. T. Schmidt. ‘Bispectral mode decomposition of nonlinear flows’. In: *Nonlinear Dynamics* 102.4 (2020), pp. 2479–2501 (cited on pages 83, 85, 92, 117).
- [111] O. Lucca-Negro and T. O’doherthy. ‘Vortex breakdown: a review’. In: *Progress in Energy and Combustion Science* 27.4 (2001), pp. 431–481 (cited on page 84).
- [112] M. P. Escudier and N. Zehnder. ‘Vortex-flow regimes’. In: *Journal of Fluid Mechanics* 115 (1982), pp. 105–121 (cited on pages 84, 91, 109).
- [113] P. Billant, J.-M. Chomaz, and P. Huerre. ‘Experimental study of vortex breakdown in swirling jets’. In: *Journal of Fluid Mechanics* 376 (1998), pp. 183–219 (cited on page 84).
- [114] K. Oberleithner, C. O. Paschereit, R. Seele, and I. Wygnanski. ‘Formation of turbulent vortex breakdown: intermittency, criticality, and global instability’. In: *AIAA J.* 50.7 (2012), pp. 1437–1452 (cited on page 84).
- [115] M. Vanierschot. ‘On the dynamics of the transition to vortex breakdown in axisymmetric inviscid swirling flows’. In: *European Journal of Mechanics - B/Fluids* 65 (2017), pp. 65–69 (cited on page 84).
- [116] T. B. Benjamin. ‘Theory of the vortex breakdown phenomenon’. In: *Journal of Fluid Mechanics* 14.4 (1962), pp. 593–629 (cited on page 84).
- [117] W. J. Grabowski and S. A. Berger. ‘Solutions of the Navier-Stokes equations for vortex breakdown’. In: *Journal of Fluid Mechanics* 75.3 (1976), pp. 525–544 (cited on pages 84, 89).
- [118] H. Liang and T. Maxworthy. ‘An experimental investigation of swirling jets’. In: *Journal of Fluid Mechanics* 525 (2005), pp. 115–159 (cited on page 84).
- [119] S. Pasche, F. Avellan, and F. Gallaire. ‘Onset of chaos in helical vortex breakdown at low Reynolds number’. In: *Physical Review Fluids* 3.6 (2018), p. 064701 (cited on pages 85, 111).
- [120] M. Vanierschot, J. S. Müller, M. Sieber, M. Percin, B. W. van Oudheusden, and K. Oberleithner. ‘Single- and double-helix vortex breakdown as two dominant global modes in turbulent swirling jet flow’. In: *Journal of Fluid Mechanics* 883 (2020) (cited on pages 85, 118).

- [121] J. P. Kubitschek and P. D. Weidman. ‘The effect of viscosity on the stability of a uniformly rotating liquid column in zero gravity’. In: *Journal of Fluid Mechanics* 572 (2007), pp. 261–286 (cited on page 85).
- [122] R. Hreiz, C. Gentric, N. Midoux, R. Lainé, and D. Fünfschilling. ‘Hydrodynamics and velocity measurements in gas–liquid swirling flows in cylindrical cyclones’. In: *Chemical Engineering Research and Design* 92.11 (2014), pp. 2231–2246 (cited on page 85).
- [123] M. Maly, O. Cejpek, M. Sapik, V. Ondracek, G. Wigley, and J. Jedelsky. ‘Internal flow dynamics of spill-return pressure-swirl atomizers’. In: *Experimental Thermal and Fluid Science* 120 (2021), p. 110210 (cited on page 85).
- [124] C. E. Hickox. ‘Instability due to viscosity and density stratification in axisymmetric pipe flow’. In: *Physics of Fluids* 14.2 (1971), pp. 251–262 (cited on pages 85, 109).
- [125] A. P. Hooper and W. G. C. Boyd. ‘Shear-flow instability at the interface between two viscous fluids’. In: *Journal of Fluid Mechanics* 128 (1983), pp. 507–528 (cited on pages 85, 109).
- [126] R. H. Kraichnan. ‘Inertial ranges in two-dimensional turbulence’. In: *Physics of Fluids* 10.7 (1967), pp. 1417–1423 (cited on page 85).
- [127] A. D. D. Craik. ‘Non-linear resonant instability in boundary layers’. In: *Journal of Fluid Mechanics* 50.2 (1971), pp. 393–413 (cited on page 85).
- [128] S. Schmidt, O. Tammisola, L. Lesshafft, and K. Oberleithner. ‘Global stability and nonlinear dynamics of wake flows with a two-fluid interface’. In: *Journal of Fluid Mechanics* 915 (2021) (cited on pages 86, 88, 89).
- [129] M. R. Ruith, P. Chen, and E. Meiburg. ‘Development of boundary conditions for direct numerical simulations of three-dimensional vortex breakdown phenomena in semi-infinite domains’. In: *Computers & Fluids* 33.9 (2004), pp. 1225–1250 (cited on page 90).
- [130] K. Oberleithner, C. O. Paschereit, and I. Wygnanski. ‘On the impact of swirl on the growth of coherent structures’. In: *Journal of Fluid Mechanics* 741 (2014), pp. 156–199 (cited on page 91).
- [131] C. W. Rowley, I. Mezić, S. Bagheri, P. Schlatter, and D. S. Henningson. ‘Spectral analysis of nonlinear flows’. In: *Journal of Fluid Mechanics* 641 (2009), pp. 115–127 (cited on page 91).
- [132] P. J. Schmid. ‘Dynamic mode decomposition of numerical and experimental data’. In: *Journal of Fluid Mechanics* 656 (2010), pp. 5–28 (cited on page 91).
- [133] U. A. Qadri, D. Mistry, and M. P. Juniper. ‘Structural sensitivity of spiral vortex breakdown’. In: *Journal of Fluid Mechanics* 720 (2013), pp. 558–581 (cited on pages 96, 112).
- [134] J. Jeong and F. Hussain. ‘On the identification of a vortex’. In: *Journal of Fluid Mechanics* 285 (1995), pp. 69–94 (cited on page 98).
- [135] E. J. Hinch. ‘A note on the mechanism of the instability at the interface between two shearing fluids’. In: *Journal of Fluid Mechanics* 144 (1984), pp. 463–465 (cited on page 109).
- [136] O. Desjardins and V. Moureau. ‘Methods for multiphase flows with high density ratio’. In: *Center for Turbulent Research, Summer Programm 2010* (2010), pp. 313–322 (cited on page 120).
- [137] J.-M. Chomaz. ‘Global instabilities in spatially developing flows: non-normality and nonlinearity’. In: *Annual Review of Fluid Mechanics* 37 (2005), pp. 357–392 (cited on page 120).
- [138] G. Floquet. ‘Sur les équations différentielles linéaires à coefficients périodiques’. In: *Annales scientifiques de l’École normale supérieure*. Vol. 12. 1883, pp. 47–88 (cited on page 121).
- [139] L. Shaabani-Ardali, D. Sipp, and L. Lesshafft. ‘Vortex pairing in jets as a global Floquet instability: modal and transient dynamics’. In: *Journal of Fluid Mechanics* 862 (2019), pp. 951–989 (cited on page 121).
- [140] K. Kumar and L. S. Tuckerman. ‘Parametric instability of the interface between two fluids’. In: *Journal of Fluid Mechanics* 279 (1994), pp. 49–68 (cited on page 121).
- [141] A. E. Adou and L. S. Tuckerman. ‘Faraday instability on a sphere: Floquet analysis’. In: *Journal of Fluid Mechanics* 805 (2016), pp. 591–610 (cited on page 121).
- [142] G. Karniadakis and S. Sherwin. *Spectral/hp element methods for computational fluid dynamics*. Oxford University Press, 2013 (cited on page 121).

- [143] A. Peplinski, P. Schlatter, P. F. Fischer, and D. S. Henningson. ‘Stability tools for the spectral-element code Nek5000: Application to jet-in-crossflow’. In: *Spectral and High Order Methods for Partial Differential Equations-ICOSAHOM 2012*. Springer, 2014, pp. 349–359 (cited on page 121).
- [144] A. Harten, B. Engquist, S. Osher, and S. R. Chakravarthy. ‘Uniformly high order accurate essentially non-oscillatory schemes, III’. In: *Upwind and high-resolution schemes*. Springer, 1987, pp. 218–290 (cited on page 121).
- [145] S. K. Lele. ‘Compact finite difference schemes with spectral-like resolution’. In: *Journal of Computational Physics* 103.1 (1992), pp. 16–42 (cited on page 121).
- [146] R. Saye. ‘High-order methods for computing distances to implicitly defined surfaces’. In: *Communications in Applied Mathematics and Computational Science* 9.1 (2014), pp. 107–141 (cited on page 121).
- [147] M. Sussman and M. Ohta. ‘High-order techniques for calculating surface tension forces’. In: *Free Boundary Problems*. Springer, 2006, pp. 425–434 (cited on page 121).